Helicon wave propagation and plasma equilibrium in high-density hydrogen plasma in converging magnetic fields

Juan Francisco Caneses Marin

A thesis submitted for the degree of

Doctor of Philosophy

of the Australian National University

Plasma Research Laboratory

Research School of Physics and Engineering

ANU college of Physical and Mathematical Sciences

October 2015

Declaration

This thesis is an account of research undertaken between February 2010 and October 2015 at the Research School of Physics and Engineering, ANU college of Physical and Mathematical Sciences, The Australian National University, Canberra, Australia. Except where acknowledged in the customary manner, the material presented in this thesis is, to the best of my knowledge, original and has not been submitted in whole or part for a degree in any university.

Juan Francisco Caneses Marin

October 2015

Acknowledgements

I would like to thank my supervisor Dr. Boyd Blackwell for his invaluable guidance, impressive physical insight and advice during these five years. He always seemed to have time whenever I knocked on his office door for questions. I am very grateful to both Dr. Boyd Blackwell and Professor John Howard for allowing me to undertake this PhD in Plasma Physics in spite of my Mechanical Engineering background. It has been an exciting journey of self-discovery, learning and character building.

I would like to extend my gratitude to the people at the PRL, especially to John Wach, Michael Blacksell, Mark Gwynneth, Peter Alexander, Dr Cormac Corr and Dr. Horst Punzmann for their support during the design and construction of MAGPIE and their assistance in building diagnostics for my PhD. I would like to thank Daniel Tempra, Dennis Gibson, and Tristan Steele from the Electronics Unit for their support in setting up the RF systems in MAGPIE. In addition, Craig Young and Miro from the Mechanical Workshop for making parts for my diagnostics on short notice. I am grateful to my colleagues Dr. Lei Chang who provided important wave simulation results for my PhD thesis and Dr. Fenton Glass for helping me build the microwave interferometer for my experiments. I would like to thank Uyen for helping organize my overseas research trips and purchasing components online for my experiments. I would like to express my gratitude to Karen Nulty for her patience, diligence and support with my innumerable program extensions. I am very grateful for the many friends I made during my stay at the PRL: James, Nandi, Shaun, Cameron, Romana, Haitao, Trevor, Jessica, Wes, Stuart, Dave, Timo and Lei.

When it comes to inspiration, I would like to thank my best friend Joshua Griffin in Brisbane for invaluable discussions in math and physics and for inspiring me to try something new. I would also like to thank Dr. Frank Chang Diaz, whom I have not met in person but inspired me five years ago, through his personal journey, to pursue the goal of thermonuclear fusion. At that point, I decided to contact Professor John Howard from the PRL. I would like to thank my parents Marta and Roberto, for believing in me and their words of encouragement throughout my PhD. I am very grateful for all those times in my childhood when they supported me in my dream of becoming an “inventor”. Little I knew at the age of eight, that I was going to be become “obsessed” with thermonuclear fusion 15 years down the track. I remember all those times when they drove me to the warehouse or to the carpenter’s workshops in El Salvador to get components for my garage “experiments”.

I am very grateful to my wife Courtney and my son Adrian. I have received so much support, encouragement and love from Courtney. Thank you for looking after me during those times that I felt frustrated or exhausted during the PhD and reminding me of the power of “quiet time”. Remember the times you reminded me to get out of the “cave”, have a shower, get fresh air and something to eat? Thank you. I am very grateful for Adi, for bringing joy into our lives and showing me the pleasure of just hanging out. Thank you for being there in my office with me almost every day for a 6 am start. I dedicate this work to my wife and son.

Publications

This thesis has resulted in a number of publications in peer reviewed journals, as listed below. Some of the results presented in the chapters to follow have been adapted from the material in these publications.

“Transport simulations of linear plasma generators with the B2.5-Eirene and EMC3-Eirene codes”
J. Rapp, L. W. Owen, X. Bonnin, **J. F. Caneses**, J. M. Canik, C. Corr, and J. D. Lore
Journal of Nuclear Materials, vol. 463, pp. 510–514, Aug. 2015.

“RF compensation of Double Langmuir Probes – modelling and experiment”,
J. F. Caneses, B. D. Blackwell
Plasma Sources Sci. Technol., vol. 24, no. 3, p. 035024, Jun. 2015.

“Design and characterization of the Magnetized Plasma Interaction Experiment (MAGPIE): a new source for plasma–material interaction studies”,
B. D. Blackwell, **J. F. Caneses**, C. M. Samuell, J. Wach, J. Howard, and C. Corr
Plasma Sources Sci. Technol., vol. 21, no. 5, p. 055033, Oct. 2012.

“**Wave modeling in a cylindrical non-uniform helicon discharge**”
L. Chang, M. J. Hole, **J. F. Caneses**, G. Chen, B. D. Blackwell, and C. S. Corr
Physics of Plasmas, vol. 19, no. 8, pp. 083511–083511–10, Aug. 2012.

Abstract

In this thesis, we investigate wave propagation and plasma equilibrium in MAGPIE, a helicon based linear plasma device constructed at the Australian National University, to study plasma-material interactions under divertor-relevant plasma conditions. We show that MAGPIE is capable of producing low temperature (1–8 eV) high density hydrogen plasma ($2\text{–}3\times10^{19}$ m^{-3}) with 20 kW of RF power when the confining magnetic field is converging.

The original research herein described comprises: (1) Characterization of hydrogen plasma in MAGPIE, (2) Analysis of the RF compensation of double Langmuir probes, (3) Excitation, propagation and damping of helicon waves in uniform and non-uniform magnetic fields and (4) Steady-state force balance and equilibrium profiles in MAGPIE.

We develop an analytical model of the physics of floating probes to describe and quantify the RF compensation of the DLP technique. Experimental validation for the model is provided. We show that (1) whenever finite sheath effects are important, overestimation of the ion density is proportional to the level of RF rectification and suggest that (2) electron temperature measurements are weakly affected.

We develop a uniform plasma full wave code to describe wave propagation in MAGPIE. We show that under typical MAGPIE operating conditions, the helical antenna is not optimized to couple waves in the plasma; instead, the antenna's azimuthal current rings excites helicon waves which propagate approximately along the whistler wave ray direction, constructively interfere on-axis and lead to the formation of an axial interference pattern. We show that helicon wave attenuation can be explained entirely through electron-ion and electron-neutral collisions. Results from a two-dimensional full wave code reveal that RF power deposition is axially non-uniform with both edge and on-axis components associated with the TG and helicon wave respectively.

Finally, force balance analysis in MAGPIE using a two-fluid "Braginskii" type formalism shows that the electron fluid exists in a state of dynamic (flowing) equilibrium between the electric, pressure and thermal forces. The pressure gradient, driven by the non-uniform RF heating, accelerates the plasma into the target region to velocities close to the ion sound speed. From the measured axial plasma flux we find that the plasma column in MAGPIE can be divided into an ionizing and a recombining region. For the conditions investigated, a large fraction of the plasma created in the ionizing region is lost in the recombining region and only a small fraction reaches the end of the device. The equilibrium plasma density along the length of

MAGPIE can be quantitatively explained using a 1D transport calculation which includes volumetric particle sources and magnetic compression. We show that the plasma is transported, by the electron pressure gradient, from under the antenna (0.5×10^{19} m^{-3}) into the target region where it reaches maximum density ($2\text{-}3\times10^{19}$ m^{-3}).

Using the results herein presented, this thesis explores the relationship between the RF power deposition in MAGPIE, parallel plasma transport and the production of high density plasma in the target region.

Contents

Declaration

Acknowledgements

Publications

Abstract

Contents

Chapter 1 Introduction 1

1.1 Controlled thermonuclear fusion: entering a new stage in the 21st century 1

1.1.1 The ITER experiment 3

1.2 Plasma-Material Interaction under fusion relevant conditions 5

1.2.1 The divertor 6

1.3 The role of Linear Plasma Devices in advancing fusion Science and Technology 9

1.4 Motivation 10

1.5 Thesis structure 10

Chapter 2 The MAGnetized Plasma Interaction Experiment (MAGPIE) 12

2.1 Introduction 12

2.2 Plasma production with Helicon sources 15

2.2.1 Non-uniform magnetic fields 15

2.2.2 Light-ion plasma 16

2.2.3 Neutral depletion 17

2.3 Device description 18

2.3.1 Vacuum system 20

2.3.2 RF plasma source 20

2.3.3 Magnetic system 23

2.4 Device characterization during 20 kW operation in hydrogen 25

2.4.1 “Strong mirror” magnetic configuration 26

2.4.2 Scaling with magnetic field 32

2.4.3 Scaling with RF power 37
2.4.4 Scaling with fill pressure 41

Chapter 3 Diagnostics 44

3.1 Introduction 44
3.2 Microwave interferometer 46
3.2.1 Description 46
3.2.2 Principle of operation 47
3.3 Double Langmuir probes 49
3.3.1 Description 49
3.3.2 RF effects 51
3.3.3 Magnetic field effects 54
3.3.4 Effect of Molecular gases 57
3.4 RF magnetic probes 61
3.4.1 Description 61
3.4.2 Amplitude demodulation 62
3.4.3 Calibration 63

Chapter 4 Modelling the RF compensation of the Double Langmuir Probe method.... 65

4.1 Introduction 66
4.2 Theory 67
4.2.1 Assumptions 67
4.2.2 DC floating potential 67
4.2.3 Sheath rectification 68
4.2.4 Model of a double Langmuir probe (DLP) in RF environment 69
4.2.5 The driven floating probe 69
4.2.6 Passively driven Double Langmuir Probes (DLP) 76
4.2.7 Compensation of a floating probe 78
4.2.8 Probe design considerations 81
4.2.9 Effect of RF rectification on DLP measurements 85
4.3 Actively driven probe experiment 88
4.3.1 Apparatus 88
4.3.2 Results and analysis 90
4.4 DLP measurements in the presence of RF 92
4.4.1 Annaratone’s DLP experimental setup 92

4.4.2 Results 92
4.5 Discussion 95
4.5.1 RF compensation of the DLP 95
4.5.2 Effects of RF rectification on DLP measurements 96
Appendix 4A. DC floating and self-bias potentials 97
Appendix 4B. Sheath displacement current 98
Appendix 4C. Passively driven floating probe 99
Appendix 4D. Asymptotic analysis of the driven probe equation 101
Appendix 4E. Actively driven floating probe 102
Appendix 4F. Passively driven DLP 104

Chapter 5 Cold plasma waves in MAGPIE 106

5.1 Introduction 106
5.2 Helicon and Trivelpiece-Gould waves 107
5.2.1 Dispersion relation 107
5.2.2 Effect of collisions 108
5.2.3 Wave damping 112
5.3 Waves in cylindrically bounded cold magnetized plasma 117
5.3.1 Governing equations 117
5.3.2 Plasma wavefields 119
5.3.3 RF antenna 122
5.3.4 Boundary conditions 124
5.3.5 Wave excitation by an RF antenna 125
5.3.6 Power deposition mechanism 127
Appendix 5A. Waves in unbounded cold magnetized plasma 128
5A.1 Conductivity 128
5A.2 The cold dielectric tensor 129
5A.3 Dispersion relation 131
Appendix 5B. Electrostatic and Electromagnetic content of plasma waves: 134
Appendix 5C. Vacuum wavefields 135
5C.1 Parallel fields 135
5C.2 Transverse fields 136
5C.3 Region II basis function 136
5C.4 Region III basis function 138

Appendix 5D. Power deposition and heat transport in cold plasma.......139
5D.1 RF power deposition.......139
5D.2 Heat transport in plasma.......142
5D.3 Power balance.......144

Chapter 6 Wave excitation, propagation and damping in MAGPIE.......146

6.1 Introduction.......146
6.2 Experimental setup.......149
6.3 Wave dispersion and attenuation relations.......150
6.3.1 The WKB approximation.......151
6.4 Helicon wave propagation in quasi-uniform magnetic fields.......153
6.4.1 Axial wave propagation.......156
6.4.2 Radial wave structures.......158
6.4.3 Whistler wave ray direction.......159
6.4.4 Wave excitation mechanism in MAGPIE.......162
6.5 Helicon wave propagation in non-uniform magnetic fields.......167
6.5.1 Experimental observations.......167
6.5.2 Axial wave attenuation.......169
6.5.3 2D full wave code simulation.......171
6.5.4 Origin of the interference pattern.......175
6.5.5 RF power deposition in MAGPIE.......176
6.6 Summary.......178
Appendix 6A. The WKB approximation.......179
6A.1 Solution in 1D with attenuation.......179
6A.2 Validity criterion.......180
Appendix 6B. Input data for the 2D wave code.......181
6B.1 Radial profiles.......181
6B.2 Axial profiles.......182

Chapter 7 Plasma force balance and equilibrium profiles in MAGPIE.......185

7.1 Introduction.......186
7.2 Experimental setup.......187
7.3 Experimental measurements.......188
7.3.1 Plasma density and electron temperature.......188
7.3.2 Plasma flow velocity.......188

7.3.3 Floating and plasma potential 189
7.3.4 Electron pressure and thermal ionization 191
7.3.5 Plasma magnetization 192
7.3.6 Radial profiles 193
7.4 Theory 195
7.4.1 Assumptions 195
7.4.2 Dissociation of molecular hydrogen 195
7.4.3 Neutral gas depletion 196
7.4.4 Momentum exchange processes 196
7.4.5 Momentum transport 199
7.4.6 Particle transport 202
7.4.7 Volumetric processes 202
7.4.8 Equilibrium plasma density 205
7.5 Results 206
7.5.1 Electron fluid force balance 206
7.5.2 Particle sources and sinks 208
7.5.3 Plasma flow velocity 211
7.5.4 Equilibrium plasma density 213
7.5.5 Estimating the neutral depletion and dissociation degree 214
7.6 Summary and conclusions 217
Appendix 7A. “Braginskii” two fluid formalism 220
Appendix 7B. Ion-neutral momentum transfer 222
Appendix 7C. Fluid magnetic mirror force 224
7C.1 Plasma anisotropy 224
Appendix 7D. Neutral depletion in low-beta plasmas 225

Chapter 8 Conclusions and further research 227

8.1 Introduction 227
8.2 Characterization of MAGPIE 227
8.3 RF compensation of double Langmuir probes 228
8.4 Wave propagation in MAGPIE 229
8.5 Formation of equilibrium density profiles in MAGPIE 230

Bibliography 233

Chapter 1 Introduction

1.1 Controlled thermonuclear fusion: entering a new stage in the 21st century 1

1.1.1 The ITER experiment 3

1.2 Plasma-Material Interaction under fusion relevant conditions 5

1.2.1 The divertor 6

1.3 The role of Linear Plasma Devices in advancing fusion Science and Technology 9

1.4 Motivation 10

1.5 Thesis structure 10

1.1 Controlled thermonuclear fusion: entering a new stage in the 21st century

The concept of energy is a central aspect of modern society and will continue to do so as energy consumption increases and the need to diversify into other viable energy sources becomes apparent. According to Friedberg [1], the standard of living is directly proportional to the amount of energy consumption; energy is required for the production and transportation of food, the manufacturing of goods, lighting, heating and cooling of residential and industrial areas, etc. As the population and its standard of living is increased throughout the world, the consumption of energy will inexorably increase; more food, lighting, heating and transportation will be required. Currently, the main source of energy is fossil fuels and it has been debated that its consumption is responsible for the production of greenhouse gases which have adverse effects on climate and the environment [2]. On the one hand, there is strong motivation to increase the use of fossil fuels to meet the demands of the world’s increasing energy appetite, and on the other hand there is a need to reduce greenhouse emissions of which consumption of fossil fuels is responsible. So we are reaching a point where the production of energy must be supplemented and eventually replaced by other forms of energy that are (1) more compatible with the environment, (2) have energy densities equal or greater than fossil fuels and (3) can provide a continuous and uninterrupted energy supply for the implementation of base load power.

The primary natural resources used to produce energy fall into three main categories: (1) fossil fuels, (2) nuclear fuels and (3) sunlight [1]. These resources may be used directly towards desired applications or used indirectly to produce electricity. To cope with both the need to reduce greenhouse emissions and produce the required amount of energy, the use of fossil fuels needs to be supplemented and eventually replaced by new forms of base load energy systems. Some suggest the use of a combination of renewable energy sources such as solar, wind and geothermal power but these energy sources do not have either competitive energy densities or do not have availability required for base load power. One possible avenue is to use a combination of renewable energy sources and using nuclear fission as a base load power source; although attractive to the environment from a standpoint of greenhouse emissions there are great concerns with using nuclear fission due to its inherent radioactive nature and the long lived radioactive waste that it produces; industrial accidents such as Chernobyl, Three Mile Island and recently the Fukushima case have led to a reassessment of the desirability of nuclear fission. This is where thermonuclear fusion may play an important part in the energy scenario.

Currently thermonuclear fusion is still in its experimental stage with the deuterium-tritium (D-T) based reaction as the main concept being pursued. This form of thermonuclear fusion has the capability to provide a long term base load energy source since fuel reserves for D-T fusion reactors are abundant and readily accessible [1]; deuterium can be extracted from sea water and tritium can be bred from lithium which is readily available from the earth’s crust. However, some specialized construction materials are less abundant than the fuel, such as the rare metals used to make the superconducting magnets. Energy from thermonuclear fusion is characterized by an almost unlimited fuel reserve, near environmental perfection and is a candidate for replacing hydrocarbon driven base load energy sources. Despite the attractiveness of fusion energy, there are major scientific and engineering challenges to be overcome before its commercial implementation.

During the last 50 years, the main research effort in controlled thermonuclear fusion has been focused on finding magnetic configurations that could create and confine sufficiently hot and dense plasma for long enough time to achieve ignition conditions. Initial concepts such as linear mirror confinement devices were superseded by the more successful Tokamak concept. The goal of confining fusion plasma could have been easily achieved if magnetic confinement was not accompanied by a plethora of MHD instabilities and turbulence.

Despite these obstacles, magnetic confinement of plasmas has been greatly advanced; in fact, during the 90s two Tokamak fusion devices, TFTR and JET, demonstrated the scientific feasibility of controlled thermonuclear fusion by producing 10.7 and 16 MW of fusion output power respectively in D-T plasmas and also successfully demonstrating the safe use and handling of tritium [3], [4], [5], [6]. TFTR produced its celebrated 10.7 MW shot on November 2nd 1994 for an input power of 39.5 MW from Neutral Beam Injection (NBI) over a period of about 0.2 seconds leading to a Q of 0.27 [3]. Q is defined as the instantaneous total fusion power divided by the total injected NBI power. JET produced its celebrated 16 MW shot (No. 42976) on October 31st 1997 for an input power of 22 MW NBI and 3 MW ICRF over a period of about 0.2 seconds leading to a Q of 0.66 [4], [5]. In addition, in that same year JET produced a quasi-steady state discharge producing 4 MW fusion power output for an input power of 22 MW over a period of 4 seconds leading to Q of 0.18 [5], [6]. Discharge duration was limited only by restrictions on neutron production.

In spite of the success of these experiments, the operating conditions produced in these machines are still far from the ones to be encountered in a fusion reactor, namely steady state operation and alpha particle self-heating of the plasma. Nevertheless the results from JET, TFTR and other Tokamak experiments in the 80s and 90s provided the final data points needed to extrapolate to a machine with significantly increased plasma parameters and considerable power amplification. This next generation machine, shown in Figure 1, is called ITER (International Thermonuclear Experimental Reactor) and has the aim to explore areas that are inaccessible in present day fusion experiments, namely the physics of burning fusion plasmas and to demonstrate key fusion reactor technologies [7]. Hence, at the start of the 21st century, with ITER at the forefront, we are entering a new stage in the development of controlled thermonuclear fusion where both the scientific and engineering feasibility will need to be demonstrated, a stage where the main focus will be in the development of fusion reactor technologies rather than just plasma physics. ITER together with IFMIF (International Fusion Material Irradiation Facility) [8], [9] and DEMO (Demonstration power plant) [10] will form the pathway to realizing magnetically confined fusion power.

1.1.1 The ITER experiment

The ITER experiment (Figure 1) will explore new areas in fusion science by being the first experiment to study burning D-T plasmas in quasi-steady state conditions. According to reference [7] the aims of the ITER experiment are:

- Produce and study inductively driven burning plasmas at power amplification factors greater than 10 and discharges in the order of 400 seconds.
- Produce and study quasi-steady state burning plasmas with non-inductive current drive at power amplification factors greater than 5.
- Demonstrate essential fusion reactor technologies.
- Test components for future reactors including tritium breeding concepts.

The first two aims are concerned with answering burning plasma physics questions such as the effect of energetic particles, associated instabilities and self-heating of the plasma [11], the formation of transport barriers, the effect of turbulence in particle and energy transport [12], the mitigation and control of instabilities such as ELMs [13], etc. Reference [7] gives an overview of the most important burning plasma physics issues to be addressed in ITER.

The last two aims are related to the development of fusion technologies, for example the manufacturing and maintenance of the superconducting magnets [14], the development of suitable plasma facing materials with long enough lifetimes and low hydrogen retention for steady state operation [14], [15], [16], the development low activation structural materials with stable thermo-mechanical properties under steady state neutron irradiation [17], remote handling of plasma facing components in the reactor vessel such as divertor cassettes and first wall tiles, scaling up of neutral beam injection systems and other heating systems, the development of tritium breeding and handling systems just to mention a few.

ITER and IFMIF will prepare the technological pathway to build the first electricity-producing demonstration fusion power plant; this first fusion power plant known as DEMO [10], and for it to be successful the aforementioned plasma physics and technological issues will need to be resolved. Resolving these problems will require the combined effort of ITER, IFMIF and other specialized facilities to study conditions relevant to, and even beyond, ITER. The most pressing problems in fusion technology are directly related to the steady state operation of a fusion power plant and the performance of its materials.

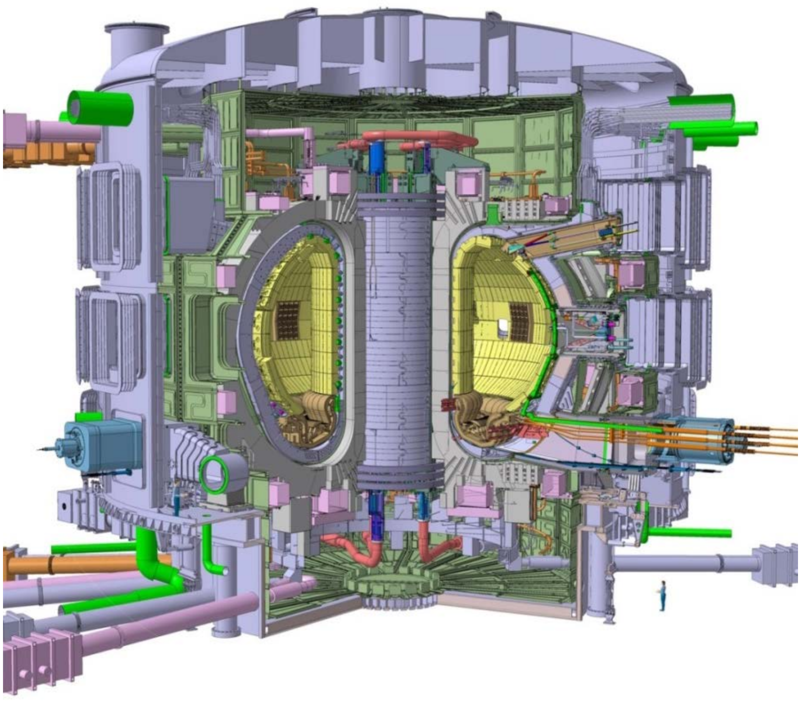

Figure 1, Schematic of the ITER fusion reactor (source: ITER Organization).

1.2 Plasma-Material Interaction under fusion relevant conditions

In controlled thermonuclear fusion research Plasma-Material Interaction (PMI) refers all the processes that occur between the plasma and the solid materials in a fusion reactor, in particular the first wall and structural materials [14]. An example of the effects of PMI in a fusion reactor is the boronization of vacuum chamber walls to improve discharge conditions and achieve higher plasma densities [18].

In a fusion reactor, plasma interacts with the reactor’s wall through radial particle transport across the magnetic field and transient electromagnetic events (ELMs and disruptions). However, there are deliberate and essential sources of Plasma-Material Interactions (PMIs) such as the divertor [19] and lithium blankets. In the divertor region helium is extracted and fuel recycled by allowing the plasma from the Scrape Off Layer (SOL) to interact with a material target for neutralization and removal; furthermore, the tritium breeding and main heat extraction systems depend on the interaction of energetic neutrons with the lithium blankets to fulfil their functions. Our incomplete understanding of various PMI processes originates from the following:

- Present day fusion devices cannot access the energy density/long pulsed operation expected in ITER; as a result, PMIs that will be important in ITER can only be partially observed in present day fusion devices.
- The absence of neutron sources with reactor relevant fluxes (10^{19} n $m^{-2}s^{-1}$) and energy spectrum (14 MeV) [20] to test structural components and characterize low activation materials.

Bridging this knowledge gap will be absolutely required for the successful development of fusion power. The lack of understanding of key PMI issues relevant to ITER and the absence of suitable infrastructure has motivated the need to build dedicated PMI facilities to bridge the knowledge gap and solve critical problems of Tokamak based fusion reactors. Specialised facilities, such as IFMIF [8], [9], have been proposed to study neutron related interactions relevant to fusion devices such as DEMO; additionally, various Linear Plasma Devices (LPDs) are been designed or have been constructed (MPEX [21], MAGNUM PSI [22], [23], PISCES [24]) to study Plasma-Surface Interactions (PSI) physics relevant to ITER. These LPDs are capable of providing ion and heat fluxes relevant to ITER, which are inaccessible in present day Toroidal fusion devices. Kreter [25] provides an overview of PMI studies performed in LPDs relevant to fusion devices.

1.2.1 The divertor

A key component and perhaps one of the main sources of PMI in a fusion reactor will be the divertor region; here the plasma is deliberately brought into contact with a material target, allowing neutralization of plasma and removal of fusion by-products, namely helium. The divertor is a key component in a fusion reactor because without it helium and impurities in the plasma would accumulate, thereby adversely affecting the performance of the reactor. Figure 2 shows a poloidal cross-section of an ITER-like divertor. In this figure the major parts are shown: (1) the plasma core, (2) the Last Closed Flux Surface (LCFS), (3) the scrape of layer (SOL), (4) the separatrix, (5) the X point, and (6) the divertor region. Impurities from the plasma core are transported across the magnetic field and reach the SOL; in this region parallel impurity diffusion is much greater than the radial component, and for this reason most of the particles that reach the SOL are transported towards the neutralization zone in the divertor region. The main functions of the divertor are the following:

Define the Last Closed Flux Surface: As opposed to a limiter, a divertor defines the boundary and the shape of the plasma using magnetic fields. This prevents the plasma core from directly coming into contact with a limiter by locating the interaction surface on a dedicated system; namely, the divertor target plates.

Reduce impurity content: The magnetic geometry of the divertor allows PSIs to be isolated from the confined plasma. The plasma flow and magnetic field geometry formed in the divertor prevent impurities from escaping divertor, penetrating the plasma edge and entering the core.

Removal of alpha particle power: In a D-T fusion reactor, 80% of the power generated leaves the plasma confinement region through the neutron flux. The remaining 20 % of the power is associated with alpha particles, is confined by the magnetic field and in steady state operation must be removed. In a fusion reactor with a divertor, the alpha particle power is intercepted by the SOL, which is then transported to the divertor region where it is removed by both volumetric processes and conduction.

Removal of helium: Helium must be removed to prevent fuel dilution. At the divertor region the plasma is neutralized at the contact surface and with enough neutral gas pressure, typical of the “detached” divertor operation, the helium can be pumped out of the reactor.

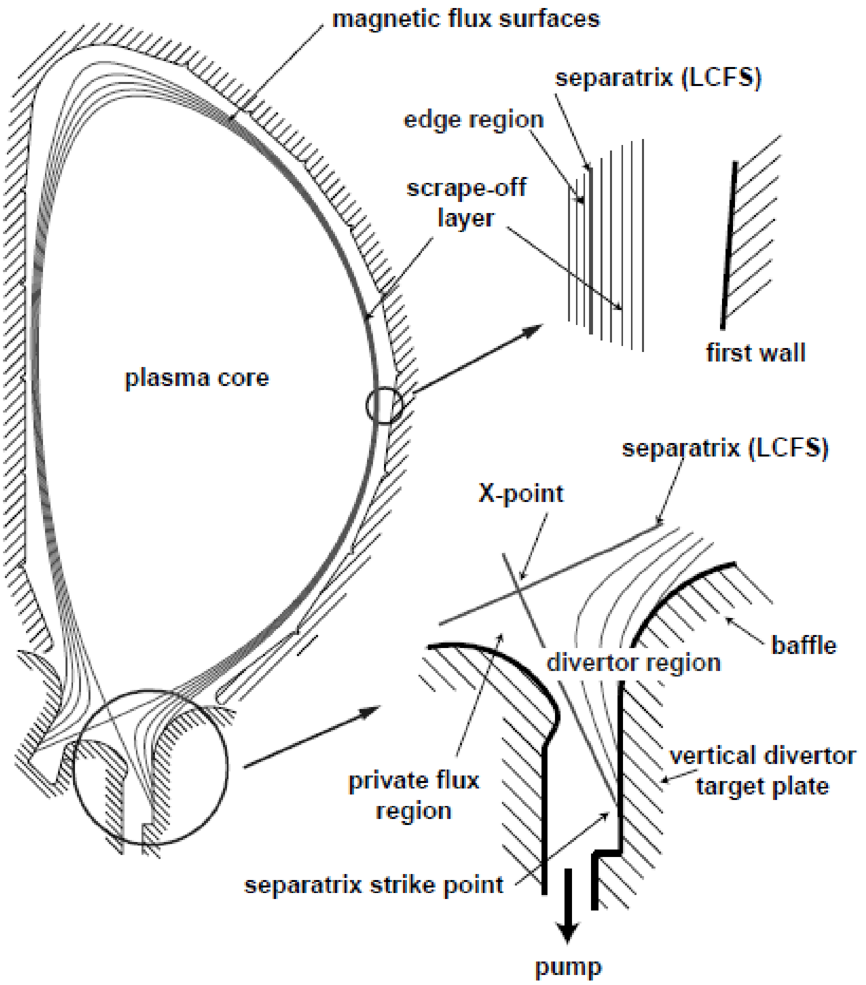
magnetic flux surfaces
separatrix (LCFS)
edge region
scrape-off
layer
first wall
plasma core
separatrix (LCFS)
X-point
baffle
divertor region
vertical divertor
target plate
private flux
region
separatrix strike point
pump

Figure 2, Cross sectional view of a single null divertor geometry. Figure obtained from reference [14]

During the operation of a fusion power plant, the amount of steady state heat flux the divertor must remove can be up to 30-100 MWm^{-2} in the case of a 1.5 GW reactor [26, p. 139]; no solid material or cooling system can withstand these heat loads in steady state, so before reaching the target plates the incoming power must be dispersed through various techniques. The techniques to be employed to reduce power loads on the ITER divertor are the following [14], [26]:

- Target is tilted with respect to the magnetic field lines to increase the effective area:
- Magnetic field lines are flux expanded into the divertor region.
- Energy is transferred to neutral particles in the divertor through charge exchange processes and collisions.
- Volumetric radiation cooling by excited neutrals.

Using these techniques the total power flux can be reduced by a factor of about 20 according to reference [14]. Under these circumstances, the ITER divertor will operate in the so called “detached” regime [14], [26]. The detached divertor operation is characterized by a reduction in plasma temperature adjacent to the target plates, coincident with significant decrease in plasma particle and power fluxes and increase in neutral pressure. During the detached operation the high neutral density and local impurity content will cause significant power dispersal through volumetric radiation and recombination processes in the attempt to prevent thermo-mechanical failure of the divertor components. During the detached regime, the divertor in ITER is expected to receive ion fluxes of 10^{24} m^{-2} s^{-1}, power fluxes of 10-20 MWm^{-2} [14, p. 1999], [22] and have electron densities in the order of 10^{19}-10^{21} m^{-3} and temperatures of 1-30 eV [27], [28].

An area of concern is the effects of transient heat loads particularly ELMs, on divertor components since the aforementioned power dispersal methods may not be enough to reduce their severity to an acceptable level. The damage caused on the PFCs becomes an important source of impurities for the plasma. The choice of operating conditions with low amplitude ELMs and the suppression of ELMs is an area of ongoing research and development [13]. It seems that the resolution of the problems associated with transient heat loads will require a coordinated effort from both material science and plasma confinement physics.

1.3 The role of Linear Plasma Devices in advancing fusion Science and Technology

Part of our incomplete understanding of PMI relevant to fusion devices stems from the inability of present day fusion experiments to provide suitable plasma conditions for PMI to be fully studied. Fusion experiments such as JET and other present day toroidal plasma devices operate in plasma regimes that closely approximate those on ITER in many ways, namely, the high confinement mode, magnetic divertor, D-T mixtures (only JET), etc. However, PMI studies on present day tokamaks have been limited by their inability to provide ion, heat and neutron fluxes relevant to ITER; it is for this reason there are still knowledge gaps in the area of PMI. These knowledge gaps have motivated the construction of dedicated PMI facilities such as IFMIF for neutron related studies and Linear Plasma Devices (LPDs) for PSI studies such as MPEX [21], Magnum PSI [22], [23], PISCES [24]. More specifically, the motivation to develop LPDs to study PSI relevant to fusion reactors stems directly from their operational advantages over toroidal plasma devices; the main advantages are the following:

- The plasma production process is not coupled to the PMI region leading to stable plasmas with controllable parameters.
- Steady state operation with ion and heat fluxes relevant to ITER
- Linear geometry provides simpler diagnostic access.
- A simpler geometry reduces the complexities associated with modelling PMI
- Simulations of plasma regimes that are difficult to access and control in Toroidal Plasma Devices such as ELMs, disruptions or detached divertor conditions.
- Lower construction and operating cost.

Flexibility in operation makes the exchange of material samples, plasma parameters, operating gases, amongst others, a relatively simple task. Due to their unique capabilities, LPDs will play a critical role in advancing our understanding of key PMI issues. Despite the aforementioned advantages, LPDs may not be capable of studying some aspects that are intrinsic to Toroidal magnetic geometries; for this reason, the pathway for resolving important PMI issues relevant to fusion devices will need to be in collaboration with both Linear and toroidal plasma devices.

1.4 Motivation

The work presented in this thesis has been motivated by the need to develop LPDs for the purpose of investigating PMI under fusion reactor relevant conditions. While present LPDs provide high ion fluxes at low electron temperatures at the location of targets, they only provide short duration pulses at low magnetic fields. The next generation LPDs will provide long pulse or steady state operation with magnetic fields that closely approximate the conditions in a reactor relevant divertor. Over the years, helicon based plasma sources have attracted considerable interest due to their capability to produce high density plasma with relatively low RF power (1-5 kW) and without the use of electrodes exposed to the plasma. For this reason, helicon sources are well suited for the production of high density plasma for the next generation PMI experiments.

The principal aim of this thesis is to develop, characterize and optimize the production of high density hydrogen plasma in a helicon heated prototypical LPD. The outcomes of this research will guide the development of a higher RF power purposely built LPD. To carry out this task, we have focused our investigation to topics such as correct implementation of electrostatic probes in high power RF discharges, helicon wave excitation, propagation and absorption in high density plasma and the formation of the equilibrium plasma density, etc.

1.5 Thesis structure

This thesis is composed of 8 Chapters and it is structured as follows:

Chapter 1 provides an overview of the problems associated with steady state operation of a magnetically confined thermonuclear fusion reactor. We provide an introduction to the field of Plasma-Material Interactions (PMI) and describe the need for dedicated facilities to study PMI relevant to fusion reactors.

In Chapter 2, we describe the MAGnetized Plasma Interaction Experiment (MAGPIE), a helicon heated prototypical linear plasma device constructed at the ANU for basic PMI studies. In addition, we provide experimental data that describes “typical” hydrogen discharges in MAGPIE during 20 kW operation.

In Chapter 3, we describe the diagnostics used in this work, namely, a microwave interferometer, double Langmuir probes and RF magnetic probes. We describe the design of RF compensated double Langmuir probes using the concepts developed in Chapter 4.

In Chapter 4, we provide a detailed analysis of the RF compensation of the double Langmuir probe method. We provide means for assessing under what conditions the double Langmuir probe method can be considered RF compensated and provide examples of RF compensated probe design. We elaborate on the effects of RF rectification on double Langmuir probe measurements of ion density and electron temperature.

In Chapter 5, we provide a theoretical background of cold plasma waves in MAGPIE with special attention given to Helicon-Trivelpiece-Gould (H-TG) waves in the presence of collisions. We provide expressions that describe their propagation and attenuation. In addition, we describe the development of a semi-analytical uniform plasma (0D) full wave code to model the propagation of electromagnetic waves in cylindrically bounded cold magnetized plasma.

In Chapter 6, we describe the excitation, propagation and absorption of helicon waves in MAGPIE using full wave codes and experimental data. First, we analyse wave propagation in "quasi-uniform" plasma. We then analyse wave propagation and RF power deposition in non-uniform plasma.

In Chapter 7, using a 1D fluid model and experimental data we investigate the mechanism that leads to the formation of high density plasma in MAGPIE. We focus on the transport of plasma along the magnetic field.

Chapter 8 summarizes the most important findings reported in this thesis and provides recommendations for further research.

Chapter 2 The MAGnetized Plasma Interaction Experiment (MAGPIE)

2.1 Introduction........12
2.2 Plasma production with Helicon sources........15
  2.2.1 Non-uniform magnetic fields........15
  2.2.2 Light-ion plasma........16
  2.2.3 Neutral depletion........17
2.3 Device description........18
  2.3.1 Vacuum system........20
  2.3.2 RF plasma source........20
  2.3.3 Magnetic system........23
2.4 Device characterization during 20 kW operation in hydrogen........25
  2.4.1 "Strong mirror" magnetic configuration........26
  2.4.2 Scaling with magnetic field........32
  2.4.3 Scaling with RF power........37
  2.4.4 Scaling with fill pressure........41

2.1 Introduction

The Plasma Research Laboratory at the Australian National University has constructed a prototypical Linear Plasma Device referred to as the "MAGnetized Plasma Interaction Experiment" (MAGPIE). This device has been motivated by the need to investigate Plasma-Surface Interaction (PSI) physics relevant to fusion devices and to develop advanced remote diagnostics to understand these interactions. Chapter 1 and references [14], [29] discuss in detail the most relevant PSI physics relevant to fusion devices.

Linear plasma devices for PSI studies mainly differ on the plasma production process employed, and to some degree on the strength of the background magnetic field. Currently, the most ITER relevant PSI experiments produce their plasma using arc sources [22], [23], [27]. MAGPIE produces its plasma using a helicon source and as shown in this thesis, low temperature (~ 1–8 eV) high density plasma in H_2 (~$1–3 \times 10^{19}$ m^{-3}) can be produced for RF powers ≤ 20 kW. Other researchers have also shown that these sources are capable of producing high density plasma (~2×10^{19} m^{-3}) in heavy gases such as argon [30], [31] and in light gases such as hydrogen and helium [32], [33]. In addition, due to the electrode-less nature of helicon sources, there is a reduced risk of introducing impurities into the plasma, therefore the only impurities to be expected are the ones produced by the material sample being studied. Furthermore, MAGPIE uses a converging magnetic field geometry to increase the plasma density as shown by Mori in the Mini- RFTF linear plasma device [33], [34]. In Chapter 7, we investigate the role of the magnetic field geometry in increasing plasma density.

The principal aims of MAGPIE are (1) to produce high density H_2 and D_2 plasmas capable of approximating the ITER divertor regime[1], (2) to serve as a test bed for developing remote in situ diagnostics for PSI and (3) to provide a flexible and highly diagnosed PSI experiment. In this section and throughout this document we describe MAGPIE in its prototypical form. Characteristic features of MAGPIE are described in Table 1. In the sections that follow, we discuss plasma production in helicon sources when operated with non-uniform magnetic fields and light-ion plasma. Moreover, we describe the experimental setup of MAGPIE during its prototypical stage; namely, the vacuum system, the RF plasma source and magnetic field system. Finally, we provide experimental measurements that describe "typical" discharges in MAGPIE under normal operation.

---

[1] Expected ITER divertor conditions: $n_e \sim 10^{19}$–10^{21} m^{-3}, $T_e \sim$ 1–30 eV, ion energy 1–200 eV [27].

Table 1, Characteristic features of MAGPIE during its prototypical stage

Source type	Helicon
Antenna	Left-handed half-turn helical
RF power	≤ 20 kW
RF frequency	7 and 13.56 MHz
Pulse length	$<$ 5 ms at 20 kW
Shot frequency	$<$ 15 Hz at 20 kW
Electron density n_e	10^{17}–3×10^{19} m^{-3} in H_2
Electron temperature T_e	0.1–8 eV
Plasma diameter	5 and 2.5 cm (Source and Target region)
Ion flux[2] Γ_+ (H^+)	10^{20}–5×10^{23} m^{-2} s^{-1}
Power flux[3] (H^+)	$<$ 1.5 MWm^{-2}
Background magnetic field B_0	≤ 0.18 T (Target region)
Gas species	argon, helium, hydrogen
Fill pressure	0.2–4 Pa

---

[2] Ion flux Γ_+ is estimated from: $n_e\sqrt{T_e/M_i}$, where M_i is the ion mass, T_e the electron temperature in eV.

[3] Power flux is estimated from: $\Gamma_+ E_i$, where E_i is the ion energy taken as $3T_e$ and assuming $T_e \gg T_i$

2.2 Plasma production with Helicon sources

Most research on plasma production with helicon sources has been focused on uniform magnetic field geometries with heavy ions [35], [36], [37], [38] and to a lesser extent with light-ions [32], [39], [40]. In addition, research on helicon sources with non-uniform magnetic field geometries with heavy ions [30], [41], [42], [43] and light-ions has also been performed [33], [34], [44], [45]. In this section, we describe some effects on plasma production caused by the choice of magnetic geometry and gas species. We briefly discuss neutral depletion.

2.2.1 Non-uniform magnetic fields

The application of non-uniform magnetic fields in helicon based linear plasma devices can be classified in term of: (1) location where the non-uniformity is applied; namely, at the antenna or away from the antenna region and (2) geometry of magnetic field; namely, converging or diverging away from the antenna region.

The geometry of the magnetic field away from the antenna has a large effect on the plasma operation; for example, the formation of current-free double layers and the subsequent supersonic ion acceleration requires the use of diverging magnetic fields as discussed by Charles [45]. In addition, Takahashi in CHI-KUNG [43] and Prager [31] provide examples of discharges with diverging magnetic fields away from the antenna region. Typically, the electron density decreases away from the antenna region in these discharges.

Discharges with converging fields at the antenna region are known to exhibit different performance than uniform and diverging cases. Chen [41], Virko [42], Guo [30] and Mori [34] using the “focus” configuration provide examples of discharges with converging fields at the antenna region. Application of converging magnetic fields at the antenna region has been reported to provide: (1) smooth transition from low to high density as a function of RF power (no discontinuous density jumps) [34], (2) increased plasma density [30], [41], [42], (3) increased helicon wave amplitude and attenuation for same RF power [30], (5) increased antenna impedance [30] and (6) in argon discharges the characteristic “blue core” is brighter [30].

The smoothness in the transition from low to high density is explained by Mori [34] by noting that a non-uniform field under the antenna allows the helicon dispersion relation to be satisfied in the vicinity of the antenna for a broader range of conditions; thus, abrupt “resonance” conditions are less likely to occur. The increased brightness of the argon “blue core” is explained by Guo [30] in a similar manner but in terms of a wider range of local wave phase velocities which lead to more effective electron acceleration to ionizing energies near the antenna. Virko [42] explains that the increase in plasma density may be related to a shift from Trivelpiece-Gould (TG) dominated to helicon dominated RF power deposition as the angle of inclination of the background magnetic field with respect to dominant antenna current strap is varied under the antenna. Numerical results from the aforementioned reference indicate that for angles of inclination of the magnetic field below the electrostatic wave resonance cone, the TG RF power deposition is dominant, localized along the resonance cone and near the antenna. However for angles of inclination greater than the electrostatic wave resonance cone, helicon wave RF power deposition is dominant and leads to deep penetration of power flux along the converging magnetic field lines. In this case volumetric plasma heating, rather than surface localized, is probably responsible for the enhanced plasma production. The author comments that these effects may be important in any discharge with significant field non-uniformity under the antenna region.

The aforementioned studies indicate that converging magnetic fields at the antenna region lead to higher plasma densities, although only in reference to heavy ion plasma operation. Mori's hydrogen and helium experiments with various magnetic field configurations reported in [34] indicate that a uniform magnetic field at the antenna region together with a converging field away from antenna region provided the highest plasma densities in the Mini-RFTF; about 2×10^{19} and 4×10^{19} m^{-3} for hydrogen and helium operation at 5 kW respectively[4]. This configuration is labelled as "flat" in the aforementioned reference. The improved operation of the "flat" configuration over other configurations therein reported appears to be explained by magnetic field lines that do not intersect any surface in the discharge chamber; hence, particle losses are reduced. In MAGPIE, the magnetic field is approximately uniform at the antenna region and has a converging geometry away from it.

2.2.2 Light-ion plasma

Light-ion plasma production in helicon sources has been reported in the literature in uniform magnetic fields [32], [39], [40] and more recently in non-uniform magnetic fields [33], [34], [44], [45]. It is well known that operation with light-ion plasma is more difficult that in heavy ion plasma. The production of high density light ion plasma requires more RF power than in heavy ion discharges due to the following reasons: (1) lower ion mass leads to larger sound speeds and thus larger particle and power losses in linear devices; (2) operation with molecular gases such as H_2, O_2 and N_2 require larger values of heating power to drive ionization events due to their larger degrees of freedom. This is quantified by the collisional energy loss per electron-ion pair created as shown in figure 1 in reference [46] for H_2, H and Ar as a function of electron temperature. For example, for electron temperatures from 2 to 5 eV, molecular hydrogen requires about 10 to 4 times more energy per ionization event than argon respectively. Therefore, with increased particle losses and higher energetic cost per ionization event, it is not surprising that hydrogen plasma densities in linear devices are lower than argon plasma densities for a given RF power level.

---

[4] The plasma diameter under the antenna in the Mini-RFTF device is about 4.5 cm, while that in MAGPIE is about 10 cm; hence, to a first approximation the plasma volume in MAGPIE is about 4 times larger given the approximately equal discharge lengths (~ 1 m). This is consistent with the observation that MAGPIE requires about 4 times more RF power (20 kW) to produce similar hydrogen plasma densities as in the Mini-RFTF (~2×10^{19} m^{-3}at 5 kW).

Moreover, it has been observed that light-ion plasma densities saturate at magnetic fields that satisfy to the Lower Hybrid Resonance (LHR) condition at the antenna region. Any increase in magnetic field beyond the LHR leads to a reduction in plasma density. In MAGPIE during hydrogen plasma operation, we observe density saturation with considerable low frequency fluctuations ($\tilde{n}_e/n_e \leq 15$ %, < 100 kHz) near the LHR condition. The density saturation effect has been explained by Light [39] through gradient driven low frequency instabilities which increase radial transport, degrade confinement and lead to low plasma densities. Sakawa [40], [47], Light [39], Mori [33], [48] and Kikuchi [32] provide examples of LHR density saturation in light-ion plasma. However, Mori's experiments [33], [34], [48] show that it is possible to overcome and produce high density hydrogen plasma well beyond the LHR condition whenever enough RF power above a certain threshold can be supplied to the discharge. It is important to note that as the ion mass is increased, the presence of density saturation at the LHR is reduced as shown experimentally by Light [39] and Sakawa [40], [47].

2.2.3 Neutral depletion

This process refers to the reduction in neutral particle density during the discharge relative to the density before the discharge. As the electron pressure becomes comparable to the neutral gas pressure, region of high electron pressure become deprived of neutral gas and neutral depletion become important as discussed in [49], [50], [51]. Neutral depletion is expected to become important in high power helicon discharges and may impose limits to the highest achievable plasma densities due to the depletion of neutrals in the ionizing region [52]. In addition, neutral depletion can lead to the excitation of low frequency oscillations (~kHz), where the plasma jumps between an inductive and wave-heated mode [33], [53], [54]. In section 7.4.3 and Appendix 7D in Chapter 7, we discuss neutral depletion in more detail.

2.3 Device description

MAGPIE is divided into two main regions: a) the source and b) the target region as shown in Figure 3. The source region is where the RF plasma source is located; it is composed of a helicon antenna wrapped around the vacuum vessel and permeated by an approximately uniform magnetic field. In the target region the magnetic field is non-uniform and supports the production of high plasma density (2 to 3×10^{19} m^{-3}) whenever converging geometries are implemented. Hereafter, the regions $z \leq -20$ cm and $z \geq 0$ cm as depicted in Figure 3 are referred to as "upstream" and "downstream" of the source region respectively. Maximum plasma densities are produced in the downstream target region and it is the recommended location for the insertion of samples for Plasma-Surface Interaction (PSI) experiments. Plasma diagnostics are also located in the target region. Double Langmuir Probes (DLP) and RF Magnetic Probes (MP) are inserted in the target region to provide both axially (-20 cm to 65 cm) and radially resolved (-4 cm to 4 cm) measurements. In addition, a DLP with radial resolution (-7 to 7 cm) and a 140 GHz heterodyne interferometer are located at z = 11 cm and 14 cm respectively. These diagnostics are described in Chapter 3. Next, the main components of MAGPIE; namely, (1) the vacuum vessel, (2) the RF plasma source and (3) the magnetic system are described in more detail.

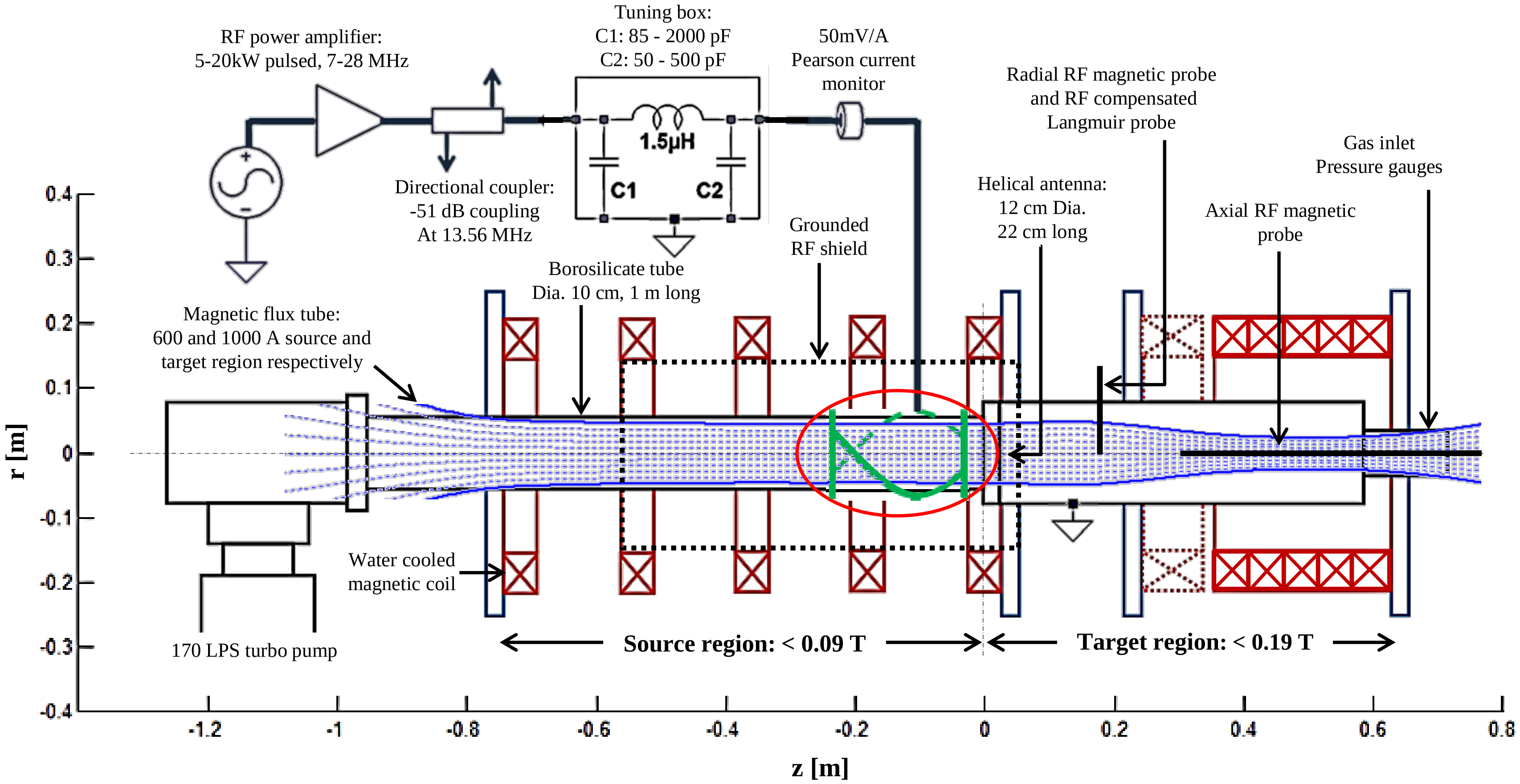
RF power amplifier:
5-20kW pulsed, 7-28 MHz
Tuning box:
C1: 85 - 2000 pF
C2: 50 - 500 pF
1.5μH
C1
C2
50mV/A
Pearson current
monitor
Radial RF magnetic probe
and RF compensated
Langmuir probe
Gas inlet
Pressure gauges
Directional coupler:
-51 dB coupling
At 13.56 MHz
Grounded
RF shield
Helical antenna:
12 cm Dia.
22 cm long
Axial RF magnetic
probe
Borosilicate tube
Dia. 10 cm, 1 m long
Magnetic flux tube:
600 and 1000 A source and
target region respectively
Water cooled
magnetic coil
170 LPS turbo pump
Source region: < 0.09 T
Target region: < 0.19 T
r [m]
0.4
0.3
0.2
0.1
0
-0.1
-0.2
-0.3
-0.4
-1.2
-1
-0.8
-0.6
-0.4
-0.2
0
0.2
0.4
0.6
0.8
z [m]

Figure 3. Schematic of MAGPIE.

2.3.1 Vacuum system

The vacuum vessel is made of a 1 m long, 9.8 cm inner diameter borosilicate tube and connected to the aluminium target chamber 0.7 m in length. It is inserted coaxially inside 2 sets of water cooled solenoids, each with a 0.3 m internal diameter. The operating gas is fed downstream of the target chamber (right hand side of Figure 3) and removed upstream by a 170 litres per second turbo pump. A gate valve, located at the throat of the turbo pump, allows control of the effective pumping rate. The gas pressure is measured at the target chamber with a hot cathode Bayard-Alpert Ionization gauge (< 0.01 Pa), a Convectron® (Atm to 0.1 Pa) and a Baratron pressure gauge (10 to 0.01 Pa) for process pressures. Base pressure is typically about 6×10^{-4} Pa (5×10^{-6} Torr). Argon, helium and hydrogen are available for use in experiments at fill pressures of 0.2-4 Pa (1.6-30 mTorr).

An important aspect not available in MAGPIE is differential pumping; this means that different gas pressures cannot be obtained in the source and target region simultaneously. This may be required when one needs to set the gas pressure on the source at a particular level for optimum plasma production and set different gas pressures at the target to study pressure effects on surface interaction physics. This situation arises, for example, when trying to model the conditions of the ITER divertor in order to observe the effects of detached plasmas; namely, a high neutral pressure at the target due to recycling [29]. An example of differential pumping can be seen in reference [22].

2.3.2 RF plasma source

The main components of the RF plasma source are (1) the RF amplifying unit, (2) the matching circuit and (3) the RF antenna. The RF amplifying unit consists of a 150 W broadband (3-35 MHz) pre-amplifying unit (A-150 ENI) driving a 20 kW pulsed RF amplifier. Forward and reflected power are measured with a directional coupler (-51 dB coupling at 13.56 MHz) and a power meter located between the RF amplifier and the matching circuit. The matching circuit consists of a pi network designed to match the impedance of the antenna to the RF amplifier (50 Ω) from 7 to 28 MHz. The pi network is composed of a fixed value 1.5 μH inductor and two variable 3kV vacuum capacitors (50-500 and 85-200 pF). Additionally, the matching circuit is housed in an air cooled grounded copper box to confine the RF radiation from the oscillating currents. Inside the copper box, a 50 mV/A Pearson 6600 current monitor measures the RF current flowing through the antenna. A diagram of the matching circuit can be seen in Figure 3.

The left-handed half turn helical antenna[5] (Figure 4) is 22 cm in length (centre to centre), 12 cm in diameter and it is used to (1) initiate the discharge through gas break down, (2) provide plasma heating through RF waves (fast and slow wave components) and drive ionization. A left-handed helical antenna has a helicity such that it launches $m = +1$ helicon waves anti-parallel to the direction of the magnetic field vector and launches $m = -1$ helicon waves parallel to the magnetic field vector [55]; the $m = -1$ mode is evanescent and does not propagate, thus leaving only the $m = +1$ propagating anti-parallel to the magnetic field vector. In MAGPIE, the direction of the magnetic field has been selected to point towards the pump side so that RF waves excited by the left-handed antenna propagate into the target region. In addition, the antenna is surrounded by a grounded aluminium cylindrical mesh in order to keep electromagnetic radiation confined inside the source region and protect the users.

Plasma sources based on arcing [23], [56] or thermionic emission [24], [57], [58] are known to introduce impurities in the plasma due to electrode sputtering. Helicon plasma sources, as opposed to arc based sources, have no electrode inside the plasma region and thus the risk of introducing impurities by damaged electrodes is removed. The electrode-less nature and capability to produce high density plasma with hydrogen and helium [33], [34], [44] , make helicon sources attractive for PSI experiments relevant to fusion.

During this initial stage, we have been able to deliver up to 20 kW of RF power at 7 MHz with a pulse width of 2 ms at 10 Hz repetition rate. With the use of converging magnetic fields, the highest plasma densities measured are in the range of $2.5 – 3 \times 10^{19}$ m^{-3}. Typical electron temperatures are in the range of 1 to 8 eV.

---

[5] The handedness of the antenna can be obtained by checking the rotation of the antenna helical current strap in the direction of the wave vector. A rotation consistent with the right hand rule in the direction of the wave vector corresponds to a left-handed antenna. This definition is consistent with that given by Light in reference [36].

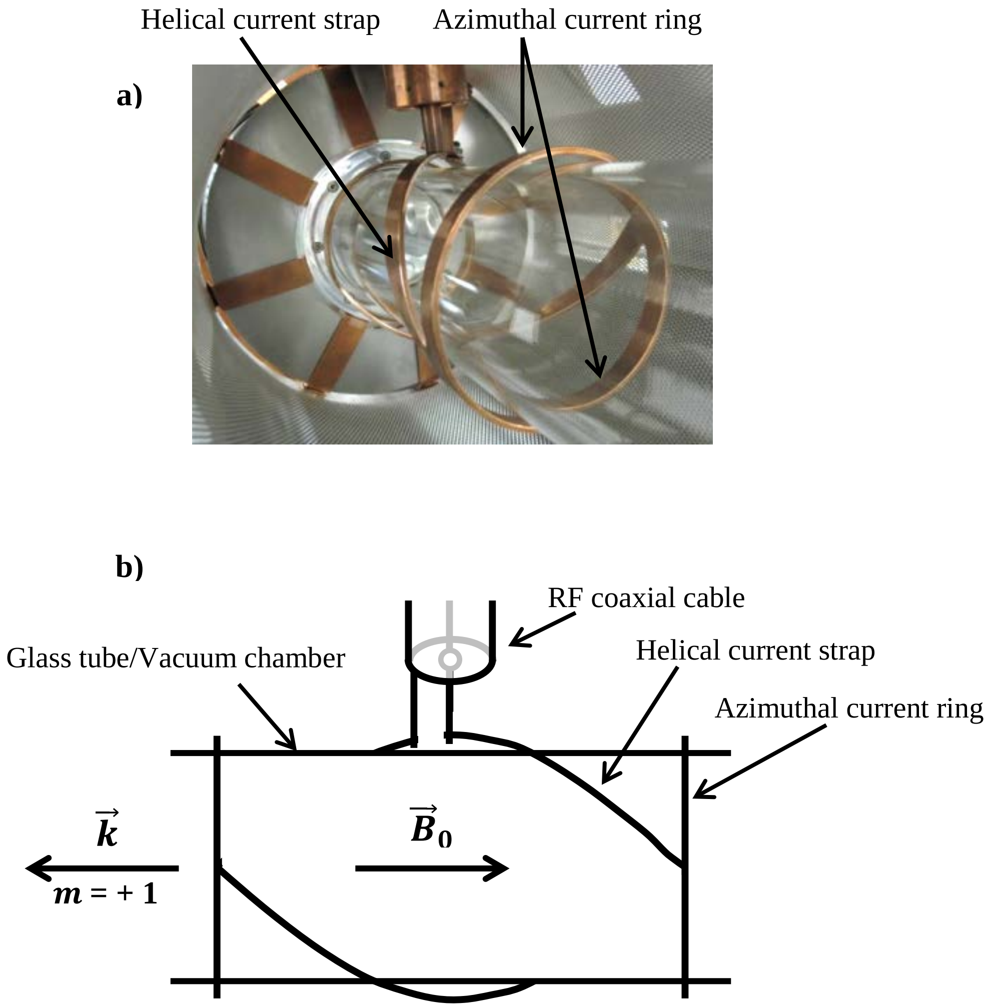
Helical current strap
Azimuthal current ring
a)
b)
RF coaxial cable
Glass tube/Vacuum chamber
Helical current strap
Azimuthal current ring
$\vec{k}$
$\vec{B}_0$
$m = +1$

Figure 4, a) Left-handed half-turn helical antenna and RF shield in MAGPIE. b) Diagram of left-handed half-turn helical antenna. Direction of background magnetic field in MAGPIE and wavevector of $m = +1$ helicon wave are indicated by the thick horizontal arrows.

2.3.3 Magnetic system

In MAGPIE the background magnetic field performs three main tasks: (1) enable the operation of the helicon source for plasma production, (2) radially confine and transport the plasma from the source to the target region and (3) support the production of high plasma density ($2 - 3 \times 10^{19}$ m^{-3}) whenever converging magnetic fields are implemented "downstream" of the source region (Figure 5).

For description purposes, the magnetic field system can be divided into the following subsystems: (1) magnetic solenoid system, (2) the DC power supply/conductor system and (3) the water cooling system. MAGPIE uses two separate solenoid sets to produce the magnetic field, one for the source region and the other for the target region. Each solenoid set contains 5 water cooled electromagnets. The geometry of the solenoid sets is shown in Figure 6. Each electromagnet has 0.3 m internal diameter, approximately 14 turns, 3.3 mΩ of resistance and covered with an epoxy resin. Each solenoid is individually powered by a 20V, 1000A 20 kW DC power supply in order to allow independent control of the DC currents. In general the magnetic field in each solenoid is different; this results in an axially non-uniform magnetic field such as the one seen on Figure 5. In addition, the magnetic field geometry determines the shape of the magnetic flux tubes passing through the source region, which determine the confinement region of the plasma. Figure 5 part "a" illustrates the magnetic flux tubes in MAGPIE and part "b" provides an image of the resulting compression of the plasma column in the target region. Maximum magnetic field strengths of 900 G and 1900 G can be produced at the source and the target regions respectively when operating the DC power supplies at maximum capacity (1000A). At these fields, the solenoid sets can be operated for about 3 minutes before thermal shutdown occurs provided the cooling system is on; without the cooling system the operational time is reduced to about 1 minute. For a current of 450 A, the solenoids can be operated in steady state provided the cooling system is on.

The cooling system pumps water through copper pipes inside the electromagnets and removes the heat through forced convection. Each solenoid has a separate water cooling circuit, each providing a pressure difference of 350 kPa and approximately 2 litres per minute of water at 20 degrees. The thermal shutdown is activated by the experiment's interlock system when the solenoids exceed a temperature of 50 degrees. The temperature of the solenoids is monitored by thermal switches located directly on the copper and when the threshold is reached they trigger the interlock system and shuts down both the RF and magnetic system. The system is reactivated in standby mode once the temperature of the solenoids is below the thermal threshold of 50-60 degrees.

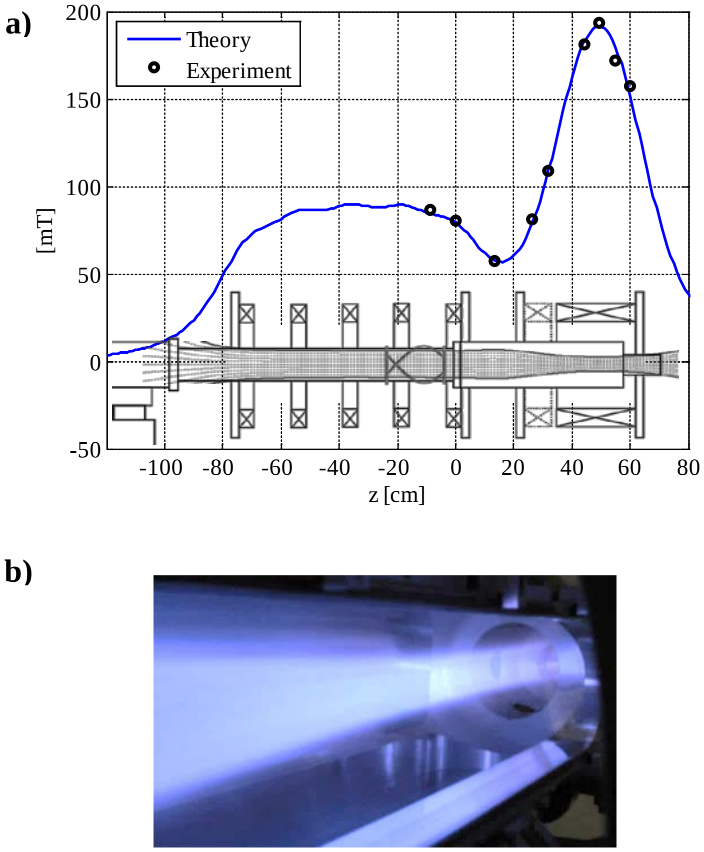

Figure 5, a) Maximum magnetic field strength along the axis of MAGPIE using 1000 A in the source and target solenoids respectively. The magnetic field was measured with a Gaussmeter. The source's magnetic flux tubes are shown for reference. b) Plasma column in the target chamber showing the compression effect of the converging magnetic field.

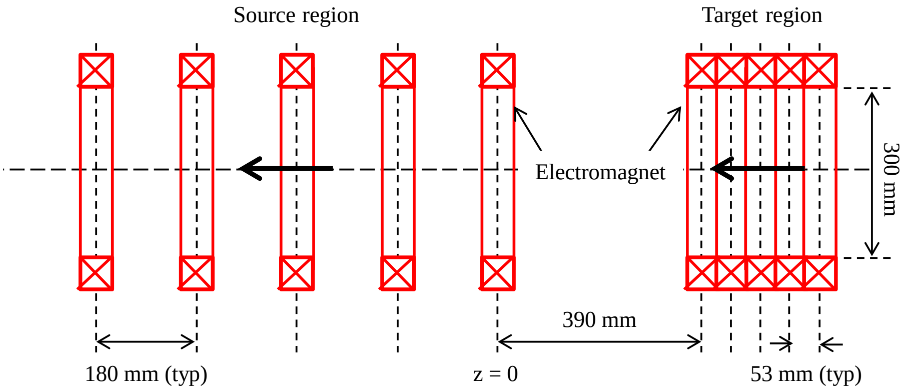
Source region
Target region
Electromagnet
300 mm
390 mm
180 mm (typ)
z = 0
53 mm (typ)

Figure 6, Solenoid geometry in MAGPIE. The machine's datum is represented by "z = 0". The arrows represent the direction of the magnetic field on axis.

2.4 Device characterization during 20 kW operation in hydrogen

Characterization of the plasma production in MAGPIE revealed that some magnetic field configurations sustained quiescent ($\tilde{n}_e/n_e < 5$ %) and stable high density (~10^{19} m^{-3}) plasma with low levels of reflected RF power. These favourable conditions could be achieved provided the source magnetic field was kept below 80 G at 7 MHz regardless of the target region magnetic field. It was later found that discharge stability or the lack thereof was related to the presence of low frequency instabilities excited during magnetic field configurations that satisfied the lower hybrid resonance condition at the source. In MAGPIE the lower hybrid resonance conditions at 7 MHz is satisfied in the vicinity of the source when operating with magnetic fields between 80 and 120 G.

In this section we focus our attention to magnetic field configurations that sustain quiescent and stable plasma; namely, those with source magnetic fields less than 80 G. In Figure 7 we illustrate a series of magnetic field configurations that provide stable operation and are relevant to this thesis. These magnetic configurations differ only in the magnitude of the target solenoid current. The configuration represented with the thick red line is hereafter referred as the “strong mirror” magnetic field configuration. The importance of this configuration is that it allows the production of stable discharges while providing the highest plasma densities so far measured in MAGPIE at 20 kW. The configuration represented with the thick blue line is referred to as the “Quasi-uniform” magnetic field configuration and it provides an approximately constant field underneath the antenna region. In addition, magnetic field configurations in MAGPIE are usually identified by the DC current in the target (T) and source region (S) solenoids. For example, the “strong mirror” configuration is labelled as “T450A S50A” because it carries 450 A and 50 A at the target (T450A) and source (S50A) region solenoids respectively.

In what follows, we report on typical discharge behaviour in MAGPIE over a range of operating parameters and using the “quiescent” magnetic field configurations (Figure 7). Plasma diagnostics implemented include: (1) microwave interferometer, (2) double Langmuir probes and (3) RF magnetic probes. These diagnostics are described in Chapter 3. The aim of this section is to present the reader with an overview of what discharge conditions to expect in MAGPIE under “typical” operation. The operating conditions associated with this section (“device characterization”) and also with this thesis are described in Table 2. The underlying physical processes that drive this so called “typical” behaviour are discussed in subsequent chapters. First, we report on plasma density, electron temperature and helicon wave measurements during 20 kW operation and using the “strong mirror” magnetic field configuration (T450A S50A). Next, we explore how the plasma production scales with magnetic configuration, RF power and hydrogen fill pressure.

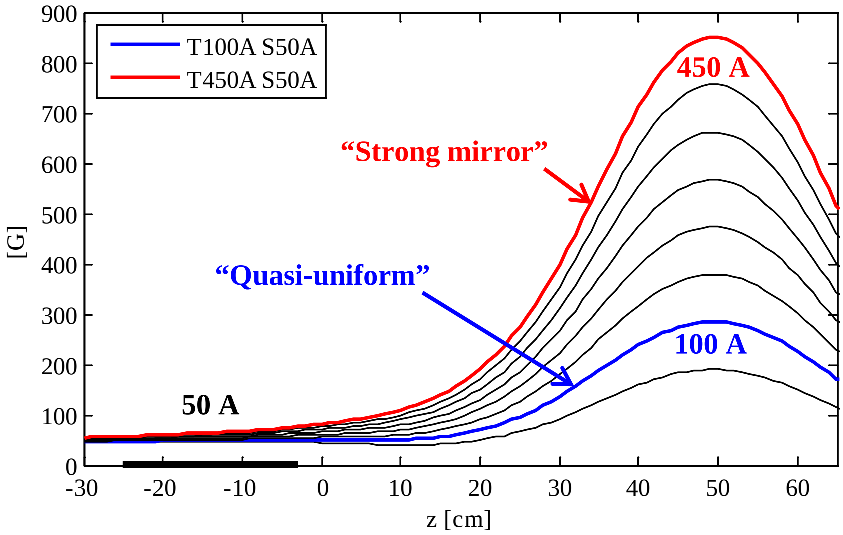

Figure 7, Magnetic field configurations in MAGPIE relevant to this thesis. Location of antenna is represented by thick black line. The source solenoid current is fixed at 50 A.

Table 2, Operating conditions associated with experimental data shown in this chapter.

Operating gas	H_2 at 8 mTorr	Antenna radius	5.2 cm
RF power (nominal)	~20 kW at 7 MHz	Antenna Location	-25 < z < -3 cm
Antenna type	Half-turn helical	Source solenoid current	50 A
Handedness	Left	Target solenoid current	50 - 450 A
Antenna current	180 A amplitude	Source field	40 – 80 G
Antenna length	22 cm	Maximum Target field	100 – 850 G

2.4.1 "Strong mirror" magnetic configuration

In this section we report on DLP measurements axially resolved along the length of MAGPIE (-20 < z < 65 cm) at r = 0 cm. The discharge operating conditions are summarized in Table 2. The "strong mirror" (T450A S50A) magnetic field configuration is used. In Chapter 3, we show that under these conditions protons are the dominant ions. The corresponding plasma density, electron temperature and plasma potential measurements along the length of MAGPIE are shown in Figure 8 and Figure 9 respectively. The plasma potential V_s in hydrogen discharges is calculated using $V_s = V_f + 3.3T_e$. This calculation assumes the electrons are Maxwell-Boltzmann distributed. In addition, the electron pressure and the proton thermal ionization rate profiles are shown in Figure 10. The antenna location is represented by horizontal thick black line along the “z” axis. The proton thermal production rate ($G_{iz}^{H} = n_e \nu_{iz}^{H}$), where n_e is the electron density and ν_{iz}^{H} is the ionization frequency, is based on the local electron temperature and plasma density measurements. It assumes that atomic hydrogen is 1/10th of the molecular hydrogen density. This calculation is described in more detail in Chapter 7.

In Figure 8a, the ion density increases approximately linearly away from the antenna, reaches a maximum and plateaus near the maximum magnetic field strength and rapidly decays in the vicinity of the end plate. In addition, the electron temperature is largest under the antenna and monotonically decreases towards the end plate where it has very low temperatures. In part (b), we provide a close up of the electron temperature near the end plate. The fast decay in plasma density near the end plate is associated with very low electron temperature (< 0.5 eV). In addition, the structures in the electron temperature under the antenna may indicate localized RF heating; however, further work is required to settle this point. Figure 9 suggests the presence of an axial electric field for z > 0 cm that accelerates ions and decelerates electrons in the direction of the target region. Figure 10 indicates that the electron pressure peaks downstream of the source region while the bulk of the thermal proton generation occurs in the vicinity of the antenna in the region -20 < z < 20 cm. In Chapter 7, we analyse these measurements using a two-fluid approach and provide an explanation for the observed equilibrium plasma density.

Radial ion density and electron temperature profiles measured at z = 11 cm are shown in Figure 11. The triangular radial density profile and the edge peaked electron temperature are typical of MAGPIE discharges for conditions as per Table 2. The corresponding radial floating and plasma potential measurements are shown in Figure 12 and indicate an ion confining radial electric field.

Additional characterization of MAGPIE has shown that the shape (not magnitude) of the ion density and electron temperature radial profiles are approximately preserved along the magnetic field lines [59]. Using the axial and radial measurements presented in Figure 8 to Figure 11, preserving the shape of radial profiles along the magnetic field lines and approximating the electron temperature for z < -20 cm with a 10 cm exponential decay, we have produced two dimensional (2D) cubic interpolated representations of the ion density and electron temperature over the entire volume of MAGPIE (Figure 13). In addition, using these contour plots the corresponding 2D electron pressure and proton thermal ionization profiles are shown in Figure 14.

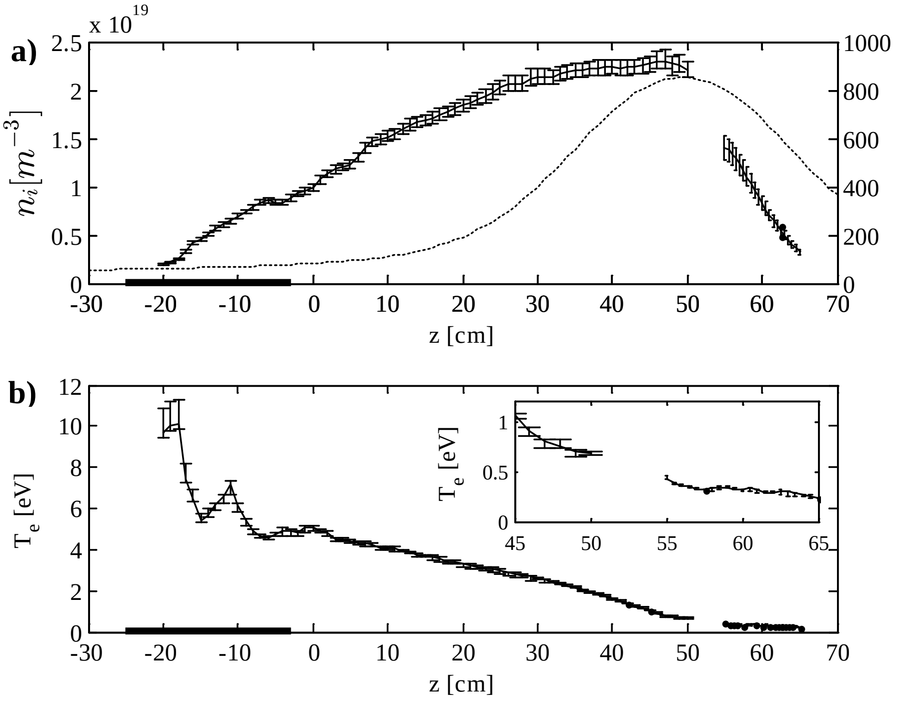

Figure 8, a) Plasma density and b) electron temperature measured on-axis along the length of MAGPIE. Background magnetic field strength (“strong mirror” T450A S50A) indicated by the dashed line in top insert.

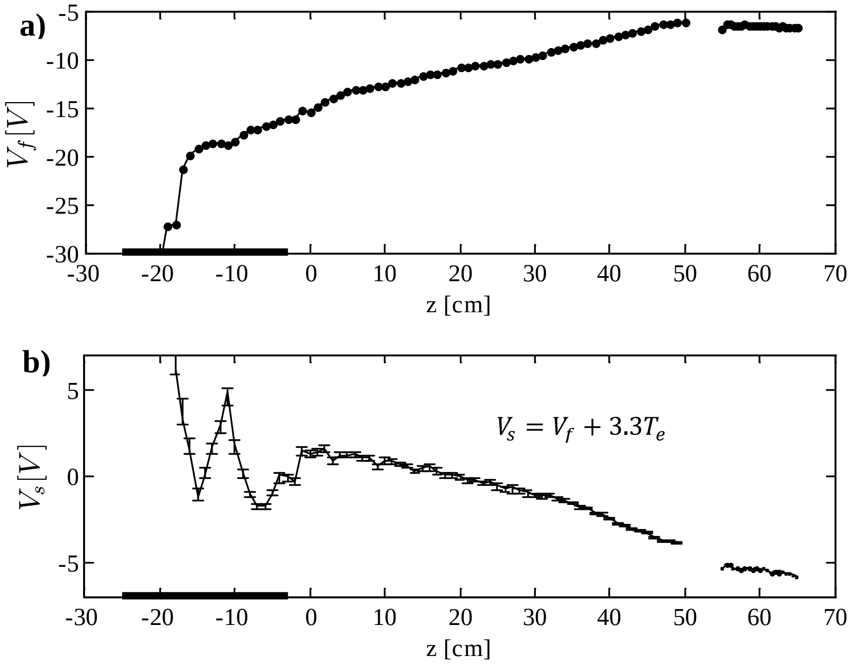

Figure 9, a) Floating potential and b) plasma potential measured on-axis along the length of MAGPIE. “Strong mirror” magnetic configuration.

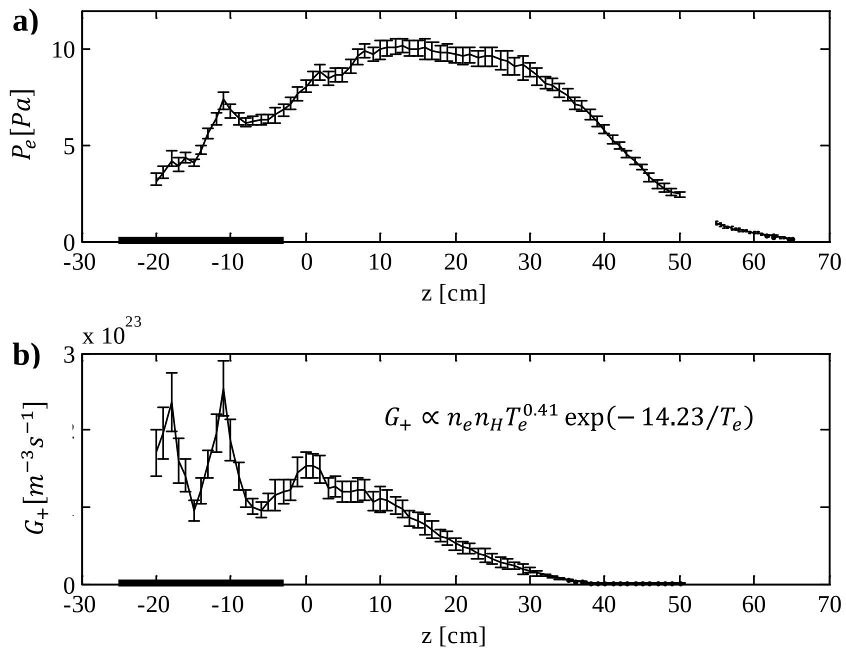

Figure 10, a) Electron pressure and b) proton thermal production rate on-axis along the length of MAGPIE. Estimates are based on local plasma density and electron temperature measurements. “Strong mirror” magnetic configuration.

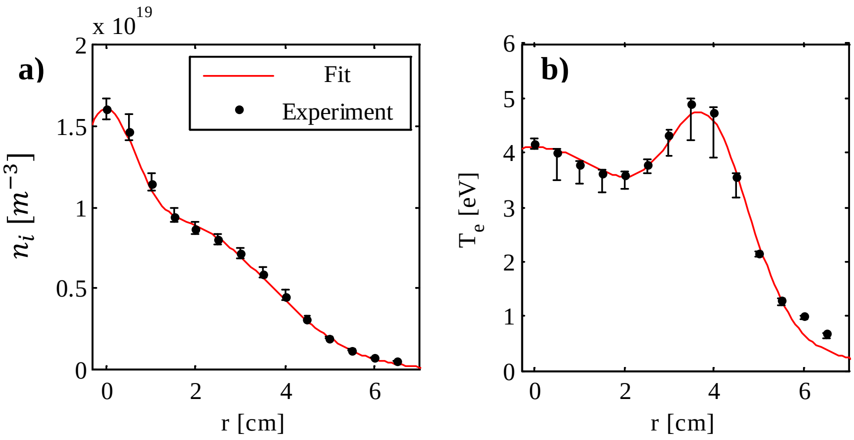

Figure 11, (a) Radial plasma density and (b) electron temperature at z = 11 cm. Ion density calculations assume a pure proton plasma. The red line represents a smooth curve fitted to the data. “Strong mirror” magnetic configuration.

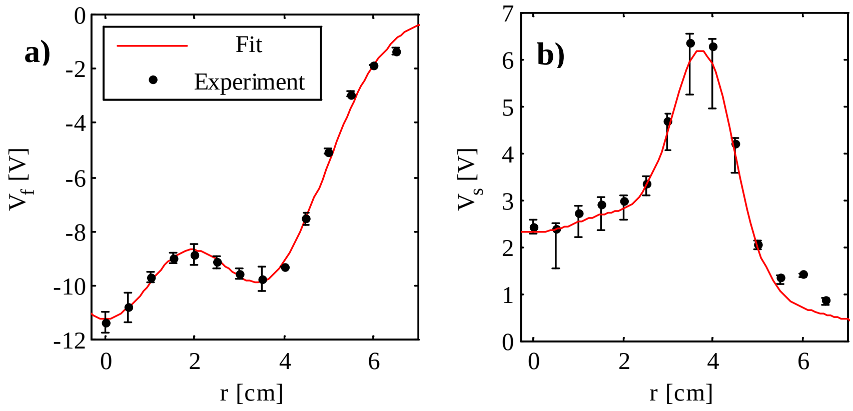

Figure 12, (a) Radial floating potential and (b) plasma potential. “Strong mirror” magnetic configuration.

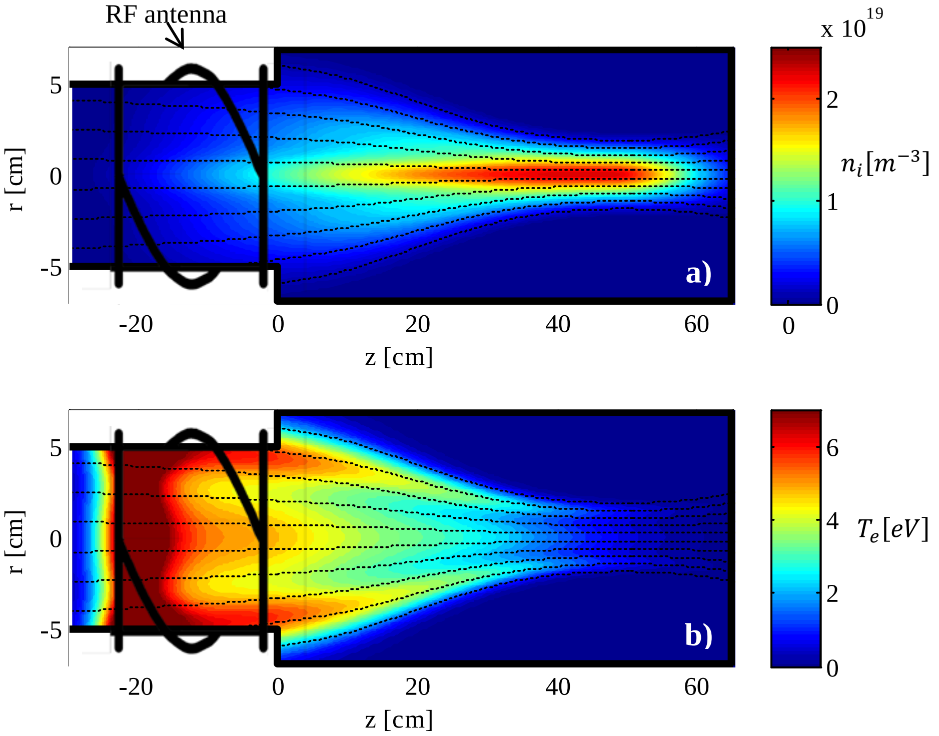

Figure 13, (a) Ion density and (b) electron temperature. Dashed lines represent magnetic field lines. “Strong mirror” magnetic configuration.

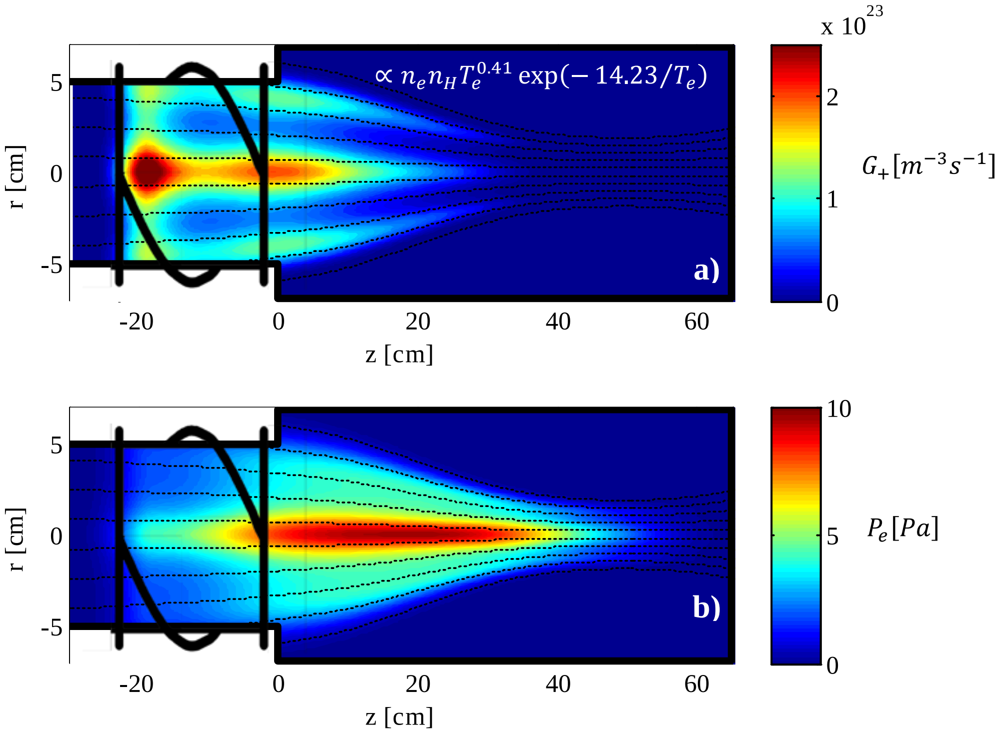

Figure 14, (a) Proton thermal generation rate and (b) electron pressure associated with Figure 13.

2.4.2 Scaling with magnetic field

In this section, we systematically vary the magnetic field in the target region and show how the ion density, electron temperature, electron pressure and helicon wavefields are modified for operating conditions as per Table 2.

Axially resolved measurements

Figure 15 shows axially resolved (a) ion density, (b) electron temperature and (d) electron pressure measurements as a function of the magnetic field configurations shown in part (c). The source solenoid current was fixed at 50 A while the target solenoid current was increased in intervals of 50 A until the “strong mirror” T450A S50A configuration (red thick line) was reached. In all the plots the red, black and blue thick lines are associated with the T450A, T200A and T050A S50A magnetic field configurations respectively. Increasing the magnetic field in the target region leads to an increase in plasma density and a decrease in electron temperature away from the antenna. In addition, the plasma density at the target region appears to increase proportionally with magnetic field strength.

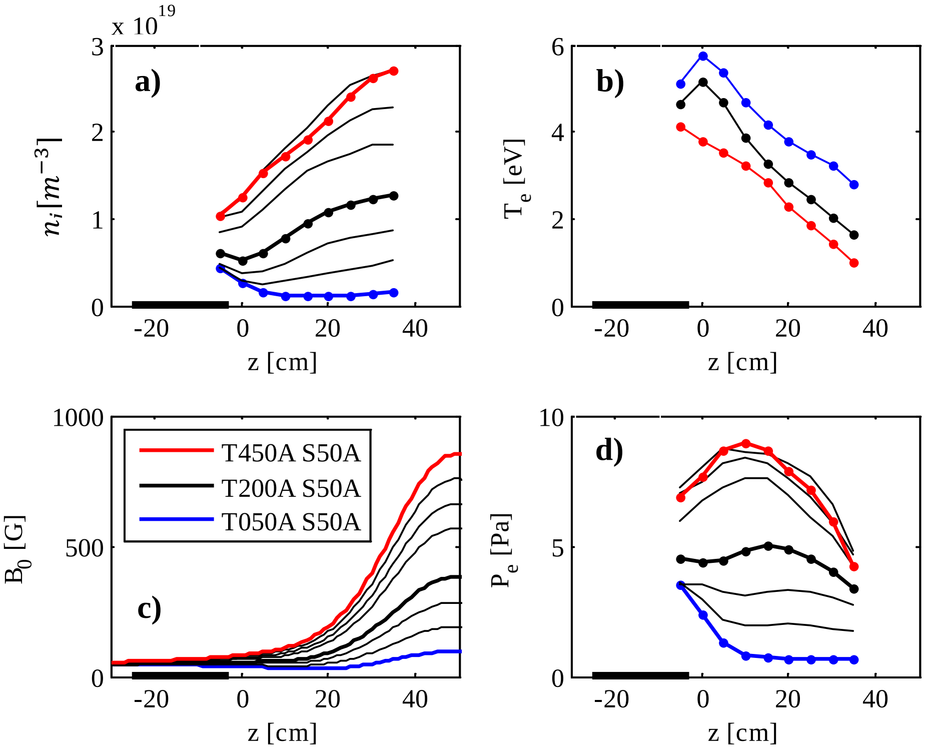

Figure 15, On-axis (a) ion density, (b) electron temperature and (d) electron pressure measurements along the length of MAGPIE for the various magnetic field configurations shown in (c). Location of antenna represented by thick black line along the “z” axis. Operating conditions as per Table 2.

Radially resolved measurements

Radial plasma density profiles associated with the measurements shown in Figure 15 were measured with an axial DLP at various locations. These are shown in Figure 16 and Figure 17 for the T200A S50A and T450A S50A magnetic field configurations respectively. The measurement‘s axial location is denoted by the label on top of each plot. The most distinct aspect of these measurements is the centrally peaked (approximately triangular) density profile at all axial positions. Near the antenna, the radial density profiles are concave at mid radius. However, as we move away from the antenna ($z > 15$ cm) the profiles become convex. The “locally concave” profile may be indicative of a local particle source (thermal ionization) while the convex profiles may be indicative of diffusive processes in the absence of particle sources. These observations are consistent with the proton thermal ionization profiles shown in Figure 10 and Figure 14; more specifically, the concavity of the radial density profiles in Figure 17 correlates with the thermal ionization profiles. In addition, in both Figure 16 and Figure 17 we observe that increases in plasma density are always accompanied with a corresponding reduction in the plasma radius. This is indicative of an increase in density due to magnetic compression.

Additional measurements were taken with a DLP located at $z = 11$ cm with an increased range of $-7 < r < 7$ cm. These measurements are shown in Figure 18 during 20 kW operation. Each plot is labelled by its corresponding magnetic configuration. Measurements show the typical “triangular” density profile observed in helicon sources. It can be seen that the plasma density increases as we increase the target region solenoid current from 150A to 550 A. However, the mean electron temperature appears to be independent of the magnetic field configuration and remains constant at about 4 eV. Nevertheless, there is indication of electron heating at the edge and increases with increasing magnetic field. At low magnetic fields, the electron temperature profile is rather flat and falls off at the edge of the plasma. At higher magnetic fields, the electron temperature begins to form distinct central and edge structures. In addition, magnetic field line calculations indicate that the edge peaks in all electron temperature radial profiles are coincident with the edge of the plasma as demonstrated in Figure 13. Due to the high thermal conductivity along the magnetic field, the shape (not magnitude) of the electron temperature profiles is approximately preserved along the magnetic field lines. In Chapter 6, calculations from a 2D full wave code (EMS2D) suggests that the peak in electron temperature at the edge may originate from surface heating under the antenna due to the electrostatic TG wave and the central peak due to on-axis heating due to the helicon wave.

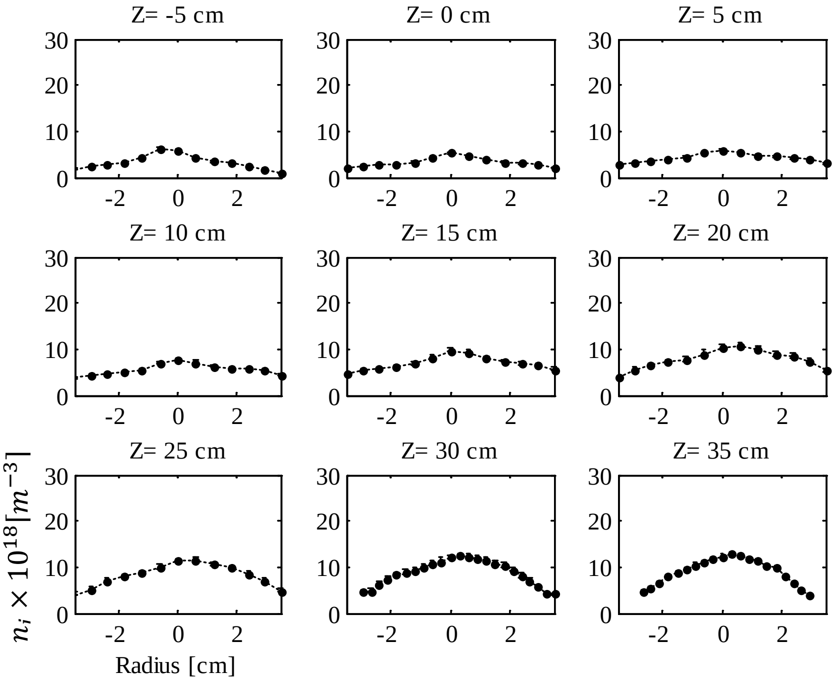

Figure 16, Radial plasma density measurements along the length of MAGPIE for the T200A S50A magnetic configuration. Labels indicate axial positon where measurement was taken.

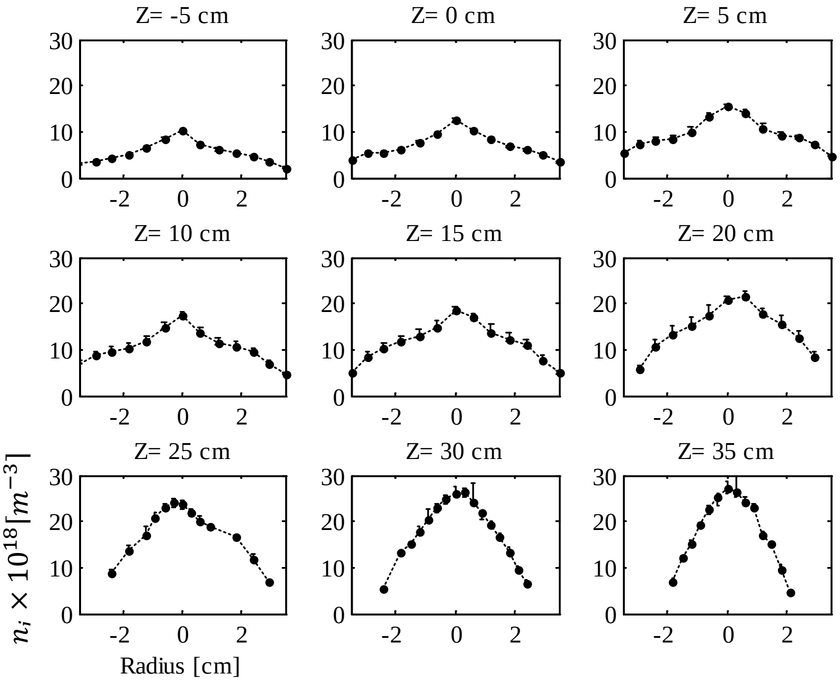

Figure 17, Radial plasma density measurements along the length of MAGPIE for the “strong mirror” (T450A S50A) magnetic configuration. Labels indicate axial positon where measurement was taken.

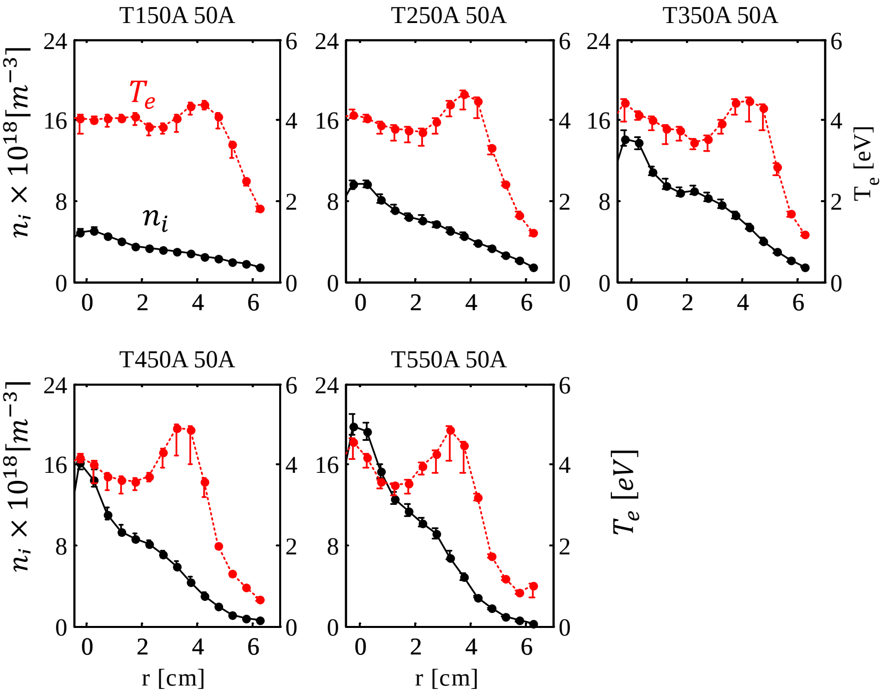

Figure 18, Radial plasma density and electron temperature measurements at z = 11 cm for various magnetic configuration at 20 kW. Labels indicate the specific magnetic configuration. Operating conditions as per Table 2.

Helicon wave propagation

As the magnetic field in the target region is increased, experimental measurements indicate changes in the helicon wavefields as shown in Figure 19. The operating conditions are as per Table 2. Part (a) presents on-axis $\underline{B_r}$ helicon wave measurements along the length of MAGPIE for different magnetic configurations. For each trace, the source solenoid current was fixed at 50 A while the target solenoid current was varied as indicated by the labels from 50 to 450 A. For convenience, we include the corresponding on-axis ion density and magnetic field strength along the length of MAGPIE in parts (b) and (c) respectively. The blue and red lines in parts (a), (b) and (c) are associated with the “Quasi-uniform” (T100A S50A) and “strong mirror” (T450A S50A) magnetic field configurations respectively. As the magnetic field in the target region is increased, the magnitude of the helicon wave at z = 0 cm increases proportionally; hence, suggesting increased helicon wave coupling for the same RF power. In addition, increasing the target magnetic field leads to “compression” of the wave’s axial interference pattern. In Chapter 6, we explore the formation of this interference pattern.

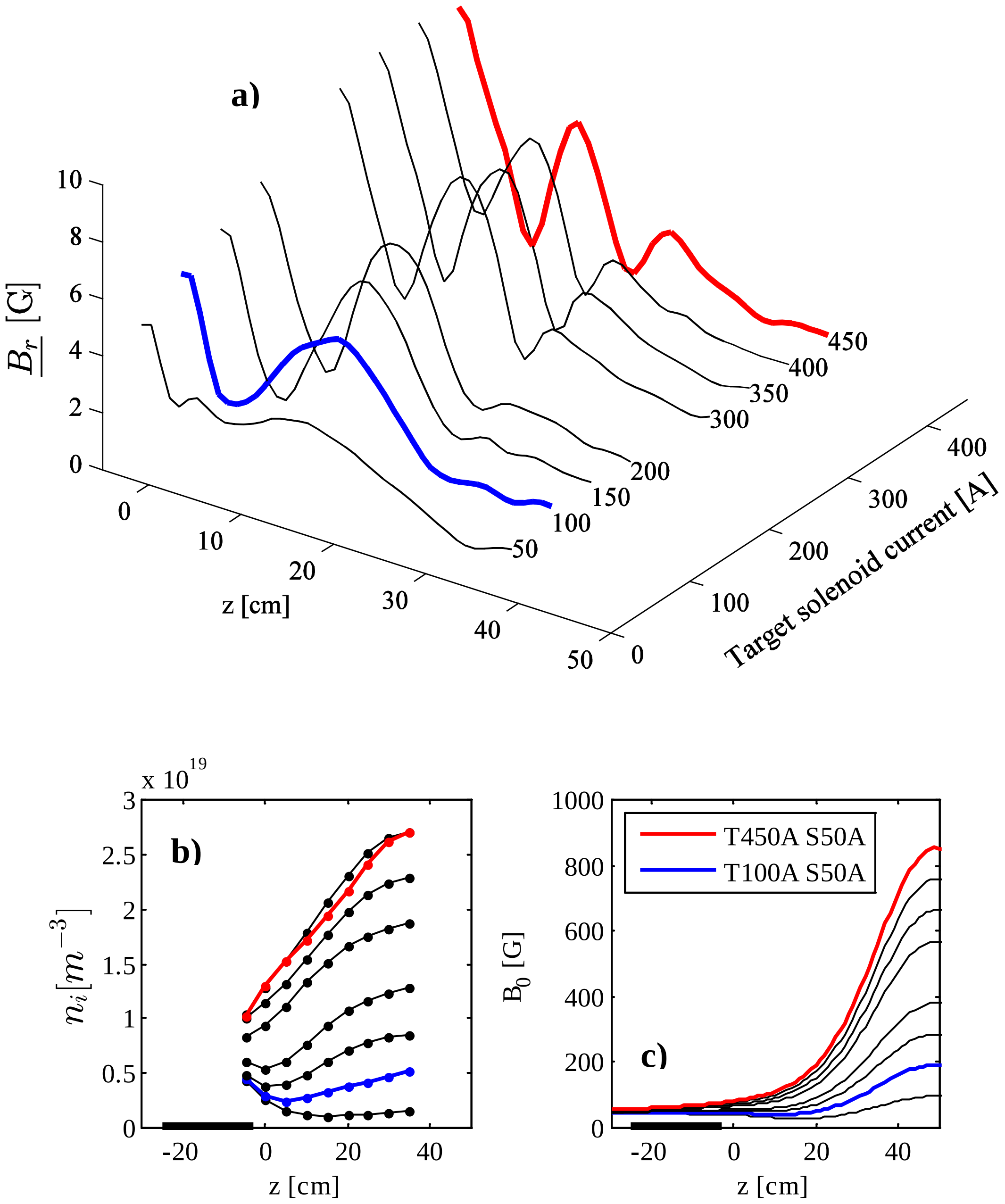

Figure 19, On-axis (a) $\underline{B_r}$ helicon wave and (b) ion density for the magnetic configurations in (c). Red and blue curves correspond to the “strong mirror” (T450A S50A) and “Quasi-uniform” (T100A S50A) magnetic field configurations respectively. The operating conditions are as per Table 2.

2.4.3 Scaling with RF power

In this section, we present measurements of plasma density and electron temperature as a function of RF power for the “strong mirror” (T450A S50A) magnetic configuration and operating conditions as per Table 2.

Microwave interferometer

In Figure 20, we show on-axis peak electron density measurements taken at z = 14 cm for various RF power levels. The insert within the figure illustrates a typical radial density profile measured with a DLP at z = 11 cm under the same discharge conditions. Peak electron density was estimated from the line integrated interferometer measurement and assuming a “triangular” density profile with a plasma diameter of 10.5 cm ± 1 cm based on DLP ion density radial measurements. Measurements indicate the presence of a discharge mode transition at about 5 kW. For RF power levels below 5 kW, comparison between DLP and interferometer measurements suggests H_2^+ and H_3^+ ions are dominant as discussed in Chapter 3. However, above 10 kW DLP and interferometer comparative measurements suggest H^+ ions are dominant. In addition, over the entire power range the electron density increases linearly with RF power and reaches a maximum value of about 2.3×10^{19} m^{-3} at about 20 kW. Axial DLP measurements indicate that ion density (Figure 15) near z = 40 cm is approximately 20% higher than at z = 14 cm. This suggests that maximum electron densities in MAGPIE at 20 kW could be close to 3×10^{19} m^{-3} in the target region.

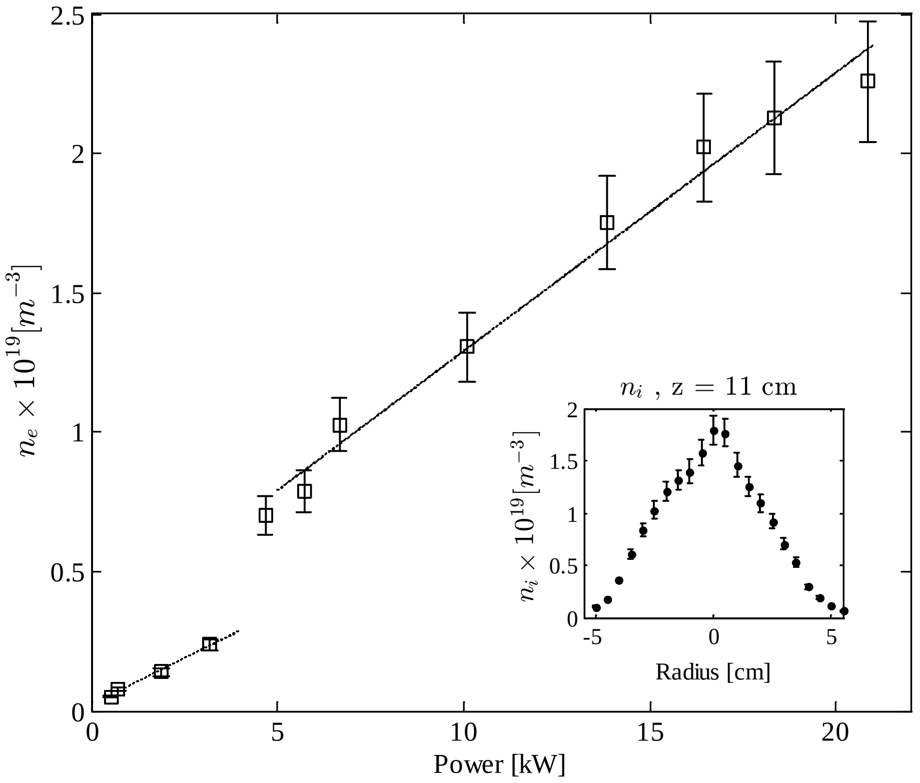

Figure 20, On-axis peak electron density measurements taken with microwave interferometer at z = 14 cm for various RF power levels, hydrogen at 8 mTorr and “strong mirror” (T450A S50A) magnetic configuration. The insert shows a typical “triangular” density profile in MAGPIE measured at z = 11 cm.

Edge heating

Measurements indicate that as the RF power is increased the radial electron temperature profile changes. Figure 21 shows radial electron temperature and ion density profiles measured with a DLP at z = 11 cm for different RF power levels, hydrogen at 8 mTorr and the “strong mirror” T450A S50A magnetic configuration. Parts (a) and (c) correspond to 17 kW. Parts (b) and (c) correspond to 5 kW. Red dashed lines represent the edge and on-axis Gaussian curves fitted to the experimental data. These measurements indicate that the electron temperature at the edge increases with increasing RF power as shown in parts (a) and (b). This suggests an increased contribution of RF heating at the edge with RF power. For completeness, the corresponding radial ion density measurements are shown in parts (c) and (d) for the 17 and 5 kW discharges respectively. Notice that for the higher RF power measurements (a) and (c) the relative contribution of the Gaussian curve at the edge, in both temperature and density measurements, is increased relative to the lower RF power measurements (b) and (d).

As the RF power was increased, we observed that the reflected power increased from 2% at 5 kW to about 20% at 20 kW. It was considered that the larger reflected power could lead to capacitive coupling in the plasma and produce the observed edge heating. For a fixed net input RF power, the voltage on the antenna should be independent of the reflected power since the antenna is grounded at one end. Nevertheless, we measured electron temperature and ion density in a 5 kW discharge at various levels of reflected power from 2% up to 40% to verify that discharge conditions are independent of the reflected power. The measurements in Figure 22 indicate that both ion density and electron temperature radial profile are independent of the level of reflected power and thus we can consider the edge peaking of the electron temperature as an effect of wave power deposition or inductive heating at the edge. In Chapter 6, using a 2D full wave code we find evidence of edge localized RF heating due to the electrostatic Trivelpiece-Gould (TG) wave and on-axis RF power deposition due to the helicon wave.

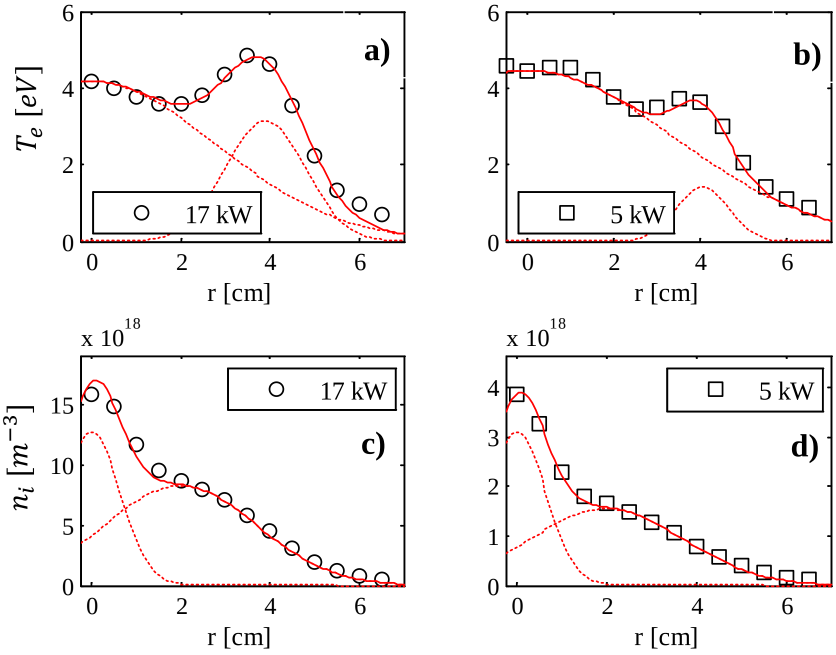

Figure 21, Radial electron temperature (a)-(b) and ion density profiles (c)-(d) measured with a DLP at z = 11 cm for different RF power levels (5 and 17 kW), hydrogen at 8 mTorr and "strong mirror" (T450A S50A) magnetic configuration. Red dashed lines represent the edge and on-axis Gaussian curves fitted to the data.

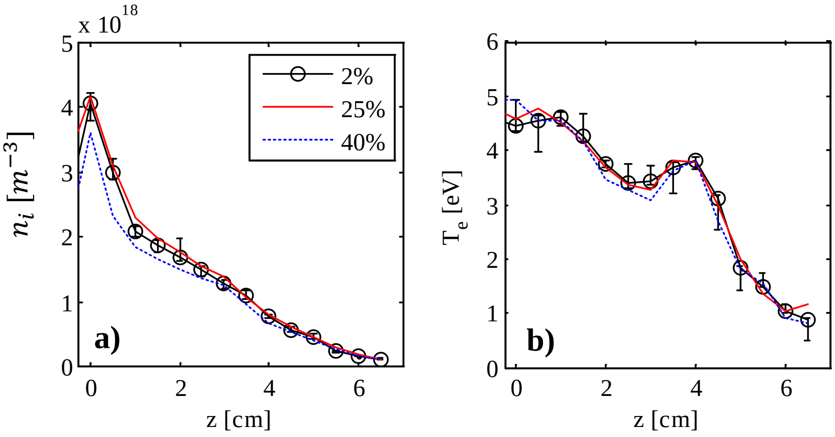

Figure 22, (a) Ion density and (b) electron temperature radial profiles measured with a DLP at z = 11 cm, total RF power of 5 kW for different levels of reflected power (2, 25 and 40 %), hydrogen at 8 mTorr and "strong mirror" (T450A S50A) magnetic configuration.

2.4.4 Scaling with fill pressure

In this section, the hydrogen fill pressure is systematically increased from 2 mTorr to 12 mTorr at 20 kW and using the “strong mirror” T450A S50A magnetic field configuration.

Figure 23 shows ion density (a) and electron temperature (b) radial profiles measured with a DLP at z = 11 cm for various fill pressures. Measurements indicate that the ion density is centrally peaked and reaches a maximum value of about 1.8×10^{19} m^{-3} somewhere between 4 and 8 mTorr. The electron temperature radial profiles can be described by a centre and an edge structure. This suggests the presence of on-axis and edge RF heating respectively. Both of these temperature structures increase in magnitude with decreasing fill pressure. However, the edge structure appears to be more affected by the fill pressure. This can be understood by noting that as the plasma density decreases towards the edge, the effective collision frequency is determined more by electron-neutral collisions than by Coulomb collisions; as a result, collisional damping and electron cooling at the edge depends strongly on the fill pressure.

Figure 24 illustrates on-axis ion density, electron temperature and plasma potential measurements along the length of MAGPIE for different hydrogen fill pressures. The operating conditions are 20kW, 3 to 8 mTorr and T450A S50A magnetic configuration. The antenna location is represented by the thick black line along the “z” axis. The on-axis background magnetic field is represented by the thin black line in the top insert. Increasing the hydrogen fill pressure leads to an increase in ion density which reaches a maximum at 8 mTorr and z~40 cm. Plasma “detachment” is observed near the end plate (z > 55 cm) for pressures greater than 6 mTorr. In addition, increasing fill pressure leads to a global reduction in electron temperature and a much stronger reduction near the end plate. In fact, for cases where the plasma appears “detached” the electron temperature is falls below 1 eV near the end plate. Moreover, plasma potential measurements and their corresponding gradients for z > 0 cm appear to indicate a small increase in the axial electric field (E_z) as the fill pressure is increased.

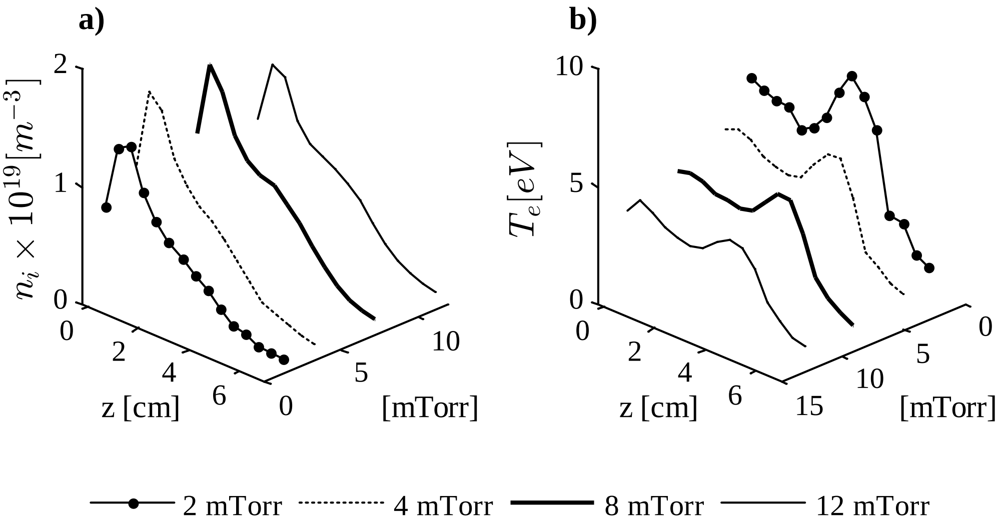

Figure 23, (a) Ion density and (b) electron temperature radial profiles measured with DLP at z = 11 cm at different hydrogen fill pressures from 2 mTorr to 12 mTorr at 20 kW and “strong mirror” (T450A S50A) magnetic configuration.

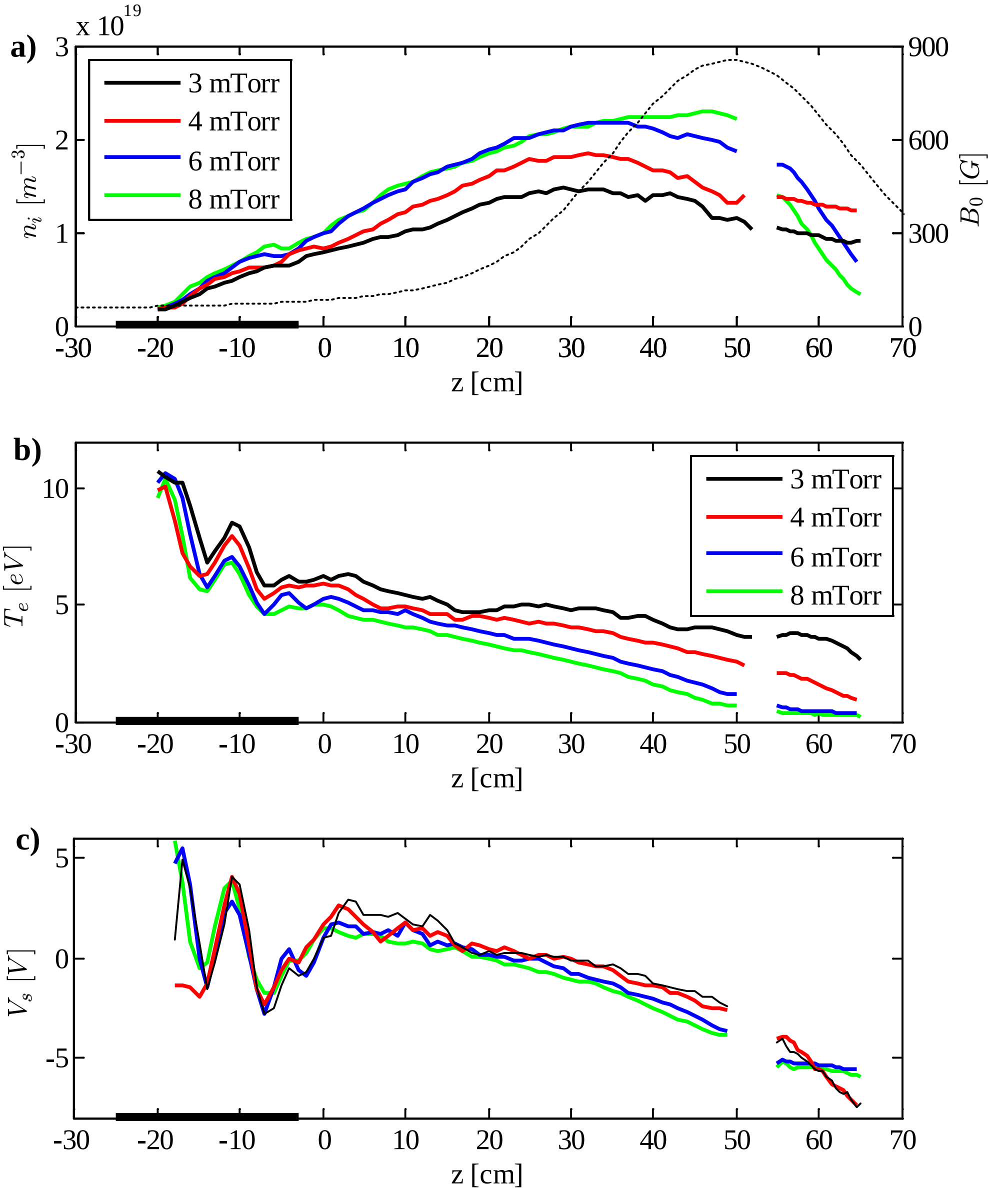

Figure 24, (a) Ion density, (b) electron temperature and (c) plasma potential measurements on-axis and along the length of MAGPIE as a function of hydrogen fill pressure. The operating conditions are 20kW, 3 to 8 mTorr and “strong mirror” (T450A S50A) magnetic configuration. Background magnetic field is illustrated in part (a) with the thin black line. Antenna location represented by thick black line along the “z” axis.

Chapter 3 Diagnostics

3.1 Introduction 44
3.2 Microwave interferometer 46
  3.2.1 Description 46
  3.2.2 Principle of operation 47
3.3 Double Langmuir probes 49
  3.3.1 Description 49
  3.3.2 RF effects 51
  3.3.3 Magnetic field effects 54
  3.3.4 Effect of Molecular gases 57
3.4 RF magnetic probes 61
  3.4.1 Description 61
  3.4.2 Amplitude demodulation 62
  3.4.3 Calibration 63

3.1 Introduction

In this Chapter we provide a brief outline of the plasma diagnostics used in this work, namely, (1) a 140 GHz Microwave Interferometer (MWI), (2) Double Langmuir Probes (DLPs) and (3) a RF Magnetic Probe (MP). The MWI is primarily used to take absolute values of electron density and to calibrate DLP based measurements. The DLPs are used to take radially and axially resolved plasma density, floating potential and electron temperature measurements in the region downstream of the plasma source. The MPs are used to make axially and radially resolved helicon wave measurements and investigate the wave propagation physics in MAGPIE.

The diagnostic access in MAGPIE is shown in Figure 25. DLPs and MPs are inserted through Port 1 to provide axially (-20 to 65 cm) and radially resolved (-4 to 4 cm) measurements. This setup allows detailed measurements under the helicon antenna and well into the target region where the background magnetic field reaches a maximum. A radially resolved (-7 to 7 cm) DLP is inserted through Port 3 located at z = 11 cm. In addition, the MWI beam is launched radially into the plasma through Port 2 located at z = 14 cm.

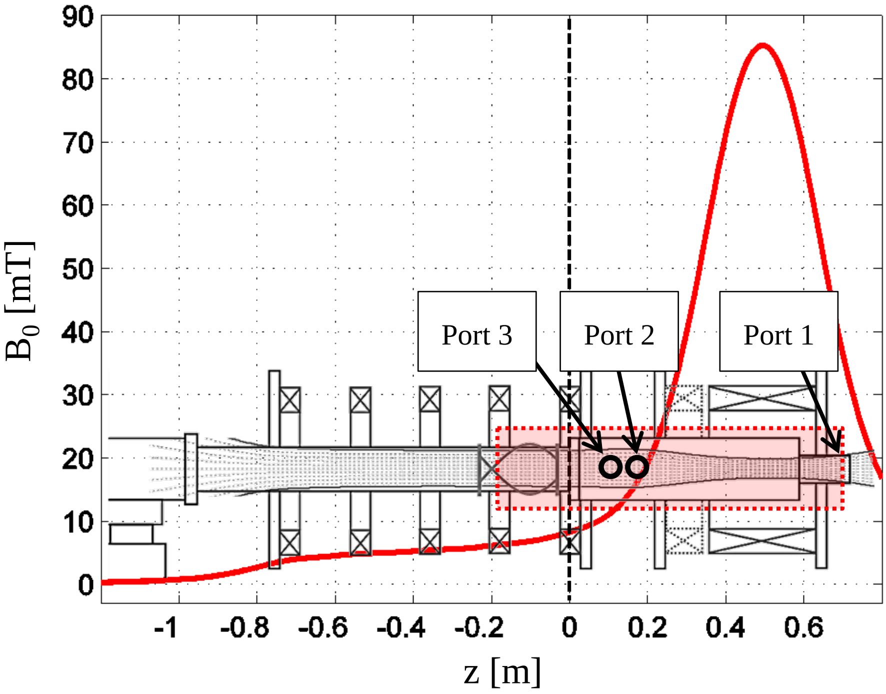

Figure 25, Diagnostic access in MAGPIE. The region enclosed by the red rectangle illustrates the volume accessible with both the DLP and MP.

3.2 Microwave interferometer

By launching waves across a plasma volume, this diagnostic infers the electron density by measuring the refractive index of the plasma. To penetrate the plasma without any significant interaction electromagnetic waves with frequencies much higher than the plasma frequency are required; generally, in the microwave range. The refractive index is measured from the phase delay of the wave as it traverses the volume of plasma. By combining the “probing” beam with a coherent “reference” beam the phase delay is inferred from an interference pattern. For microwave frequencies much greater than the plasma frequency the phase delay and the line integrated electron density are related by Eq. 1 [60]. The terms $\Delta\phi, n_e$ and n_c represent the phase delay, electron density and cut-off density for the given microwave frequency ω respectively. The variable “s” describes the path length of the beam. The terms c, ϵ_0, m_e and e represent the speed of light, permittivity of free space, electron mass and electron charge respectively. For more details on this diagnostic refer to the following books [60], [61] or articles [62], [63], [64]. Due to their non-intrusive nature and simpler theoretical framework based on the cold plasma approximation MWI measurements are considered to be more reliable than electrostatic probes. The main contribution of the MWI in this work is to provide absolute electron density measurements and allow calibration of the DLPs.

$$\Delta\phi = \frac{\omega}{2cn_c}\int n_e(s)\,ds \quad n_c = \frac{\epsilon_0 m_e \omega^2}{e^2} \tag*{Eq. 1}$$

3.2.1 Description

The type of MWI implemented in MAGPIE is referred to as a “double pass 140 GHz heterodyne polarization interferometer”. The term “heterodyne” refers to the use of two distinct frequencies; namely, (1) a microwave and (2) a modulating (intermediate) frequency. The topology of the MWI in MAGPIE corresponds to a Michelson interferometer and its setup is illustrated in Figure 26. A Voltage Controlled Oscillator (VCO) provides plane polarized microwave radiation with a Gaussian radial profile at a central frequency of 140 GHz and a bandwidth Δf of 2 GHz. A 100 kHz sawtooth waveform is used to linearly modulate the VCO’s radiation from 139 to 141 GHz. At this frequency (140 GHz), quasi-optical theory has to be used to describe the propagation of the microwave beam [64]. The microwave radiation from the VCO is separated into two coherent beams using a 45 degree wire beam splitter. We refer to these as the “reference” and “probe” beams. Using an elliptical mirror, the “probe” beam is focused down to 3 cm in diameter and injected into the plasma through a TPX window in Port 2 (Figure 25) at z = 14 cm.

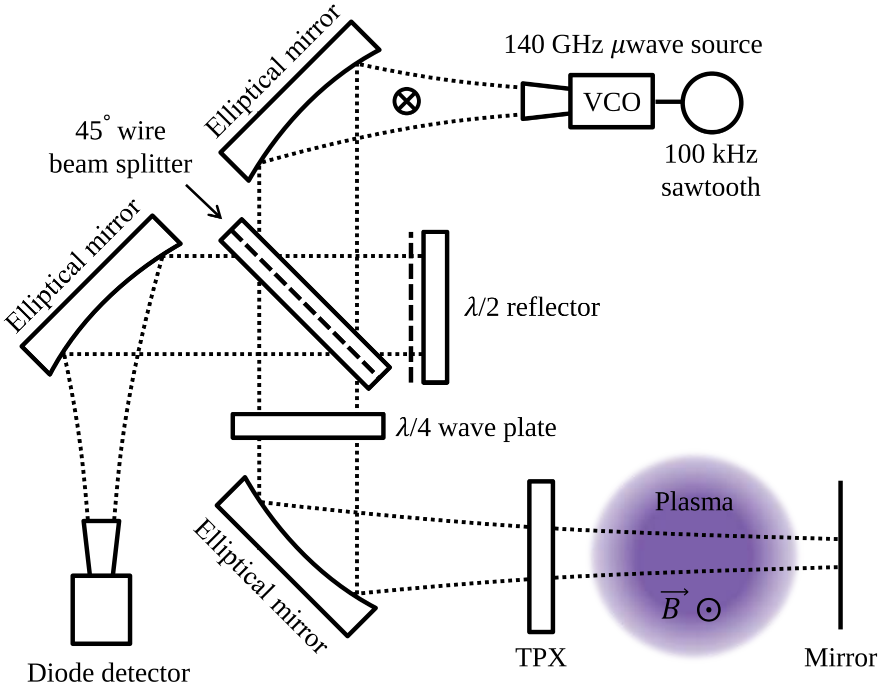
Elliptical mirror
140 GHz μwave source
VCO
100 kHz
sawtooth
45° wire
beam splitter
Elliptical mirror
$\lambda/2$ reflector
$\lambda/4$ wave plate
Plasma
$\vec{B}$ ⊙
Elliptical mirror
Diode detector
TPX
Mirror

Figure 26, Schematic of the microwave interferometer in MAGPIE

The TPX window is tilted a few degrees to reduce reflections back into the interferometric setup. The "probe" beam traverses the plasma volume twice as it is reflected from a mirror across the plasma. The reflected outgoing "probe" beam is separated from the incoming "probe" beam using a quarter wave plate by rotating the beam's polarization 45 degrees per pass for a total rotation of 90 degrees. The incoming "probe" and "reference" beam are combined at a microwave diode detector and the interference pattern is measured as a function of time. As the plasma density increases at the start of every RF pulse, the "probe" beam experiences a phase delay with respect to the "reference" beam due to the changing refractive index of the plasma and the resulting interference pattern changes accordingly.

3.2.2 Principle of operation

The equations describing the operation of the heterodyne polarization interferometer are described next. The "reference" and "probe" beams are described by two complex electric field plane waves as in Eq. 2 and denoted with subscripts 1 and 2 respectively. We represent the length traversed by the beams with the symbol "s". In addition, both beams are coherent and thus share the same frequency and wavenumber. However, due to path length difference and the effect of plasma phase shift they will in general have different phases ϕ_n. If we assume both beams have the same magnitude, the resultant electric field at the diode detector is given by the superposition of the “reference” and “probe” beams (Eq. 3). The terms ΔL and $\Delta\phi$ represent the difference in path length and phase between the beams. The terms ΣL and $\Sigma\phi$ represent the sum of the path lengths and phases of the beams. By linearly varying the radiation’s wavenumber using the 100 kHz sawtooth modulation on the VCO, the total electric field (Eq. 3) can be viewed as the product of a high frequency GHz carrier modulated by a low frequency kHz envelope. In general, diode detectors measure the square of the electric field (power) and only the slow frequency modulation component. Therefore, after neglecting the GHz component and using trigonometric identities, the kHz signal measured by the diode detector is given by Eq. 4. The time varying component of Eq. 4 is labelled as δE_t^2 and is given in Eq. 5. We notice that the plasma induced phase shift $\Delta\phi$ can be extracted from this expression by eliminating the known VCO induced phase shift ($k\Delta L$) by means of Fourier or Hilbert transforms. Using Eq. 1 and the extracted plasma induced phase shift $\Delta\phi$ one can estimate the line integrated electron density. These results are equally valid when the “probe” and “reference” beams are not of equal amplitude. In Figure 32 to Figure 34, examples of MWI measurements are shown and compared with DLP measurements under various operating conditions.

$$\boldsymbol{E}_n(s,t) = \overline{\boldsymbol{E_n}} \exp[i(ks - \omega t + \phi_n)] \quad n = 1,2 \qquad \text{Eq. 2}$$

$$\boldsymbol{E}_t = 2\overline{\boldsymbol{E_1}} \cos\left(\frac{k\Delta L + \Delta\phi}{2}\right) \exp\left[i\left(\frac{k\Sigma L + \Sigma\phi}{2} - \omega t\right)\right] \qquad \text{Eq. 3}$$

$$E_t^2 = 2\overline{E_1}^2 + 2\overline{E_1}^2 \cos(k\Delta L + \Delta\phi) \qquad \text{Eq. 4}$$

$$\delta E_t^2 = 2\overline{E_1}^2 \cos(k\Delta L + \Delta\phi) \qquad \text{Eq. 5}$$

3.3 Double Langmuir probes

In the diagnosis of low temperature plasma the electrostatic probe method is generally implemented since it provides a simple and inexpensive setup compared to other more elaborate diagnostics. For the work presented in this thesis, a symmetric double Langmuir probe (DLP) [65], [66] has been chosen over the more common RF compensated single Langmuir probe (SLP) [67]. At the RF power (20 kW) and densities ($\sim 1\text{x}10^{19}$ m^{-3}) relevant to this thesis, it was considered that the delicate RF compensating circuity of the SLP could become compromised through thermal damage. For this reason, a more rugged electrostatic probe diagnostic was required and hence the DLP. However, there are additional circumstances in MAGPIE that influence the implementation of electrostatic probes such as RF potentials, magnetic fields and molecular ion effects.

3.3.1 Description

Two DLPs are used in MAGPIE: (1) an “axial” DLP and (2) a “radial” DLP. The “axial” DLP is inserted through Port 1 (Figure 25) and provides axial access in MAGPIE from -20 cm to 65 cm. The “axial” DLP has a 3.5 cm ceramic segment joined at right angles to the end of the probe and allows angular motion for taking radially resolved measurements across the plasma from -4 to 4 cm (Figure 27). The “radial” DLP is inserted through Port 3 (Figure 25) at z = 11 cm and provides radially resolved measurements across the plasma from -7 to 7 cm.

Figure 28 provides a schematic of the DLPs, where “L” is the effective length of the probe and is 1 meter for the “axial” DLP and 30 cm for the “radial” DLP. Each DLP consists of a 6 mm OD electrically grounded stainless steel tube enclosing a pair of 50 Ohm coaxial cables. The inner conductor of each coaxial cable is connected to a 0.17 mm diameter molybdenum current collecting tip. At the other end, the outer conductor of each coaxial cable is grounded while the inner conductor is connected to a RF choke tuned at 7 MHz to provide RF isolation between the DLP and the DC biasing circuitry. The RF chokes are of the inline type as described in [67]. At 7 MHz, each RF choke provides an impedance of about 60 kΩ. The RF chokes restrict the effective capacitance of the DLP to that of the coaxial cables in the “DLP assembly” (Figure 28). The stray capacitance of the “DLP assembly” with the RF chokes in place was measured to be about 100 pF and 30 pF for the “axial” and “radial” DLPs respectively. This value of stray capacitance is only valid for frequencies where the length “L” can be considered electrically short.

The DC biasing circuit consists of a power amplifier providing up to ± 100 V peak to peak swept at 17 kHz and magnetically coupled to the DLP through a 2:1 transformer. The potential of each probe ϕ^n is measured on the filtered side of the RF chokes using x10 high impedance probes and the associated current $I(\Delta\phi)$ with a Hall-effect RF current monitor. The molybdenum probe tips are routinely cleaned with electron saturation current at 60 V, 3.5 A during 1 ms pulses at 10 Hz repetition rate. The analysis of the DLP characteristics incorporates Laframboise's theory [68] using the procedure described by Beal [69]. RF rectification, magnetic field and molecular ion effects are discussed next.

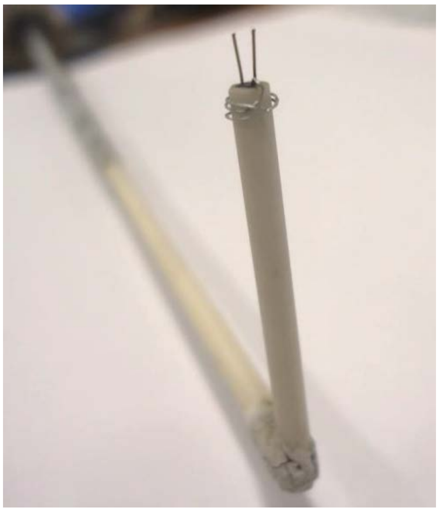

Figure 27, "Axial" DLP showing the right angled segment necessary for making radially resolved measurements along the length of MAGPIE.

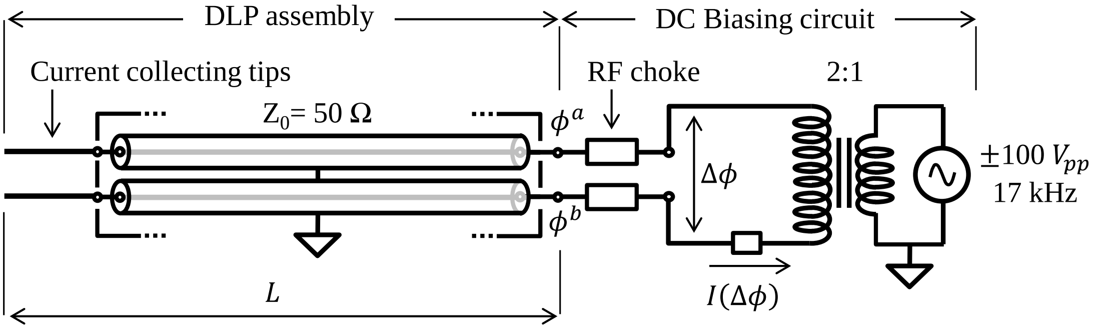
DLP assembly
DC Biasing circuit
Current collecting tips
RF choke
2:1
Z$_0$= 50 Ω
ϕ^a
ϕ^b
$\Delta\phi$
±100 V_{pp}
17 kHz
L
$I(\Delta\phi)$

Figure 28, Schematic of the DLP implemented in MAGPIE. The diagnostic can be divided into the "DLP assembly" and the "DC biasing circuit". These parts are separated by the RF chokes. In MAGPIE, the "DLP assembly" is located inside the vacuum chamber; whereas, the "DC biasing circuit" including the RF chokes are located external to the "DLP assembly" and outside the vacuum chamber.

3.3.2 RF effects

It is known that oscillating RF plasma potentials can distort probe characteristics and lead to measurement errors [67], [70]. The DLP, being of the floating type, can in principle respond to the oscillating plasma potentials and thus provide intrinsic RF compensation. We address this matter in Chapter 4. To design DLPs with adequate RF compensation, we follow the ideas presented in Chapter 4 section 4.2.8 and the examples therein.

In what follows, we focus on the operating conditions summarized in Table 3 below. These correspond to the conditions used throughout most of the work presented in this thesis. The corresponding ion density and electron temperature profiles are shown in Chapter 2 section 2.4.1. The magnitude of the time varying plasma potential $\overline{V_{p1}}$ under the antenna (z = 0 cm) and near the MWI port (z = 14 cm) was measured on-axis (r = 0 cm) with a large area electrode floating probe (Figure 29). The RF floating probe consists of a helical molybdenum electrode 0.17 mm in diameter and 12 cm in length wound around a 4 mm diameter ceramic former. The electrode was connected to the inner conductor of a 1 m long 50 Ohm coaxial cable and isolated at one end with an RF choke tuned at 7 MHz providing about 60 kOhms of impedance. The effective stray capacitance of the probe was measured to be about 100 pF. The ion saturation current I_+ corresponding to the large area electrode was measured to be about 1 A using a -45 V bias, 1 ms pulse at a repetition rate of 10 Hz. The potentials on the probe V_1 and V_2 were measured with x10 high impedance probes to avoid loading the circuit. Based on the ion saturation current (1 A), stray capacitance (100 pF) and electron temperature (4.5 eV) the corresponding value of $\omega\tau_+$ (Eq. 23 in Chapter 4) is 0.02. To accurately measure the plasma potential, the RF floating probe must be able to closely follow the RF potential. Using the concepts from Chapter 4, this requires a rectification strength $\xi < 1/100$ (Eq. 30) which imposes the condition $\omega\tau_+\overline{\phi_{p1}} < 0.4$, where the term $\overline{\phi_{p1}}$ represents the dimensionless magnitude of the time varying plasma potential. Using $\omega\tau_+ = 0.02$, this condition leads to $\overline{\phi_{p1}} < 20$ or $\overline{V_{p1}} < 20\,T_e$. Hence, this RF probe is suitable for measuring the RF plasma potential provided the magnitude is less than $\overline{V_{p1}} <$ 90 V or 180 V peak to peak.

Table 3, Operating conditions relevant to this chapter

Operating gas	H_2 at 8 mTorr	Magnetic configuration	“Strong mirror”
RF power	~20 kW at 7 MHz	Source and Target current	50 A and 450 A

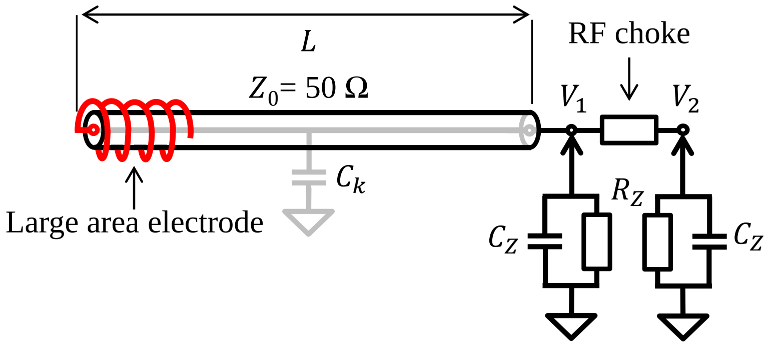

Figure 29, Schematic of the floating RF probe implemented in MAGPIE to measure the magnitude of the time varying plasma potential. The RF chokes are tuned at 7 MHz and provide an impedance of about 60 kΩ. The term C_k represents the effective stray capacitance of the probe, C_Z and R_z represent the stray capacitance (15 pF) and resistance (10 MΩ) respectively of the x10 high impedance probes used to measure the signals.

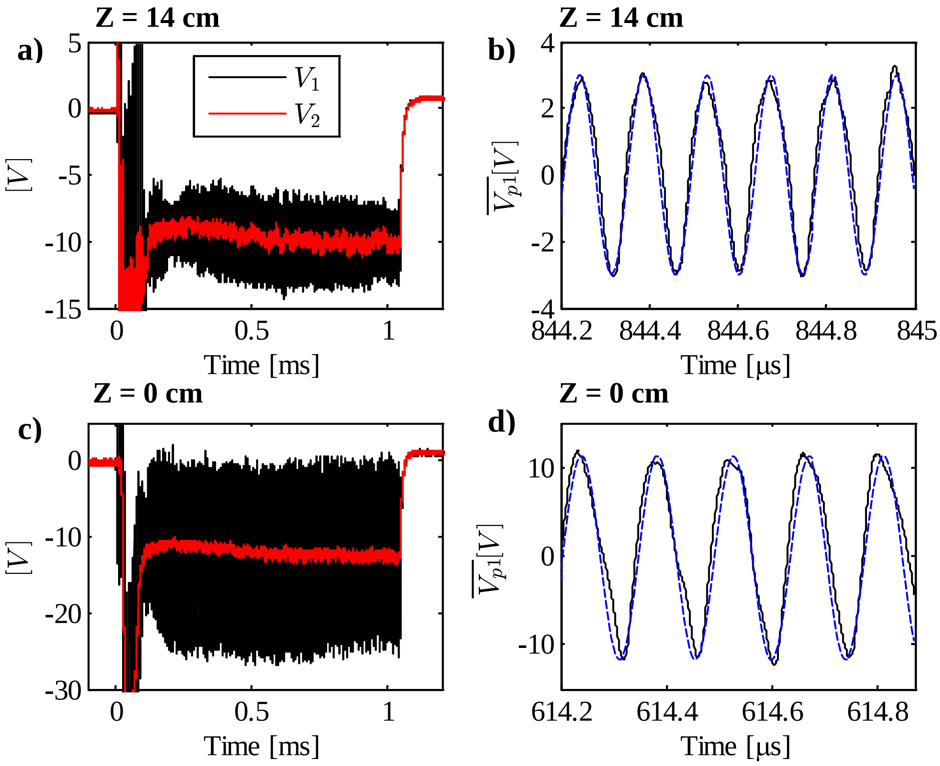

Figure 30, Measurements of the time varying plasma potential using the floating RF probe. Parts (a) and (c) corresponds to the potentials V_1 and V_2 measured at z = 14 and z = 0 cm respectively. Parts (b) and (d) show the RF plasma potential resolved in time over several RF periods. The blue dashed lines represent sine waves at 7 MHz that best fit the data.

In Figure 30, we show measurements of the RF plasma potential under the antenna (z = 0 cm) and at the MWI port (z = 14 cm). Parts (a) and (b) show measurements of V_1 and V_2 for the duration of the RF plasma pulse and indicate the presence of a DC and RF component. Under the antenna the RF component is clearly strongest. Parts (b) and (d) show the corresponding RF component resolved over several RF periods at z = 14 cm and z = 0 cm respectively. Both indicate the presence of a 7 MHz signal with minimal higher order harmonics. The magnitude of the RF plasma potential is approximately 22 and 6 V peak to peak under the antenna (z = 0 cm) and at the MWI port (z = 14 cm) respectively.

Having measured the magnitude of the RF plasma potential oscillations, we had enough information to select an appropriate length for current collecting tips for the “axial” and “radial” DLPs as follows: If we limit the rectification strength to $\xi < 1/100$, we need to satisfy the condition $\omega\tau_{+}\overline{\phi_{p1}} < 0.4$. Solving this inequality for the ion saturation current leads to the following expression: $I_{+} > \omega C_k \overline{V_{p1}}/0.4$. For the “axial” DLP, we use 22 V peak to peak at 7 MHz for the RF potential and 100 pF for the stray capacitance. This leads to $I_{+} > 120$ mA. For the aforementioned operating conditions, we can extract ion saturation currents of this magnitude (≥120 mA) under the antenna ($n_i \sim 1 \times 10^{19}$ m^{-3}) provided we use current collecting tips equal or greater than 10 mm. For the “radial” DLP, we use 22 V peak to peak at 7 MHz for the RF potential and 30 pF for the stray capacitance. This leads to $I_{+} > 36$ mA. For the aforementioned operating conditions, we can easily extract ion saturation currents greater than 40 mA near the MWI port ($n_i \sim 1.5 \times 10^{19}$ m^{-3}) with current collecting tips greater than 3 mm.

These calculations indicate that under the aforementioned discharge conditions (8 mTorr, 20 kW at 7 MHz and the “strong mirror” magnetic field configuration) we can implement RF compensated “axial” and “radial” DLPs with RF chokes placed externally to the probe assembly (outside vacuum chamber) provided we use current collecting tips of 10 and 3 mm in length respectively. The benefit of this setup is that RF chokes are not constrained to fit inside the probe shaft, they cannot be thermally damaged by the plasma and tuning can be done insitu.

3.3.3 Magnetic field effects

The presence of a background magnetic field affects current collection in electrostatic probes. This effect scales with the ratio $r_p/r_L^{e,i}$, where r_p is the probe radius and $r_L^{e,i}$ is the electron/ion Larmour radius. Stangeby [71] discusses current collection by electrostatic probes in very strong magnetic fields where $r_p/r_L^{e,i} \gg 1$. Under these conditions, both ion and electron fluxes to the probe depend on cross-field diffusion, the electron saturation current is strongly affected by the magnetic field and the I-V characteristic of the probe above the DC floating potential is not exponential. Nevertheless, as demonstrated experimentally by Tagle [72] reliable electron temperature measurements can be obtained provided the probe potential is restricted to be in the vicinity of the DC floating potential and electrons are Maxwell-Boltzmann distributed. Tagle's measurements were performed with probe surfaces of 5x10 mm^2 normal to the local magnetic field (~2 T), electron densities of ~10^{19} m^{-3} and electron temperatures of ~10 eV, leading to an approximate ratio of $r_p/r_L^e > 500$.

In low temperature laboratory plasma, where $T_i \ll T_e$ and $r_L^i \gg r_p$ are common conditions, magnetic field effects on ion current collection can be ignored. In addition, whenever the condition $r_p/r_L^e \ll 1$ is satisfied, magnetic field effects on electron collection can also be ignored [59], [73]. Under these conditions, the EEDF up to the plasma potential can be measured reliably. On the other hand, whenever $r_p/r_L^e \approx 1$ and $r_p/r_L^e \gg 1$ the electron current away from the DC floating potential is strongly affected by the magnetic field and the EEDF near the plasma potential cannot be reliably measured. However, Batani [74] states that the electron temperature can be measured in both of these cases using the slope of the I-V characteristic near the DC floating potential. As an example, electron current measurements performed by Sudit and Chen [67] in a magnetized plasma where $r_p/r_L^e \approx 1$ demonstrate that the electron current is exponential in the vicinity of the DC floating potential over two orders of magnitude in current variation. The electron current was collected with a 0.3 mm diameter RF compensated Langmuir probe biased near the DC floating potential in an argon (10 mTorr) helicon discharge with a background magnetic field of 80 mT, electron temperature of 4 eV and plasma density of about 10^{19} m^{-3}.

The aforementioned results from the literature show that in cases where $r_p/r_L^e \approx 1$ or even when $r_p/r_L^e \gg 1$, the electron temperature can be measured from the slope of the I-V characteristic near the DC floating potential. We emphasise that this method relies on the tail of the EEDF and implicitly assumes that electrons are Maxwell-Boltzmann distributed.

Measurements of ion saturation current with electrodes parallel and perpendicular to the magnetic field indicate that ion current collection is not magnetized over the length of MAGPIE for the experimental conditions relevant to this thesis (Table 3). However, the electron saturation current is strongly reduced for magnetic fields greater than 160 G. We note that the DLP technique only samples the electron current in the vicinity of the DC floating potential. As a result, in a hydrogen discharge only electrons with energies greater than 3.3 T_e are collected. Using the 3.3 T_e electron energy threshold, the ratio r_p/r_L^e can be written as in Eq. 6, where E_e is the electron energy.

$$r_p/r_L^e = r_p B_0 \sqrt{\frac{e}{m_e}\frac{1}{2E_e}} \qquad E_e \geq 3.3\,T_e \tag{Eq. 6}$$

In Figure 31a, we show electron temperature measurements taken with a DLP on-axis and along the length of MAGPIE for the operating conditions shown in Table 3. In addition, the magnitude of the background magnetic field B_0 is shown. In Figure 31b, we show the corresponding value for the ratio r_p/r_L^e based on the local electron temperature, background magnetic field and electron energies greater than 3.3 T_e. For z $<$ 30 cm, the magnetic field is less than 400 G and we have $r_p/r_L^e \ll 1$; hence, in this region magnetic field effects on electron collection can be ignored and the EEFD could be reliably measured with a single Langmuir probe if required. For z $>$ 45 cm we have $r_p/r_L^e \approx 1$ and electron collection is marginally magnetized. The largest value of the ratio r_p/r_L^e is about 2 and occurs at the peak of the background magnetic field (850 G). Since the DLP is restricted to the DC floating potential, the electron temperature measurements shown in Figure 31, including those with $r_p/r_L^e \approx 1$, can be considered reliable provided the EEDF is Maxwell-Boltzmann distributed.

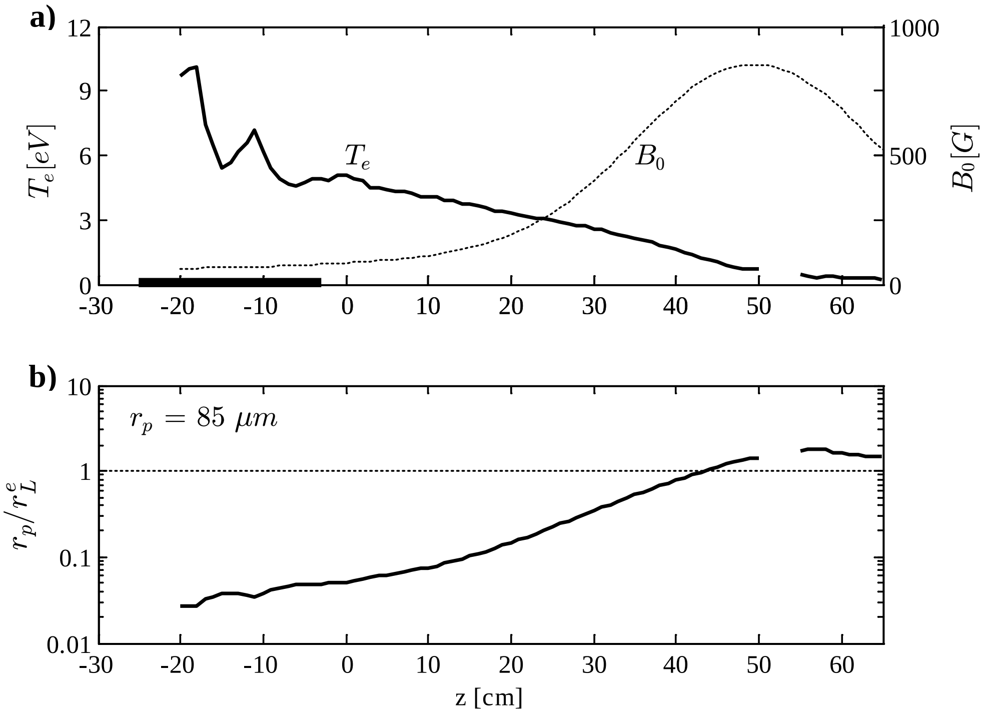

Figure 31, a) Electron temperature and background magnetic field on-axis and along the length of MAGPIE. b) Corresponding value of the ratio r_p/r_L^e for a 0.17 mm diameter probe tip.

3.3.4 Effect of Molecular gases

Hydrogen discharges, such as those in MAGPIE, are in general composed of electrons and a variety of positive and negative ion species; namely, H^-, H^+ , H_2^+ and H_3^+. As a result, the ion saturation current as measured by a probe corresponds to the contribution of all ion species. In general, the negative ion H^- is only a small fraction and can be neglected [75]. Because the different fractions of positive ions cannot be measured with a probe alone, quasi-neutrality is not sufficient to estimate the electron density.

To estimate the dominant positive ion in MAGPIE, we compared MWI and DLP line integrated densities along the same cord length in the plasma at z = 14 cm for different RF power levels and fill pressures. The “strong mirror” (T450A S50A) magnetic field configuration was used and the magnetic field at the location of measurement was 130 G. the DLP line integrated density was obtained by integrating the ion density along the cord length of the microwave beam, including the double pass contribution and assuming protons as the dominant ion. The ion density was extracted from the measured DLP characteristics using a least squares fitting method based on the work of Beal [69] which incorporates Laframboise’s theory of collisionless ion collection by cylindrical probes. Provided the fraction of positive ions does not change considerably along the cord length, the ratio between DLP and MWI line integrated density provides a measure of the dominant positive ion. Ratios that approach 1 suggest that H^+ ions are dominant. Ratios that approach $\sqrt{1/3}$ would suggest that H_3^+ ions are dominant. Generally, we observe that the dominant positive ion in MAGPIE changes with pressure and RF power.

Pressure scan

Figure 32 and Figure 33 show DLP and MWI line integrated measurements as a function of hydrogen fill pressure for 5 and 20 kW respectively. The measurements are resolved in time to demonstrate the effect of fill pressure on the rise time of the density. For discharges at 5 kW (Figure 32), DLP measurements are always less than the MWI. In fact, the ratio between MWI and DLP measurements is between $\sqrt{1/3}$ and $\sqrt{1/2}$; hence, suggesting that H_3^+ and H_2^+ are the dominant positive ions from 2 to 30 mTorr at the lower RF power.

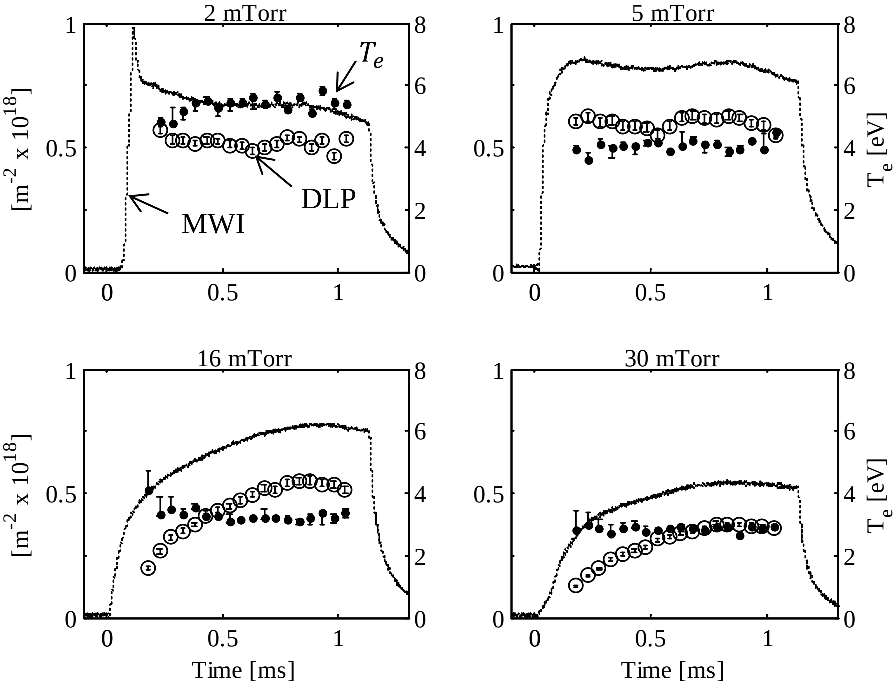

Figure 32, MWI (thin line) and DLP (open circles) line integrated densities at 5 kW of RF power for various hydrogen fill pressures (2 to 30 mTorr). Fill pressure is shown on top label of each figure. On-axis electron temperature measurements are represented by filled circles.

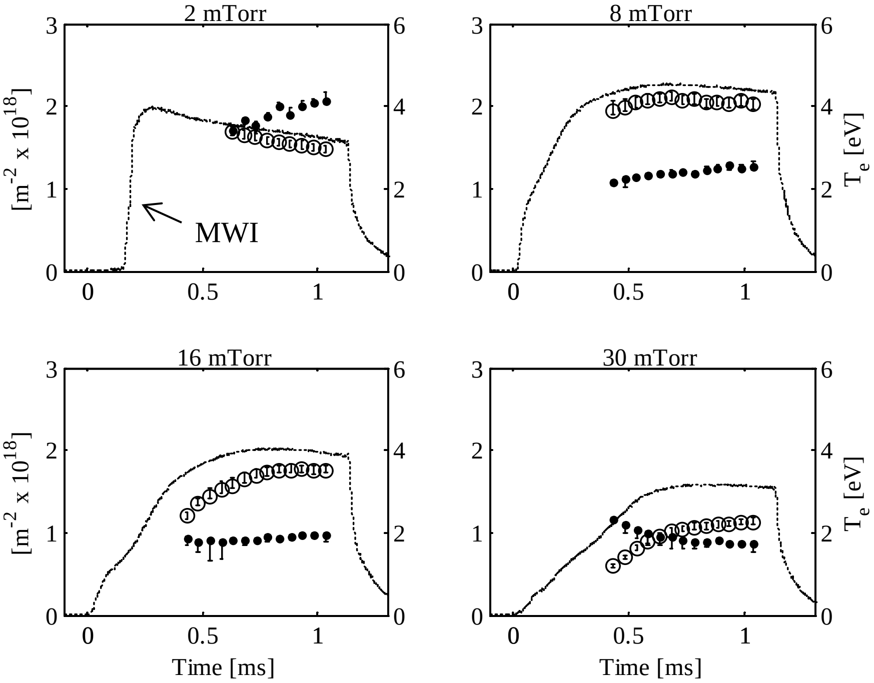

Figure 33, Same as Figure 32 but with 20 kW of RF power. The agreement between MWI and DLP is better.

For discharges at 20 kW (Figure 33), DLP measurements are consistent with MWI only at low pressures. Below 8 mTorr, protons are the dominant positive ion. Above 16 mTorr, positive ions may be a combination of H_3^+ and H_2^+. It is clear from these results that agreement between DLP and MWI improves with increasing RF power. This effect is more pronounced at low fill pressures.

We note that these estimates assume that the probe theory accurately calculates the ion density; hence, to confirm the presence of different molecular ions direct measurements are required. For example, a quadrupole mass analyser at the end of the device and/or spectroscopic measurements should be implemented.

RF power scan

In Figure 34, we show DLP and MWI line integrated measurements for hydrogen discharges at 8 mTorr as a function of RF power. At 5 kW, the DLP measurement is less than the MWI and their ratio suggest that H_3^+ and H_2^+ are dominant. Above 10 kW, DLP and MWI measurements are consistent and indicate that protons are the dominant positive ion species. Figure 32 to Figure 34, suggest that DLP measurements are within 10% of the MWI measurements provided the fill pressure is less than 8 mTorr and the RF power above 10 kW. Therefore, provided we operate in this parameter space we can use the DLP to accurately estimate the electron density.

These results are consistent with observations generally seen in the literature; namely, that in low density, low power H_2 discharges the dominant ion is generally H_3^+ [75], [76], [77]; while in high RF power, high density discharges protons are the dominant positive ion.

Approximate knowledge of the fractional positive ion densities can be obtained using other more elaborate diagnostics such as mass spectrometers [78], laser based methods or global models that describe the rich hydrogen chemistry [75], [76], [77]. Alternatively, electron based methods such as microwave interferometer, Thomson scattering or Stark effect imaging could be implemented to infer electron density directly. However, the implementation of these diagnostics is more elaborate.

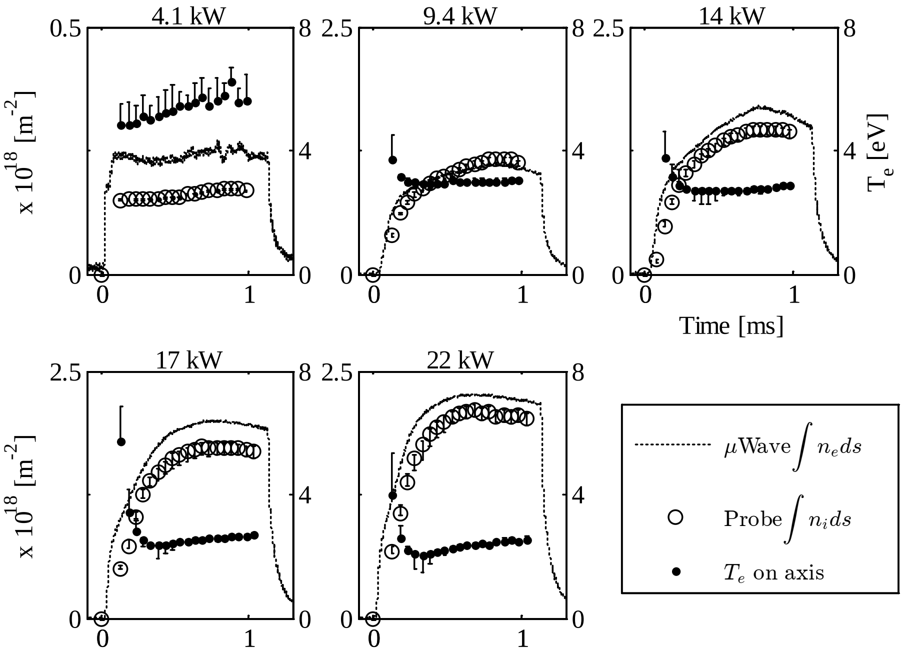

Figure 34, MWI (thin line) and DLP (open circles) line integrated densities in hydrogen discharge at 8 mTorr for various levels of RF power. RF power level is shown on top label of each insert. On-axis electron temperature measurements are represented by the filled circles.

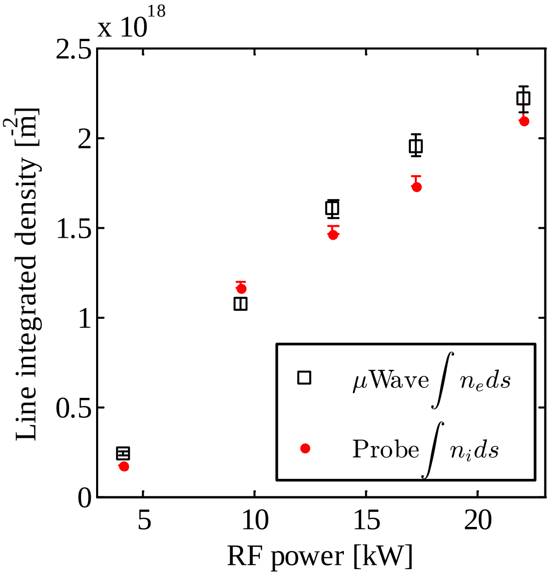

Figure 35, Steady-state part of the DLP and MWI line integrated densities shown in Figure 34.

3.4 RF magnetic probes

Plasma production and RF heating in MAGPIE is driven by both Trivelpiece-Gould (TG) and helicon waves. To study the excitation, propagation and damping of helicon waves in MAGPIE we use RF magnetic probes to measure the wave (1) amplitude and (2) phase variation with respect to the antenna current. The operation of a RF magnetic probe is based on Faraday's law of induction. By utilizing magnetic pickup coils, time varying magnetic fields can be measured from the induced potential difference. The amplitude of this potential scales with the size of the pickup coil, the RF frequency and amplitude the magnetic field as shown in Eq. 1, where $\overline{V_1}$ is the magnitude of the induced potential, ω the RF frequency, $\overline{B_1}$ the amplitude of the time varying magnetic field and A_p effective area of the magnetic probe. RF magnetic probes can only measure waves with a strong electromagnetic component. RF magnetic probes are described in greater detail in following references [35], [79], [80], [81].

$$\overline{V_1} = \omega \overline{B_1} A_p \qquad \text{Eq. 7}$$

3.4.1 Description

The RF magnetic probe implemented in MAGPIE consists of 3 mutually perpendicular balanced pickup coils situated at the end of a 1 m long probe shaft and enclosed inside a 4 mm diameter borosilicate capillary tube (Figure 37). Each pickup coil has 10 turns, 1 mm in diameter and is connected to a pair of 50 Ohm coaxial cables housed inside a 1m long grounded stainless steel tube to provide additional EM shielding.

The presence of time varying plasma potentials in RF discharges leads to electrostatic coupling between the probe and plasma. This mechanism generates spurious common mode signals in the probe, whereas those associated with helicon wave activity are differential in nature. For this reason, each pair of coaxial cables is connected to a current balun to reject common mode signals and pass differential signals. In addition, the balun converts the two-cable balanced setup into a single-cable unbalanced setup; beyond this point, each pickup coil signal is carried through a single 50 Ohm coaxial cable and properly terminated (50 Ohm) to prevent reflections. The signals from the pickup coils are (1) processed by a Quadrature Amplitude Demodulator (QAD) and then (2) digitized with an oscilloscope.

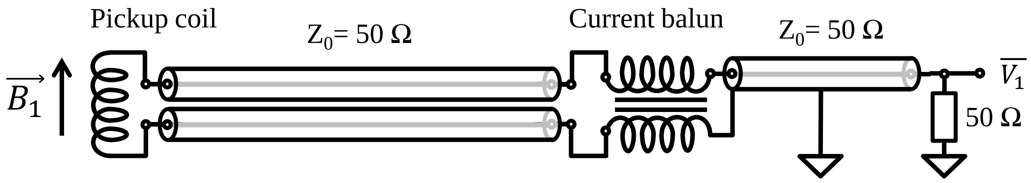

Figure 36, schematic of the RF magnetic probe. Only a single pickup coil is shown.

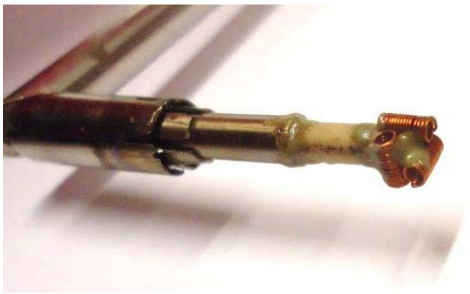

Figure 37, RF magnetic probe used in MAGPIE during this thesis. The borosilicate capillary tube enclosing the pickup coils has been removed for clarity.

The common mode rejection of the current balun[6] was tested by inserting the RF magnetic probe in a faraday cup driven at 100 V peak to peak from 1 to 30 MHz as described in [80]. Tests with and without the current balun indicate that for frequencies between 5 and 10 MHz, common mode signals are attenuated by factor of 100.

3.4.2 Amplitude demodulation

Using this approach, the RF magnetic probe signal is viewed as a carrier wave at the RF frequency with an arbitrary phase and amplitude modulated in the kHz frequency range. The Quadrature Amplitude Demodulator (QAD) is implemented to extract (1) amplitude and (2) phase of the RF magnetic probe signal with respect to a reference signal, which in this case is the RF antenna current.

In the demodulation process, the reference signal is split and converted into a quadrature pair (in phase and 90 degrees out of phase). The RF probe signal and the quadrature reference pair are combined in double balanced mixers. This process results in the product of the RF probe with the antenna current signal. Using a low pass filter, the RF component is supressed while retaining only the amplitude modulation component in the kHz frequency range. The output of the QAD is a pair of signals (“Q” and “I”) that contain the amplitude $\overline{V_1}$ and phase $\Delta\beta_1$ of the

---

[6] The “current balun” is a variant of the centre-tapped transformer method which uses the transformer action to extract the differential (magnetic) signal and reject the common mode (electrostatic) signal. Common mode signals experience high impedance at the current balun; while, differential signals pass unimpeded.

RF magnetic probe signal. These quantities are extracted using Eq. 8 and Eq. 9 respectively, where I_{RF} is the magnitude of the RF current and k_{QAD} is the gain of the QAD.

$$\overline{V_1} = \frac{1}{k_{QAD} I_{RF}} \sqrt{Q^2 + I^2} \qquad \text{Eq. 8}$$

$$\Delta\beta_1 = \tan^{-1}(Q/I) \qquad \text{Eq. 9}$$

3.4.3 Calibration

Absolute calibration of RF magnetic probes is important because knowledge of the wave amplitude allows direct comparison between experiment and theoretical predictions from full wave codes as described in Chapter 6. Absolute calibration of the RF magnetic probe was performed using a Helmholtz coil to provide a uniform and known magnetic field. The Helmholtz coil consisted of two current loops 2.5 cm in radius. The current through the Helmholtz coil was measured with an absolutely calibrated hall-effect current monitor with 500 MHz bandwidth. For frequencies below 40 MHz the Helmholtz coil was considered electrically short and the magnetic field was related to the current through $B = kI$, where k is constant of proportionality measured to be about 0.308 G per Ampere.

The calibration process was performed as follows: RF currents in the range of 40-200 mA at frequencies of 1-20 MHz where systematically driven through the Helmholtz coil and producing magnetic fields in the range of 1 to 6 μT. Each pickup coil was inserted in the region of uniform field and the induced potential difference was measured (1-4 mV) as a function of frequency as shown in Figure 38a. At low frequencies, the potential increases approximately linearly with frequency in agreement with Eq. 7; however, as the frequency increases the potential reaches an asymptote due to the finite inductance of the pickup coil. The sensitivity of the coil is defined as $S = \overline{B_1}/\overline{V_1}$ and is shown in Figure 38b. This result shows that the probe sensitivity increases linearly with frequency. At 7 MHz the probe sensitivity is about 0.5-0.6 V/mT.

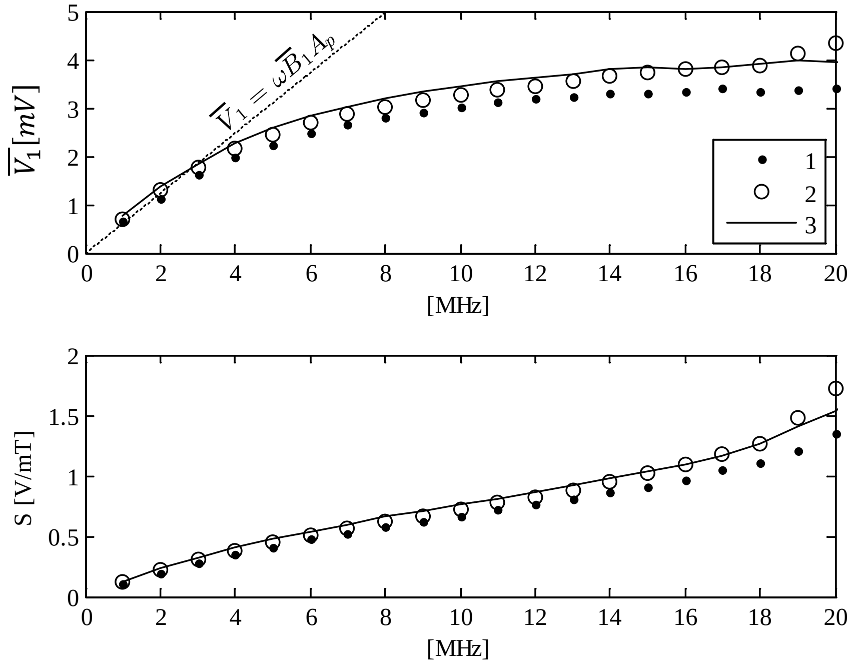

Figure 38 a) Output potential of the RF magnetic probe as a function of frequency. The dashed line represents the calculation based on Eq. 7. b) Probe sensitivity for each pickup coil with respect to RF frequency.

Chapter 4 Modelling the RF compensation of the Double Langmuir Probe method

4.1 Introduction 66

4.2 Theory 67

- 4.2.1 Assumptions 67
- 4.2.2 DC floating potential 67
- 4.2.3 Sheath rectification 68
- 4.2.4 Model of a double Langmuir probe (DLP) in RF environment 69
- 4.2.5 The driven floating probe 69
- 4.2.6 Passively driven Double Langmuir Probes (DLP) 76
- 4.2.7 Compensation of a floating probe 78
- 4.2.8 Probe design considerations 81
- 4.2.9 Effect of RF rectification on DLP measurements 85

4.3 Actively driven probe experiment 88

- 4.3.1 Apparatus 88
- 4.3.2 Results and analysis 90

4.4 DLP measurements in the presence of RF 92

- 4.4.1 Annaratone’s DLP experimental setup 92
- 4.4.2 Results 92

4.5 Discussion 95

- 4.5.1 RF compensation of the DLP 95
- 4.5.2 Effects of RF rectification on DLP measurements 96

Appendix 4A. DC floating and self-bias potentials 97

Appendix 4B. Sheath displacement current 98

Appendix 4C. Passively driven floating probe 99

Appendix 4D. Asymptotic analysis of the driven probe equation 101

Appendix 4E. Actively driven floating probe 102

Appendix 4F. Passively driven DLP 104

4.1 Introduction

The effects of RF plasma potential oscillations on Langmuir probes and how to circumvent them has been discussed widely in the literature with much attention given to the single RF compensated Langmuir probe [67], [82], [83], [84]. However, the Double Langmuir Probe's (DLP) inherent RF compensation capabilities are not well documented. In the DC regime, the DLP equations [65] assume the plasma potential is time independent; hence, RF effects are not included. In the RF regime, Annaratone [85] discusses the DLP theory in the presence of time varying potentials; however, the DLP is assumed not to respond to the RF fields, thus leading to RF rectification. The DLP technique, being of the floating type, can in principle respond to the RF fields and provide intrinsic RF compensation; however, neither the DC nor RF formulation of the DLP incorporates this behaviour. In spite of examples of DLP implementation in RF discharges [85], [86], [87], there is no quantitative analysis that explores under what conditions the DLP provides RF compensation. In short, intrinsic RF compensation in DLPs is a question that has not been addressed in the literature and remains open[7].

In this work, we address this question by developing an analytical model that describes the physics of driven floating probes and is applied to model the RF compensation of the DLP technique. Using this model, we assess under what conditions the DLP provides RF compensation. The model is based on the theory of the RF self-bias effect as described in Braithwaite's work [90], which we extend to include time-resolved behaviour. This analysis is aimed at low temperature laboratory plasma; namely, plasma densities from 10^{16} to 10^{19} m^{-3}, electron temperatures from 1 to 10 eV and driving frequencies from a few kHz up to a few tens of MHz. The physics of the floating potential in time varying plasma has not been explored as extensively as the DC case; nevertheless, recent work in this area has shown novel applications [90], [91], [92].

This article is divided into theory, experiment and discussion sections. In the theory section, we develop a model that describes the RF compensation of DLPs. Using these ideas, we provide examples of RF compensated probe design. We discuss RF rectification effects on the estimation of ion density and electron temperature in DLPs. In the experimental section, we validate the driven floating probe theory presented and confirm that RF rectification in electrostatic probes can be described with these models. In addition, we report on DLP experiments in the presence of RF rectification, which indicate that (1) whenever sheath thickness effects are important, overestimation of the ion density is proportional to RF rectification and suggest that (2) the electron temperature measurement is only weakly affected.

---

[7] It was noted by one of the reviewers of this thesis that a paper from 1978 [88] discusses the effects of RF on the DLP. The author of this thesis and the reviewers of [89] were not aware of this effort. The material presented in this chapter, however, discusses the effects of RF on DLPs in much greater detail than in [88] and provides recommendations for the design of electrostatic probes.

4.2 Theory

4.2.1 Assumptions

In the theoretical analysis that follows, we assume that electrons are Maxwell-Boltzmann distributed at a temperature T_e, plasma density and electron temperature are time-independent, ions are cold and comprise a single positive ion species and no negative ions, time varying potentials oscillate at a single frequency ω anywhere from a few kHz up to a few tens of MHz and probe lengths are modelled as electrically short transmission lines with respect to the driving frequency. In addition, we assume low frequency (DC) sheaths in the collisionless and planar limit; hence, ion saturation current is independent of potential (planar sheath). In addition, ions arrive at the sheath at the sound speed (Bohm criterion) and magnetic field effects on current collection are neglected. Although the Bohm criterion holds in RF discharges with arbitrary frequency ratios ω/ω_{pi} [93], where ω_{pi} represents the ion plasma frequency, the "DC sheath condition" requires that $\omega/\omega_{pi} \ll 1$ [67], [94]. Hence, the frequency range of validity for this analysis is limited by either the "DC sheath" or the "electrically short probe" condition, whichever is lower. Henceforth all potentials ϕ are normalized with respect to the electron temperature T_e. Equilibrium and time varying components are denoted with subscripts 0 and 1 respectively. The equilibrium plasma potential ϕ_{p0} is taken as the reference and is assigned a value of zero.

4.2.2 DC floating potential

In the absence of plasma potential oscillations, an electrically isolated surface exposed to plasma characterized by the aforementioned assumptions will attain a potential negative with respect to the plasma referred to as the DC floating potential ϕ_f (Eq. 10). A derivation for this expression is given in Appendix 4A. The terms m_e and m_p represent the electron and proton masses respectively and A_i the ionic mass in AMU. At this potential, the electron thermal flux ($\mathit{\Gamma}_e$) equals the ion flux ($\mathit{\Gamma}_+$) and no net DC current is extracted from the plasma.

$$\phi_f = -\ln\left(\frac{\mathit{\Gamma}_e}{\mathit{\Gamma}_+}\right) = -\ln\left(\frac{1}{0.61}\sqrt{\frac{m_p A_i}{2\pi m_e}}\right) \qquad \text{Eq. 10}$$

4.2.3 Sheath rectification

The presence of time varying potentials across the surface's sheath causes the zero DC current condition to occur at a voltage negative with respect to the DC floating potential ϕ_f. This effect is known as sheath rectification and the associated potential as the self-bias ϕ_B (Eq. 11). A derivation for this expression is provided in Appendix 4A. The terms ϕ_u , $\overline{\phi_{p1}}$ and $\mathcal{I}_0$ represent the "effective floating potential", the magnitude of the time-varying plasma potential and the zeroth-order modified Bessel function of the first kind respectively. References [90], [95], [96] discuss the self-bias potential in the context of RF plasma.

$$\phi_u = \phi_f + \phi_B \quad \phi_B = -\ln\left[\mathcal{I}_0\left(\overline{\phi_{p1}}\right)\right] \qquad \text{Eq. 11}$$

In RF discharge applications sheath rectification is used to bias substrates and increase ion energy [97], as a plasma diagnostic tool [90], [91], [92], [98] and it is also known to cause distortion on Langmuir probe characteristics [70], [85], [95]. Figure 39 shows the effect of sheath rectification on an ideal single Langmuir probe I-V characteristic. The principal effect of sheath rectification is to shift the time averaged floating potential to increasingly negative values and distort the electron retardation (ER) region away from the floating potential.

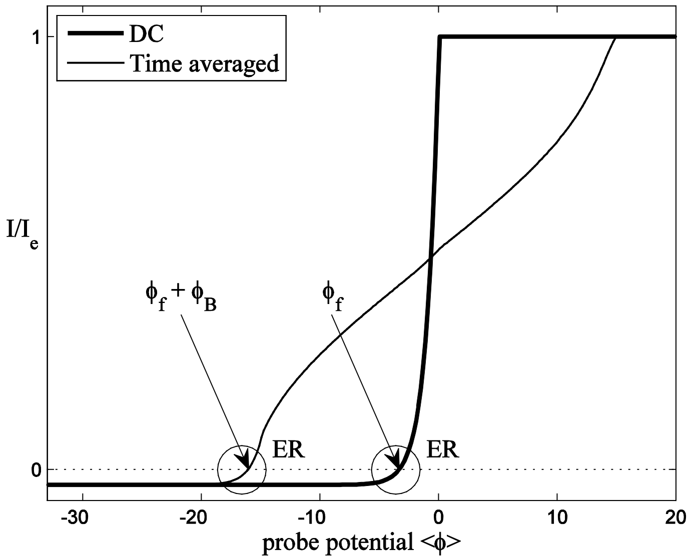

Figure 39, Ideal DC Langmuir probe I-V characteristic (thick line) and the time averaged case (thin line) in the presence of sheath rectification driven at $\overline{\phi_{p1}} = 15$. The plasma is composed of protons and Maxwell-Boltzmann distributed electrons at $T_e = 1$ eV. The region labelled "ER" and included in the circle represents the electron retardation region that is in the vicinity of the floating potential.

4.2.4 Model of a double Langmuir probe (DLP) in RF environment

In its most basic form the DLP consists of two probes with DC biased current collecting tips separated by a distance shorter than the skin depth and electrically isolated from the ground potential of the discharge. A detailed review of the DLP technique in the DC regime is given in [65], [66], [99]. Analysis of the DLP in the RF regime requires inclusion of the sheath dynamics and the stray capacitance of the probe assembly as illustrated in Figure 40a. The plasma potential, the applied DC potential between probes and stray capacitance are represented by ϕ_p, $\Delta\phi$ and C_k^i respectively. The sheath is described by its circuit equivalent [100], [101] and each probe shaft assumed to be electrically short and simply modelled as a shunt capacitance to ground. In addition, RF chokes isolate the RF potentials from the probe's DC bias circuitry and restrict the total stray capacitance to that of the probe shafts only. The RF chokes are of the inline type as shown in reference [67]. Each isolated probe is in fact a floating probe driven by the time varying plasma potential, as depicted in Figure 40b. We therefore start our analysis by describing the physics of driven floating probes and their ability to follow plasma potential oscillations. We then introduce the concept of probe compensation. Floating probes may be operated in two different ways: (1) passively or (2) actively driven. "Passively driven" means that the probe's potential is forced by the time-varying plasma potential whereas in the "actively driven" case the probe's potential is forced by sources external to the plasma such as power amplifiers. In the next section we present a general expression for a driven floating probe under both passive and active drive (Figure 40c).

4.2.5 The driven floating probe

Figure 40c shows a probe that is both actively and passively driven. The probe potential and external driving potential are represented by $\phi \; and \; \phi_s$ respectively. The term i_d represents the sheath displacement current, C_s the sheath capacitance, C_k the stray capacitance of the probe to ground and C_c the DC blocking capacitor through which the external source ϕ_s drives the floating probe. Using references [100], [101], the sheath is modelled with its circuit equivalent. Under the DC sheath condition ($\omega/\omega_{pi} \ll 1$), the sheath capacitance is a function of the instantaneous sheath potential difference $\left(\phi - \phi_{p1}\right)$. The displacement current associated with the sheath capacitance is shown in Eq. 12 and its derivation in Appendix 4B.

The total current to a probe biased to an arbitrary potential (Eq. 13) is composed of (1) the ion saturation current, (2) the electron contribution and (3) the sheath displacement current. The total current flows into the stray capacitance C_k and the DC blocking capacitor C_c (Eq. 14). Using both Eq. 13 and Eq. 14, implementing dimensionless quantities and collecting like terms we obtain Eq. 15, which hereafter is labelled “GDP” for “**G**eneral **D**riven **P**robe equation”. The GDP describes the time evolution of the potential of a floating probe ϕ driven by arbitrary time varying potentials (active and passive). The dimensionless quantities relevant to GDP (Eq. 15) are given in Eq. 16, where the term Γ_+ is the ion flux, Γ_e the electron thermal flux and A_p the current collecting area of the probe. In the context of RF discharges, solving this equation provides means of assessing whether or not a given probe is able to follow the oscillations of the plasma potential and thus provide RF compensation.

We note that $\alpha(\phi_{sh})$ is the only term that involves the sheath capacitance $C_{sh}(\phi_{sh})$ and it is precisely this term which makes GDP (Eq. 15) non-linear and not solvable by analytical methods. However, analytical solutions can be obtained whenever the following conditions are simultaneously satisfied: (1) the stray capacitance is much larger than the sheath capacitance and (2) the probe is either passively or actively driven by a single frequency source at a time. Solutions beyond these approximations can be obtained numerically and will be the subject of another study.

$$i_d = T_e C_s(\phi_{sh})\frac{d\phi_{sh}}{dt} \qquad \phi_{sh} = \phi - \phi_{p1} \tag*{Eq. 12}$$

$$I = I_+ - I_e \exp(\phi_{sh}) - T_e C_s(\phi_{sh})\frac{d\phi_{sh}}{dt} \tag*{Eq. 13}$$

$$I = T_e C_k \frac{d\phi}{dt} + T_e C_c \frac{d}{dt}(\phi - \phi_s) \qquad \phi_s = \phi_{s0} + \phi_{s1} \tag*{Eq. 14}$$

$$[1 + \alpha(\phi_{sh}) + \beta]\frac{d\phi_{sh}}{dt} + \frac{\exp(\phi_{sh})}{\tau_e} = \frac{1}{\tau_+} - \frac{d\phi_{p1}}{dt} - \beta\frac{d(\phi_{p1} - \phi_{s1})}{dt} \tag*{Eq. 15}$$

$$\tau_+ = \frac{T_e C_k}{\Gamma_+ A_p} \quad \tau_e = \frac{T_e C_k}{\Gamma_e A_p} \quad \beta = C_c/C_k \quad \alpha(\phi_{sh}) = C_s(\phi_{sh})/C_k \tag*{Eq. 16}$$

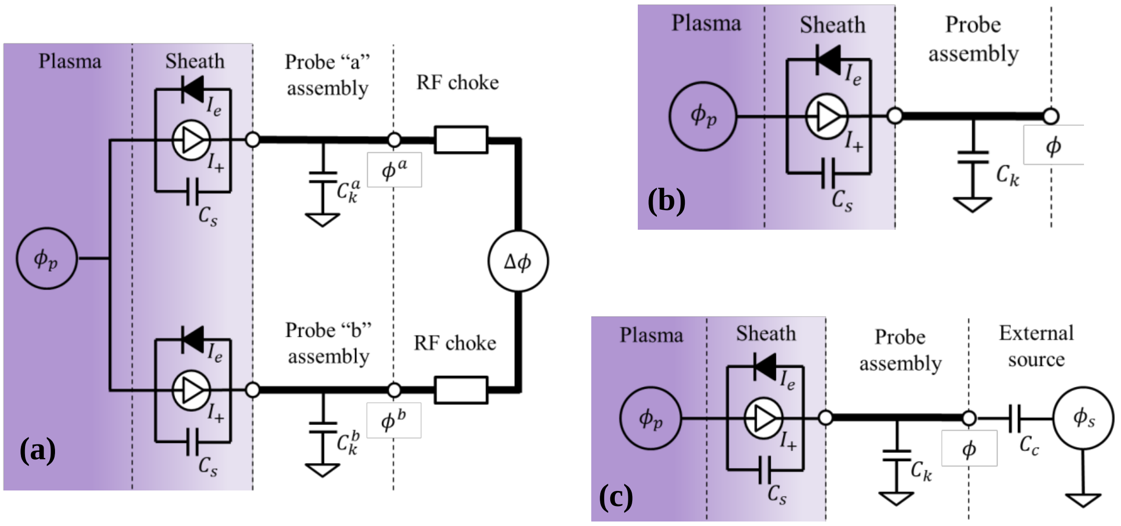
Plasma
Sheath
Probe "a" assembly
RF choke
I_e
I_+
C_s
C_k^a
ϕ^a
ϕ_p
$\Delta\phi$
Probe "b" assembly
RF choke
C_k^b
ϕ^b
(a)
Plasma
Sheath
Probe assembly
ϕ_p
C_k
ϕ
(b)
Plasma
Sheath
Probe assembly
External source
ϕ_p
C_k
ϕ
C_c
ϕ_s
(c)

Figure 40, Diagram of (a) double Langmuir probe in RF environment, (b) passively driven floating probe and (c) floating probe driven under general conditions

Large stray capacitance

Whenever the stray-to-sheath capacitance ratio is large, the term $\alpha(\phi_{sh})$ becomes much less than unity and the GDP (Eq. 15) can be simplified to the expression shown in Eq. 17. To understand when the condition $\alpha(\phi_{sh}) \ll 1$ is satisfied, consider a typical probe with a tip 10 mm in length and 85 μm in radius, plasma densities in the range of 1x10^{16} to 15x10^{18} m^{-3}, electron temperature of 4 eV and a 1 m long probe shaft using a 50 Ohm coaxial cable. In addition, consider the frequency of the driving potentials to be less than 20 MHz, so that the 1 m coaxial cable can be considered electrically short and modelled as a 100 pF stray capacitance to ground. Based on [94], the sheath capacitance for these conditions is shown in Figure 41 for various probe potentials. At high densities (~10^{19} m^{-3}), the maximum sheath capacitance is about 6 pF and the condition $\alpha(\phi_{sh}) \ll 1$ is approximately satisfied. At low densities (<1x10^{17} m^{-3}), the sheath capacitance is about 1 pF and the condition $\alpha(\phi_{sh}) \ll 1$ is well satisfied. Hence, Eq. 17 is suitable for scenarios commonly encountered in low temperature plasma experiments. Next, we analytically solve Eq. 17 for cases where a floating probe is driven either (a) passively or (b) actively by time varying potentials.

$$[1+\beta]\frac{d\phi}{dt} + \frac{exp(\phi - \phi_{p1})}{\tau_e} = \frac{1}{\tau_+} + \beta\frac{d\phi_{s1}}{dt} \qquad \text{Eq. 17}$$

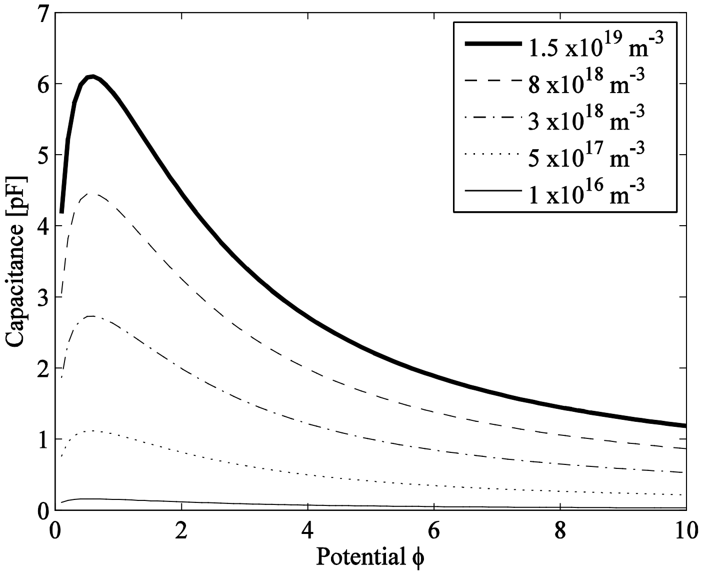

Figure 41, Sheath capacitance based on reference [94] for a probe tip with $r_p = 85\mu m,\ L = 10\ mm$ for various plasma densities and probe potentials. The electron temperature is 4 eV.

Passively driven floating probe

This case is illustrated in Figure 40b. By setting the DC blocking capacitor to zero ($\beta = 0$) and the time varying plasma potential to $\phi_{p1} = -\overline{\phi_{p1}}\cos(\omega t)$ in Eq. 17 we obtain Eq. 18. This expression represents a passively driven floating probe and is hereafter labelled "PDP" for "**P**assively **D**riven **P**robe equation". The terms τ_+ and τ_e represent characteristic time constants of the model and are defined in Eq. 19. The ion saturation current is given by $I_+ = \Gamma_+ A_p$.

$$\frac{d\phi}{dt} + \frac{\exp\left(\phi + \overline{\phi_{p1}}\cos(\omega t)\right)}{\tau_e} = \frac{1}{\tau_+} \tag*{Eq. 18}$$

$$\tau_+ = \frac{T_e C_k}{\Gamma_+ A_p} \quad \tau_e = \frac{T_e C_k}{\Gamma_e A_p} \tag*{Eq. 19}$$

The solution to the PDP (Eq. 18) is given in Eq. 20 and its derivation in Appendix 4C. In section 4.2.6, we show that this expression describes the intrinsic RF compensation of the DLP.

$$\begin{gathered}\phi = \phi_f + \phi_B \\ \phi_B = -\ln\left[\mathcal{J}_0\left(\overline{\phi_{p1}}\right) + 2\sum_{n=1}^{\infty}\mathcal{J}_n\left(\overline{\phi_{p1}}\right)\left(\frac{\cos(n\omega t) + n\omega\tau_+\sin(n\omega t)}{1 + (n\omega\tau_+)^2}\right)\right]\end{gathered} \tag*{Eq. 20}$$

The important parameters in Eq. 20 are (1) the magnitude of the plasma potential oscillations $\overline{\phi_{p1}}$ and (2) the value of $\omega\tau_+$. In fact, as demonstrated in section 4.2.7, it is the product $\omega\tau_+\overline{\phi_{p1}}$ that determines the asymptotic behaviour of ϕ_B (Eq. 20). Numerical solutions of Eq. 20 reveal that whenever $\omega\tau_+\overline{\phi_{p1}} \ll 1$ the probe is able to closely follow the oscillations in the plasma potential. Under these conditions, the self-bias ϕ_B (Eq. 20) can be written as in Eq. 21 and using the Bessel identity in Eq. 54 it becomes $\phi_B = -\overline{\phi_{p1}}\cos(\omega t)$. In addition, the time averaged self-bias $\langle\phi_B\rangle$ becomes zero and the time averaged probe potential $\langle\phi\rangle$ equals the DC floating potential ϕ_f. On the other hand, whenever $\omega\tau_+\phi_{p1} \gg 1$ the self-bias is reduced to $\phi_B = -\ln\left[\mathcal{J}_0\left(\overline{\phi_{p1}}\right)\right]$, the probe cannot follow the plasma potential oscillations and the time averaged probe potential $\langle\phi\rangle$ is shifted to increasingly negative values. This is indicative of sheath rectification.

$$\phi_B = -\ln\left[\mathcal{J}_0\left(\overline{\phi_{p1}}\right) + 2\sum_{n=1}^{\infty}\mathcal{J}_n\left(\overline{\phi_{p1}}\right)\cos(n\omega t)\right] \tag*{Eq. 21}$$

It is important to notice that these results are still valid even when the sheath capacitance is comparable or greater than the stray capacitance ($\alpha \geq 1$). Although analytical solutions cannot be found in this case ($\alpha \geq 1$), an asymptotic analysis of the GDP (Eq. 15) reveals that the time-averaged probe potential $\langle\phi\rangle$ equals the DC floating potential ϕ_f whenever the condition $\omega\tau_+\overline{\phi_{p1}} \ll 1$ is satisfied. This asymptotic analysis is described in Appendix 4D. The behaviour of ϕ_B (Eq. 20) indicates that the value of $\omega\tau_+\overline{\phi_{p1}}$ can be used to assess if a passively driven probe can follow the plasma potential oscillations

We now provide a physical interpretation of $\omega\tau_+$ as follows: If we define the sheath resistance R_{sh} as in reference [67] and the probe's stray capacitive impedance to ground Z_k as in Eq. 22, the term $\omega\tau_+$ can be understood as the ratio between these quantities (Eq. 23). Therefore, whenever $\omega\tau_+\overline{\phi_{p1}} \ll 1$ it implies that the sheath resistance is much smaller than the stray impedance ($R_{sh} \ll Z_k/\overline{\phi_{p1}}$) and that most of the driving potential will be drop across the stray impedance. On the other hand, whenever $\omega\tau_+\overline{\phi_{p1}} \gg 1$ it implies $R_{sh} \gg Z_k/\overline{\phi_{p1}}$ and that most of the driving potential occurs across the sheath.

$$R_{sh} = \frac{T_e}{\Gamma_+ A_p} \quad Z_k = \frac{1}{\omega C_k} \qquad \text{Eq. 22}$$

$$\omega\tau_+ = \frac{R_{sh}}{Z_k} \qquad \text{Eq. 23}$$

Actively driven floating probe

This case is illustrated in Figure 40c. By assuming the DC blocking capacitor is much larger than the stray capacitance ($\beta \gg 1$), setting the time varying plasma potential to zero ($\phi_{p1} = 0$) and the external potential source to $\phi_{s1} = \overline{\phi_{s1}}\cos(\omega t)$ in Eq. 17 we obtain Eq. 24. This expression represents an actively driven floating probe and is hereafter labelled "ADP" for "**A**ctively **D**riven **P**robe equation". The terms τ_+^* and τ_e^* represent characteristic time constants of the model (Eq. 25), but unlike the PDP these time constants (Eq. 25) depend on the DC blocking capacitor C_c and not on the probe's stray capacitance C_k. The ion saturation current is given by $I_+ = \Gamma_+ A_p$.

$$\frac{d\phi}{dt} + \frac{\exp(\phi)}{\tau_e^*} = \frac{1}{\tau_+^*} + \frac{d\overline{\phi_{s1}}\cos(\omega t)}{dt} \qquad \text{Eq. 24}$$

$$\tau_+^* = \frac{T_e C_c}{\Gamma_+ A_p} \quad \tau_e^* = \frac{T_e C_c}{\Gamma_e A_p} \qquad \text{Eq. 25}$$

The solution to the ADP (Eq. 24) is given in Eq. 26 and its derivation in Appendix 4E. Although the self-bias expressions in Eq. 20 and Eq. 26 have the same mathematical form, a distinction between them must be made because the former depends on the probe's stray capacitance C_k, while the latter on the DC blocking capacitor C_c. Therefore, all terms denoted with a star as a superscript will be hereafter associated with the ADP (Eq. 24) and its solution (Eq. 26).

$$\phi = \phi_f + \overline{\phi_{s1}}\cos(\omega t) + \phi_B^*$$
$$\phi_B^* = -\ln\left[\mathcal{J}_0\left(\overline{\phi_{s1}}\right) + 2\sum_{n=1}^{\infty}\mathcal{J}_n\left(\overline{\phi_{s1}}\right)\left(\frac{\cos(n\omega t) + n\omega\tau_+^*\sin(n\omega t)}{1 + (n\omega\tau_+^*)^2}\right)\right] \qquad \text{Eq. 26}$$

In a similar way as in ϕ_B in Eq. 20, the term $\omega\tau_+^*$ can be understood as the ratio between the sheath resistance and the impedance of the DC blocking capacitor. Whenever $\omega\tau_+^*\overline{\phi_{s1}} \ll 1$ in Eq. 26, using the Bessel identity in Eq. 54 the self-bias can be expressed as $\phi_B^* = -\overline{\phi_{s1}}\cos(\omega t)$ and its time averaged value vanishes $\langle\phi_B^*\rangle = 0$. As a result, the time averaged probe potential $\langle\phi\rangle$ becomes equal to the DC floating potential ϕ_f and there is no sheath rectification. On the other hand, whenever $\omega\tau_+^*\overline{\phi_{s1}} \gg 1$ the self-bias is reduced to $\phi_B^* = -\ln[\mathcal{J}_0(\overline{\phi_{s1}})]$ and the time averaged probe potential $\langle\phi\rangle$ is shifted to increasingly negative values due to sheath rectification.

4.2.6 Passively driven Double Langmuir Probes (DLP)

The DLP (Figure 40a) can be considered as a pair of independent passively driven probes that interchange DC currents. Hereafter we denote all quantities relating to either probes 1 or 2 with superscripts “a” or “b” respectively. Following the procedure described in Appendix 4F, the potential of a DLP driven by the time varying plasma potential $\phi_{p1} = -\overline{\phi_{p1}}\cos(\omega t)$ is given by Eq. 27 to Eq. 29.

$$\phi^n = \phi_f + \Omega^n + \phi_B \quad n = a, b \tag{Eq. 27}$$

$$\Omega^a = \ln\left[1 - \tanh\left(\frac{\Delta\phi}{2}\right)\right] \quad \Omega^b = \ln\left[1 + \tanh\left(\frac{\Delta\phi}{2}\right)\right] \quad \Delta\phi = \phi^b - \phi^a \tag{Eq. 28}$$

$$\phi_B = -\ln\left[\mathcal{I}_0\left(\overline{\phi_{p1}}\right) + 2\sum_{n=1}^{\infty}\mathcal{I}_n\left(\overline{\phi_{p1}}\right)\left(\frac{\cos(n\omega t) + n\omega\tau_+\sin(n\omega t)}{1 + [n\omega\tau_+]^2}\right)\right] \tag{Eq. 29}$$

This expression states that the potential of DLP is equal to the DC floating potential plus the term Ω^n (Eq. 28) and the self-bias ϕ_B (Eq. 29). The term Ω^n is hereafter referred to as the “DC bias” and it is controlled by the experimenter through the applied DC potential $\Delta\phi$ in order to measure I-V characteristic of a DLP. The self-bias ϕ_B describes the ability of the DLP to follow the oscillations in the plasma potential, e.g. the intrinsic compensation of the DLP. Notice that the self-bias in Eq. 29 is precisely the same expression that describes rectification of the passively driven floating probe (Eq. 20). For this reason, the DLP is equivalent to the passively driven floating probe described by Eq. 20 but with a DC bias component. All the previous conclusions pertaining to the passively driven floating probe are applicable to the DLP; namely, compensation and rectification occur whenever $\omega\tau_+\overline{\phi_{p1}} \ll 1$ and $\omega\tau_+\overline{\phi_{p1}} \gg 1$ respectively.

Intrinsic RF compensation

To put these results into context, the most recent theoretical treatment in the literature of the DLP in RF discharges was provided by Annaratone [85] in the thin sheath regime. However, the DLP was assumed unable to follow the RF fields and therefore in a state of complete RF rectification, so the intrinsic RF compensation of the DLP was not dealt with. In fact, to the author’s knowledge there is no detailed analysis in the literature of the intrinsic RF compensation of the DLP. An important and novel contribution of our work is Eq. 27 to Eq. 29, which describe the ability of the DLP to follow the plasma potential oscillations and states that DLPs can provide intrinsic RF compensation whenever the condition $\omega\tau_+\overline{\phi_{p1}} \ll 1$ is satisfied.

Unifying the DC and RF regimes

In addition, whenever $\omega\tau_+\overline{\phi_{p1}} \gg 1$ (full rectification) the expressions in Eq. 27 to Eq. 29 are equivalent to Annaratone's high frequency (RF) DLP solution [85], namely equations 14 and 15 therein. On the other hand, whenever $\omega\tau_+\overline{\phi_{p1}} \ll 1$ (no rectification), the time average of Eq. 27 becomes equivalent to Swift and Schwar's low frequency (DC) DLP solution [65]. As a result, we propose that Eq. 27 to Eq. 29 not only describe the DLP intrinsic RF compensation but also extend the current DLP theory by unifying the low (DC) and high (RF) regimes into a single expression through the self-bias ϕ_B expression provided in Eq. 29.

4.2.7 Compensation of a floating probe

Definition

In the context of electrostatic probes, compensation occurs whenever the probe's potential is able to closely follow the oscillations in the plasma potential. For both single and double Langmuir probes, this process can be described with the self-bias ϕ_B of a passively driven floating probe, namely Eq. 20, whenever the condition $\omega\tau_+\overline{\phi_{p1}} \ll 1$ is satisfied. Under these circumstances, the sheath potential difference becomes time independent and consequently no self-bias ϕ_B is produced.

Quantifying sheath rectification

We now use Eq. 20 to explore the compensation of a floating probe as a function of the dimensionless quantities $\omega\tau_+$ and $\overline{\phi_{p1}}$. The following is applicable to both the DLP and the passively driven floating probe. Provided the assumptions in section 4.2.1 are satisfied, the results from Figure 42 and Figure 43 that follow are applicable to a wide range of plasma densities (10^{16} to 10^{19} m^{-3}), electron temperatures (1 to 10 eV) and frequencies (kHz to MHz). In Figure 42, we show a calculation of the time averaged self-bias $\langle\phi_B\rangle$ (Eq. 20) for a value of $\overline{\phi_{p1}} = 7.2$ as a function of $\omega\tau_+$. The horizontal dashed line represents the self-bias under complete sheath rectification (Eq. 11). The open circles represent the self-bias $\langle\phi_B\rangle$ for different values of the product $\omega\tau_+\overline{\phi_{p1}}$ as denoted by the labels. For values of $\omega\tau_+\overline{\phi_{p1}} < 1$, the self-bias $\langle\phi_B\rangle$ is small and restricted to be above the "knee" of the curve. For $\omega\tau_+\overline{\phi_{p1}} \ll 1$, the self-bias $\langle\phi_B\rangle$ vanishes. For values of $\omega\tau_+\overline{\phi_{p1}} > 1$, the self-bias $\langle\phi_B\rangle$ increases rapidly towards complete sheath rectification $\langle\phi_B\rangle = -\ln\left[\mathcal{J}_0\left(\overline{\phi_{p1}}\right)\right]$. This curve suggests that whenever the condition $\omega\tau_+\overline{\phi_{p1}} < 1$ is satisfied, sheath rectification is small.

To quantify sheath rectification, we compare the magnitude of the time averaged self-bias $\langle\phi_B\rangle$ relative to the DC floating potential ϕ_f using Eq. 30 where the term ξ is hereafter referred to as the "rectification strength". Using Eq. 10, the DC floating potential can be written as $\phi_f \approx -3.3 - \ln\sqrt{A_i}$, where A_i is the ion mass in AMU. Whenever the condition $\xi \ll 1$ is satisfied, we consider sheath rectification to be negligible; consequently, the probe potential closely follows the plasma potential oscillations. We now explore the behaviour of ξ as a function of $\overline{\phi_{p1}}$ and $\omega\tau_+$.

$$\xi = \langle\phi_B\rangle/\phi_f \qquad \text{Eq. 30}$$

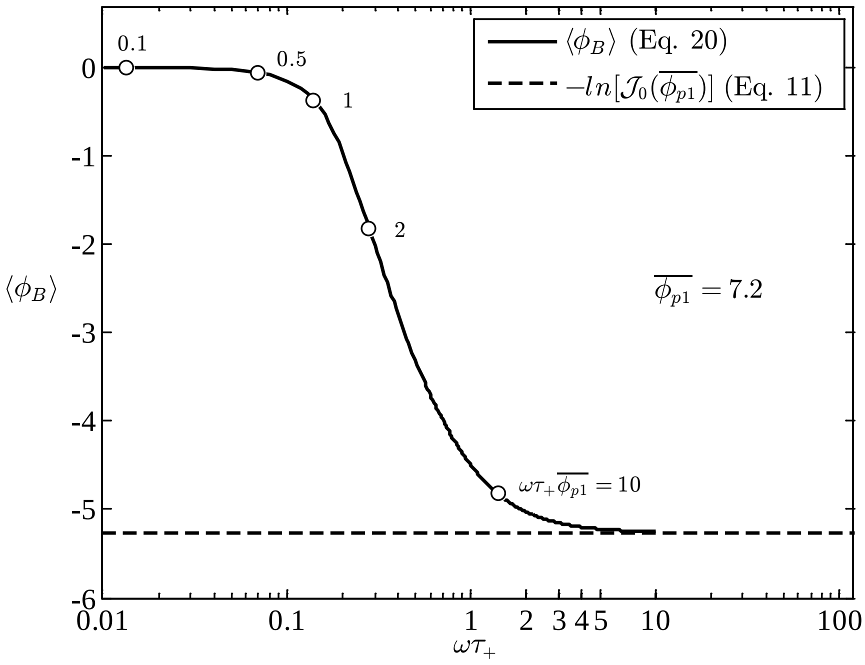

Figure 42, Time averaged self-bias $\langle\phi_B\rangle$ of floating probe or DLP passively driven at $\overline{\phi_{p1}}$ =7.2 as a function of $\omega\tau_+$. Calculation based on Eq. 20.

In Figure 43 we show a calculation of ξ (Eq. 30) using Eq. 20 for different values of $\overline{\phi_{p1}}$ and $\omega\tau_+$. The black lines represent contour lines of constant "rectification strength" ξ, where the values of ξ are defined for various ion masses A_i in Table 4. Calculations indicate that for each contour line in Figure 43 the product $\omega\tau_+\overline{\phi_{p1}}$ is approximately constant and can be approximated with $\omega\tau_+\overline{\phi_{p1}} = 1$, 0.75, 0.5 and 0.4 as indicated by the labels therein. Since the contour lines in Figure 43 are not exactly straight lines over the entire region, these values of $\omega\tau_+\overline{\phi_{p1}}$ are only approximations. However, they can be used to provide an estimate of the parameter space of $\omega\tau_+$ and $\overline{\phi_{p1}}$ for a given rectification strength. For instance, any combination of $\overline{\phi_{p1}}$ and $\omega\tau_+$ in Figure 43 that satisfies the condition $\omega\tau_+\overline{\phi_{p1}} \leq 0.4$ will correspond to $\xi \leq 1/100$ and 1/156 for protons and argon ions respectively. Next we discuss the implications of these results in terms of probe design by making the plasma/operating conditions explicit.

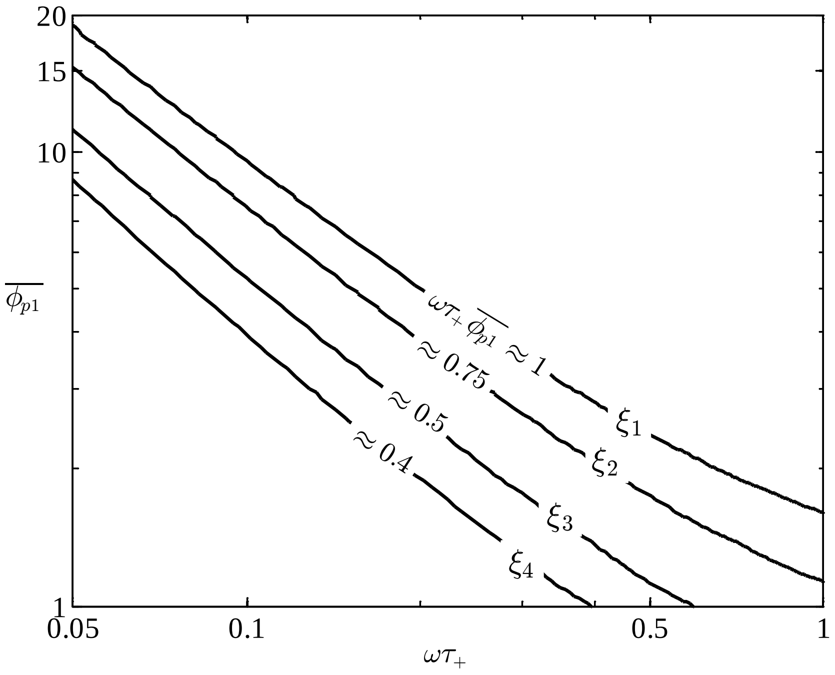

Figure 43, Rectification strength ξ (Eq. 30) as a function of $\omega\tau_+$ and $\overline{\phi_{p1}}$. This calculation is based on Eq. 20 and is applicable to both single and double Langmuir probes. The values of ξ_i for i = 1-4 are shown in Table 4 for protons and argon ions. To compute the values of ξ_i for other ion masses, multiply the values of ξ for A_i = 1 shown in Table 4 by 3.3 / (3.3 + $\ln\sqrt{A_i}$). For example, if argon is used (A_i = 40) multiply by 0.64 to convert the values of ξ_i to approximately 1/15, 1/31, 1/78 and 1/156.

Table 4, Rectification strength ξ of contour lines in Figure 43 for protons (A_i = 1) and argon (A_i = 40).

	$A_i = 1$	$A_i = 40$
ξ_1	1/10	1/15
ξ_2	1/20	1/31
ξ_3	1/50	1/78
ξ_4	1/100	1/156

4.2.8 Probe design considerations

Generally, the magnitude of the plasma potential oscillations $\overline{\phi_{p1}}$, driving frequency ω, plasma density and electron temperature are determined by the discharge conditions; however, the value of $\omega\tau_+$ can be controlled by the experimenter to some extent. Based on Eq. 22 and Eq. 23, the value of $\omega\tau_+$ can be reduced by (1) decreasing the probe's stray capacitance C_k and/or (2) increasing the ion saturation current I_+. For this reason, the importance of Figure 43 is that it allows estimation of an appropriate value for $\omega\tau_+$ for a given $\overline{\phi_{p1}}$ and a desired rectification strength ξ. Clearly, the smaller the rectification strength ξ desired the smaller the value of $\omega\tau_+$ required.

Once the value of $\omega\tau_+$ has been determined from Figure 43, an appropriate probe design can be specified that will satisfy the condition $\xi \ll 1$ and consequently provide compensation. The probe's stray capacitance is generally reduced by decreasing the length of the probe shaft exposed to the time varying potentials. In practice, this is done by isolating the probe shaft at a certain distance L away from probe's current collecting tip using inline chokes tuned at the driving frequency [67], [82], [102]. If the probe shaft can be considered electrically short, the probe's stray capacitance C_k is proportional to the distance L. Based on the required value of $\omega\tau_+$ and the available ion saturation current, the maximum stray capacitance and hence distance L tolerable can be estimated. The ion saturation current is generally increased by enlarging the current collecting area of the probe. Alternatively, a very large area "auxiliary" electrode can be AC coupled to the probe shaft through a capacitor C_x much greater than C_k [67], [84]. We now provide some examples of probe design.

Double Langmuir Probe design example

Suppose a symmetric DLP is to be exposed to a proton discharge ($A_i = 1$) with plasma potentials oscillations of 30 V peak to peak at 7 MHz. Suppose each probe of the DLP has a 0.2 mm diameter current collecting tip and using isolating RF chokes, the effective length L of each probe shaft is 1 m. If the probe shafts are made of 50 Ohm coaxial cable (100 pF per meter), the effective stray capacitance per probe is about 100 pF. Suppose the electron temperature and plasma density are expected to be about 5 eV and $1\text{x}10^{19}$ m^{-3}. For a desired rectification strength of $\xi \leq 1/20$, the length of the current collecting tip of an individual probe is calculated as follows: from Table 4 ($\xi = 1/20$ and $A_i = 1$), the relevant contour line in Figure 43 for a proton plasma is ξ_2 which requires the condition $\omega\tau_+\overline{\phi_{p1}} \leq 0.75$. For a value of $\overline{\phi_{p1}} = 3$, this leads to $\omega\tau_+ \leq 0.25$. Based on the given stray capacitance (100 pF), driving frequency (7 MHz) and electron temperature (5 eV), this value of $\omega\tau_+$ results in $I_+ \geq 88$ mA. Using Bohm's sheath criterion and the expected density, a current collecting tip length greater than 7 mm is required. Suppose the desired rectification strength is now $\xi \leq 1/100$, using ξ_4 from Figure 43 ($\omega\tau_+\overline{\phi_{p1}} \leq 0.4$) we require $\omega\tau_+ \leq$ 0.133 which leads to $I_+ \geq 165$ mA; consequently, the current collecting tip must be at least 12 mm in length. For the interested reader, in Chapter 3 section 3.3.2 we describe the design of a RF compensated DLP for use in MAGPIE using a procedure similar to the one just presented.

Notice that at these operating conditions (proton plasma at 1x10^{19} m^{-3} and 5 eV) a DLP with 12 mm tip lengths can provide RF compensation ($\xi \leq$ 1/100) when exposed to plasma potential oscillations of 30 V peak to peak at 7 MHz even when the isolating RF chokes are located 1 m away from the current collecting tips. This allows the experimenter to locate the RF chokes external to the DLP assembly and vacuum chamber; therefore, circumventing the need for delicate RF chokes near the current collecting tip and reducing the complexity of probe construction.

For the same discharge conditions, suppose the operating gas is changed to argon ($A_i = 40$). The ion sound speed at the sheath is reduced by a factor $\sqrt{40}$ relative to the proton plasma; consequently, for the same values of ion saturation current ($I_+ >$ 88 and 165 mA), the current collecting tips must be increased by a factor of $\sqrt{40}$. Hence, RF compensation requires probe tip lengths greater than 45 and 76 mm respectively. Alternatively, the stray capacitance can be reduced by reducing the probe shaft length L by a factor of $\sqrt{40}$.

If the probe length cannot be reduced and/or the current collecting tip cannot be further increased, the RF compensation of the DLP can be increased by the addition of AC coupled "auxiliary electrodes" as described in the next example.

Single Langmuir Probe design example

Suppose an isolated probe with a 0.2 mm diameter current collecting tip is to be exposed to an argon plasma ($A_i = 40$) with plasma potential oscillations of 100 V peak to peak at 13.56 MHz. Using isolating RF chokes, the effective length of the probe is chosen to be L = 10 cm. Using 50 Ohm coaxial cable for the probe shaft, the effective stray capacitance is about 10 pF. Suppose the plasma density and electron temperature are expected to be about 5x10^{18} m^{-3} and 4 eV. For a desired rectification strength $\xi \leq$ 1/150, the required length for current collecting tip is calculated as follows: from Table 4 (ξ = 1/156 and A_i = 40), the relevant contour line in Figure 43 is ξ_4 which imposes the condition $\omega\tau_+\overline{\phi_{p1}} \leq 0.4$; therefore, for a value of $\overline{\phi_{p1}}$ = 12.5 we require $\omega\tau_+ \leq$ 0.032. Based on the given stray capacitance (10 pF), driving frequency

(13.56 MHz) and electron temperature (4 eV), this requires $I_+ \geq 107$ mA. Using Bohm's sheath criterion and the expected plasma density, the current collecting tip must be at least 100 mm in length.

A length of 100 mm may be considered too long to make "point" measurements in a typical laboratory plasma experiment. However, we can build an "auxiliary" electrode [67] by winding the 100 mm current collecting tip around an insulating former and AC coupling it to the main probe shaft through a DC blocking capacitor C_x as shown in Figure 44a. The DC blocking capacitor C_x must be much greater than the stray capacitance C_k and for this example a 1 nF DC capacitor will suffice. At this point, we can use a smaller length ($<$ 10 mm) for the current collecting tip while the 100 mm "auxiliary" electrode enables the isolated probe to closely follow the RF plasma potential oscillations and provide RF compensation. Under these circumstances, the current collecting tip can be DC biased to obtain an I-V characteristic unaffected by RF rectification. In this example, we assume that the current collecting tip and "auxiliary" electrode sample the same time varying potential.

Measuring the RF plasma potential

In continuation of the previous example, suppose the magnitude of the plasma potential oscillations is not known, but it is suspected to be less than 100 V peak to peak at 13.56 MHz. In this case, the 100 mm "auxiliary" electrode can be used to measure the actual magnitude of the plasma potential oscillations by replacing the RF choke and the DC biasing circuitry with a high impedance probe, such as a "x10" or "x100" oscilloscope probe as shown in Figure 44b. Suppose the high impedance probe has an input capacitance of about 10 pF. This means that the total stray capacitance becomes about 20 pF; therefore to allow measurements of RF potentials up to 100 V peak to peak at 13.56 MHz the length of the "auxiliary" electrode will need to be doubled (200 mm). This setup measures both the DC floating potential and the time varying plasma potential.

In this example, we assume the 10 cm probe shaft is long enough to locate the high impedance probe external to the vacuum chamber. For plasma potential oscillations greater than 100 V peak to peak at 13.56 MHz, the length of the auxiliary electrode will need to be increased and can be recalculated according to the procedure described in the previous example.

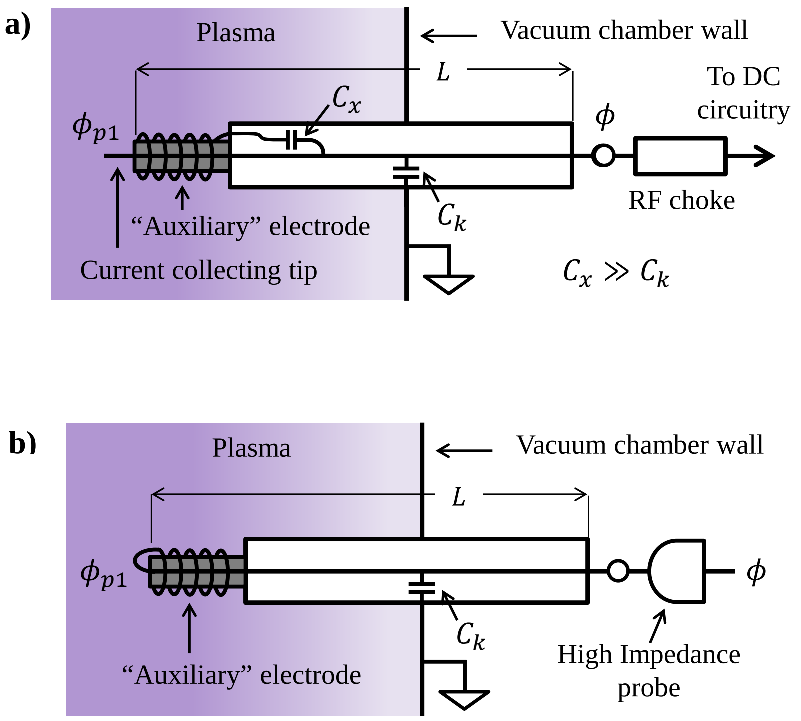
a)
Plasma
Vacuum chamber wall
L
To DC circuitry
C_x
ϕ_{p1}
ϕ
RF choke
C_k
"Auxiliary" electrode
Current collecting tip
$C_x \gg C_k$
b)
Plasma
Vacuum chamber wall
L
ϕ_{p1}
ϕ
C_k
High Impedance probe
"Auxiliary" electrode

Figure 44, a) Schematic of an isolated probe with an AC coupled "auxiliary" electrode. The large area of the "auxiliary" electrode allows the probe potential ϕ to follow the time varying plasma potential ϕ_{p1} as described by Eq. 20. The DC blocking capacitor C_x prevents the "auxiliary" electrode from drawing DC currents from the plasma. b) Schematic of an isolated probe using an "auxiliary" electrode and a high impedance probe to measure time varying plasma potential and the DC floating potential.

4.2.9 Effect of RF rectification on DLP measurements

In the previous section, we discussed under what conditions RF compensation occurs; however, in this section we are interested in what happens to DLP measurements under complete RF rectification. Under these conditions, the self-bias ϕ_B is time independent and given by Eq. 11, namely $\phi_B = -\ln\left[\mathcal{J}_0\left(\overline{\phi_{p1}}\right)\right]$.

Measuring ion density

It is known that the collection of ion current in cylindrical and spherical probes does not saturate [68], [103], [104] and it increases with negative potentials. Laframboise [68] shows that this effect scales with the ratio r_p/λ_d, where r_p represents the probe radius and λ_d the Debye length. Whenever $r_p/\lambda_d \gg 1$, current collection is weakly dependent on potential and approaches that of a planar probe. Whenever $r_p/\lambda_d \sim 1$, the angular momentum of ions cannot be neglected and current collection scales with the applied potential. This effect leads to overestimation of the ion density unless it can be accounted for by using methods such as those described in reference [105] for single Langmuir probes and reference [69] for DLPs.

Using Laframboise's numerical results [68] and Steinbruchel's parameterization [103], [105], the ion current collected by a cylindrical or spherical probe can be expressed with Eq. 31, where ϕ is the dimensionless probe potential and the parameters $\mathcal{A}$ and $\mathcal{B}$ are functions of the ratio r_p/λ_d as defined in reference [105]. The term I_{+0} is the ion current at the sheath edge given by Eq. 32, where e is the electron charge, A_p the probe surface area, n_i the ion density in the bulk plasma and M_i is the ion mass.

$$I_+(\phi) = I_{+0}\mathcal{A}(-\phi)^{\mathcal{B}} \qquad \text{Eq. 31}$$

$$I_{+0} = eA_p n_i\sqrt{eT_e/2\pi M_i} \qquad \text{Eq. 32}$$

In a DLP, the potential of the nth probe (ϕ^n) is given by Eq. 27 and the corresponding ion current, using Eq. 31, is shown in Figure 45. In the absence of RF rectification or applied DC potential, the probe will be at the DC floating potential ϕ_f and the corresponding ion current is labelled as $I_+\left(\phi_f\right)$ as shown by the open circle "A". In the presence of RF rectification, the potential of the probe will become more negative and the ion current will increase towards "B". Upon application of a DC potential to the DLP, the ion current of the most negative probe will increase towards point "C". Experimentally, cylindrical DLPs show an approximate linear increase in ion current with the applied potential [69], [85], [106], [107]. Hence, approximating the ion current between points “A” and “C” with a straight line of slope “m”, Eq. 31 can be approximated with Eq. 33.

$$I_+^n = I_+(\phi_f) + m(\phi_B + \Omega^n) \tag{Eq. 33}$$

Consider that in DLP measurements, the ion density is extracted from the measured ion current. Since these quantities are linearly related for a fixed electron temperature (Eq. 32) we anticipate that the ion density measurement error (δn_i) due to RF rectification in DLPs with $r_p/\lambda_d \sim 1$ will scale linearly with (1) the magnitude of the RF self-bias ϕ_B and (2) the slope “m” of the ion current (Eq. 34). However, if the sheath thickness is much smaller than the probe radius ($r_p/\lambda_d \gg 1$), the ion saturation current will depend weakly on the applied potential. Under these circumstances, the ion density measurement error due to RF rectification will be reduced.

$$\delta n_i \propto m\phi_B \tag{Eq. 34}$$

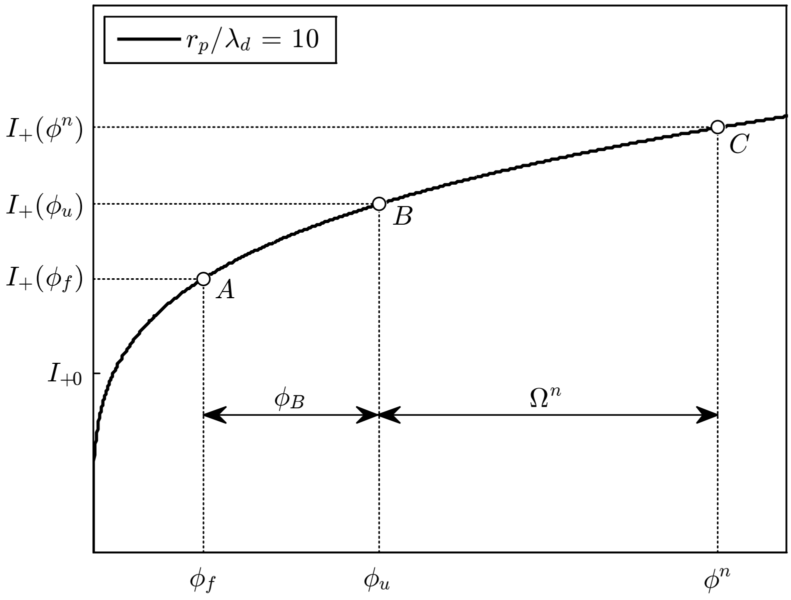

Figure 45, Ion current collected by a cylindrical probe as a function of the probe potential based on Eq. 31. In this example, the potential is from the nth probe in a DLP (Eq. 27). The term ϕ_B and Ω^n describe the shift in probe potential due to RF rectification and the applied DC potential in a DLP respectively

Measuring electron temperature

It is important to note that the DLP method can only access the high energy tail of the electron energy distribution function (EEDF) and relies on this tail to estimate the electron temperature. This process assumes that the entire EEDF is Maxwell-Boltzmann. If the EEDF is not Maxwell-Boltzmann, electron temperature measurements with DLPs can lead to considerable error. In the absence of additional information, the DLP method does not provide a way of knowing whether the EEDF is Maxwell-Boltzmann or not. However, to further explore the applicability of the DLP, the following assumes the EEDF is Maxwell-Boltzmann.

In the presence of potential dependent ion currents $I_+(\phi)$, the I-V characteristic of DLP can be written as in Eq. 35 based on reference [69]. Taking the derivative of Eq. 35 with respect to the applied DC potential $\Delta\phi$, evaluating $\Delta\phi = 0$ and describing the potential dependant ion currents with Eq. 33, the electron temperature can be expressed as in Eq. 36. This expression indicates that the electron temperature depends on the product of two terms. The first term scales with “m” and the RF self-bias ϕ_B. The second term represents the slope of the DLP I-V characteristic at $\Delta\phi = 0$; however, from the theory presented its behaviour in the presence of RF rectification is not known. Therefore, using theory along the scaling of the electron temperature measurement error (δT_e) with RF rectification cannot be inferred.

$$I(\Delta\phi) = I_+^a(\phi^a)\tanh\left(\frac{\Delta\phi}{2}\right) + \left(\frac{I_+^a(\phi^a) - I_+^b(\phi^b)}{e^{\Delta\phi} + 1}\right) \qquad \text{Eq. 35}$$

$$T_e = \left(\frac{I_+(\phi_u) - m}{2}\right)\left(\left.\frac{\partial I}{\partial \Delta V}\right|_{\Delta V=0}\right)^{-1} \quad I_+(\phi_u) = I_+(\phi_f) + m\phi_B \qquad \text{Eq. 36}$$

In relation to single Langmuir probes, RF rectification distorts the electron retardation region [67], [70], [85], [95] and leads to incorrect EEDF measurements [102], [108], [109]. It is this effect that is reported in the literature as the source of electron temperature measurement errors in RF discharges. However, the electron retardation region in the vicinity of the floating potential (marked “ER” in Figure 39 page 68) is less affected by RF rectification as discussed by Oksuz[70] and correct measurement of the electron temperature in Maxwell-Boltzmann distributed plasma can still be made provided it is limited the tail of the EEDF [67], [70], [85], [95]. Since DLPs rely on the tail of the EEDF, we anticipate that DLP electron temperature measurement in plasmas with Maxwell-Boltzmann distributed electrons will be weakly affected by RF rectification.

4.3 Actively driven probe experiment

In the theory section, we presented expressions that describe floating probes under both passive (Eq. 20) and active (Eq. 26) drive. In fact, a DLP in an RF environment could be viewed as a floating probe passively driven by the time varying plasma potential (Eq. 27 to Eq. 29). Since the rectification behaviour of all these expressions is described by the self-bias ϕ_B, a natural progression for this work is to compare the theoretical self-bias with experiment. Due to the symmetry between the self-bias of a passive and active probe as shown in Eq. 20 and Eq. 26 respectively, validation of one enables the validation of the other. In our experimental setup, it was not possible to control the magnitude of the time varying RF plasma potential without changing the discharge conditions. As a result, in order to validate the Eq. 20 we employed an actively driven probe to control the sheath potential difference and validate Eq. 26.

4.3.1 Apparatus

The actively driven probe experiment (Figure 46) was performed in the MAGPIE helicon plasma source [44]. The discharge was operated in hydrogen at 6 mTorr, 2.5 kW at 7 MHz, repetition rate of 10 Hz, 1 ms RF pulse and a magnetic field of 20 mT. The plasma density and electron temperature were measured with a DLP to be $6\text{x}10^{17}$ m^{-3} and 3.5 eV respectively. The actively driven probe consisted of a 1 m long stainless steel shaft enclosing a 50 Ohm coaxial cable with outer conductor grounded at the vacuum port. This leads to ~100 pF stray capacitance to ground. The molybdenum probe tip was 11 mm in length and 0.17 mm in diameter and routinely cleaned with electron saturation current at 60 V, 3.5 A and 1 ms at 10 Hz repetition rate. The probe was actively driven at 50 V peak to peak and 30 kHz, hence $\overline{\phi_{s1}}$ = 7.2. The ion saturation current I_+ was measured to be 6 mA. The coupling capacitor C_c located between the probe and the power amplifier was varied from 0.5 to 100 nF; consequently, the term $\omega\tau_+^*$ (Eq. 25) was varied from 0.02 to about 100. The corresponding values of $\omega\tau_+^*\overline{\phi_{s1}}$ ranged from 0.2 to 740; hence, the compensation ($\omega\tau_+^*\overline{\phi_{s1}} \ll 1$) and rectification ($\omega\tau_+^*\overline{\phi_{s1}} \gg 1$) conditions were tested. The probe ϕ and driving potential $\overline{\phi_{s1}}$ where measured with high impedance probes each with 10 pF of input capacitance and 500 MHz bandwidth. Since the coupling capacitors C_c used in the experiment were in the nF range, the input capacitance of the high impedance probes (10-15 pF) was neglected relative to C_c and the effect of measuring ϕ ignored in the analysis.

Magnetic field effects

The presence of a background magnetic field affects current collection in electrostatic probes. This effect scales with the ratio $r_p/r_L^{e,i}$, where r_p is the probe radius and $r_L^{e,i}$is the electron/ion

Larmour radius. Generally $r_L^i \gg r_L^e$ due to the larger ion mass, hence magnetic field effects on electron collection are expected to be more important. Whenever the condition $r_p/r_L^e \ll 1$ is satisfied, magnetic field effects on electron collection can be neglected [59], [73]. Due to the floating nature of the probe implemented, only electrons at the DC floating potential are collected e.g. electrons with energies greater than 3.3 T_e in a hydrogen plasma. For an electron temperature of 3.5 eV, only electrons with energies greater than 11.5 eV are collected. Hence, for the 20 mT background magnetic field we obtain $r_p/r_L^e \leq 0.14$ and magnetic field effects on the actively driven probe can be ignored.

RF effects at 7 MHz

The experiment herein described was performed 20 cm away from the helicon antenna. Using a high impedance probe (10-15 pF input capacitance) with a large area electrode (140 mm^2) exposed to the plasma, similar to the 3rd example in section 4.2.8, the time varying plasma potential associated with the helicon source was measured to be less than 4 V peak to peak at 7 MHz with negligible higher harmonic content at the location of the experiment. The large area electrode consisted of 0.2 mm diameter tungsten wire, 22 cm in length and wound around a 5 mm diameter ceramic former. For an electron temperature of 3.5 eV, the associated RF self-bias was estimated (Eq. 11) to be -0.3 V which is much smaller than the DC floating potential; hence, rectification effects due to the 7 MHz potentials can be ignored.

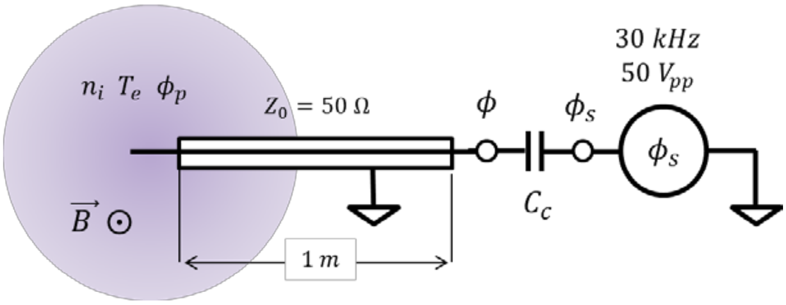

Figure 46, Driven floating probe experimental setup

4.3.2 Results and analysis

In Figure 47, we compare the measured and theoretical (Eq. 26) potential ϕ of the actively driven probe for different values of $\omega\tau_{+}^{*}\overline{\phi_{s1}}$. The conditions are described in the figure's caption. The small time offset between the traces is caused by the 500 kHz upper 3 dB frequency of the data acquisition difference amplifiers. For all values of $\omega\tau_{+}^{*}\overline{\phi_{s1}}$ shown, theory and experiment are consistent. For $\omega\tau_{+}^{*}\overline{\phi_{s1}} = 0.2$, the potential approaches the DC floating potential and indicates the absence of sheath rectification. As the value of $\omega\tau_{+}^{*}\overline{\phi_{s1}}$ is increased, the time averaged potential $\langle\phi\rangle$ shifts towards increasingly negative values and indicates sheath rectification.

In Figure 48, we show the time averaged self-bias $\langle\phi_{B}^{*}\rangle$ for different values of $\omega\tau_{+}^{*}$ for the same conditions as in Figure 47. The solid line represents theory (Eq. 26) and the open circles the experimental data with the associated value of $\omega\tau_{+}^{*}\overline{\phi_{s1}}$. For all values of $\omega\tau_{+}^{*}\overline{\phi_{s1}}$ shown, the theory describes very well the experimental data. For conditions $\omega\tau_{+}^{*}\overline{\phi_{s1}} \ll 1$, the results show that the time averaged self-bias vanishes and indicates the absence of sheath rectification. For conditions $\omega\tau_{+}^{*}\overline{\phi_{s1}} \gg 1$, the time averaged self-bias becomes increasingly negative, indicates full sheath rectification and is well described by Eq. 11.

Although we carried out the experiment at 30 kHz, the ion plasma frequency corresponding to this experiment was about 160 MHz. Hence, for frequencies much less than 160 MHz, such as ≤ 20 MHz, sheath dynamics can be considered a succession of DC states. Numerical studies of RF sheaths [110], [111] support the concept of DC sheath dynamics for frequencies well below the ion plasma frequency. Therefore, we argue that ion dynamics at 30 kHz and ≤ 20 MHz are approximately equal. For this reason, we consider that the results in Figure 48 are applicable to the MHz frequency range provided the DC sheath condition is satisfied.

In addition, due to the physical and mathematical symmetry between ϕ_{B} and ϕ_{B}^{*} as shown in Eq. 20 and Eq. 26 respectively, we consider that the results in Figure 48 are equally applicable to the passively driven probe and DLP. Therefore, these experimental results provide evidence that (a) RF compensation is achieved whenever the condition $\omega\tau_{+}^{*}\overline{\phi_{p1}} \ll 1$ is satisfied and (b) RF rectification takes place whenever the condition $\omega\tau_{+}^{*}\overline{\phi_{p1}} \gg 1$ is satisfied.

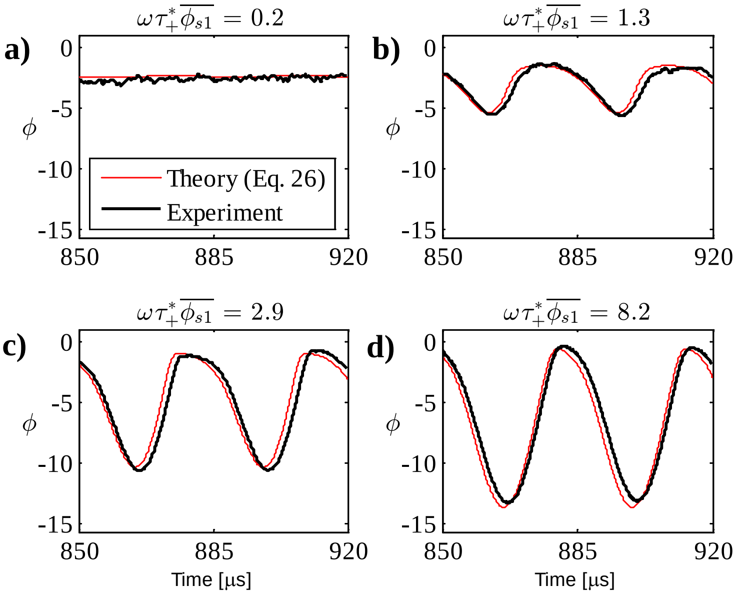

Figure 47, Measured and theoretical (Eq. 26) potentials ϕ of the actively driven probe for different values of $\omega\tau_+^*\overline{\phi_{s1}}$. The conditions are T_e= 3.5 eV, I_+= 6 mA and $\overline{\phi_{s1}}$ = 7.2 at 30 kHz. The coupling capacitors C_c used are: 0.1, 1.7, 3.9 and 11 nF for a) to d) respectively. The corresponding values of $\omega\tau_+^*$ are 0.02, 0.18, 0.41 and 1.1 for a) to d) respectively.

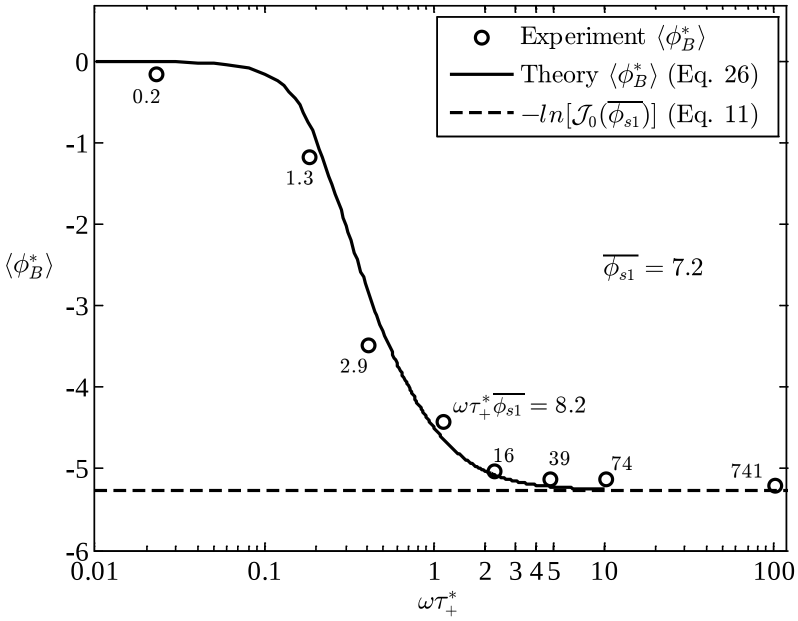

Figure 48, Time averaged self-bias $\langle\phi_B^*\rangle$ of the actively driven probe based on Eq. 26 as a function of $\omega\tau_+^*$. Same conditions as Figure 47. The open circles represent the experimental data with the associated value of $\omega\tau_+^*\overline{\phi_{s1}}$. The dashed horizontal line represents full sheath rectification based on Eq. 11.

4.4 DLP measurements in the presence of RF

In section 4.2.9, we argued that the error in the ion density measurement (δn_i) scales linearly with the RF self-bias (ϕ_B) as shown in Eq. 34 (page 86). In addition, by referring to the single Langmuir probe literature we argued that the electron temperature measurement using DLPs is weakly affected by RF rectification provided the EEDF is Maxwell-Boltzmann. Next, we provide further analysis of Annaratone's DLP experiment [85] which supports these arguments.

4.4.1 Annaratone's DLP experimental setup

In Annaratone's experiment [85], DLP measurements were performed in a capacitively coupled argon RF discharge at 13.56 MHz and a fill pressure of 5 Pa. At the location of measurement, the EEDF was found to be Maxwell-Boltzmann with an electron temperature of 3 eV and the time varying plasma potential 23 V peak to peak at the RF frequency. Two DLPs were used, each with current collecting tips measuring 0.45 and 0.125 mm in diameter, which are therein referred to as "thick" and "thin" probes respectively. The DLPs were actively driven at the RF frequency with a variable phase amplifier. The amplitude and phase of the amplifier were systematically changed in order to control the magnitude of the RF potential acting on the DLPs from 0 to 83 V peak to peak.

4.4.2 Results

For each RF potential, we have digitized the DLP characteristics as shown in Figure 49, where the term $\Delta\phi$ represents the DC potential applied to the DLPs. In addition, the thick solid lines represent DLP characteristics with zero RF potentials and correspond to RF compensated cases. The other line types represent DLP characteristics with varying levels of RF rectification. Notice that as RF rectification is increased, the DLP characteristics are deformed relative to the compensated case. The vertical arrow indicates the response of the DLP characteristics as the magnitude of the RF rectification is increased. Using Eq. 11, the corresponding RF self-biases normalized to the electron temperature ϕ_B are shown in the legend. In both Figure 49a and Figure 49b, the ion saturation current increases with the magnitude of the RF potential. In addition, the slope of the characteristic at $\Delta\phi = 0$ steepens as the magnitude of the RF potential increases.

For each of the characteristics shown in Figure 49, we have extracted the associated ion density and electron temperature values using the DLP equation (Eq. 35) and a least squares fitting algorithm. The results are shown in Figure 50, where the values extracted from the RF compensated characteristics are pointed out. The error bars are based on the variability of the least square fit when initialized with different initial solutions and uncertainty in the slope of the characteristic at the ion saturation region respectively. Figure 50a indicates that the electron temperature value extracted from DLP characteristics deformed by RF rectification is weakly affected by RF rectification. For all these cases the EEDF is Maxwell-Boltzmann. The RF inmmunity of the DLP shown here is consistent with [88]. Figure 50b indicates that the ion density value extracted from DLP characteristics deformed by RF rectification scales linearly with the magnitude of the RF self-bias potential in rough agreement with Eq. 34.

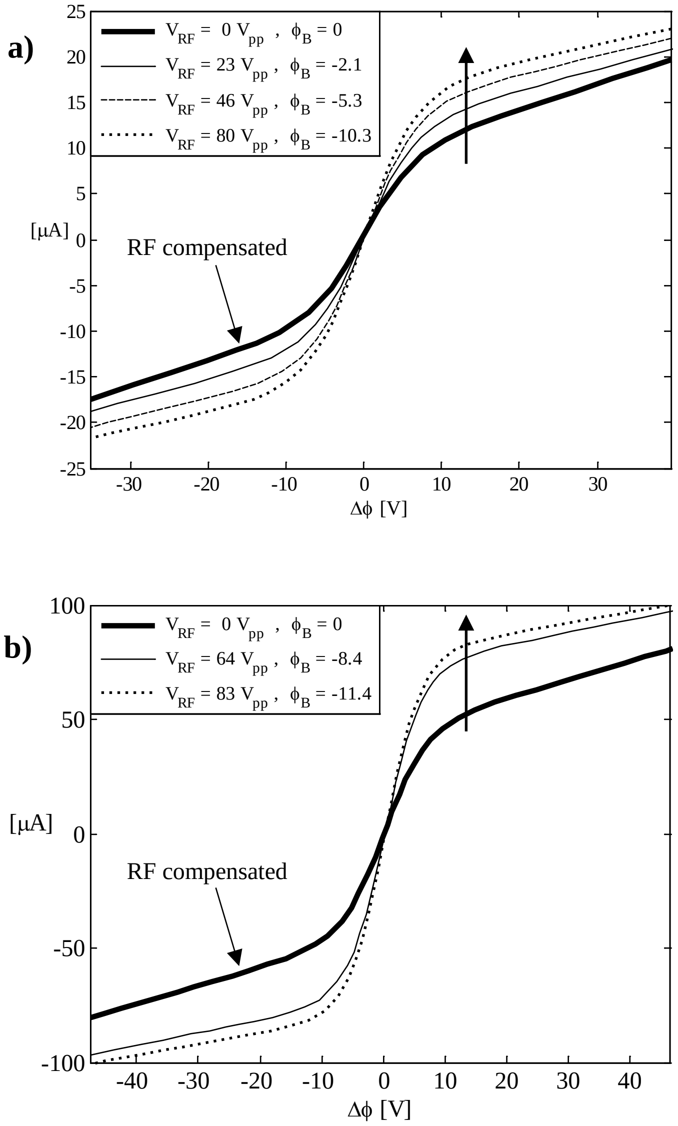

Figure 49, a) “Thick” and b) “thin” DLP characteristic for various levels of RF rectification from reference [85]. The vertical arrow indicates the response of the DLP characteristics as the magnitude of RF rectification is increased. The thick line represents the RF compensated characteristic.

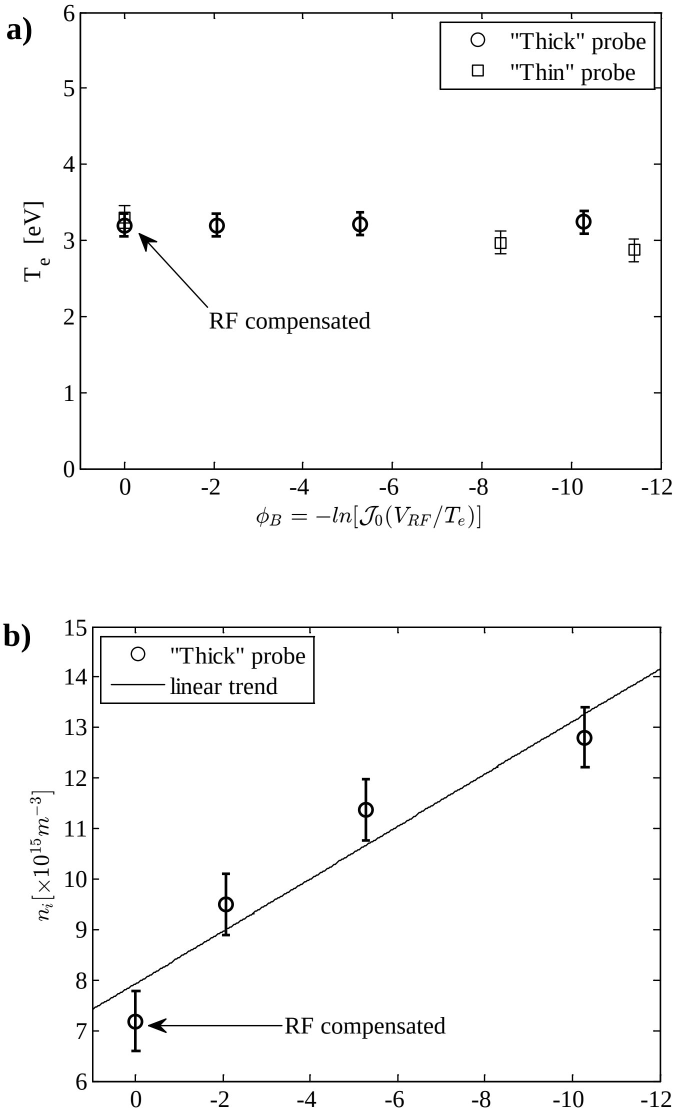

Figure 50, Effect of RF rectification on the a) electron temperature and b) ion density extracted from the DLP characteristics presented in Figure 49. The data points labelled “RF compensated” corresponds to DLP measurements in the absence of rectification.

4.5 Discussion

The implications of the work presented can be divided into (1) RF compensation of the DLP and (2) effects of RF rectification on DLP measurements. Broadly speaking, the former discusses how to achieve RF compensation, while the latter discusses what happens when RF rectification affects the DLP.

4.5.1 RF compensation of the DLP

In the theoretical analysis, we describe the DLP in an RF environment as a pair of floating probes passively driven by the time varying plasma potential. Assuming a single driving frequency and a large stray-to-sheath capacitance ratio, analytical solutions to the problem were obtained. For more general cases, such as multiple frequencies and/or arbitrary values of sheath capacitance, numerical solution methods are required.

An important contribution of this analysis is the expression for the self-bias ϕ_B shown in Eq. 20. In section 4.2.6, we show that this expression describes the intrinsic RF compensation of the DLP, where the key parameters are: (1) the magnitude of the dimensionless time varying potential $\overline{\phi_{p1}}$ and (2) the dimensionless parameter $\omega\tau_+$, where $\tau_+ = T_e C_s / I_+$. We provided a physical interpretation of the parameter $\omega\tau_+$ as the ratio between the sheath resistance and the stray impedance of the probe shaft. Viewed in this manner, RF compensation occurs whenever the sheath resistance is much less than the stray impedance. Formally speaking, the self-bias ϕ_B is determined by the value of the product $\omega\tau_+\overline{\phi_{p1}}$. Specifically, RF compensation occurs whenever the condition $\omega\tau_+\overline{\phi_{p1}} \ll 1$ is satisfied and RF rectification occurs whenever the condition $\omega\tau_+\overline{\phi_{p1}} \gg 1$ is satisfied. In section 4.3, we provide experimental validation for these ideas and conclude that RF compensation indeed occurs whenever $\omega\tau_+\overline{\phi_{p1}} \ll 1$. Therefore, using theory and supported by experiment we provide a tool to quantitatively determine the intrinsic RF compensation of the DLP method for a given set of probe and plasma parameters contained in the product: $\omega\tau_+\overline{\phi_{p1}}$.

In addition, the DLP model presented in section 4.2.6 (Eq. 27-Eq. 29) not only describes the DLP intrinsic RF compensation, but also extends the current DLP theory by unifying the DC and RF regimes into a single expression through the parameter $\omega\tau_+\ \overline{\phi_{p1}}$ and the continuously varying self-bias ϕ_B.

Furthermore, we quantify the level of rectification using the ratio of the time averaged self-bias and the DC floating potential. This ratio $\xi = \langle\phi_B\rangle/\phi_f$ is referred to as the “rectification strength" and we considered that RF compensation occurs whenever $\xi \ll 1$. We demonstrate numerically that the conditions $\omega\tau_{+}\ \overline{\phi_{p1}} < 1$, 0.75, 0.5 and 0.4 correspond (approximately) to "rectification strengths" of 1/10, 1/20, 1/50 and 1/100 in a hydrogen plasma.

In section 4.2.8, based on the aforementioned ideas we describe the design of: (1) a RF compensated DLP, (2) a RF compensated single Langmuir probe and (3) a floating probe for measuring the RF plasma potential oscillations, under conditions relevant to low temperature laboratory RF plasma.

4.5.2 Effects of RF rectification on DLP measurements

The analysis of Annaratone's DLP experiments (section 4.4) shows that the effect of the RF rectification is to increase the ion current collected by a DLP; thereby, causing an overestimation of the ion density relative to the RF compensated case. Results shown in Figure 50b indicate that the overestimation of ion density scales approximately linearly with the RF self-bias, in rough agreement with Eq. 34. In addition, whenever $r_p/\lambda_d \gg 1$, where r_p represents the probe radius and λ_d the Debye length, current collection approaches that of a planar probe and the ion density measurement error due to RF rectification is expected to be small. This situation can be expected to occur in high density plasmas with electrostatic probes that satisfy the condition $r_p/\lambda_d > 50$.

Moreover, analysis of Annaratone's DLP experiments suggest that the electron temperature measurement is weakly affected by RF rectification provided the EEDF is Maxwell-Boltzmann. The RF inmmunity of the DLP shown in this work is consistent with [88][8]. To confirm the expected RF immunity of the electron temperature measurement, it is advisable to extend Annaratone's DLP rectification experiment to a wider range of plasma densities, gas species, RF frequencies and RF potentials.

---

[8] See footnote on page 66.

Appendix 4A. DC floating and self-bias potentials

In a unmagnetized plasma with Maxwell-Boltzmann distributed electrons, the total particle flux Γ to a biased surface is given by Eq. 37, where the term Γ_+ is the ion flux, Γ_e the electron thermal flux, ϕ the surface potential and ϕ_{p1} the time-varying part of the plasma potential normalized to the electron temperature T_e. The electron thermal flux is given by Eq. 38 and provided the Bohm criterion applies, the ion flux is given by Eq. 39. The terms m_e and m_p represent the electron and proton masses respectively, A_i the ionic mass in AMU and n_0 the density where the presheath and bulk plasma join.

$$\Gamma = \Gamma_+ - \Gamma_e \exp(\phi - \phi_{p1}) \qquad \text{Eq. 37}$$

$$\Gamma_e = \frac{n_0}{4}\sqrt{\frac{8\,eT_e}{\pi m_e}} \qquad \text{Eq. 38}$$

$$\Gamma_+ = 0.61 n_0 \sqrt{\frac{eT_e}{m_p A_i}} \qquad \text{Eq. 39}$$

In the absence of time varying potentials across the sheath ($\phi_{p1} = 0$), setting the net particle flux to zero ($\Gamma = 0$) in Eq. 37 leads to the DC floating potential (Eq. 40). At this point, the electron and ion fluxes are equal and no net DC current is extracted from the plasma.

$$\phi_f = -\ln\left(\frac{\Gamma_e}{\Gamma_+}\right) = -\ln\left(\frac{1}{0.61}\sqrt{\frac{m_p A_i}{2\pi m_e}}\right) \qquad \text{Eq. 40}$$

Suppose the time varying plasma potential is given by $\phi_{p1} = -\overline{\phi_{p1}}\cos(\omega t)$, where ω is the driving frequency and $\overline{\phi_{p1}}$ is the magnitude of the plasma potential oscillations. In addition, suppose the surface potential ϕ cannot follow the plasma potential so as to be considered a constant over times in the order of ω^{-1}. If we define the time averaging operation as in Eq. 41, setting the time averaged particle flux in Eq. 37 to zero ($\langle\Gamma\rangle = 0$) leads Eq. 42, where ϕ_u is the “effective” floating potential. Using the identity in Eq. 43 taken from reference [112], the effective floating potential is given by Eq. 44. The term $\mathcal{J}_0$ represents the zeroth-order Bessel function of the first kind and ϕ_B is the self-bias potential.

$$\langle f(t)\rangle = \frac{1}{T}\int_o^T f(t)\,dt \quad T = \frac{2\pi}{\omega} \qquad \text{Eq. 41}$$

$$\phi_u = \phi_f - ln\left(\frac{1}{T}\int_o^T \exp(\overline{\phi_{p1}}\cos(\omega t))\,dt\right) \qquad \text{Eq. 42}$$

$$\frac{1}{T}\int_o^T \exp(a\cos(\omega t))\,dt = \mathcal{J}_0(a) \qquad \text{Eq. 43}$$

$$\phi_u = \phi_f + \phi_B \quad \phi_B = -\ln\left[\mathcal{J}_0\left(\overline{\phi_{p1}}\right)\right] \qquad \text{Eq. 44}$$

Appendix 4B. Sheath displacement current

In references [67], [94], [113], [114], [115], the sheath capacitance is shown to be a function of the sheath potential difference and defined as in Eq. 45, where Q represents the charge in the sheath and ϕ_{sh} the sheath potential difference normalized to the electron temperature T_e. If we define the displacement current as in Eq. 46 and use the definition of the sheath capacitance in Eq. 45 the displacement current can be expressed as in Eq. 47.

$$C_s(\phi_{sh}) = \frac{1}{T_e}\frac{dQ}{d\phi_{sh}} \qquad \text{Eq. 45}$$

$$i_d = \frac{dQ}{dt} = \frac{dQ}{d\phi_{sh}}\frac{d\phi_{sh}}{dt} \qquad \text{Eq. 46}$$

$$i_d = T_e C_s(\phi_{sh})\frac{d\phi_{sh}}{dt} \qquad \text{Eq. 47}$$

Appendix 4C. Passively driven floating probe

Using the change of variables in Eq. 48 in the PDP (Eq. 18) leads to a 1st order differential equation (Eq. 49).

$$\phi = -\ln y \quad \frac{d\phi}{dt} = -\frac{1}{y}\frac{dy}{dt} \qquad \text{Eq. 48}$$

$$\frac{dy}{dt} + y\frac{1}{\tau_+} = \frac{\exp\left(\overline{\phi_{p1}}\cos(\omega t)\right)}{\tau_e} \qquad \text{Eq. 49}$$

Using the integration factor method, the solution of Eq. 49 can be written as in Eq. 50 where C_1 is a constant to be defined by initial conditions and “Q” and “M” are defined in Eq. 51.

$$y = \frac{1}{M}\left(\int QM\,dt + C_1\right) \qquad \text{Eq. 50}$$

$$M = \exp\int\frac{1}{\tau_+}dt \quad Q = \frac{\exp\left(\overline{\phi_{p1}}\cos(\omega t)\right)}{\tau_e} \qquad \text{Eq. 51}$$

Using the change of variables (Eq. 48), Eq. 50 can be written as in Eq. 52. The term F is given by the integral in Eq. 53.

$$\phi = \frac{t}{\tau_+} - \ln\left[\frac{1}{\tau_e}\right] - \ln[F + C_1] \qquad \text{Eq. 52}$$

$$F = \int \exp\left(\overline{\phi_{p1}}\cos(\omega t)\right)\exp\left(\frac{t}{\tau_+}\right)dt \qquad \text{Eq. 53}$$

Using the Bessel identity in Eq. 54 and the integral in Eq. 55, the solution to F (Eq. 53) can be expressed as in Eq. 56. The term $\mathcal{J}_n$ represents the nth-order modified Bessel function of the first kind.

$$\exp[A\cos(\omega t)] = \mathcal{J}_0(A) + 2\sum_{n=1}^{\infty}\mathcal{J}_n(A)\cos(n\omega t) \qquad \text{Eq. 54}$$

$$\int \exp\left(\frac{t}{\tau_+}\right)\cos(n\omega t)\,dt = \tau_+\exp\left(\frac{t}{\tau_+}\right)\left[\frac{\cos(n\omega t) + n\omega\tau_+\sin(n\omega t)}{1 + (n\omega\tau_+)^2}\right] \qquad \text{Eq. 55}$$

$$F = \tau_+ \exp\left(\frac{t}{\tau_+}\right)\left(\mathcal{J}_0\left(\overline{\phi_{p1}}\right) + 2\sum_{n=1}^{\infty} \mathcal{J}_n\left(\overline{\phi_{p1}}\right)\left[\frac{\cos(n\omega t) + n\omega\tau_+ \sin(n\omega t)}{1 + (n\omega\tau_+)^2}\right]\right) \tag{Eq. 56}$$

Substituting Eq. 56 into Eq. 52 the general solution to PDP (Eq. 18) is shown in Eq. 57.

$$\begin{aligned} \phi = -\ln\left[\frac{\tau_+}{\tau_e}\right] - \ln\Bigg[\mathcal{J}_0\left(\overline{\phi_{p1}}\right) &+ 2\sum_{n=1}^{\infty} \mathcal{J}_n\left(\overline{\phi_{p1}}\right)\left(\frac{\cos(n\omega t) + n\omega\tau_+ \sin(n\omega t)}{1 + (n\omega\tau_+)^2}\right) \\ &+ C_1 \exp\left(-\frac{t}{\tau_+}\right)\Bigg] \end{aligned} \tag{Eq. 57}$$

Using the definition of τ_+ and τ_e (Eq. 19) and the expression for the DC floating potential (Eq. 10) in Eq. 57, the solution to the PDP (Eq. 18) for $t \gg t_+$ is shown in Eq. 58.

$$\begin{gathered} \phi = \phi_f + \phi_B \\ \phi_B = -\ln\left[\mathcal{J}_0\left(\overline{\phi_{p1}}\right) + 2\sum_{n=1}^{\infty} \mathcal{J}_n\left(\overline{\phi_{p1}}\right)\left(\frac{\cos(n\omega t) + n\omega\tau_+ \sin(n\omega t)}{1 + (n\omega\tau_+)^2}\right)\right] \end{gathered} \tag{Eq. 58}$$

This expression describes the steady state response of a floating probe passively driven probe by a plasma potential of the form $\phi_{p1} = -\overline{\phi_{p1}}\cos(\omega t)$.

Appendix 4D. Asymptotic analysis of the driven probe equation

Neglecting the active drive terms ($\beta = 0$), retaining the sheath capacitance and setting $\phi_{p1} = -\overline{\phi_{p1}}\cos(\omega t)$ in the GDP (Eq. 15) we obtain an equation describing a passively driven floating probe (Eq. 59), where the term ϕ_{sh} represents the sheath potential difference. This expression is non-linear due to the presence of the sheath capacitance in the term α and cannot be solved analytically.

$$[1 + \alpha(\phi_{sh})]\frac{d\phi_{sh}}{dt} + \frac{\exp(\phi_{sh})}{\tau_e} = \frac{1}{\tau_+} - \omega\overline{\phi_{p1}}\sin(\omega t) \qquad \text{Eq. 59}$$

We re-express this equation to make the term $\omega\tau_+$ explicit (Eq. 60).

$$[1 + \alpha(\phi_{sh})]\omega\tau_+\frac{d\phi_{sh}}{dt}\frac{1}{\omega} + \omega\tau_+\overline{\phi_{p1}}\sin(\omega t) + \exp(\phi_{sh})\frac{\tau_+}{\tau_e} = 1 \qquad \text{Eq. 60}$$

The value of $d\phi_{sh}/dt$ exists within the interval shown in Eq. 61. When the probe potential is able to follow the plasma potential oscillations, the sheath potential becomes time independent and $d\phi_{sh}/dt = 0$. When the probe potential cannot follow, the sheath potential becomes time varying and equal to ϕ_{p1}.

$$0 \leq \frac{d\phi_{sh}}{dt} \leq \frac{d\phi_{p1}}{dt} \qquad \text{Eq. 61}$$

In the limit as $\omega\tau_+ \to 0$, we anticipate that the sheath potential difference ϕ_{sh} becomes time independent and the first term on the LHS of Eq. 60 becomes the product of two small quantities ($\omega\tau_+\ d\phi_{sh}/dt$). Neglecting this term we obtain Eq. 62.

$$\omega\tau_+\overline{\phi_{p1}}\sin(\omega t) + \exp(\phi_{sh})\frac{\tau_+}{\tau_e} = 1 \qquad \text{Eq. 62}$$

Using $\phi_f = \ln(\tau_e/\tau_+)$, we can solve for ϕ_{sh}(Eq. 63).

$$\phi_{sh} = \phi_f + \ln\left[1 - \omega\tau_+\overline{\phi_{p1}}\sin(\omega t)\right] \qquad \text{Eq. 63}$$

Whenever $\omega\tau_+\overline{\phi_{p1}} \ll 1$, the time dependent term vanishes with respect to unity and the sheath potential difference ϕ_{sh} becomes a constant equal to the DC floating potential ϕ_f. Hence, the condition $\omega\tau_+\overline{\phi_{p1}} \ll 1$ implies that the probe potential can follow the plasma potential oscillations regardless of the value of α.

Appendix 4E. Actively driven floating probe

Using the change of variables in Eq. 48 in the ADP (Eq. 24) leads to a 1st order differential equation (Eq. 64).

$$\frac{dy}{dt}+y\left(\frac{1}{\tau_+^*}+\frac{d\overline{\phi_{s1}}\cos(\omega t)}{dt}\right)=\frac{1}{\tau_e^*} \qquad \text{Eq. 64}$$

Using the integration factor method, the solution to Eq. 64 is written as in Eq. 65, where C_1 is a constant to be defined by initial conditions and "Q" and "M" are defined in Eq. 66.

$$y=\frac{1}{M}\left(\int QM\,dt+C_1\right) \qquad \text{Eq. 65}$$

$$M=\exp\left(\frac{t}{\tau_+^*}+\overline{\phi_{s1}}\cos(\omega t)\right) \quad Q=\frac{1}{\tau_e^*} \qquad \text{Eq. 66}$$

Using the change of variables (Eq. 48), Eq. 65 can be written as in Eq. 67. The term F^* is given by the integral in Eq. 68.

$$\phi=\frac{t}{\tau_+^*}-\ln\left[\frac{1}{\tau_e^*}\right]+\overline{\phi_{s1}}\cos(\omega t)-\ln(F^*+C_1) \qquad \text{Eq. 67}$$

$$F^*=\int \exp\left(\overline{\phi_{s1}}\cos(\omega t)\right)\exp\left(\frac{t}{\tau_+^*}\right)dt \qquad \text{Eq. 68}$$

Note that the integral in Eq. 68 has the same form as the integral in Eq. 53; hence, the solution of Eq. 68 is given in Eq. 69.

$$F^*=\tau_+^*\exp\left(\frac{t}{\tau_+^*}\right)\left(\mathcal{I}_0\left(\overline{\phi_{s1}}\right)+2\sum_{n=1}^{\infty}\mathcal{I}_n\left(\overline{\phi_{s1}}\right)\left[\frac{\cos(n\omega t)+n\omega\tau_+^*\sin(n\omega t)}{1+(n\omega\tau_+^*)^2}\right]\right) \qquad \text{Eq. 69}$$

Substituting Eq. 69 into Eq. 67, the general solution to the ADP (Eq. 24) is shown in Eq. 70.

$$\begin{aligned}\phi=&-\ln\left[\frac{\tau_+^*}{\tau_e^*}\right]+\overline{\phi_{s1}}\cos(\omega t)\\&-\ln\left(\mathcal{I}_0\left(\overline{\phi_{s1}}\right)+2\sum_{n=1}^{\infty}\mathcal{I}_n\left(\overline{\phi_{s1}}\right)\left[\frac{\cos(n\omega t)+n\omega\tau_+^*\sin(n\omega t)}{1+(n\omega\tau_+^*)^2}\right]\right.\\&\left.+C_1\exp\left(-\frac{t}{\tau_+^*}\right)\right)\end{aligned} \qquad \text{Eq. 70}$$

Using the definition of τ_+^* and τ_e^* (Eq. 25) and the expression for the DC floating potential (Eq. 10) in Eq. 70, the solution to the ADP (Eq. 24) for $t \gg t_+$ is shown in Eq. 71.

$$\phi = \phi_f + \phi_B^* + \overline{\phi_{s1}}\cos(\omega t)$$

$$\phi_B^* = -\ln\left[\mathcal{J}_0\left(\overline{\phi_{s1}}\right) + 2\sum_{n=1}^{\infty}\mathcal{J}_n\left(\overline{\phi_{s1}}\right)\left(\frac{\cos(n\omega t) + n\omega\tau_+^*\sin(n\omega t)}{1 + (n\omega\tau_+^*)^2}\right)\right] \qquad \text{Eq. 71}$$

This expression describes the steady state response of a floating probe actively driven probe by an external potential of the form $\phi_{s1} = \overline{\phi_{s1}}\cos(\omega t)$.

Appendix 4F. Passively driven DLP

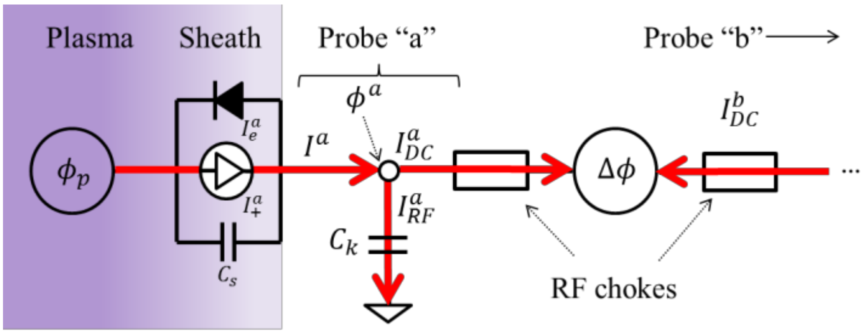

Figure 51, RF and DC currents in a DLP system passively driven by a time varying plasma potential ϕ_p.

Figure 51 illustrates in detail the RF and DC current paths in a DLP passively driven by the time varying plasma potential. The DLP is composed of two floating probes which we label with superscripts “a” and “b”. We use the assumptions from section 4.2.1, assume the DLP is symmetric and the applied DC potential between probes $\Delta\phi$ is essentially a constant on the time scales of ϕ_{p1}. Using the symmetric DLP assumption, the sheath capacitance, stray capacitance and ion saturation current of the probes “a” and “b” are taken to be identical and hence we omit the “a” and “b” superscript notation for these terms.

The current balance for the nth probe is given in Eq. 72, where i_d^n represents the sheath displacement current, I_{DC}^n the current driven by the applied DC potential $\Delta\phi$ and I_{RF}^n the RF current flowing into the stray capacitance of the nth probe respectively. The sheath displacement current is based on Appendix 4B and is given in Eq. 73. The DC and RF currents are shown in Eq. 74. The applied DC potential between probes is defined in Eq. 75.

$$I_+ - I_e\, exp\left(\phi^n - \phi_{p1}\right) - i_d^n = I_{DC}^n + I_{RF}^n \quad n = a, b \tag*{Eq. 72}$$

$$i_d^n = T_e C_s \frac{d\left(\phi^n - \phi_{p1}\right)}{dt} \tag*{Eq. 73}$$

$$I_{DC}^a = -I_{DC}^b \quad I_{RF}^n = T_e C_k \frac{d\phi^n}{dt} \tag*{Eq. 74}$$

$$\Delta\phi = \phi^b - \phi^a \tag*{Eq. 75}$$

Adding the probe “a” and probe “b” current balance (Eq. 72), using the expression in Eq. 75 and $d\Delta\phi/dt = 0$ we obtain Eq. 76. This expression describes the sheath potential difference of a DLP driven by time varying plasma potentials.

$$\begin{gathered}(1+\alpha)\frac{d\phi_{sh}^{a}}{dt}+\frac{1}{\tau_e}\exp(\phi_{sh}^{a})\left(\frac{\exp\Delta\phi+1}{2}\right)=\frac{1}{\tau_+}-\frac{d\phi_{p1}}{dt}\\ \alpha=\frac{C_s}{C_k}\quad \tau_+=\frac{T_eC_k}{\Gamma_+A_p}\quad \tau_e=\frac{T_eC_k}{\Gamma_eA_p}\quad \phi_{sh}^{a}=\phi^{a}-\phi_{p1}\end{gathered}\tag{Eq. 76}$$

We can solve this equation analytically if we assume a large stray-to-sheath capacitance ratio ($\alpha \ll 1$, see section 4.2.5) and $\phi_{p1}=-\overline{\phi_{p1}}\cos(\omega t)$. Under these assumptions Eq. 76 can be written as in Eq. 77.

$$\frac{d\phi^{a}}{dt}+\frac{1}{\tau_e}\exp(\phi^{a})\left[\exp\left(\overline{\phi_{p1}}\cos(\omega t)\right)\left(\frac{\exp\Delta\phi+1}{2}\right)\right]=\frac{1}{\tau_+}\tag{Eq. 77}$$

Using the change of variables in Eq. 78 leads to a 1st order differential equation (Eq. 79).

$$\phi^{a}=-\ln y\quad \frac{d\phi^{a}}{dt}=-\frac{1}{y}\frac{dy}{dt}\tag{Eq. 78}$$

$$\frac{dy}{dt}+y\frac{1}{\tau_+}=\frac{\exp\left(\overline{\phi_{p1}}\cos(\omega t)\right)}{\tau_e}\left[\frac{\exp\Delta\phi+1}{2}\right]\tag{Eq. 79}$$

$$\frac{2}{\exp\Delta\phi+1}=1-\tanh\left(\frac{\Delta\phi}{2}\right)\tag{Eq. 80}$$

Using a procedure similar to that described in Appendix 4C and the identity in Eq. 80, the steady state solution of Eq. 79 is given below by Eq. 81 to Eq. 83, where the term Ω^{n} is referred to as the DC bias and ϕ_B as the self-bias. This solution represents the potential of a DLP driven by a time varying plasma potential of the form $\phi_{p1}=-\overline{\phi_{p1}}\cos(\omega t)$.

$$\phi^{n}=\phi_f+\Omega^{n}+\phi_B\quad n=a,b\tag{Eq. 81}$$

$$\Omega^{a}=\ln\left[1-\tanh\left(\frac{\Delta\phi}{2}\right)\right]\quad \Omega^{b}=\ln\left[1+\tanh\left(\frac{\Delta\phi}{2}\right)\right]\tag{Eq. 82}$$

$$\phi_B=-\ln\left[\mathcal{J}_0\left(\overline{\phi_{p1}}\right)+2\sum_{n=1}^{\infty}\mathcal{J}_n\left(\overline{\phi_{p1}}\right)\left(\frac{\cos(n\omega t)+n\omega\tau_+\sin(n\omega t)}{1+[n\omega\tau_+]^2}\right)\right]\tag{Eq. 83}$$

Chapter 5 Cold plasma waves in MAGPIE

5.1 Introduction......106
5.2 Helicon and Trivelpiece-Gould waves......107
  5.2.1 Dispersion relation......107
  5.2.2 Effect of collisions......108
  5.2.3 Wave damping......112
5.3 Waves in cylindrically bounded cold magnetized plasma......117
  5.3.1 Governing equations......117
  5.3.2 Plasma wavefields......119
  5.3.3 RF antenna......122
  5.3.4 Boundary conditions......124
  5.3.5 Wave excitation by an RF antenna......125
  5.3.6 Power deposition mechanism......127
Appendix 5A. Waves in unbounded cold magnetized plasma......128
  5A.1 Conductivity......128
  5A.2 The cold dielectric tensor......129
  5A.3 Dispersion relation......131
Appendix 5B. Electrostatic and Electromagnetic content of plasma waves:......134
Appendix 5C. Vacuum wavefields......135
  5C.1 Parallel fields......135
  5C.2 Transverse fields......136
  5C.3 Region II basis function......136
  5C.4 Region III basis function......138
Appendix 5D. Power deposition and heat transport in cold plasma......139
  5D.1 RF power deposition......139
  5D.2 Heat transport in plasma......142
  5D.3 Power balance......144

5.1 Introduction

The simplest description of wave physics in magnetized plasma is given by the cold plasma approximation (Appendix 5A). This treatment is appropriate when phase velocities are much larger than particle thermal velocities so that wave-particle interaction and kinetic effects can be neglected. In the absence of external currents this model describes the high frequency normal modes of oscillations that can occur in cold magnetized plasma. There exist more elaborate treatments in order to deal with thermal and finite Larmour radius effects but for our purposes the cold plasma treatment will suffice. This chapter is divided into two sections. In section 5.2, we review the physics of Helicon wave propagation in collisional cold magnetized plasma. In section 5.3, we describe the development of a semi-analytical uniform plasma (0D) full wave code to model the propagation of electromagnetic waves in cylindrically bounded cold magnetized plasma. We include realistic antenna geometries, the effect of collisional dissipation and discuss wave excitation and power deposition mechanisms relevant to MAGPIE. This code is applied to MAGPIE in Chapter 6.

5.2 Helicon and Trivelpiece-Gould waves

5.2.1 Dispersion relation

To describe wave propagation in the "Helicon-Trivelpiece-Gould (H-TG)" regime [116], [117], [118], [119], [120], [121] we use the frequency ordering of Eq. 84, introduce the complex dimensionless quantity δ_* (Eq. 85), denote complex parallel and transverse wave numbers as κ and μ, use subscripts "R" and "I" to denote real and imaginary components respectively and reduce the components of the collisional dielectric tensor (Eq. 161 - Eq. 164) as shown in Eq. 86 to Eq. 88.

$$\Omega_i \ll \omega \ll \Omega_e \quad \Omega_e \ll \omega_{pe} \quad \nu \sim \omega$$ Eq. 84

$$\delta_* = \delta_R + i\delta_I \quad \delta_R = \frac{\omega}{\Omega_e} \quad \delta_I = \frac{\nu}{\Omega_e} \quad \nu^* = \frac{\nu}{\omega}$$ Eq. 85

$$R = -P\left[\frac{\delta_*}{1-\delta_*}\right] \quad L = P\left[\frac{\delta_*}{1+\delta_*}\right]$$ Eq. 86

$$S = -P\left[\frac{\delta_*^2}{1-\delta_*^2}\right] \quad D = -P\left[\frac{\delta_*}{1-\delta_*^2}\right]$$ Eq. 87

$$P = -\frac{\omega_{pe}^2}{\omega\Omega_e}\left[\frac{1}{\delta_*}\right]$$ Eq. 88

Using the aforementioned dielectric tensor components the propagating solution of Eq. 172 is given by Eq. 89, where k and k_w represent the total and free space "whistler" wavenumbers respectively. Substitution of $k\cos\theta = \kappa$ into Eq. 89 leads to Eq. 90 and hereafter referred to as the "H-TG" dispersion relation. We note that Eq. 89 and Eq. 90 are equivalent, however they differ in the choice of the independent variable (θ or κ). For a given parallel wavenumber κ, the collisionless "H-TG" dispersion relation (Eq. 90) describes 2 waves for a given parallel wavenumber κ. However, when collisions are included it describes in general 3 waves, each with a distinct imaginary parallel wavenumber κ_I.

$$k^2 = \left[\frac{k_w^2}{\cos\theta - \delta_*}\right] \qquad k_w^2 = \frac{\omega\omega_{pe}^2}{\Omega_e c^2} \qquad \text{Eq. 89}$$

$$k^2 - \left(\frac{\kappa}{\delta_*}\right)k + \left(\frac{k_w^2}{\delta_*}\right) = 0 \qquad \text{Eq. 90}$$

5.2.2 Effect of collisions

Electrostatic content of H-TG waves

Using Eq. 183 (Appendix 5B) and the dielectric tensor components relevant to this analysis (Eq. 86 to Eq. 88) the electrostatic content of the H-TG wave is given by Eq. 91. For arbitrary propagation angles θ the H-TG wave has both ES and EM characteristics as shown in Figure 52 for various collisionality levels ($\nu^* = \nu/\omega$) and a value of $\delta_R = 1/8$. Notice that for propagation angles θ close to the background magnetic field ($\theta < \pi/8$) the EM component dominates ($E_\perp \gg E_\parallel$); whereas for propagation approaching the resonance cone θ_{res} the ES component dominates. In general, as the propagation angle increases so does the ES content and the wave becomes more strongly damped. Notice that as the collisionality is increased the ratio of parallel to transverse electric field strength is reduced. In section 5.2.3 we derive a generalized expression that describes the damping of the H-TG wave.

$$\frac{E_\parallel}{E_\perp} = \frac{\tan\theta}{1 - \delta_*^2 \sec^2\theta} \qquad \text{Eq. 91}$$

Figure 52. Electrostatic content of the H-TG wave (Eq. 91) for various collisionality levels ($\nu^* = \nu/\omega$) and a value of $\delta_R = 1/8$. In this example $\theta_{res} = 83°$.

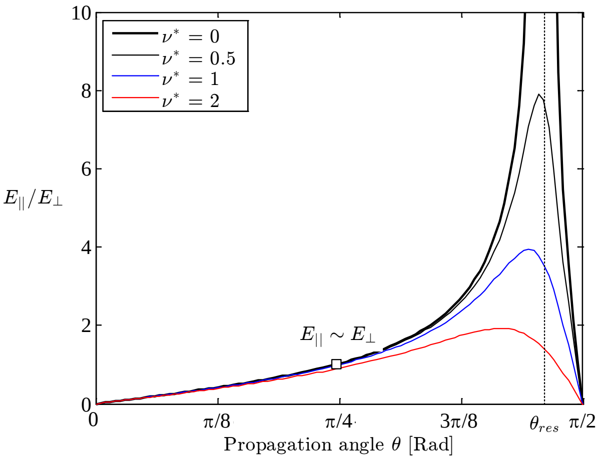

Propagation of waves at arbitrary angles

We now describe the characteristics of the HT-G dispersion relation as a function of angle (Eq. 89) in both the collisionless and collisional case. The plasma and background magnetic field are assumed to be uniform and neglect boundary effects. In continuation to Figure 52, we choose the RF frequency to be 7 MHz and a background magnetic field of 20 G so that δ_R = 1/8. In addition, we choose a plasma density of 1x10^{19} m^{-3}. Under these conditions, the "whistler" wavenumber is approximately 210 m^{-1} and the electron cyclotron frequency is 56 MHz.

In Figure 53 we show the collisionless case. The dotted line presents the phase velocity resonance cone angle (83°) with respect to the background magnetic field. Wave dispersion can be divided into the "Helicon" (H) and "Trivelpiece-Gould" (TG) branches as labelled in the figure. In this example, the "H" and "TG" branches merge at about κ = 150 m^{-1} with a corresponding angle of 76 degrees and electrostic content (Eq. 91) of $E_{\|}/E_{\perp}$~ 4. This indicates that the TG wave is confined to propagate essentially at the resonance cone (76 to 83 degrees) as an electrostatic wave. Moreover, the "Helicon" branch becomes truly electromagnetic ($E_{\|}/E_{\perp} < 0.3$) only for angles less than 20 degrees. At these shallow angles of propagation, the "Helicon" wavenumber approaches that of the "whistler" (210 m^{-1}). Notice that for every parallel wavenumber, between 150 and 230 m^{-1}, there are two distinct transverse wavenumbers that satisfy the dispersion relation, each corresponding to the H and TG wave respectively.

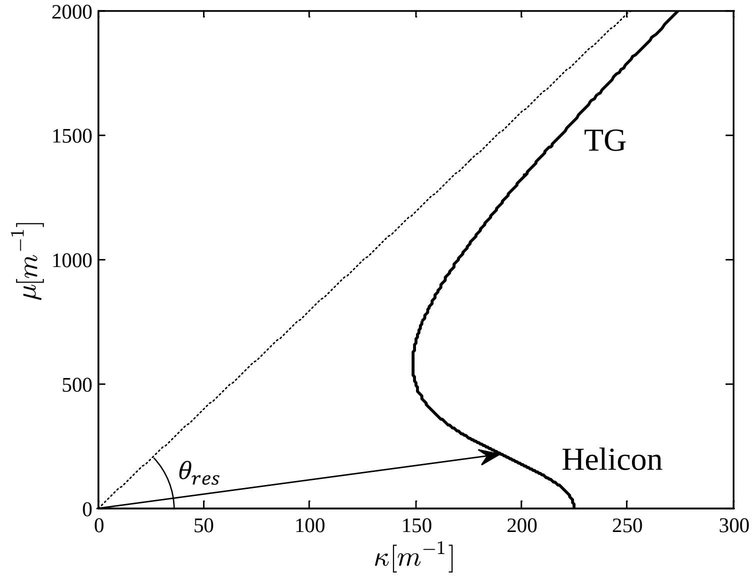

Figure 53, H-TG dispersion relation (Eq. 89) in the collisionless case. The dotted line represents the phase velocity resonance cone angle. In this example it is 83 degrees.

The arrow represents an arbitrary wave vector propagating at an angle of 48 degrees with respect to the background magnetic field (κ =190 m^{-1} and μ = 215 m^{-1}). At these conditions, the electrostatic content (Eq. 91) of the wave is $E_{\|}/E_{\perp} \sim 1$; hence, the wave is neither purely electromagnetic nor electrostatic. However, it can be approximately described by the "Helicon" branch.

We now discuss collisional effects. Under these circumstances, both κ and μ have real and imaginary parts and describe the propagation and damping characteristics of the wave respectively. In Figure 54, we show the real part of the dispersion relation for different values of collisionality using the parameter $\nu^* = \nu/\omega$, where ν is the electron momentum transfer collision frequency. For reference, the collisionless case ($\nu^* = 0$) previously discussed is denoted by the thick black line. The collisionality parameter ν^* is varied from the collisionless ($\nu^* = 0$) to the strongly collisional case (ν^* =1.3). The most important effect is the reduction in the "TG" branch. In fact, for $\nu^* \geq 0.53$ the "TG" branch can no longer be identified. However, the "Helicon" branch is only weakly affected by collisions, especially for $\kappa > 200$ m^{-1} which corresponds to the electromagnetic region ($E_{\|}/E_{\perp} \leq 1$).

In Figure 55, we show the imaginary part of the dispersion relation for the same values of $\nu^* = \nu/\omega$. The results indicate that wave damping is strongly directional and occurs essentially along the resonance cone angle. As collisionality is increased, there is a reduction in the transverse damping while the parallel damping is increased. By combining the results from Figure 54 and Figure 55, it can be shown that at the resonance cone angle both the real and imaginary wavenumbers are equal. Below the resonance cone, the real wavenumber dominates and wave propagation is possible; however, above the resonance cone the imaginary wavenumber dominates and all waves are collisionally evanescent.

It is important to mention that inclusion of collisional effects in the H-TG dispersion relation (Eq. 89) lead to the following puzzling result: For every parallel wavenumber in Figure 54 between 160 and 230 m^{-1} and for $\nu^* > 0.27$ there are three distinct transverse wavenumbers that satisfy the dispersion relation. One can be associated with the "Helicon" wave; while the remaining waves can be identified as TG-like since they are confined to propagate along the resonance cone. The "TG-like" solution with the highest transverse wavenumber exists mostly above the resonance cone; therefore, it is collisionally evanescent. For this reason, the remaining TG-like solution can be associated with the "TG" branch from the collisionless case. We are compelled to ask if the "additional" wave is a physical solution or a mathematical artefact. At the conditions under which this "additional" wave exists, i.e. above the resonance cone, the phase velocity may be comparable to the electron thermal velocity and wave-particle interaction and kinetic effects cannot be ignored. Under these circumstances, the "cold" plasma theory is inappropriate and the "additional" wave may be considered as a mathematical artefact due to the limitations of the theory. However, additional work is required to resolve this matter.

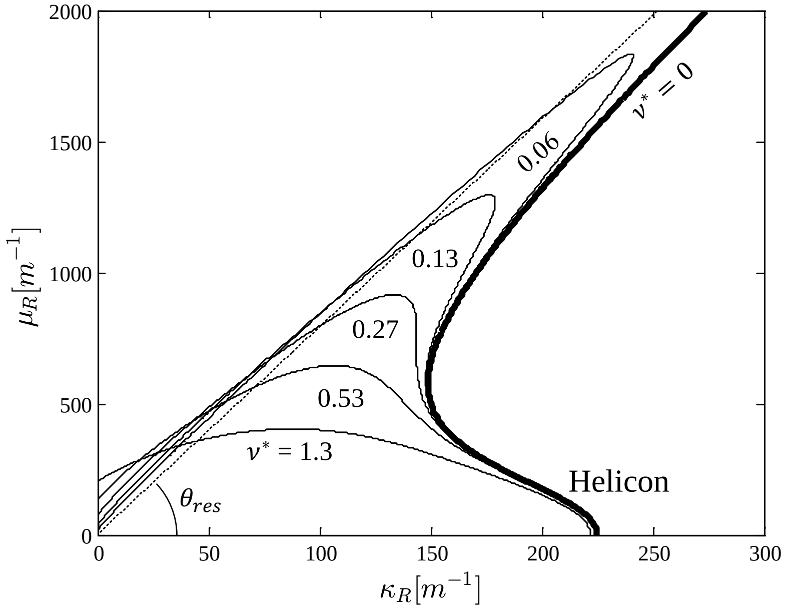

Figure 54, Real part of the H-TG dispersion relation (Eq. 89) in the collisional case as a function of $\nu^* = \nu/\omega$.

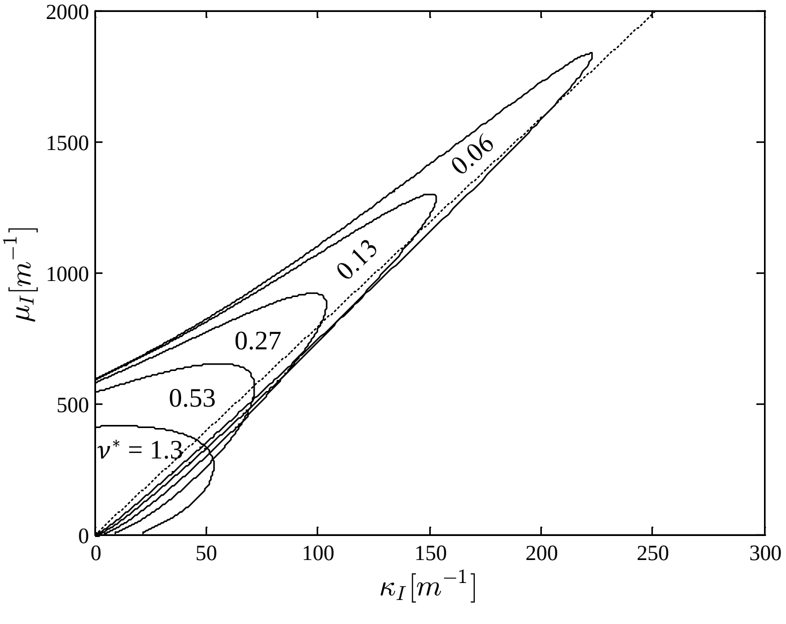

Figure 55, Imaginary part of the H-TG dispersion relation (Eq. 89) in the collisional case as a function of $\nu^* = \nu/\omega$. The dotted line represents the phase velocity resonance cone angle. In this example it is 83 degrees.

5.2.3 Wave damping

In the previous section, we evaluated the H-TG wave propagation and damping as a function of angle θ using Eq. 89. We found that as the angle of propagation is increased so does damping. From an experimental perspective, it is sometimes desirable to calculate wave damping as a function of parallel wavenumber κ. For example, when operating helicon sources, measurements of the fundamental parallel wavenumber (κ_R) using magnetic probes (Chapter 3) can be used to predict the helicon wave attenuation length (κ_I^{-1}) using Eq. 90 . In what follows, we derive an expression for precisely this purpose, namely, calculation of κ_I for any value of κ_R.

First, we take H-TG dispersion relation of Eq. 90 and expand all wave numbers into their real and imaginary parts. After some algebra, Eq. 90 can be written as in Eq. 92, where the relevant coefficients are defined in Eq. 93 and subscripts “R” and “I” denote real and imaginary parts respectively.

$$\begin{gathered} D_R + iD_I = 0 \\ D_R = k_R^2 - k_R\mathcal{R} - k_I^2 - k_I\mathcal{P} + \mathcal{Q}\delta_R \quad D_I = 2k_Rk_I - k_I\mathcal{R} + k_R\mathcal{P} - \mathcal{Q}\delta_I \end{gathered} \tag{Eq. 92}$$

$$\mathcal{R} = \left(\frac{\kappa_R\delta_R + \kappa_I\delta_I}{\delta_R^2 + \delta_I^2}\right) \quad \mathcal{P} = \left(\frac{\kappa_R\delta_I - \kappa_I\delta_R}{\delta_R^2 + \delta_I^2}\right) \quad \mathcal{Q} = \left(\frac{k_w^2}{\delta_R^2 + \delta_I^2}\right) \tag{Eq. 93}$$

By restricting the propagation angle θ to be purely real, the ratio of complex wave numbers ($\tan\theta = \mu/\kappa$) must also be real. This restriction results in the condition $k_I = k_R(\kappa_I/\kappa_R)$ shown in Eq. 179 (Appendix 5A). Implementing this condition reduces Eq. 92 to the form shown in Eq. 94, where the coefficients are defined as in Eq. 95.

$$\begin{gathered} D_R + iD_I = 0 \\ D_R = \mathcal{B}k_R^2 - \mathcal{E}k_R + \mathcal{Q}\kappa_R^2\delta_R \quad D_I = \mathcal{A}k_R^2 - \mathcal{F}k_R - \mathcal{Q}\kappa_R^2\delta_I \end{gathered} \tag{Eq. 94}$$

$$\begin{gathered} \mathcal{A} = 2\kappa_R\kappa_I \quad \mathcal{B} = \kappa_R^2 - \kappa_I^2 \\ \mathcal{E} = \left(\frac{\kappa_R}{\delta_R^2 + \delta_I^2}\right)(\delta_R\mathcal{B} + \delta_I\mathcal{A}) \quad \mathcal{F} = \left(\frac{\kappa_R}{\delta_R^2 + \delta_I^2}\right)(\delta_R\mathcal{A} - \delta_I\mathcal{B}) \end{gathered} \tag{Eq. 95}$$

Since the real and imaginary parts (D_R and D_I respectively) in Eq. 94 must simultaneously vanish, Eq. 94 represents a pair of coupled quadratic equations. We can express the problem in matrix form (Eq. 96) and solve for k_R and k_R^2 as shown in Eq. 97.

$$\begin{bmatrix} k_R^2 \\ k_R \end{bmatrix} = \frac{\mathcal{Q}\kappa_R^2}{\mathcal{E}\mathcal{A} - \mathcal{B}\mathcal{F}} \begin{bmatrix} -\mathcal{F} & \mathcal{E} \\ -\mathcal{A} & \mathcal{B} \end{bmatrix} \begin{bmatrix} -\delta_R \\ \delta_I \end{bmatrix} \tag{Eq. 96}$$

$$k_R = \left(\frac{k_w^2}{\delta_I}\right)\kappa_R\left(\frac{\mathcal{A}\delta_R + \mathcal{B}\delta_I}{\mathcal{A}^2 + \mathcal{B}^2}\right) \quad k_R^2 = \frac{k_w^2\kappa_R^2}{\delta_I}\left(\frac{\mathcal{A}}{\mathcal{A}^2 + \mathcal{B}^2}\right) \tag{Eq. 97}$$

Combining the solutions in Eq. 97 to eliminate k_R leads to a quintic equation of κ_I as a function of κ_R. Normalized with respect to κ_R the quintic equation is given by Eq. 98 with coefficients defined as in Eq. 99 and Eq. 100, where the term $\mathcal{K}$ is hereafter referred to as the damping strength. Solving the quintic equation (Eq. 98) yields the parallel wave damping (κ_I) for any given κ_R. In Chapter 6, we compare this H-TG wave damping calculation with experimental measurements of helicon wave attenuation.

$$\mathcal{K}^5 c_5 + \mathcal{K}^4 c_4 + \mathcal{K}^3 c_3 + \mathcal{K}^2 c_2 + \mathcal{K} c_1 + c_0 = 0 \tag{Eq. 98}$$

$$\begin{gathered} \mathcal{K} = \frac{\kappa_I}{\kappa_R} \quad c_5 = 2\delta_I \quad c_4 = -\frac{\Psi_R}{4}\nu^*\delta_I \quad c_3 = \delta_I(4 + \Psi_R) \\ c_2 = \Psi_R\delta_R\left(\frac{\nu^{*2}}{2} - 1\right) \quad c_1 = \delta_I(2 - \Psi_R) \quad c_0 = -\frac{\Psi_R}{4}\nu^*\delta_I \end{gathered} \tag{Eq. 99}$$

$$\Psi_R = 4\frac{k_w^2}{\kappa_R^2}\delta_R \quad \nu^* = \frac{\nu}{\omega} \tag{Eq. 100}$$

It can be shown that two of the five roots produced by the quintic equation (Eq. 98) are always complex conjugates of each other. Since κ_I is defined as a real number, the complex conjugate solutions of Eq. 98 are not physically relevant and can be ignored. The remaining 3 roots can be real or complex depending on the plasma conditions. When these roots are real, their substitution into the H-TG dispersion relation (Eq. 90) reveals the existence of 3 distinct waves for any given κ_R, in accordance with the findings discussed in the previous section. In the strongly collisional case ($\nu^* \geq 1$), only one root is real and corresponds to the “Helicon” branch. This case is illustrated in Figure 54 for $\nu^* > 0.5$, where the TG branch is strongly reduced and only the H branch can be identified.

The helicon approximation

The quintic (Eq. 98) describes the parallel damping of the H-TG wave for arbitrary values of real parallel wavenumbers; however, it is not readily evaluated. It would be desirable to have a simpler expression that provides insight into the effect of plasma conditions (magnetic field, density, collisions, etc) on wave damping. We now derive an expression for helicon wave damping by approximating the quintic equation (Eq. 98). First, we must assume very low damping ($\mathcal{K} \ll 1$) so that we can neglect higher order terms in Eq. 98 and produce a quadratic equation (Eq. 101). It will be later shown how small $\mathcal{K}$ must be. This quadratic equation describes 2 out of the 3 possible waves; namely, the H wave and the least damped of the TG-like waves. The terms Ψ_R and ν^* are defined in Eq. 100. The solution to the quadratic can be written as in Eq. 102.

$$\mathcal{K}^2 - \mathcal{K}\frac{2}{\Psi_R}\nu^* + \frac{\nu^{*2}}{4} = 0 \qquad \text{Eq. 101}$$

$$\mathcal{K} = \frac{\tau}{\Psi_R}\left(1 \pm \sqrt{1 - \frac{\Psi_R^2}{4}}\right) \qquad \text{Eq. 102}$$

Separating the solutions in Eq. 102 requires that $\Psi_R \ll 1$, which corresponds to the case where the "H" and "TG" branches are well separated and hence distinguishable. For separable conditions ($\Psi_R \ll 1$), the quadratic equation (Eq. 102) can be Taylor expanded to first order as shown in Eq. 103. The roots are given in Eq. 104. The "+ve" and "-ve" roots correspond to the TG and H waves respectively.

$$\mathcal{K} = \frac{\nu^*}{\Psi_R}\left[1 \pm \left(1 - \frac{\Psi_R^2}{8}\right)\right] \qquad \text{Eq. 103}$$

$$\mathcal{K}_+ = \left(\frac{2\nu^*}{\Psi_R}\right) \quad \mathcal{K}_- = \left(\frac{\nu^*}{2}\right)\left(\frac{\Psi_R}{4}\right) \quad where \quad \kappa_{I\pm} = \kappa_R \mathcal{K}_\pm \qquad \text{Eq. 104}$$

These roots reveal that the TG wave damping strength is stronger than that of the H by a factor of $16/\Psi_R^2$. However, for this approximate analysis to be valid we require $\mathcal{K}_\pm \ll 1$; using the expression for $\mathcal{K}_+$ (Eq. 104) the upper bound for the collision frequency is $\nu^* \ll \Psi_\mathrm{R}/2$. For plasma conditions that do not satisfy this inequality the expression for the TG wave damping strength (Eq. 104) is no longer valid and higher order terms from the quintic equation (Eq. 98) are required to fully describe the damping process. However, the expression for the H wave damping strength is valid over a much larger parameter space provided $\nu^* \ll 8/\Psi_R$. Whenever these inequalities are satisfied ($\mathcal{K}_{\pm} \ll 1$), the H and TG damping expressions in Eq. 103 and Eq. 104 can be written as in Eq. 105 and Eq. 106 respectively. The expression in Eq. 105 indicates that helicon wave damping increases with the collision frequency and decreases with the magnetic field. On the other hand, Eq. 106 indicates that TG wave damping increases with magnetic field strength. In Chapter 6, we compare Eq. 105 with experimental measurements of helicon wave attenuation.

$$\kappa_{I-} = \frac{k_w^2}{\kappa_R}\left(\frac{\nu}{2\Omega_e}\right) \qquad \text{Helicon (H) wave damping} \qquad \text{Eq. 105}$$

$$\kappa_{I+} = \frac{\kappa_{R+}}{\delta_R}\left(\frac{\nu}{2\omega}\right)\left(\frac{\kappa_R}{k_w}\right)^2 \qquad \text{Trivelpiece-Gould (TG) wave damping} \qquad \text{Eq. 106}$$

Using the real part of Eq. 94 ($D_R = 0$), the damping strength expressions in Eq. 104 in the low damping limit ($\mathcal{K}_{\pm} \ll 1$), expressions for the H and TG dispersion relations can be obtained. These are shown in Eq. 107 and Eq. 108 respectively.

$$k_{R-} = \frac{k_w^2}{\kappa_R} \qquad \text{Helicon (H) wave dispersion} \qquad \text{Eq. 107}$$

$$k_{R+} = \frac{\kappa_R}{\delta_R} \qquad \text{Trivelpiece-Gould (TG) wave dispersion} \qquad \text{Eq. 108}$$

These dispersion relations are consistent with those found in the work of Chen [117] and Shamrai [116]. The H wave damping rate κ_{I-} is consistent with those found in Eq. 8.26 in reference [112] and Eq.76 in reference [122] for $\mu_R \gg \kappa_R$. Shamrai provides an expression for the TG wave transverse damping rate which differs from Eq. 106 in sign. We note that because $\kappa_R/k_w \sim 1$ when the TG and H branches are well separated, the magnitude of Eq. 106 is comparable to that given by Shamrai. Nevertheless, Shamrai justifies the negative sign of the TG wave damping rate, without details, by noting that TG waves have a transverse phase velocity opposite to that of the group velocity.

If we assume κ to be complex and extract the imaginary part of k by solving Eq. 90 in the $\Psi_R \ll 1$ limit, the sign of the TG wave damping rate is determined by the sign of $(\mathcal{K}_+ - \nu^*)$, a difference of two small numbers. However, if κ is a priori assumed to real, as it is done in Shamrai's work [116], the procedure just described leads to a negative TG wave damping expression which is identical to that presented in [116]. Instead of assuming $\kappa_{+I} \neq 0$ a priori but use Eq. 104, the term $(\mathcal{K}_+ - \nu^*)$ becomes positive since $\mathcal{K}_+ \gg \nu^*$ and leads to a positive TG wave damping rate (Eq. 106). We believe that this is the correct way of calculating the TG wave damping rate. However, we have no experimental validation for Eq. 106 due to the difficulty of measuring the TG wave; in this case, comparison with full wave codes is recommended. We now further clarify Shamrai's $\kappa_{+I} = 0$ assumption. In reference [116], the analysis therein presented considers only low aspect ratio plasma sources, where the plasma cavity defines the values of parallel wavenumbers. At that point in the analysis, both the angular frequency ω and the parallel wavenumber κ are defined as purely real; therefore, implicitly assuming that the parallel damping is identically zero ($\kappa_{+I} = 0$).

5.3 Waves in cylindrically bounded cold magnetized plasma

In this section we describe the development of a semi-analytical uniform plasma (0D) full wave code to model the propagation of electromagnetic waves in cylindrically bounded cold magnetized plasma. We include realistic antenna geometries, the effects of collisional dissipation and discuss wave excitation and power deposition mechanisms relevant to MAGPIE. In this model, waves in the plasma are excited by an RF antenna of length "L", which is modelled as a linear combination of infinitely long current sheets radially located r_a as shown in Figure 56. The plasma length is assumed to be infinite along the "z" direction, surrounded by a vacuum layer and enclosed by a conducting wall (Figure 56). The background magnetic field and the plasma radial density profile are assumed to be uniform in space (0D). This boundary value problem hereafter is referred to as the "partially filled plasma waveguide" problem and is based on Swanson [123], Arnush [118], Hipp [124] and Cato [125].

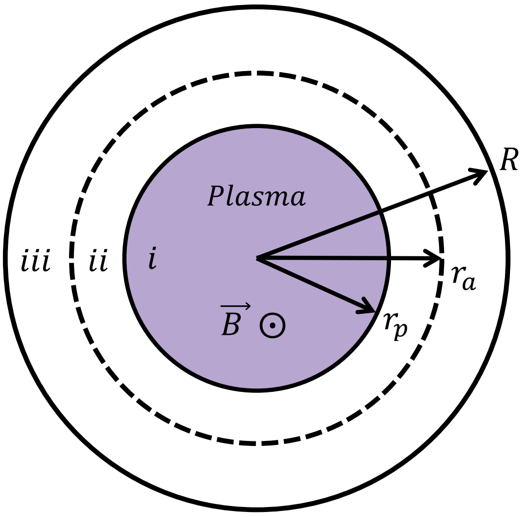

Figure 56. Cylindrical geometry of a partially filled plasma waveguide. The plasma edge and antenna surface current are located at $r = r_p$ and $r = r_a$ respectively. The conducting wall is located at $r = R$. The waveguide is divided into plasma volume (region *i*) and two vacuum layers (region *ii* and *iii*).

5.3.1 Governing equations

Electromagnetic fields are described in cylindrical coordinates and are assumed to (1) propagate in the axial "z" direction and to (2) form standing waves in both the radial "r" and azimuthal "ϕ" directions. The total field is described as a linear combination of axially propagating waves over a range of angular frequencies ω and axial wavenumbers κ. This can be expressed using a Fourier integral (Eq. 109) for the "sth" component of an arbitrary vector field $\underline{\boldsymbol{V}}$ (e.g. electric, magnetic or current density), where the parallel wavenumber κ is purely real. The scalar $\underline{V_s}$ (underlined) represents a field in real space, while V_s represent its Fourier transforms.

$$\underline{V_s}(r,\phi,z,t) = \frac{1}{2\pi}\iint_{-\infty}^{\infty} V_s(r,\phi,\kappa,\omega)\exp[i(\kappa z-\omega t)]\,d\kappa\,d\omega \quad s = r,\phi,z \qquad \text{Eq. 109}$$

Fourier transforming the 1st and 2nd of Maxwell's equations (Eq. 110) over κ and ω we obtain (Eq. 111-Eq. 116).

$$\nabla \times \underline{\boldsymbol{B}} = \mu_0 \frac{\partial \underline{\boldsymbol{D}}}{\partial t} \quad \underline{\boldsymbol{D}} = \underline{\boldsymbol{P}} + \epsilon_0 \underline{\boldsymbol{E}} \quad \nabla \times \underline{\boldsymbol{E}} = -\frac{\partial \underline{\boldsymbol{B}}}{\partial t} \qquad \text{Eq. 110}$$

$$(\nabla \times \boldsymbol{E})_r \rightarrow \qquad \frac{1}{r}\frac{\partial}{\partial\phi}E_z - i\kappa E_\phi = i\omega B_r \qquad \text{Eq. 111}$$

$$(\nabla \times \boldsymbol{E})_\phi \rightarrow \qquad i\kappa E_r - \frac{\partial}{\partial r}E_z = i\omega B_\phi \qquad \text{Eq. 112}$$

$$(\nabla \times \boldsymbol{E})_z \rightarrow \qquad \frac{1}{r}\frac{\partial}{\partial r}(rE_\phi) - \frac{1}{r}\frac{\partial}{\partial\phi}E_r = i\omega B_z \qquad \text{Eq. 113}$$

$$(\nabla \times \boldsymbol{B})_r \rightarrow \qquad \frac{1}{r}\frac{\partial}{\partial\phi}B_z - i\kappa B_\phi = -i\frac{\omega}{c^2}(SE_r - iDE_\phi) \qquad \text{Eq. 114}$$

$$(\nabla \times \boldsymbol{B})_\phi \rightarrow \qquad i\kappa B_r - \frac{\partial}{\partial r}B_z = -i\frac{\omega}{c^2}(iDE_r + SE_\phi) \qquad \text{Eq. 115}$$

$$(\nabla \times \boldsymbol{B})_z \rightarrow \qquad \frac{1}{r}\frac{\partial}{\partial r}(rB_\phi) - \frac{1}{r}\frac{\partial}{\partial\phi}B_r = -i\frac{\omega}{c^2}PE_z \qquad \text{Eq. 116}$$

Eq. 111-Eq. 116 can be combined to form a pair of coupled complex PDEs for B_z and E_z (Eq. 117 and Eq. 118), where $\nabla_\perp = \partial/\partial r\,\hat{\boldsymbol{r}} + r^{-1}\,\partial/\partial\phi\,\hat{\boldsymbol{\phi}}$ .The relevant coefficients can be found in Eq. 119 where "S", "D" and "P" are the cold dielectric tensor components as given in Eq. 160 to Eq. 165 (Appendix 5A). These equations can be decoupled into fourth order PDEs (Eq. 120) and for constant coefficients (no plasma radial gradients) it can be decomposed into a pair of Helmholtz equations as shown in Eq. 121, where the transverse wavenumber μ_n is defined by the bi-quadratic equation shown in Eq. 122. This dispersion relation is equivalent to that obtained from the cold dielectric tensor (Eq. 174, Appendix 5A). The effect of collisions and hence wave spatial damping, is included entirely in the definition of the cold dielectric tensor components "S", "D" and "P" (Eq. 160 to Eq. 165, Appendix 5A). In what follows, we provide solutions for the standing wavefields in the plasma volume (region *i*) and vacuum layers (region *ii* and *iii*).

$$c\nabla_{\perp}^{2}E_{z} + d\nabla_{\perp}^{2}B_{z} - i\omega B_{z} = 0 \tag{Eq. 117}$$

$$c\nabla_{\perp}^{2}B_{z} + q\nabla_{\perp}^{2}E_{z} + (i\beta_{3}/\omega)E_{z} = 0 \tag{Eq. 118}$$

$$a = -\frac{i\kappa\gamma}{\rho} \quad b = \frac{i\omega\beta_{2}}{\rho} \quad c = -\frac{i\kappa\beta_{2}}{\rho} \quad d = \frac{i\omega\gamma}{\rho}$$

$$p = -\frac{i}{\omega}\left(\frac{\kappa^{2}\beta_{2}}{\rho}\right) \quad q = -\frac{i}{\omega}\left(\frac{\beta_{1}\gamma - \beta_{2}^{2}}{\rho}\right) \tag{Eq. 119}$$

$$\beta_{1} = \frac{\omega^{2}}{c^{2}}S \quad \beta_{2} = \frac{\omega^{2}}{c^{2}}iD \quad \beta_{3} = \frac{\omega^{2}}{c^{2}}P \quad \gamma = \kappa^{2} - \beta_{1} \quad \rho = \gamma^{2} + \beta_{2}^{2}$$

$$\mathbb{A}\nabla_{\perp}^{4}\begin{bmatrix} B_{z} \\ E_{z} \end{bmatrix} + \mathbb{B}\nabla_{\perp}^{2}\begin{bmatrix} B_{z} \\ E_{z} \end{bmatrix} + \mathbb{C}\begin{bmatrix} B_{z} \\ E_{z} \end{bmatrix} = 0$$

$$\mathbb{A} = c^{2} - qd \quad \mathbb{B} = i\omega q - i(d\beta_{3}/\omega) \quad \mathbb{C} = -\beta_{3} \tag{Eq. 120}$$

$$(\nabla_{\perp}^{2} + \mu_{1}^{2})(\nabla_{\perp}^{2} + \mu_{2}^{2})\begin{bmatrix} B_{z} \\ E_{z} \end{bmatrix} = 0 \tag{Eq. 121}$$

$$SN_{\perp}^{4} + \left(N_{\parallel}^{2}[S + P] - [RL + PS]\right)N_{\perp}^{2} + P\left(N_{\parallel}^{2} - L\right)\left(N_{\parallel}^{2} - R\right) = 0$$

$$N_{\perp n} = \frac{\mu_{n}c}{\omega} \quad N_{\parallel} = \frac{\kappa c}{\omega} \tag{Eq. 122}$$

5.3.2 Plasma wavefields

Due to anisotropic nature of magnetized plasma two waves exist whose dispersion is given by the roots of Eq. 122. Each root is identified with subscript "n" from 1 to 2 and referred to as the "fast" and "slow" wave respectively. Subscript "n" from 3 to 8 are reserved for the waves in the vacuum gaps, namely, region II and III (Figure 56). In addition, all field quantities can be expressed as linear combinations of the parallel magnetic field B_z and its radial derivatives.

Parallel fields

From the PDEs in Eq. 117 and Eq. 118 it is clear that B_z and E_z must be linearly dependent (Eq. 123), where Φ is a constant. This property indicates that E_z is parallel and proportional to B_z. Substituting Eq. 123 and $\nabla_{\perp}^{2}E_{zn} = -\mu_{n}^{2}E_{zn}$ into the PDEs in Eq. 117 and Eq. 118 and adding them leads to a relationship between $\Phi_{\pm}$ and $\mu_{\pm}$ as shown in Eq. 124, where the relevant coefficients are shown in Eq. 119. Using separation of variables, the general solution to the "nth" root of Eq. 121 is given in Eq. 125. The total field in the plasma volume is given by the contribution of both "slow" and "fast" waves (Eq. 126).

$$E_z = \Phi B_z \qquad \text{Eq. 123}$$

$$\Phi = \frac{i\omega + (c+d)\mu_n^2}{i\beta_3/\omega - (c+q)\mu_n^2} \qquad \text{Eq. 124}$$

$$B_{zn}^i = \sum_{m=-\infty}^{\infty} A_{mn} J_m(\mu_n r)\, e^{im\phi} \quad E_{zn}^i = \sum_{m=-\infty}^{\infty} \Phi_n A_{mn} J_m(\mu_n r)\, e^{im\phi} \qquad \text{Eq. 125}$$

$$B_z^i = B_{z1} + B_{z2} \quad E_z^i = E_{z1} + E_{z2} \qquad \text{Eq. 126}$$

Transverse fields

Upon substitution of Eq. 123 into Maxwell's equations (Eq. 111 to Eq. 116) we obtain expressions for the standing transverse magnetic and electric fields as shown in Eq. 127 and Eq. 128 respectively. These expressions are valid in all three regions. The relevant coefficients are shown in Eq. 129 and Eq. 119.

$$B_{rn} = -\frac{1}{r}\frac{\partial B_{zn}}{\partial\phi} H_{an} - \frac{\partial B_{zn}}{\partial r} H_{bn}$$
$$B_{\phi n} = -\frac{1}{r}\frac{\partial B_{zn}}{\partial\phi} H_{bn} + \frac{\partial B_{zn}}{\partial r} H_{an} \qquad \text{Eq. 127}$$

$$E_{rn} = -\frac{1}{r}\frac{\partial B_{zn}}{\partial\phi} G_{an} + \frac{\partial B_{zn}}{\partial r} G_{bn}$$
$$E_{\phi n} = \frac{1}{r}\frac{\partial B_{zn}}{\partial\phi} G_{bn} + \frac{\partial B_{zn}}{\partial r} G_{an} \qquad \text{Eq. 128}$$

$$H_{an} = (q\Phi_n + c) \quad H_{bn} = (p\Phi_n - a)$$
$$G_{an} = (c\Phi_n + d) \quad G_{bn} = (a\Phi_n - b) \qquad \text{Eq. 129}$$

Region I basis function

The standing fields in the plasma (Eq. 127 to Eq. 128) can be described in terms of basis functions $\boldsymbol{v_{smn}}$ as shown in Eq. 130 for the "sth" component of an arbitrary vector $\boldsymbol{V}$. The subscript "n" represents a summation over the roots of Eq. 122. Roots 1 and 2 are referred to as the "fast" and "slow" waves respectively. A complete set of magnetic and electric field basis functions for the plasma volume applicable for $n = 1,2$ is shown in Eq. 131 and Eq. 132 respectively, where the coefficients H_n and G_n are defined as in Eq. 129. Basis function notation is used throughout this document in order to reduce the size of the expressions. For the interested reader, the fields and the basis functions for the vacuum (regions II and III) are presented in Appendix 5C of this chapter.

$$V_s = \sum_n \sum_{m=-\infty}^{\infty} A_{mn}\, \boldsymbol{v_{smn}}\, e^{im\phi} \quad s = r, \phi, z \tag{Eq. 130}$$

$$\begin{aligned} \boldsymbol{b_{rmn}} &= -H_{an}\frac{im}{r}J_m(\mu_n r) - H_{bn}\mu_n J_m'(\mu_n r) \\ \boldsymbol{b_{\phi mn}} &= H_{an}\mu_\pm J_m'(\mu_n r) - H_{bn}\frac{im}{r}J_m(\mu_n r) \\ \boldsymbol{b_{zmn}} &= J_m(\mu_n r) \end{aligned} \tag{Eq. 131}$$

$$\begin{aligned} \boldsymbol{e_{rmn}} &= G_{bn}\mu_\pm J_m'(\mu_n r) - G_{an}\frac{im}{r}J_m(\mu_n r) \\ \boldsymbol{e_{\phi mn}} &= G_{bn}\frac{im}{r}J_m(\mu_n r) + G_{an}\mu_n J_m'(\mu_n r) \\ \boldsymbol{e_{zmn}} &= \Phi_n J_m(\mu_n r) \end{aligned} \tag{Eq. 132}$$

5.3.3 RF antenna

In real space the antenna is modelled as a surface current located at a radius r_a (Eq. 133) and illustrated in Figure 56. Its geometry is modelled as a linear combination of infinitely long current sheets over a range of m, κ, ω values as described by the Fourier integral in Eq. 134. Therefore, the vector $\boldsymbol{K}_m$ defines the m, κ, ω spectra of the antenna surface current. In addition, we neglect the electrostatic fields from the antenna (Eq. 135) and hence the tangential currents are related in Fourier space through Eq. 136. In MAGPIE, a Half-turn Helical (HH) antenna is employed to excite helicon waves. Using reference [118], the Fourier transform in m, κ, ω space of a helical antenna is given by Eq. 137. The transform is zero for even "m" azimuthal numbers and finite for odd. The terms L, θ and $I(\omega)$ represent the antenna length, half the twist angle of the antenna[9] and the antenna current frequency spectrum respectively. For a single frequency the antenna current spectrum $I(\omega)$ is given by Eq. 138 and I_0 is the total antenna current in Amperes. The power spectrum of a 22 cm long Right handed HH antenna $(2\theta = \pi)$, $\underline{I} = \cos(\omega t)$ and $m = \pm 1$ azimuthal numbers is shown in Figure 57. From the figure it is clear that HH antennas have inherent directionality. Waves with positive helicity $(m = +ve)$ are launched parallel to the background magnetic field $(\kappa = +ve)$. Waves with negative helicity are launched antiparallel to the background magnetic field (dotted line Figure 57). The absence of $m = -1$ waves in helicon experiments is caused by the symmetry breaking effect of non-uniform radial density profiles as explained by Kamenski, Arnush and Schneider in [38], [118], [126] respectively. The 0D model herein described assumes uniform radial density profiles; hence, the $m = \pm 1$ asymmetry is not present.

$$\underline{\boldsymbol{J}}(r, \phi, z, t) = \delta(r - r_a)\underline{\boldsymbol{K}}(\phi, z, t) \qquad \text{Eq. 133}$$

$$\underline{\boldsymbol{K}}(\phi, z, t) = \frac{1}{2\pi} \iint_{-\infty}^{\infty} \left[\sum_{m=-\infty}^{\infty} \boldsymbol{K}_m(\kappa, \omega)\, e^{im\phi} \right] e^{i(\kappa z - \omega t)}\, d\kappa\, d\omega \qquad \text{Eq. 134}$$

$$\nabla \cdot \underline{\boldsymbol{J}} = 0 \qquad \text{Eq. 135}$$

$$K_{zm} = -\frac{m}{\kappa r_a} K_{\phi m} \qquad \text{Eq. 136}$$

---

[9] Positive/negative values of θ lead to Right/Left handed helical antennas.

$$K_{\phi m}(\kappa,\omega) = -I(\omega)\mathbb{I}(m,\kappa) \quad m = \pm 1,3,5\,\ldots \quad 2\theta = \pi$$

$$\mathbb{I}(m,\kappa) = \left[\frac{2}{\pi}\frac{\kappa L}{2m}\frac{sin(\kappa L/2 - m\theta)}{\kappa L/2 - m\theta}\right]$$

Eq. 137

$$I(\omega) = I_0\sqrt{2\pi}\left(\frac{\delta(\omega-\omega_0)+\delta(\omega+\omega_0)}{2}\right)$$

Eq. 138

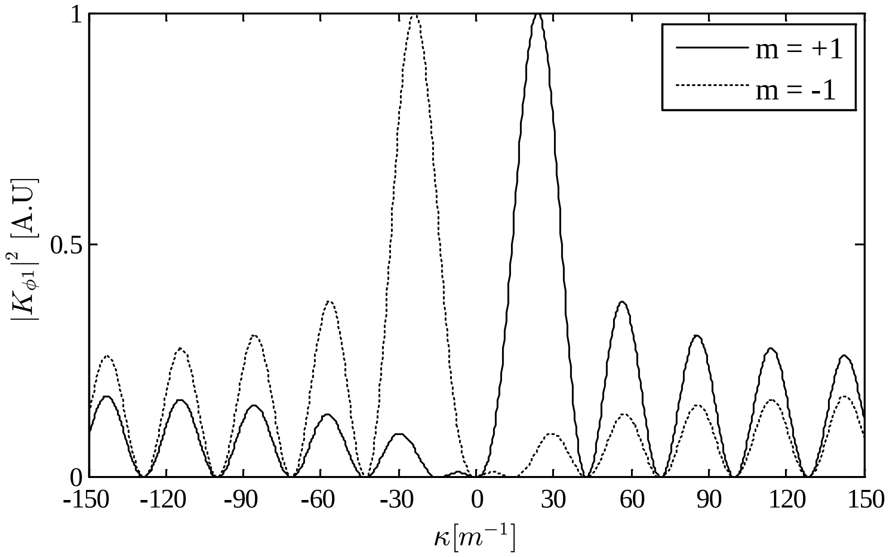

Figure 57. Normalized power spectrum of a Half-turn Helical (HH) antenna $(2\theta = \pi)$ as a function of parallel wavenumber κ , $m = \pm 1$ and $L = 22$ cm (Eq. 137). This spectrum corresponds to the antenna in MAGPIE.

5.3.4 Boundary conditions

To uniquely define the amplitudes A_{nm} for each wave we must impose boundary conditions on the fields for every azimuthal mode “m” and parallel wavenumber κ. At each boundary the tangential electric and magnetic fields must be continuous. However, the tangential magnetic field is discontinuous across the antenna surface current. In what follows, we use basis function notation for the plasma (region I) and vacuum (region II and III) fields. The boundary conditions to be imposed at $r = r_p$ and $r = r_a$ for every “m” azimuthal mode and parallel wavenumber κ are given in Eq. 139. The superscripts ii and iii indicate the region under consideration. This process leads to a determinate system of 8 equations (Eq. 140) which solves for A_{nm} from “n” equals 1 to 8. Similar methods are employed in references [124], [125], [127].

$$\begin{array}{ll}
\text{At } r = r_p & \text{At } r = r_a \\
E^{i}_{zm} - E^{ii}_{zm} = 0 & E^{ii}_{zm} - E^{iii}_{zm} = 0 \\
E^{i}_{\phi m} - E^{ii}_{\phi m} = 0 & E^{ii}_{\phi m} - E^{iii}_{\phi m} = 0 \\
B^{i}_{zm} - B^{ii}_{zm} = 0 & B^{ii}_{zm} - B^{iii}_{zm} = \mu_0 K_{m\phi} \\
B^{i}_{\phi m} - B^{ii}_{\phi m} = 0 & B^{ii}_{\phi m} - B^{iii}_{\phi m} = -\mu_0 K_{mz}
\end{array}$$

Eq. 139

$$\mathcal{B} \cdot \mathcal{A} = \mathcal{J}$$

$$\mathcal{B} = \begin{bmatrix}
e^{r_p}_{zm1} & e^{r_p}_{zm2} & 0 & 0 & -e^{r_p}_{zm5} & -e^{r_p}_{zm6} & 0 & 0 \\
e^{r_p}_{\phi m1} & e^{r_p}_{\phi m2} & -e^{r_p}_{\phi m3} & -e^{r_p}_{\phi m4} & -e^{r_p}_{\phi m5} & -e^{r_p}_{\phi m6} & 0 & 0 \\
b^{r_p}_{zm1} & b^{r_p}_{zm2} & -b^{r_p}_{zm3} & -b^{r_p}_{zm4} & 0 & 0 & 0 & 0 \\
b^{r_p}_{\phi m1} & b^{r_p}_{\phi m2} & -b^{r_p}_{\phi m3} & -b^{r_p}_{\phi m4} & -b^{r_p}_{\phi m5} & -b^{r_p}_{\phi m6} & 0 & 0 \\
0 & 0 & 0 & 0 & e^{r_a}_{zm5} & e^{r_a}_{zm6} & 0 & -e^{r_a}_{zm8} \\
0 & 0 & e^{r_a}_{\phi m3} & e^{r_a}_{\phi m4} & e^{r_a}_{\phi m5} & e^{r_a}_{\phi m6} & -e^{r_a}_{\phi m7} & -e^{r_a}_{\phi m8} \\
0 & 0 & b^{r_a}_{zm3} & b^{r_a}_{zm4} & 0 & 0 & -b^{r_a}_{zm7} & 0 \\
0 & 0 & b^{r_a}_{\phi m3} & b^{r_a}_{\phi m4} & b^{r_a}_{\phi m5} & b^{r_a}_{\phi m6} & -b^{r_a}_{\phi m7} & -b^{r_a}_{\phi m8}
\end{bmatrix}$$

Eq. 140

$$\mathcal{A} = \begin{bmatrix} A_{m1} \\ A_{m2} \\ A_{m3} \\ A_{m4} \\ A_{m5} \\ A_{m6} \\ A_{m7} \\ A_{m8} \end{bmatrix} \qquad \mathcal{J} = \mu_0 \begin{bmatrix} 0 \\ 0 \\ 0 \\ 0 \\ 0 \\ 0 \\ K_{m\phi} \\ -K_{mz} \end{bmatrix}$$

5.3.5 Wave excitation by an RF antenna

Solution of the boundary condition matrix (Eq. 140) yields the amplitude spectrum A_{mn} of the waves in the plasma waveguide excited by an arbitrary antenna. For example, Figure 58 shows the $m = +1$ amplitude spectrum of the fast wave ($n = 1$) excited by a HH antenna 22 cm in length for typical MAGPIE operating conditions. The asymmetry in the spectrum is expected since we have used a HH antenna (Figure 57). Notice that the spectrum peaks at certain axial wavenumbers which correspond to transverse eigenmode resonances of the waveguide. However, the dominant peaks do not necessarily correspond to peaks in the antenna power spectrum (Figure 57). From an experimental point of view, this means that the observed wavelength is not necessarily that which is impressed by the antenna’s largest spectral feature. This can be understood by noting that the plasma waves are the forced response to the antenna’s field; hence, from a mathematical point of view the forced response of the waveguide is the convolution of the forcing function (antenna spectra) with the system’s characteristic response (cavity resonances). To maximize wave excitation one should select an antenna whose largest spectral feature matches the plasma cavity resonances for a given set of conditions (plasma density, background magnetic field, RF frequency and radial geometry).

The plasma and vacuum wavefields can be calculated in real space by: (1) computing the amplitude spectrum A_{mn} for “n” from 1 to 8 for every κ with Eq. 140and (2) using Eq. 109 to inversely Fourier transform Eq. 130. For example, the $\underline{B_z}$ wavefield Fourier integral is given by Eq. 141. In the plasma volume (region i) the summation over “n” is from 1 to 2. In the vacuum regions the summation over “n” is from 3 to 6 and 7 to 8 for region ii and iii respectively.

$$\underline{B_{\boldsymbol{z}}}(r,\phi,z,t) = \sum_{n} \sum_{m=-\infty}^{\infty} \frac{1}{2\pi} \iint_{-\infty}^{\infty} A_{mn}\, \boldsymbol{b_{zmn}} \exp[i\,(\kappa z + m\phi - \omega t)]\, d\kappa\, d\omega \qquad \text{Eq. 141}$$

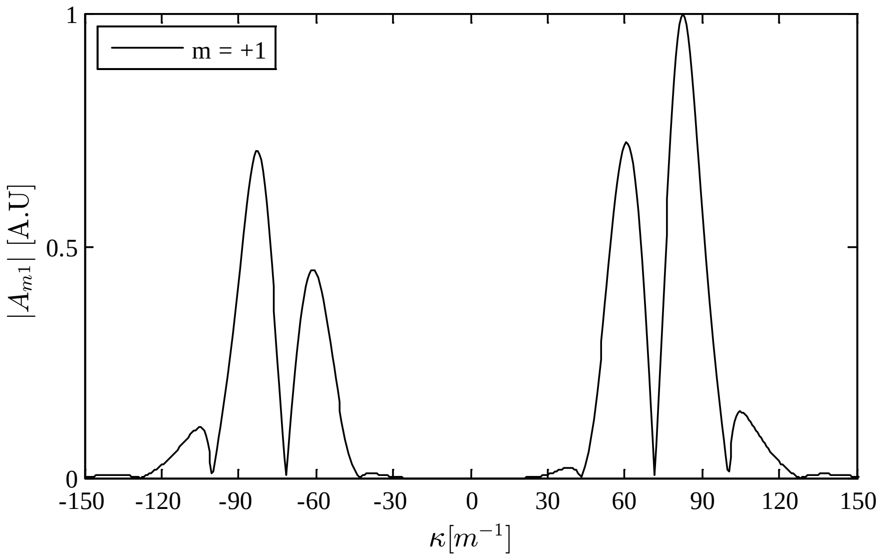

Figure 58, Normalized amplitude spectrum of the fast wave (n = 1) excited by HH antenna for typical conditions in MAGPIE: $n_e = 0.8\times 10^{19}$ m^{-3}, B_0 = 70 G, f = 7 MHz, T_e =3.5 eV, P_0 = 8 mTorr, Half-turn Helical antenna 22 cm long and 7 cm radius, Antenna current 180 A, plasma radius 4 cm. Both electron-ion and electron-neutral collisions are included.

5.3.6 Power deposition mechanism

Poynting's theorem in dielectric media

By modelling the plasma as a dielectric medium (section 5A.2), conservation of energy can be described by Poynting's theorem as shown in Eq. 142, where $\underline{\boldsymbol{S}}, \underline{\boldsymbol{D}}$, $\underline{\boldsymbol{E}}$ and $\underline{\boldsymbol{B}}$ represent the wave's Poynting vector (Eq. 143), electric displacement (Eq. 144), electric and magnetic field in real space respectively.

$$\nabla \cdot \underline{\boldsymbol{S}} + \frac{\partial}{\partial t}\left[\frac{\underline{\boldsymbol{E}} \cdot \underline{\boldsymbol{D}}}{2} + \frac{\underline{\boldsymbol{B}} \cdot \underline{\boldsymbol{B}}}{2\mu_0}\right] = 0 \qquad \text{Eq. 142}$$

Expanding the electric displacement as in Eq. 144 we re-express Poynting's theorem in a form more appropriate for our purposes (Eq. 145), where $\underline{\boldsymbol{J}}_p$ and U_{em} represent the polarization current and the electromagnetic wave energy density (Eq. 146) in real space respectively.

$$\underline{\boldsymbol{S}} = \frac{1}{\mu_0}\left(\underline{\boldsymbol{E}} \times \underline{\boldsymbol{B}}\right) \qquad \text{Eq. 143}$$

$$\underline{\boldsymbol{D}} = \underline{\boldsymbol{P}} + \epsilon_0 \underline{\boldsymbol{E}} \qquad \text{Eq. 144}$$

$$\underline{\boldsymbol{E}} \cdot \underline{\boldsymbol{J}}_p = -\frac{\partial U_{em}}{\partial t} - \nabla \cdot \underline{\boldsymbol{S}} \qquad \text{Eq. 145}$$

$$U_{em} = \frac{\epsilon_0}{2}\underline{\boldsymbol{E}} \cdot \underline{\boldsymbol{E}} + \frac{1}{2\mu_0}\underline{\boldsymbol{B}} \cdot \underline{\boldsymbol{B}} \qquad \text{Eq. 146}$$

The term $\underline{\boldsymbol{E}} \cdot \underline{\boldsymbol{J}}_{\boldsymbol{p}}$ describes the instantaneous rate of work per unit volume done on charged particles by the electric field of the wave. In a plasma waveguide operating in steady state conditions the time averaged rate of change of the electromagnetic energy density vanishes and the net power flux into the plasma $-\nabla \cdot \langle \underline{\boldsymbol{S}} \rangle$ is equal to the rate of work done by the polarization current $\langle \underline{\boldsymbol{E}} \cdot \underline{\boldsymbol{J}}_p \rangle$. In Appendix 5D, we derive expressions for calculating the specific power deposition $\langle \underline{\boldsymbol{E}} \cdot \underline{\boldsymbol{J}}_p \rangle$ in the plasma waveguide herein described in terms of the cold dielectric tensor components.

Appendix 5A. Waves in unbounded cold magnetized plasma

In this appendix, we provide a brief overview of the theory associated with waves in cold magnetized plasma. The following material is based on Stix [128], Lieberman [60], and Swanson [123].

5A.1 Conductivity

The cold plasma conductivity can be obtained by combining the current density (Eq. 147) and pressure-less momentum (Eq. 148) equations and using a 1st order perturbation expansion of the field quantities about their equilibrium (Eq. 149).

$$\underline{\boldsymbol{J}} = \sum_s q_s n_s \underline{\boldsymbol{V}}_s \tag*{Eq. 147}$$

$$m_s n_s \left[\frac{\partial}{\partial t}\underline{\boldsymbol{V}}_s + (\underline{\boldsymbol{V}}_s \cdot \boldsymbol{\nabla})\underline{\boldsymbol{V}}_s\right] = n_s q_s \left[\underline{\boldsymbol{E}} + \underline{\boldsymbol{V}}_s \times \underline{\boldsymbol{B}}\right] \tag*{Eq. 148}$$

$$\underline{\boldsymbol{E}} = \underline{\boldsymbol{E}}_{\boldsymbol{1}} \quad \underline{\boldsymbol{B}} = \underline{\boldsymbol{B}}_{\boldsymbol{0}} + \underline{\boldsymbol{B}}_{\boldsymbol{1}} \quad \underline{\boldsymbol{V}}_{\boldsymbol{s}} = \underline{\boldsymbol{V}}_{\boldsymbol{s1}} \tag*{Eq. 149}$$

The underline denotes field quantities in real space. The subscript “s”, “0” and “1” hereafter represents the particle species, equilibrium and wave part of the field quantities respectively. The quantities $\underline{\boldsymbol{E}}$, $\underline{\boldsymbol{B}}$, $\underline{\boldsymbol{V}}_s$, q_s , m_s and n_s represent the electric field, magnetic field, particle velocity, charge, mass and density of the sth particle species. Neglecting products of 1st order quantities, taking the Fourier transform[10] of Eq. 148, solving for $\boldsymbol{V}_{\boldsymbol{s}}$ as a function of $\boldsymbol{E}$ and using Eq. 147 we obtain Eq. 150. The total conductivity tensor is described as the sum of conductivities over all particle species as in Eq. 151.

$$\boldsymbol{J} = \bar{\bar{\boldsymbol{\sigma}}} \cdot \boldsymbol{E} \tag*{Eq. 150}$$

$$\bar{\bar{\boldsymbol{\sigma}}} = \sum_s \bar{\bar{\boldsymbol{\sigma}}}_{\boldsymbol{s}} \quad ; \quad \bar{\bar{\boldsymbol{\sigma}}}_{\boldsymbol{s}} = \omega_{ps}^2 \epsilon_0 \begin{bmatrix} \pi_{xx}^s & \pi_{xy}^s & 0 \\ -\pi_{xy}^s & \pi_{yy}^s & 0 \\ 0 & 0 & \pi_{zz}^s \end{bmatrix}$$

$$\pi_{xx}^s = \pi_{yy}^s = -\frac{i\omega}{\Omega_s^2 - \omega^2} \quad \pi_{xy}^s = \frac{\Omega_s}{\Omega_s^2 - \omega^2} \quad \pi_{zz}^s = \frac{i}{\omega} \quad \Omega_s = \frac{q_s B_0}{m_s} \tag*{Eq. 151}$$

---

[10] This process is equivalent to assuming that the field quantities are given by a linear combination of complex plane waves of the form $A_n \exp(i[\boldsymbol{k}_{\boldsymbol{n}} \cdot \boldsymbol{r} - \omega t])$.

The terms Ω_s and ω represent the signed cyclotron frequency[11] of the sth species and the angular frequency respectively. To include the momentum transfer collision term ν replace all $\omega \rightarrow \omega_*$ in Eq. 151 where $\omega_* = \omega + i\nu$.

5A.2 The cold dielectric tensor

The plasma is modelled as a cold, uniform, unbounded dielectric which is permeated by a uniform and static background magnetic field, which lies along the z direction ($\underline{\boldsymbol{B}}_0 = \underline{B}_0\hat{\boldsymbol{z}}$). Thermal particle motion is neglected (cold plasma) and thus charged particles motion occurs only as oscillations about their equilibrium position (polarization). The cold plasma approximation neglects wave-particle interaction and is valid only when phase velocities are much greater than particle thermal velocities. First order field quantities are related to each other through Maxwell's equations (Eq. 152 and Eq. 153). Henceforth, we will omit the subscript "1" from first order field quantities.

$$\nabla \times \underline{\boldsymbol{B}} = \mu_o \left(\underline{\boldsymbol{J}} + \epsilon_0 \frac{\partial}{\partial t} \underline{\boldsymbol{E}} \right) \qquad \text{Eq. 152}$$

$$\nabla \times \underline{\boldsymbol{E}} = -\frac{\partial}{\partial t} \underline{\boldsymbol{B}} \qquad \text{Eq. 153}$$

The charged particle current density $\underline{\boldsymbol{J}}$ in Eq. 152 is composed of (a) the external $\underline{\boldsymbol{J}}_{ext}$ and (b) polarization current $\underline{\boldsymbol{J}}_p$ contribution (Eq. 154), where $\underline{\boldsymbol{P}}$ represents the polarization vector. Since polarization manifests itself as charge displacement caused by the applied field, it can be modelled as a linear forced oscillator. As a result, the polarization vector is given by the convolution integral of Eq. 155, where $\underline{\overline{\overline{\boldsymbol{\chi}}}}$ and $\underline{\boldsymbol{E}}$ are the susceptibility tensor and electric field vector in real space respectively and the term "t" represents time.

$$\underline{\boldsymbol{J}} = \underline{\boldsymbol{J}}_{ext} + \underline{\boldsymbol{J}}_p \quad \underline{\boldsymbol{J}}_p = \frac{\partial}{\partial t} \underline{\boldsymbol{P}} \qquad \text{Eq. 154}$$

$$\underline{\boldsymbol{P}} = \epsilon_0 \int_0^t \underline{\overline{\overline{\boldsymbol{\chi}}}}(t-\tau) \cdot \underline{\boldsymbol{E}}(\tau)\, d\tau \qquad \text{Eq. 155}$$

Taking the Fourier transform of the polarization vector (Eq. 155) the polarization current can be written as in Eq. 156. Using Eq. 150 we recognize that the conductivity and susceptibility tensors are related as in Eq. 157. The importance of this equation is the connection between the plasma susceptibility and charged particle motion.

---

[11] The sign of the cyclotron frequency is that of the charge of the particle species considered.

$$\boldsymbol{J}_p = -i\omega\epsilon_0\bar{\bar{\boldsymbol{\chi}}}\cdot\boldsymbol{E} \qquad \text{Eq. 156}$$

$$\bar{\bar{\boldsymbol{\sigma}}} = -i\omega\epsilon_0\bar{\bar{\boldsymbol{\chi}}} \qquad \text{Eq. 157}$$

Taking the Fourier transform of Eq. 152 and using Eq. 156 we obtain Eq. 158. Here the quantity $\bar{\bar{\boldsymbol{\epsilon}}}$ is the cold plasma dielectric tensor and together with Eq. 157 can be written as in Eq. 159. Hereafter term $\boldsymbol{k}$ represents the total wave vector. Substituting the collisional conductivity tensor (Eq. 151) into Eq. 159 and using Stix's notation [128] the collisional cold dielectric tensor in magnetized plasma is given by Eq. 160 to Eq. 165. Notice that Ω_s changes sign with q_s but ω_{ps}^2 does not.

$$i\boldsymbol{k}\times\boldsymbol{B} = -i\omega\mu_o\epsilon_0\bar{\bar{\boldsymbol{\epsilon}}}\cdot\boldsymbol{E} + \mu_0\boldsymbol{J}_{ext} \qquad \text{Eq. 158}$$

$$\bar{\bar{\boldsymbol{\epsilon}}} = \bar{\bar{\boldsymbol{I}}} + i\frac{\bar{\bar{\boldsymbol{\sigma}}}}{\omega\epsilon_0} \qquad \text{Eq. 159}$$

$$\bar{\bar{\boldsymbol{\epsilon}}} = \begin{bmatrix} S & -iD & 0 \\ iD & S & 0 \\ 0 & 0 & P \end{bmatrix} \qquad \text{Eq. 160}$$

$$S = \frac{1}{2}(R+L) \quad D = \frac{1}{2}(R-L) \qquad \text{Eq. 161}$$

$$R = 1 - \sum_s \frac{\omega_{ps}^2}{\omega(\omega_* + \Omega_s)} \qquad \text{Eq. 162}$$

$$L = 1 - \sum_s \frac{\omega_{ps}^2}{\omega(\omega_* - \Omega_s)} \qquad \text{Eq. 163}$$

$$P = \sum_s 1 - \frac{\omega_{ps}^2}{\omega\omega_*} \qquad \text{Eq. 164}$$

$$\omega_{ps}^2 = \frac{n_{s0}q_s^2}{m_s\epsilon_0} \quad \Omega_s = \frac{q_sB_0}{m_s} \quad \omega_* = \omega + i\nu_s \qquad \text{Eq. 165}$$

5A.3 Dispersion relation

Taking the Fourier transform of the 1st and 2nd Maxwell's equations (Eq. 152 and Eq. 153) and combining them to eliminate $\boldsymbol{B}$ leads to the vector wave equation shown in Eq. 166, with the external current density as the source. This wave equation describes how individual Fourier components in a wave packet propagate in magnetized plasma.

$$\boldsymbol{k}\times(\boldsymbol{k}\times\boldsymbol{E})+\frac{\omega^2}{c^2}\bar{\bar{\boldsymbol{\epsilon}}}\cdot\boldsymbol{E}=-i\omega\mu_0\boldsymbol{J}_{ext} \qquad \text{Eq. 166}$$

Natural oscillations

To describe the natural modes of oscillation of magnetized plasma we set $\boldsymbol{J}_{ext}=0$. Using the refractive index, the wave equation (Eq. 166) may be written as in Eq. 167. Using vector identities and dyadic notation, Eq. 167 is more compactly expressed as in Eq. 168.

$$\boldsymbol{n}\times(\boldsymbol{n}\times\boldsymbol{E})+\bar{\bar{\boldsymbol{\epsilon}}}\cdot\boldsymbol{E}=0 \quad \boldsymbol{n}=\boldsymbol{k}c/\omega \qquad \text{Eq. 167}$$

$$\bar{\bar{\boldsymbol{D}}}\cdot\boldsymbol{E}=0 \qquad \bar{\bar{\boldsymbol{D}}}=\boldsymbol{nn}-n^2\bar{\bar{\boldsymbol{I}}}+\bar{\bar{\boldsymbol{\epsilon}}} \qquad \text{Eq. 168}$$

If we represent the angle between the background magnetic field $\boldsymbol{B_0}$ and $\boldsymbol{n}$ as θ, assume a Cartesian coordinate system and restrict $\boldsymbol{n}$ to be in the x,z plane, Eq. 168 can be written as in Eq. 169. Since $\boldsymbol{E}\neq 0$ the tensor $\bar{\bar{\boldsymbol{D}}}$ cannot have an inverse. This condition is equivalent to setting the determinant of $\bar{\bar{\boldsymbol{D}}}$ (Eq. 170-Eq. 171) equal to zero which yields a biquadratic equation whose solution gives the dispersion relation (Eq. 172). Solution of the dispersion relation (Eq. 172) yields a pair of refractive indices.

$$\begin{pmatrix} S-n^2\cos^2\theta & -iD & n^2\cos\theta\sin\theta \\ iD & S-n^2 & 0 \\ n^2\cos\theta\sin\theta & 0 & P-n^2\sin^2\theta \end{pmatrix}\begin{pmatrix} E_x \\ E_y \\ E_z \end{pmatrix}=0 \qquad \text{Eq. 169}$$

$$\left\|\bar{\bar{\boldsymbol{D}}}\right\|=An^4-Bn^2+C \qquad \text{Eq. 170}$$

$$A=S\sin^2\theta+P\cos^2\theta \quad B=RL\sin^2\theta+PS(1+\cos^2\theta)$$
$$C=PRL \qquad \text{Eq. 171}$$

$$n^2=\frac{B\pm\sqrt{B^2-4AC}}{2A} \qquad \text{Eq. 172}$$

Upon substitution of Eq. 173 into the dispersion relation Eq. 172 leads to an equivalent dispersion relation but in written in terms of transverse and parallel refractive indices (Eq. 174), where the terms S,P, R and L are the components of the cold dielectric tensor as given in Eq. 161 to Eq. 165. In cylindrically bounded plasma, wave dispersion is more conveniently expressed using Eq. 174, e.g. propagation parallel and perpendicular to the background magnetic field.

$$n_\perp = n\sin\theta \quad n_\parallel = n\cos\theta \qquad \text{Eq. 173}$$

$$\begin{gathered} a n_\perp^4 - n_\perp^2 b + c = 0 \\ a = S \quad b = (RL + PS) - n_\parallel^2 (P + S) \quad c = P\left(n_\parallel^2 - R\right)\left(n_\parallel^2 - L\right) \end{gathered} \qquad \text{Eq. 174}$$

In the collisionless regime the refractive index (Eq. 172) becomes infinite when its denominator vanishes. Under such conditions the phase velocity approaches zero and the propagation angle is given by Eq. 175. This restriction on the propagation angle θ is referred to as the phase velocity resonance cone. In section Appendix 5B, we show that as the wave approaches the resonance cone it becomes increasingly electrostatic and in the presence of collisions is strongly damped.

$$\tan^2\theta = -P/S \qquad \text{Eq. 175}$$

Forced oscillations

Forced oscillations are described when $\boldsymbol{J}_{ext} \neq 0$ and Eq. 168 can be written as in Eq. 176. In Fourier space, the field amplitudes are determined by taking the inverse[12] of $\bar{\bar{\boldsymbol{D}}}$ as shown in Eq. 177, where $\bar{\bar{\boldsymbol{D}}}_a$ is the adjugate matrix of $\bar{\bar{\boldsymbol{D}}}$. Notice that the denominator of $\boldsymbol{E}$ in Eq. 177 is proportional to the dispersion relation $\left\|\bar{\bar{\boldsymbol{D}}}\right\|$ (Eq. 170). Hence, whenever the external current drives plasma waves that satisfy the dispersion relation (Eq. 172) the amplitude of $\boldsymbol{E}$ grows very large. This event is referred to as “resonance coupling” [128] and is the basis of plasma heating using electromagnetic waves in bounded plasma. In addition, it can be seen that the excited $\boldsymbol{E}$ waves are (1) determined by the $\boldsymbol{k}$ and ω spectra of the external current $\boldsymbol{J}_{ext}$ and (2) modulated by the inverse of $\bar{\bar{\boldsymbol{D}}}$ which describes the characteristic behaviour of the plasma. In the presence of damping $\left\|\bar{\bar{\boldsymbol{D}}}\right\|$ can never be identically zero; therefore, $\boldsymbol{E}$ is always finite.

---

[12] The inverse of a matrix can be written as: $A^{-1} = A_a/\|A\|$ where A_a and $\|A\|$ are the adjugate matrix and determinant of A respectively.

$$\overline{\overline{\boldsymbol{D}}} \cdot \boldsymbol{E} = -\frac{i}{\omega \epsilon_0} \boldsymbol{J}_{ext} \qquad \text{Eq. 176}$$

$$\boldsymbol{E} = -\left(\frac{i}{\omega \epsilon_0 \left\| \overline{\overline{\boldsymbol{D}}} \right\|}\right) \overline{\overline{\boldsymbol{D}}}_a \cdot \boldsymbol{J}_{ext} \qquad \text{Eq. 177}$$

Relation between real and imaginary wavenumbers

The coefficients A, B and C from the dispersion relation in Eq. 172 are in general complex. With the inclusion of the collision term in the dielectric tensor (Eq. 160 - Eq. 165) the refractive indices (total, transverse and parallel) are also complex in general; that is, they have propagating and damping components. However, since the propagation angle θ is a real quantity, the ratio between complex wavenumbers must also be real (Eq. 178). This requirement constrains the values of real and imaginary wavenumbers as in Eq. 179 where subscripts "R" and "I" denote real and imaginary components respectively. It will be shown later that Eq. 179 allows calculating axial damping of waves whenever the fundamental parallel wavenumber is known. This situation arises in experiment, where the parallel wavelength of the wave is easily measured and one needs to estimate the attenuation length.

$$\frac{\kappa}{k} = \cos\theta \quad \frac{\mu}{k} = \sin\theta \qquad \text{Eq. 178}$$

$$\frac{\kappa_R}{\kappa_I} = \frac{\mu_R}{\mu_I} = \frac{k_R}{k_I} \qquad \text{Eq. 179}$$

Appendix 5B. Electrostatic and Electromagnetic content of plasma waves:

Waves propagating in magnetized plasma at an arbitrary angle θ cannot be separated into purely electrostatic (ES) or purely electromagnetic (EM) modes but exist as a combination of them. Determining which mode (ES or EM) is dominant for a given set of conditions is important because it is indicative of the strength of wave damping. Waves with large ES content are very strongly damped since most of the kinetic energy is stored in charge particle motion which is strongly susceptible to collisions; on the other hand, EM waves are weakly damped since most of the energy is stored in the magnetic field, which cannot do work directly.

We express the electric field in terms of longitudinal and transverse components (Eq. 180), substitute it into the wave equation (Eq. 166), neglect the source term and express the solution as in Eq. 181. Expanding the dielectric tensor in dyadic form (Eq. 182) and operating the dot products in Cartesian coordinates leads to Eq. 183. This expression describes the relative electrostatic/magnetic content of a wave in magnetized cold plasma as a function of (a) plasma conditions and (b) propagation angle. Notice that whenever Eq. 175 is satisfied (i.e. propagation at the resonance cone angle) the denominator in Eq. 183 vanishes and leads to a purely electrostatic wave. In the presence of collisions, the denominator of Eq. 183 cannot vanish; hence, the ratio $E_{\parallel}/E_{\perp}$ is finite and complex in general.

$$\boldsymbol{E} = E_{\parallel}\hat{\boldsymbol{k}} + E_{\perp}\hat{\boldsymbol{\phi}} \qquad \text{Eq. 180}$$

$$\frac{E_{\parallel}}{E_{\perp}} = -\frac{\hat{\boldsymbol{k}} \cdot \bar{\bar{\boldsymbol{\epsilon}}} \cdot \hat{\boldsymbol{\phi}}}{\hat{\boldsymbol{k}} \cdot \bar{\bar{\boldsymbol{\epsilon}}} \cdot \hat{\boldsymbol{k}}} \qquad \text{Eq. 181}$$

$$\bar{\bar{\boldsymbol{\epsilon}}} = S\,\hat{\boldsymbol{x}}\hat{\boldsymbol{x}} + S\,\hat{\boldsymbol{y}}\hat{\boldsymbol{y}} + P\,\hat{\boldsymbol{z}}\hat{\boldsymbol{z}} - iD\,\hat{\boldsymbol{x}}\hat{\boldsymbol{y}} + iD\,\hat{\boldsymbol{y}}\hat{\boldsymbol{x}} \qquad \text{Eq. 182}$$

$$\frac{E_{\parallel}}{E_{\perp}} = \frac{(P-S)\cos\theta\sin\theta}{S\sin^2\theta + P\cos^2\theta} \qquad \text{Eq. 183}$$

Appendix 5C. Vacuum wavefields

The vacuum region is divided into two spaces (Figure 56); namely, region *ii* and region *iii*. In what follows we provide solution to the vacuum wavefields.

5C.1 Parallel fields

In both vacuum regions the dielectric tensor components 'S", "P" and "D" take the values 1, 1 and 0 respectively. The coefficients in Eq. 119 are reduced to those shown in Eq. 184. Notice that because "c" vanishes the electric and magnetic wavefields are no longer coupled as in the plasma volume through Eq. 123 and Eq. 124.

$$\gamma = \kappa^2 - k_0^2 \quad \beta_1 = k_0^2 \quad \beta_2 = 0 \quad \beta_3 = k_0^2 \quad \rho = \gamma^2 \quad k_0 = \omega/c$$
$$a = -\frac{i\kappa}{\gamma} \quad b = 0 \quad c = 0 \quad d = \frac{i\omega}{\gamma} \quad q = -\frac{i}{\omega}\left(\frac{k_0^2}{\gamma}\right) \quad p = 0 \qquad \text{Eq. 184}$$

This allows us to express Eq. 117 and Eq. 118 as two independent Helmholtz equations with single roots each as shown in Eq. 185.

$$(\nabla_\perp^2 - \mu_v^2)\begin{bmatrix} B_z \\ E_z \end{bmatrix} = 0 \quad \mu_v^2 = \kappa^2 - k_0^2 \qquad \text{Eq. 185}$$

The general solution to Eq. 185 for region *ii* is given by Eq. 186.

$$B_z^{ii} = \sum_{m=-\infty}^{\infty} A_{3m} K_m(\mu_v r) e^{im\phi} + \sum_{m=-\infty}^{\infty} A_{4m} I_m(\mu_v r) e^{im\phi}$$
$$E_z^{ii} = \sum_{m=-\infty}^{\infty} A_{5m} K_m(\mu_v r) e^{im\phi} + \sum_{m=-\infty}^{\infty} A_{6m} I_m(\mu_v r) e^{im\phi} \qquad \text{Eq. 186}$$

Moreover, at the conducting wall $(r = R)$ the tangential electric fields vanish and the general solution to Eq. 185 in region *iii* can be expressed as in Eq. 187 and Eq. 188.

$$B_z^{iii} = \sum_{m=-\infty}^{\infty} A_{7m} S_{7m} e^{im\phi} \quad E_z^{iii} = \sum_{m=-\infty}^{\infty} A_{8m} S_{8m} e^{im\phi} \qquad \text{Eq. 187}$$

$$S_{8m} = \left[\frac{K_m(\mu_v r) I_m(\mu_v R) - K_m(\mu_v R) I_m(\mu_v r)}{I_m(\mu_v R)}\right]$$
$$P_{8m} = \left[\frac{K'_m(\mu_v r) I_m(\mu_v R) - K_m(\mu_v R) I'_m(\mu_v r)}{I_m(\mu_v R)}\right] \qquad \text{Eq. 188}$$

$$S_{7m} = \left[\frac{K_m(\mu_v r)I'_m(\mu_v R) - K'_m(\mu_v R)I_m(\mu_v r)}{I'_m(\mu_v R)}\right]$$

$$P_{7m} = \left[\frac{K'_m(\mu_v r)I'_m(\mu_v R) - K'_m(\mu_v R)I'_m(\mu_v r)}{I'_m(\mu_v R)}\right]$$

5C.2 Transverse fields

Substituting the coefficients from Eq. 184 into Eq. 127-Eq. 129, the standing transverse magnetic and electric fields in both vacuum regions are given by Eq. 189 and Eq. 190 respectively.

$$B_r = \left(-\frac{m}{r\omega}\frac{k_0^2}{\mu_v^2}\right)E_z + \left(-\frac{i\kappa}{\mu_v^2}\right)\frac{\partial B_z}{\partial r} \quad B_\phi = \left(\frac{m\kappa}{r\mu_v^2}\right)B_z + \left(-\frac{ik_0^2}{\omega\mu_v^2}\right)\frac{\partial E_z}{\partial r} \qquad \text{Eq. 189}$$

$$E_r = \left(\frac{m\omega}{\mu_v^2 r}\right)B_z + \left(-\frac{i\kappa}{\mu_v^2}\right)\frac{\partial E_z}{\partial r} \quad E_\phi = \left(\frac{m\kappa}{\mu_v^2 r}\right)E_z + \left(\frac{i\omega}{\mu_v^2}\right)\frac{\partial B_z}{\partial r} \qquad \text{Eq. 190}$$

5C.3 Region II basis function

Substituting Eq. 186 into Eq. 189-Eq. 190 allows us to express the transverse fields in region *ii* in terms of basis functions $\boldsymbol{v}_{smn}$ in a form similar to Eq. 130 for the "s^th^" component of an arbitrary vector $\boldsymbol{V}$. The summation is over $n = 3,4,5,6$. A complete set of basis functions for region *ii* vacuum layer is shown in Eq. 191 and Eq. 192 for the magnetic and electric field respectively.

$$\begin{array}{llll}
\boldsymbol{b_{rm3}} = \left(-\dfrac{i\kappa}{\mu_v}\right) K'_m(\mu_v r) & \boldsymbol{b_{rm4}} = \left(-\dfrac{i\kappa}{\mu_v}\right) I'_m(\mu_v r) & \boldsymbol{b_{rm5}} = \left(-\dfrac{m}{r\omega}\dfrac{k_0^2}{\mu_v^2}\right) K_m(\mu_v r) & \boldsymbol{b_{rm6}} = \left(-\dfrac{m}{r\omega}\dfrac{k_0^2}{\mu_v^2}\right) I_m(\mu_v r) \\[2ex]
\boldsymbol{b_{\phi m3}} = \left(\dfrac{m\kappa}{r\mu_v^2}\right) K_m(\mu_v r) & \boldsymbol{b_{\phi m4}} = \left(\dfrac{m\kappa}{r\mu_v^2}\right) I_m(\mu_v r) & \boldsymbol{b_{\phi m5}} = \left(-\dfrac{ik_0^2}{\omega\mu_v}\right) K'_m(\mu_v r) & \boldsymbol{b_{\phi m6}} = \left(-\dfrac{ik_0^2}{\omega\mu_v}\right) I'_m(\mu_v r) \\[2ex]
\boldsymbol{b_{zm3}} = K_m(\mu_v r) & \boldsymbol{b_{zm4}} = I_m(\mu_v r) & \boldsymbol{b_{zm5}} = 0 & \boldsymbol{b_{zm6}} = 0
\end{array}$$

Eq. 191

$$\begin{array}{llll}
\boldsymbol{e_{rm3}} = \left(\dfrac{m\omega}{r\mu_v^2}\right) K_m(\mu_v r) & \boldsymbol{e_{rm4}} = \left(\dfrac{m\omega}{r\mu_v^2}\right) I_m(\mu_v r) & \boldsymbol{e_{rm5}} = \left(-\dfrac{i\kappa}{\mu_v}\right) K'_m(\mu_v r) & \boldsymbol{e_{rm6}} = \left(-\dfrac{i\kappa}{\mu_v}\right) I'_m(\mu_v r) \\[2ex]
\boldsymbol{e_{\phi m3}} = \left(\dfrac{i\omega}{\mu_v}\right) K'_m(\mu_v r) & \boldsymbol{e_{\phi m4}} = \left(\dfrac{i\omega}{\mu_v}\right) I'_m(\mu_v r) & \boldsymbol{e_{\phi m5}} = \left(\dfrac{m\kappa}{r\mu_v^2}\right) K_m(\mu_v r) & \boldsymbol{e_{\phi m6}} = \left(\dfrac{m\kappa}{r\mu_v^2}\right) I_m(\mu_v r) \\[2ex]
\boldsymbol{e_{zm3}} = 0 & \boldsymbol{e_{zm4}} = 0 & \boldsymbol{e_{zm5}} = K_m(\mu_v r) & \boldsymbol{e_{zm6}} = I_m(\mu_v r)
\end{array}$$

Eq. 192

5C.4 Region III basis function

Substituting Eq. 187 into Eq. 189-Eq. 190 allows us to express the transverse fields in region *iii* in terms of basis functions $\boldsymbol{v_{smn}}$ in a form similar to Eq. 130 for the "sth" component of an arbitrary vector $\boldsymbol{V}$. The summation is over n = 7, 8. A complete set of basis functions for region *iii* vacuum layer is shown in Eq. 193 and Eq. 194 for the magnetic and electric field respectively.

$$\boldsymbol{b_{rm7}} = \left(-\frac{i\kappa}{\mu_v}\right)P_{7m} \qquad \boldsymbol{b_{rm8}} = \left(-\frac{m}{r\omega}\frac{k_0^2}{\mu_v^2}\right)S_{8m}$$

$$\boldsymbol{b_{\phi m7}} = \left(\frac{m\kappa}{r\mu_v^2}\right)S_{7m} \qquad \boldsymbol{b_{\phi m8}} = \left(-\frac{i}{\omega}\frac{k_0^2}{\mu_v}\right)P_{8m} \qquad \text{Eq. 193}$$

$$\boldsymbol{b_{zm7}} = S_{7m} \qquad \boldsymbol{b_{zm8}} = 0$$

$$\boldsymbol{e_{rm7}} = \left(\frac{m\omega}{\mu_v^2 r}\right)S_{7m} \qquad \boldsymbol{e_{rm8}} = \left(-\frac{i\kappa}{\mu_v}\right)P_{8m}$$

$$\boldsymbol{e_{\phi m7}} = \left(i\frac{\omega}{\mu_v}\right)P_{7m} \qquad \boldsymbol{e_{\phi m8}} = \left(\frac{m\kappa}{r\mu_v^2}\right)S_{8m} \qquad \text{Eq. 194}$$

$$\boldsymbol{e_{zm7}} = 0 \qquad \boldsymbol{e_{zm8}} = S_{8m}$$

Appendix 5D. Power deposition and heat transport in cold plasma

5D.1 RF power deposition

In the analysis of the plasma waveguide herein presented, we are interested in RF heating at a single frequency; therefore, the antenna current and its frequency spectrum are given by Eq. 195.

$$\underline{I}(t) = I_0\, cos(\omega_0 t) \quad I(\omega) = I_0\sqrt{2\pi}\left(\frac{\delta(\omega-\omega_0)+\delta(\omega+\omega_0)}{2}\right) \tag*{Eq. 195}$$

Solving the plasma waveguide BVP reveals that the antenna current frequency spectrum $I(\omega)$exists as a multiplication factor in all Fourier transforms. By extracting this factor we can re-express the Fourier transform of an arbitrary vector $\underline{\boldsymbol{V}}$ and the antenna current spectrum as in Eq. 196.

$$\boldsymbol{V}(r,\phi,\kappa,\omega) = \boldsymbol{V}'(r,\phi,\kappa,\omega)\sqrt{2\pi}\left(\frac{\delta(\omega-\omega_0)+\delta(\omega+\omega_0)}{2}\right) \qquad I(\omega) = I_0 \tag*{Eq. 196}$$

Hereafter we omit the explicit (r,ϕ) notation in all Fourier transform pairs in this analysis. Substitution of Eq. 196 into the inverse Fourier transform integral (Eq. 109) and using the sifting property of the Dirac delta function leads to an expression for vector fields in real space (Eq. 197).

$$\underline{\boldsymbol{V}}(z,t) = \underline{\boldsymbol{V}}'(z,\omega_0)\left[\frac{e^{-i\omega_0 t}}{2}\right] + \underline{\boldsymbol{V}}'(z,-\omega_0)\left[\frac{e^{i\omega_0 t}}{2}\right] \tag*{Eq. 197}$$

Since $\underline{\boldsymbol{V}}(z,t)$ must be purely real, it implies Eq. 198, where the superscript "*" indicates complex conjugation.

$$\underline{\boldsymbol{V}}'(z,-\omega_0) = \underline{\boldsymbol{V}}'^{*}(z,\omega_0) \tag*{Eq. 198}$$

As a result, we can express an arbitrary vector field $\underline{\boldsymbol{V}}$ in real space as in Eq. 199, where $\underline{\boldsymbol{V'}}$ is given by Eq. 200**.**

$$\underline{\boldsymbol{V}}(z,t) = \frac{\underline{\boldsymbol{V}}'(z,\omega_0)e^{-i\omega_0 t} + \underline{\boldsymbol{V}}'^{*}(z,\omega_0)e^{i\omega_0 t}}{2} \tag*{Eq. 199}$$

$$\underline{\boldsymbol{V}}'(z,\omega_0) = \frac{1}{\sqrt{2\pi}}\int_{-\infty}^{\infty}\boldsymbol{V}'(\kappa,\omega_0)\ e^{i\kappa z}d\kappa \tag*{Eq. 200}$$

In the section entitled “Poynting’s theorem in dielectric media”, it was stated that the power deposition mechanism is dominated by the rate of work done by the polarization current. Using Eq. 199 and Eq. 201 the time averaged power per unit volume deposited by the polarization current can be written as in Eq. 202.

$$\langle f \rangle = \frac{1}{T}\int_0^T f\,dt \quad T = \frac{2\pi}{\omega} \qquad \text{Eq. 201}$$

$$\langle \underline{\boldsymbol{E}} \cdot \underline{\boldsymbol{J_p}} \rangle = \frac{1}{4}\left(\underline{\boldsymbol{E}}'^{*} \cdot \underline{\boldsymbol{J}_{\boldsymbol{p}}'} + \underline{\boldsymbol{E}}' \cdot \underline{\boldsymbol{J}_{\boldsymbol{p}}'}^{*} \right) \qquad \text{Eq. 202}$$

Using Eq. 200, the Fourier transform of the polarization current (Eq. 203) and the tensor property in Eq. 204, the specific power deposition can be written as Eq. 205.

$$\boldsymbol{J}_{\boldsymbol{p}}'(\kappa, \omega_0) = \overline{\overline{\boldsymbol{\sigma}}}(\omega_0) \cdot \boldsymbol{E}'(\kappa, \omega_0) \qquad \text{Eq. 203}$$

$$\underline{\boldsymbol{E}}' \cdot \overline{\overline{\boldsymbol{\sigma}}}^{*} \cdot \underline{\boldsymbol{E}}'^{*} = \underline{\boldsymbol{E}}'^{*} \cdot \overline{\overline{\boldsymbol{\sigma}}}^{*T} \cdot \underline{\boldsymbol{E}}' \qquad \text{Eq. 204}$$

$$\langle \underline{\boldsymbol{E}} \cdot \underline{\boldsymbol{J_p}} \rangle = \begin{cases} 0 & \nu = 0 \\ \underline{\boldsymbol{E}}'^{*} \cdot \left[\dfrac{\overline{\overline{\boldsymbol{\sigma}}} + \overline{\overline{\boldsymbol{\sigma}}}^{*\boldsymbol{T}}}{4} \right] \cdot \underline{\boldsymbol{E}}' & \nu \neq 0 \end{cases} \qquad \text{Eq. 205}$$

Using the relation between the conductivity and the dielectric tensor (Eq. 159), the specific power deposition can also be written as in Eq. 206. The term ν and superscript T represent the effective momentum transfer collision frequency and the matrix transposition operator respectively. Notice that when momentum transfer collisions are absent the power deposition vanishes.

$$\langle \underline{\boldsymbol{E}} \cdot \underline{\boldsymbol{J_p}} \rangle = \begin{cases} 0 & \nu = 0 \\ i\omega_0 \epsilon_0 \underline{\boldsymbol{E}}'^{*} \cdot \left[\dfrac{\overline{\overline{\boldsymbol{\epsilon}}}^{*\boldsymbol{T}} - \overline{\overline{\boldsymbol{\epsilon}}}}{4} \right] \cdot \underline{\boldsymbol{E}}' & \nu \neq 0 \end{cases} \qquad \text{Eq. 206}$$

If we expand the collisional dielectric tensor $\overline{\overline{\boldsymbol{\epsilon}}}$ into its components, we can express the specific power deposition as Eq. 207.

$$\langle \underline{\boldsymbol{E}} \cdot \underline{\boldsymbol{J_p}} \rangle = \frac{\omega_0 \epsilon_0}{2}\, Im \left[S \left(\left| \underline{E_r}' \right|^{\boldsymbol{2}} + \left| \underline{E_\phi}' \right|^{\boldsymbol{2}} \right) + P \left| \underline{E_z}' \right|^{\boldsymbol{2}} + 2D\, Im \left[\underline{E_\phi}' \underline{E_r}'^{*} \right] \right] \qquad \text{Eq. 207}$$

By expressing the dielectric tensor components in the H-TG frequency regime as in Eq. 86 to Eq. 88 we can further refine the expression of the specific power deposition as in Eq. 208, where the “transverse”, “parallel” and “crossed” terms are defined below.

$$\begin{aligned}
\langle \underline{\boldsymbol{E}} \cdot \underline{\boldsymbol{J_p}} \rangle &= \langle \underline{\boldsymbol{E}} \cdot \underline{\boldsymbol{J_p}} \rangle_{\perp} + \langle \underline{\boldsymbol{E}} \cdot \underline{\boldsymbol{J_p}} \rangle_{\times} + \langle \underline{\boldsymbol{E}} \cdot \underline{\boldsymbol{J_p}} \rangle_{\parallel} \\
\langle \underline{\boldsymbol{E}} \cdot \underline{\boldsymbol{J_p}} \rangle_{\perp} &= \left(\frac{\epsilon_0}{2}\frac{\omega_{pe}^2}{\Omega_e}\right) Im\left[\frac{\delta_*}{1-\delta_*^2}\right] \left|\underline{E_\perp}'\right|^{\boldsymbol{2}} \\
\langle \underline{\boldsymbol{E}} \cdot \underline{\boldsymbol{J_p}} \rangle_{\parallel} &= \left(\frac{\epsilon_0}{2}\frac{\omega_{pe}^2}{\Omega_e}\right) Im\left[-\frac{1}{\delta_*}\right] \left|\underline{E_z}'\right|^{\boldsymbol{2}} \\
\langle \underline{\boldsymbol{E}} \cdot \underline{\boldsymbol{J_p}} \rangle_{\times} &= \left(\frac{\epsilon_0}{2}\frac{\omega_{pe}^2}{\Omega_e}\right) Im\left[\frac{2}{1-\delta_*^2}\right] \; Im\left[\underline{E_\phi}'\underline{E_r}'^{*}\right]
\end{aligned}$$

Eq. 208

Whenever $|\delta_*| \ll 1$, the “crossed” term vanishes and we can express the “transverse” and “parallel” specific power depositions terms as shown in Eq. 209 and Eq. 210 respectively. The ratio between the parallel and transverse terms can be written as in Eq. 211. Due to the high conductivity along the magnetic field, the transverse electric field component is much greater than the parallel component; however, even in cases where $|\delta_*| \ll 1$ it is not obvious which power deposition term dominates and all electromagnetic fields in the plasma waveguide need to be computed.

$$\langle \underline{\boldsymbol{E}} \cdot \underline{\boldsymbol{J_p}} \rangle_{\perp} = \frac{\epsilon_0}{2}\left[\frac{\omega_{pe}^2}{\Omega_e^2}\right] \nu \left|\underline{E_\perp}'\right|^{\boldsymbol{2}}$$

Eq. 209

$$\langle \underline{\boldsymbol{E}} \cdot \underline{\boldsymbol{J_p}} \rangle_{\parallel} = \frac{\epsilon_0}{2}\left[\frac{\omega_{pe}^2}{\omega^2+\nu^2}\right] \nu \left|\underline{E_z}'\right|^{\boldsymbol{2}}$$

Eq. 210

$$\frac{\langle \underline{\boldsymbol{E}} \cdot \underline{\boldsymbol{J_p}} \rangle_{\parallel}}{\langle \underline{\boldsymbol{E}} \cdot \underline{\boldsymbol{J_p}} \rangle_{\perp}} = \left[\frac{\Omega_e^2}{\omega^2+\nu^2}\right] \left|\frac{\underline{E_z}'}{\underline{E_\perp}'}\right|^{\boldsymbol{2}}$$

Eq. 211

5D.2 Heat transport in plasma

The statistical description of plasma begins with the Boltzmann equation (Eq. 212) which describes the evolution of the particle distribution function $f(\underline{\boldsymbol{r}}, \underline{\boldsymbol{v}}, t)$ in phase space under the influence of electromagnetic forces and collisional processes. All bold quantities denote vector fields and the underline represents quantities in real space as opposed to Fourier space. The term $\underline{\boldsymbol{r}}$ and $\underline{\boldsymbol{v}}$ represent the 3D position and 3D velocity coordinate in phase space. The term $q, m, \underline{\boldsymbol{E}}$ and $\underline{\boldsymbol{B}}$ represent particle charge, particle mass, electric and magnetic vector fields respectively. The term $(\partial f/\partial t)_c$ represents a particle source or sink in the distribution function due to short time-scale interparticle collisions. Appendix B in reference [60] provides a derivation for this term. It is this term that allows relaxation of the distribution function towards a Maxwell-Boltzmann distribution, allows derivation of the hydrodynamic fluid equations and leads to the frictional forces between species, e.g. neutral gas and charge particles. For more details on this matter and transport processes in plasma see Baginskii [129] and Fitzpatrick [130].

$$\frac{\partial f}{\partial t} + \underline{\boldsymbol{v}} \cdot \nabla f + \frac{q}{m}(\underline{\boldsymbol{E}} + \underline{\boldsymbol{v}} \times \underline{\boldsymbol{B}}) \cdot \nabla_{\underline{v}} f = \left(\frac{\partial f}{\partial t}\right)_c \qquad \text{Eq. 212}$$

For our present purposes, it will suffice to describe the plasma using a two fluid approach by taking velocity moments of the collisional Boltzmann equation (Eq. 212). This process leads to (1) particle, (2) momentum and (3) heat transport equations when appropriate closure is provided [130]. In addition, it allows us to define macroscopic quantities that are relevant to experiment such as particle density (Eq. 213), particle flux (Eq. 214), kinetic energy density (Eq. 215), internal energy density (Eq. 216) and heat flux (Eq. 217). The integration is performed over all velocity space. For a drifting isotropic Maxwell-Boltzmann distribution function we can define $\underline{\boldsymbol{v}} = \underline{\boldsymbol{u}} + \underline{\boldsymbol{w}}$ where $\underline{\boldsymbol{u}}$ and $\underline{\boldsymbol{w}}$ represent the particle mean drift velocity and the particle random thermal velocity respectively. More details on this subject can be found in references [1], [60], [123].

$$n = \int f \, d^3\underline{\boldsymbol{v}} \qquad \text{Eq. 213}$$

$$n\underline{\boldsymbol{u}} = \int \underline{\boldsymbol{v}} f d^3\underline{\boldsymbol{v}} \qquad \text{Eq. 214}$$

$$\frac{1}{2}mn\underline{u}^2 = \frac{1}{2}m \int \underline{u}^2 f \, d^3\underline{\boldsymbol{v}} \qquad \text{Eq. 215}$$

$$\frac{3}{2}p = \frac{1}{2}m\int \underline{w}^{\boldsymbol{2}} f\, d^3\underline{\boldsymbol{v}} \tag{Eq. 216}$$

$$\boldsymbol{q} = \frac{1}{2}m\int \underline{\boldsymbol{w}}\,\underline{w}^{\boldsymbol{2}} f\, d^3\underline{\boldsymbol{v}} \tag{Eq. 217}$$

By taking moments of the Boltzmann equation (Eq. 212), the inviscid electron fluid heat transport equation is given Eq. 218.

$$\frac{\partial}{\partial t}\left(\frac{3}{2}p_e\right) + \nabla \cdot \left(\frac{3}{2}p_e\underline{\boldsymbol{u}}\right) + \nabla \cdot \boldsymbol{q} = G - S \tag{Eq. 218}$$

The term P_e represents the internal energy density in $[J/m^3]$ of the electron fluid, which is given by Eq. 219. The term $\frac{3}{2}p_e\underline{\boldsymbol{u}}$ represents the flux of internal energy density, where $\underline{u}$ is the fluid macroscopic velocity. The term $\nabla \cdot \left(\frac{3}{2}p_e\underline{\boldsymbol{u}}\right)$ can be divided into a contribution due to macroscopic plasma flow and/or fluid compression, as described by the first and second terms in Eq. 220 respectively.

$$P_e = neT_e \tag{Eq. 219}$$

$$\nabla \cdot \left(\frac{3}{2}p_e\underline{\boldsymbol{u}}\right) = \underline{\boldsymbol{u}}\nabla \cdot \left(\frac{3}{2}p_e\right) + \frac{3}{2}p_e\nabla \cdot \underline{\boldsymbol{u}} \tag{Eq. 220}$$

The term $\boldsymbol{q}$ represents the heat flux in $[W/m^2]$ due to microscopic thermal motion. The terms G and S represent heat sources and sinks in the electron fluid respectively. In order to provide closure to the fluid equations and not invoke higher order moments of the Boltzmann equation we can represent the heat flux as in Eq. 221, where $\bar{\bar{\kappa}}$ is the electron thermal conductivity tensor with units of $[m^{-1}s^{-1}]$. Parallel and transverse components in SI units are given by Eq. 222 [131].

$$\boldsymbol{q} = -\bar{\bar{\kappa}} \cdot \nabla(eT_e) \tag{Eq. 221}$$

$$\kappa_{\parallel} = 3.2\left(\frac{neT_e}{m_e}\right)\tau_e \quad \kappa_{\perp} = 4.7\left(\frac{neT_e}{m_e}\right)\left(\frac{1}{\Omega_e^2\tau_e}\right) \tag{Eq. 222}$$

5D.3 Power balance

To describe the heat transport in the plasma waveguide herein presented we define the heat source G as the rate of work done on the electron fluid by the electric fields of the wave. This process is described in the section entitled "Poynting's theorem in dielectric media" and is expressed as ohmic dissipation of the wave driven polarization current. The heat sink S is described by the power dissipated through electron-ion and electron-neutral collisional processes. The electron-ion collisional power dissipation S_{ei} is given by Eq. 223 [1, p. 239]. This process describes the rate at which the electron fluid exchanges energy with the ion fluid. If electrons are hotter than ions, power flows from the electron fluid to the ion fluid.

$$S_{ei} = \frac{3}{2}\left(\frac{2m_e}{m_i}\right) n_e \nu_{ei}(T_e - T_i) \tag{Eq. 223}$$

The electron-neutral collisional power dissipation S_{en} includes contributions from: (1) elastic, (2) excitation and (3) ionization collisions. We describe electron-neutral collisional process by a cross section $\sigma_\beta\,(v)$, a collision rate K_β, a collision frequency ν_β and the energy lost by the electron per collision $\mathcal{E}_\beta$. The term β denotes the collision type (elastic, inelastic or ionizing). If we assume that neutral particles are moving much slower than electrons we can represent the collision rate K_β by Eq. 224, where $\boldsymbol{v}$ is essentially the relative velocity between neutrals and electrons.

$$K_\beta = \int \sigma_\beta(v)\underline{\boldsymbol{v}} f_e(\boldsymbol{v}) d^3\underline{\boldsymbol{v}} \tag{Eq. 224}$$

Furthermore, if we assume an isotropic Maxwellian electron velocity distribution $f_e(v)$ at a temperature T_e the collision rate K_β is given by Eq. 225. Notice that the collision rate is a function of electron temperature only.

$$K_\beta(T_e) = \left(\frac{m_e}{2\pi T_e}\right)^{3/2} \int_0^\infty \sigma_\beta\left(\underline{v}\right)\underline{v}\left[4\pi\underline{v}^2 \exp\left(-\frac{m_e\underline{v}^2}{2T_e}\right)\right] d\underline{v} \tag{Eq. 225}$$

The collision frequency ν_β is given by Eq. 226, where n_g is the neutral gas particle density.

$$\nu_\beta = n_g K_\beta \tag{Eq. 226}$$

In general, for a given neutral density and electron temperature the collision frequency scales with the magnitude of the cross section. The specific power dissipated by a particular collisional process S_{en}^{β} is given by Eq. 227.

$$S_{en}^{\beta} = n_e \nu_\beta \, \mathcal{E}_\beta \qquad \text{Eq. 227}$$

The total specific power dissipated through electron-neutral collisions is given by Eq. 228, where the summation is over all the relevant electron-neutral collision types (elastic, inelastic).

$$S_{en} = n_e n_g \sum_{\beta} K_\beta \mathcal{E}_\beta \qquad \text{Eq. 228}$$

Having defined the thermal heat flux as in Eq. 221, the heat generation due to the wave (Eq. 207) and the heat sinks due to collisional processes (Eq. 223 and Eq. 228) the steady state electron fluid heat transport equation relevant to the plasma waveguide can be written as in Eq. 229. This expression states that the macroscopic polarization currents $\underline{\boldsymbol{J_p}}$ driven by the wave's electric field $\underline{\boldsymbol{E}}$ become the source of heat into the plasma. The heat source must be balanced by the (1) power absorbed by microscopic collisional process (coulomb, elastic, excitation and ionization) and the power transported away through (2) microscopic heat conduction and (3) macroscopic heat convection by bulk fluid flow. In Chapter 7, we investigate how this process leads to plasma flow in MAGPIE. Reference [132] demonstrates the use of the power transport equation (Eq. 229) coupled with a 1D full wave code to self-consistently calculate wave power deposition and radial plasma density and temperature profiles.

$$\langle \underline{\boldsymbol{E}} \cdot \underline{\boldsymbol{J_p}} \rangle = S_{ei} + S_{en} + \nabla \cdot \boldsymbol{q} + \nabla \cdot \left(\frac{3}{2} p_e \underline{\boldsymbol{u}} \right) \qquad \text{Eq. 229}$$

Chapter 6 Wave excitation, propagation and damping in MAGPIE

6.1 Introduction 146
6.2 Experimental setup 149
6.3 Wave dispersion and attenuation relations 150
    6.3.1 The WKB approximation 151
6.4 Helicon wave propagation in quasi-uniform magnetic fields 153
    6.4.1 Axial wave propagation 156
    6.4.2 Radial wave structures 158
    6.4.3 Whistler wave ray direction 159
    6.4.4 Wave excitation mechanism in MAGPIE 162
6.5 Helicon wave propagation in non-uniform magnetic fields 167
    6.5.1 Experimental observations 167
    6.5.2 Axial wave attenuation 169
    6.5.3 2D full wave code simulation 171
    6.5.4 Origin of the interference pattern 175
    6.5.5 RF power deposition in MAGPIE 176
6.6 Summary 178
Appendix 6A. The WKB approximation 179
    6A.1 Solution in 1D with attenuation 179
    6A.2 Validity criterion 180
Appendix 6B. Input data for the 2D wave code 181
    6B.1 Radial profiles 181
    6B.2 Axial profiles 182

6.1 Introduction

Wave propagation in cylindrically bounded plasma can be modelled with different levels of complexity. In general, the more elaborate models can provide a better quantitative match with experiment and greater insight into the wave physics; however, the code development, implementation time, iteration time and computational resources required scale with the model's complexity.

At the lowest level of complexity, one can use the standard helicon dispersion relation and theoretical damping length (Eq. 105 and Eq. 107 in Chapter 5) to compare with experiment. This process can provide information on the dominant wavelength in the discharge and approximate WKB wave attenuation lengths even in the presence of plasma non-uniformity. However, radial power deposition profiles, wave excitation spectrum, wave amplitude and axial interference patterns cannot be modelled.

The next level of complexity is to implement a uniform plasma “0D” full wave code. Whenever the plasma non-uniformity is not too strong this approach can quantitatively predict (1) wave excitation spectrum, (2) wave absolute amplitude, (3) wave interference patterns, (4) wave attenuation lengths and (5) antenna loading. However, one can only approximate radial power deposition profiles since radial plasma non-uniformity is not included which has been shown to considerably affect power deposition profiles [118]. Up to this level of complexity, one can still solve the plasma waveguide boundary value problem analytically and separate the contributions from the” Fast” and “Slow” waves. However, to solve for the wavefields in real space driven by arbitrary shaped antennas, one must carry out the inverse Fourier transformation numerically. Chapter 5 describes a wave code of this type. Some references for codes that belong to this level of complexity are Cato [125], Hipp [124] and Colestock [127] amongst others.

The next level of complexity is to include radial plasma gradients using a “1D” full wave code. Wave codes of this kind have been developed by Arnush using a semi-analytical method (HELIC) [118], [120], Kamenski with a finite element method based code [126], Mouzouris with stratified constant density method (ANTENA) [131] and 2D finite difference method (MAXEB) [134], Melazzi (SPIRES) [135], Cho [132], [136], [137], Shamrai [138], [139], [140], Kramer [141], [141], [142], [143], [144] and Fischer [145] using finite difference schemes. Mouzouris [134] and Melazzi [135] provide a good review of 1D wave codes described in the literature. Radial plasma non-uniformity allows one to calculate realistic radial power deposition profiles. The axial uniformity assumption allows Fourier decomposition of the governing equation in the axial direction. However, the “Fast” and “Slow” wave contributions cannot be analytically separated and the governing equations must be numerically solved. An exception to this is the stratified density model which allows separation of the “fast” and “slow” wave solutions at every constant density layer. In addition, if axial plasma non-uniformity is important one cannot Fourier decompose the governing equations in the axial direction; once again solutions can only be obtained numerically. 2D full wave codes have been developed by G. Chen (EMS) [146], Whitson and Berry (MAXEB) [134] and Carter (EMIR3) [48].

All the previous cases described above require plasma density and electron temperature fields as inputs to the code in order to define the dielectric properties of the plasma. The last level of complexity relevant for our purposes is to self-consistently model the wavefields coupled with particle generation and plasma transport calculations in an iterative process. All field quantities (plasma and background magnetic field) are assumed to vary axially and radially. References for self-consistent full wave codes can be found in the work of Carter (EMIR3) [48], Cho [132] and Curreli (HELIC + transport code) [147], [148]. These self-consistent wave codes are able to model mode transition between centrally peaked to edge heating, provide insight into power threshold mechanisms and plasma density jumps. The main difference between these codes is how the particle balance is modelled and the number of dimensions considered (1D or 2D).

In this chapter we investigate the excitation, propagation and damping of helicon waves in the low temperature (1-8 eV) and high density hydrogen plasma (0.3-3x10^{19} m^{-3}) produced in the MAGPIE helicon source [44]. We have investigated wave propagation in argon plasma in MAGPIE elsewhere [149]. In this study, we use a variety of theoretical tools based on the cold dielectric tensor to model wave physics in MAGPIE with realistic antenna geometries and compare these with experimental measurements. The theoretical tools implemented are: helicon wave dispersion relation, damping lengths, 0D and 2D electromagnetic full wave codes. Helicon wave dispersion, damping relations and the 0D wave code are described in detail in Chapter 5. The 2D electromagnetic full wave code is described in references [146], [149].

6.2 Experimental setup

In what follows, we focus our attention on helicon wave propagation in the “downstream” region of the plasma source in the MAGPIE device. MAGPIE’s experimental setup is described in Chapter 2. Details specific to this section are described next.

In these experiments we employ two different magnetic field configurations which we show in Figure 59 below. The “z” scale shown therein is consistent with that introduced in Chapter 2. Hereafter, the low field case is referred to as the “quasi-uniform” configuration (thin line) while the high field case as the “strong mirror” (thick line) configurations. Alternatively, using the labelling described in Chapter 2, these are labelled T100A S50A and T450A S50A respectively. The discharge was operated in H_2 at 8 mTorr. RF power was delivered to the plasma in 2 ms pulses at a repetition rate of 10 Hz through a left-handed Half-turn Helical (HH) antenna driven at 7 MHz, 22 cm in length, 12 cm in diameter and located between -25 cm and -3 cm along the “z” axis.

For these operating conditions, it was observed that plasma and helicon wave diagnostic signals achieved steady state for times greater than 1 ms; hence, all measurements herein reported corresponds to times greater than this. RF power was measured by directional couplers and kept at 20 ± 2 kW. Antenna matching was adjusted for every magnetic configuration to maintain the reflected RF power to a minimum. Antenna current was measured to be 180 ± 10 A amplitude. Plasma density and electron temperature were measured with axially and radially resolved Double Langmuir Probes (DLP). Individual probe tips where regularly cleaned with electron saturation current at 60 V, 3.5 A, 1 ms pulse length and 10 Hz repetition rate. Plasma density calculations are based on ion saturation current and assume H^+ as the dominant ion species[13]. Helicon wave magnetic fields ($\underline{B_r}$ and $\underline{B_z}$) were measured with an axially and radially resolved RF Magnetic Probe (MP). These diagnostics are described in Chapter 3.

---

[13] In Chapter 3, a comparative study between DLPs and microwave interferometry indicates that protons are the dominant ion species in MAGPIE above 10 kW when operating with H_2 between 2 and 8 mTorr.

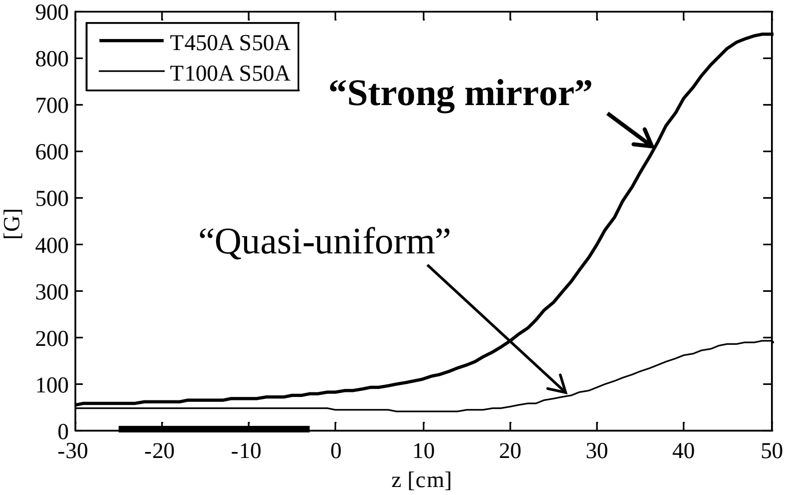

Figure 59, Magnetic field configurations relevant to the experiments described in this chapter. The location of the antenna is represented by the thick black line along the "z" axis. The thick and thin curves represent the magnetic field strength for the "strong mirror" and "quasi-uniform" magnetic field configurations respectively

6.3 Wave dispersion and attenuation relations

Our initial analysis of wave propagation begins with the H-TG dispersion relation for unbounded plasma as shown in Eq. 90 Chapter 5. By assuming (1) propagation at an arbitrary angle and (2) complex valued parallel and transverse wavenumbers we arrived at the quintic equation presented in Eq. 98 Chapter 5 which we repeat in Eq. 230 below for convenience. The relevant coefficients are defined in Eq. 231.

$$\mathcal{K}^5 c_5 + \mathcal{K}^4 c_4 + \mathcal{K}^3 c_3 + \mathcal{K}^2 c_2 + \mathcal{K} c_1 + c_0 = 0 \qquad \text{Eq. 230}$$

$$\mathcal{K} = \frac{\kappa_I}{\kappa_R} \quad c_5 = 2\delta_I \quad c_4 = -\frac{\Psi_R}{4}\nu^*\delta_I \quad c_3 = \delta_I(4+\Psi_R)$$

$$c_2 = \Psi_R\delta_R\left(\frac{\nu^{*2}}{2} - 1\right) \quad c_1 = \delta_I(2-\Psi_R) \quad c_0 = -\frac{\Psi_R}{4}\nu^*\delta_I \qquad \text{Eq. 231}$$

$$\Psi_R = 4\frac{k_w^2}{\kappa_R^2}\delta_R \quad \nu^* = \frac{\nu}{\omega} \quad \delta_R = \frac{\omega}{\Omega_e} \quad \delta_I = \frac{\nu}{\Omega_e}$$

This expression describes the parallel damping of the H-TG wave for arbitrary values of real parallel wavenumbers. In its current form it does not readily provide physical insight and is not easily evaluated. However, if we neglect terms higher than 3rd order by assuming weakly damped conditions we can derive separate expressions for the dispersion and damping of H and TG waves as shown in Eq. 105 to Eq. 108 Chapter 5. For convenience, the Helicon wave dispersion and damping relations derived in Chapter 5 are repeated below in Eq. 232 and Eq. 233, respectively.

$$k_R = \frac{k_w^2}{\kappa_R} \quad k_w^2 = \frac{\omega\omega_{pe}^2}{\Omega_e c^2} \qquad \text{Eq. 232}$$

$$\kappa_I = \frac{k_w^2}{\kappa_R}\left(\frac{\nu}{2\Omega_e}\right) \qquad \text{Eq. 233}$$

The complex parallel wavenumber is given by $\kappa = \kappa_R + i\kappa_I$ where the subscripts "R" and "I" represent real and imaginary parts. Eq. 232 and Eq. 233 are only valid for cases that satisfy $\kappa_I/\kappa_R \ll 1$. In general, this condition is satisfied for the helicon wave due to its electromagnetic nature. The terms k , k_w , ω , ω_{pe} , Ω_e and c represent the total helicon wavenumber, "whistler" wavenumber, RF angular frequency, plasma frequency, electron cyclotron frequency and the speed of light in SI units respectively. In what follows, we refer to Eq. 230 and Eq. 233 as the "Quintic" and "Helicon Approximation" wave damping relations.

6.3.1 The WKB approximation

Wave propagation can be described using a Wentzel-Kramers-Brillouin (WKB) approximation whenever the non-uniformity of the medium varies gradually relative to the wavelength. A brief description of the WKB approximation is provided in Appendix 6A. We show that for weakly damped waves ($\kappa_R \gg \kappa_I$), the WKB approximation is valid provided the gradient of the wavenumber is much less than the square of the local wavenumber (Eq. 250 in Appendix 6A). For convenience, this condition is provided below (Eq. 234).

$$\frac{\partial\kappa_R}{\partial z} \ll \kappa_R^2 \qquad \text{Eq. 234}$$

In the context of the Helicon-Trivelpiece-Gould (H-TG) wave, the electromagnetic (helicon) part is weakly damped ($\kappa_R \gg \kappa_I$) and Eq. 234 can be used to assess the validity of the WKB approximation. Helicon waves propagate approximately along the magnetic field and their dispersion relation (Eq. 232) can be approximated as shown in Eq. 235. Since the dispersion depends on the ratio between the electron density (n_e) and magnetic field (B_0), the WKB approximation can be used to model wave propagation even in cases with strong axial gradients in both n_e and B_0, provided that κ_R is approximately constant and satisfies Eq. 234. This is approximately the case in the experiments presented in this chapter. For example, in Figure 62 the phase variation of the helicon wave indicates that the parallel wavenumber is approximately constant along the length of MAGPIE even though both the plasma density and magnetic field are not (see Figure 60). In reference [35], M. Light applies the WKB method to investigate the damping of helicon waves in an Argon discharge. Figures 8 and 9 in the aforementioned reference present the experimentally measured helicon wave phase variation. Upon inspection of these plots, it can be shown that the "WKB condition" (Eq. 234) is satisfied. In addition, in Figure 14 of reference [35] Light shows that the WKB calculation is in good agreement with the experimentally measured wavefields and attenuation can be explained through Coulomb collisions alone.

$$\kappa_R^2 \approx \left(\frac{n_e}{B_0}\right) e\mu\omega \qquad \text{Eq. 235}$$

In this chapter, we describe helicon wave propagation using the WKB approximation (Eq. 236). The terms z_0 , κ and A_0 represent the location where wave is launched, parallel wavenumber and initial amplitude of wave respectively.

$$f(z,t) = A_0 \exp i \left[\int_{z_0}^{z} \kappa(s) ds - \omega t\right] \qquad \text{Eq. 236}$$

Upon separation of the parallel wavenumber (κ) into real and imaginary parts, we can write the aforementioned wave as in Eq. 237, where the amplitude $A(z)$ is given by Eq. 238. This expression describes the amplitude of an attenuated wave launched at z_0 and propagating in the "z" direction. Using the experimentally measured parallel wavenumber κ_R we can calculate the parallel helicon wave attenuation using the "Quintic" (Eq. 230) and/or "Helicon approximation" (Eq. 233) damping relations together with the WKB amplitude in Eq. 238. Hereafter, we refer to this process as a "WKB wave attenuation" calculation.

$$f(z,t) = A(z) \exp i \left[\int_{z_0}^{z} \kappa_R(s) ds - \omega t\right] \qquad \text{Eq. 237}$$

$$A(z) = A_0 \exp - \int_{z_0}^{z} \kappa_I(s) ds \qquad \text{Eq. 238}$$

6.4 Helicon wave propagation in quasi-uniform magnetic fields

For the analysis presented in this section, we have selected the “quasi-uniform” magnetic field configuration (Figure 59) which provides plasma density profiles with small axial and radial gradients compared to the “strong mirror” configuration. Under such conditions, a 0D full wave code can quantitatively reproduce the experimentally measured wavefields and provide further insight into wave generation and propagation in the MAGPIE device. The operating conditions relevant to the “quasi-uniform” configuration are described in Table 5. The associated axial and radial plasma density and electron temperature measured with a DLP are shown in Figure 60 and Figure 61 respectively.

Whether wave dispersion is governed by local or volume averaged quantities depends on the ratio between length scales of: (a) plasma gradients and (b) wave under consideration. The small scale wavelength of the TG wave means that its dispersion is determined by local quantities and thus strongly affected by the presence of plasma radial gradients. This cannot be seen from experimental measurements since RF magnetic probes sample only the EM wave component; In our experiments, helicon wave wavelengths (~10 cm) are comparable to radial and axial gradient length scales; hence, dispersion is approximately governed by volume averaged quantities. Experimentally, this is approximately true for cases with low magnetic fields (< 100 G), including the “quasi-uniform” configuration, where spatial gradients are small. At higher fields, radial gradients become important and must be taken into account.

In the analysis of wave propagation in “quasi-uniform” fields, we proceed by using the “on axis” electron temperature (4.5 eV) and the average plasma density ($3.5\text{x}10^{18}$ m^{-3}) at the antenna location as input to the 0D wave code. We include electron-neutral ($\nu_{en}\sim$ 21 MHz) and electron-ion collisions ($\nu_{ei}\sim$ 13 MHz). Furthermore, the measured antenna current (180 A) and the mean value of the magnetic field at the antenna (45 G) are used as inputs for the 0D wave code. Table 6 summarizes the relevant input data into the 0D code. The terms R, r_a and r_p represent the radius of the conducting wall, antenna radius and plasma effective radius respectively. The terms L_a, θ and I_0 represent the antenna length, half the helical antenna twist angle[14] and the antenna current respectively. We also include derived quantities such as collisional ($\nu_{e\beta}$), electron plasma (f_{ep}) and cyclotron ($f_{c\beta}$) frequencies, where β denotes particle species.

---

[14] The helical twist angle corresponds to the total angular displacement the antenna makes from one end to the other. A zero helical antenna twist angle corresponds to a Nagoya type III antenna. A half turn helical antenna will have a helical twist angle of π.

Table 5, Operating conditions relevant to the "quasi-uniform" field configuration

Neutral gas	H_2 at 8 mTorr	Antenna radius	5.2 cm
RF power (nominal)	~20 kW at 7 MHz	Location	-25 < z < -3 cm
Antenna type	Half turn helical	Source solenoid current	50 A
Handedness	Left	Target solenoid current	100 A
Antenna current	180 A amplitude	Source field	45 G
Antenna length	22 cm	Maximum Target field	200 G

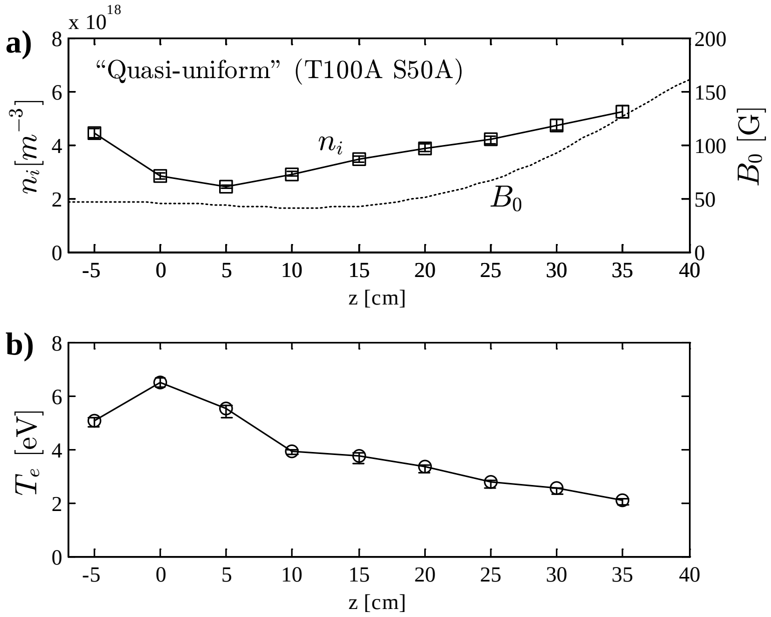

Figure 60, On-axis (a) axial plasma density and (b) electron temperature measurements

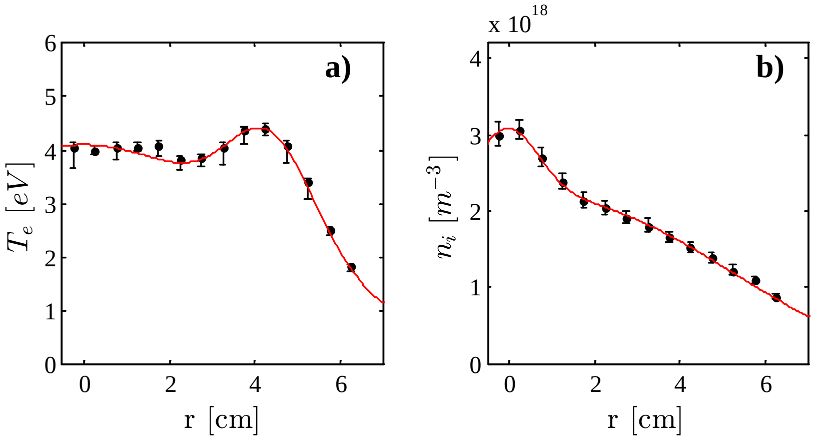

Figure 61, (a) Radial electron temperature and (b) plasma density measurements at z = 11 cm.

Table 6, Input parameters for the 0D wave code and derived quantities

B_0	45 G	θ	$\pi/2$
n_e	3.5×10^{18} m^{-3}	I_0	180 A amplitude
T_e	4.5 eV	ω	44×10^6 Rad/s
P_0	8 mTorr	ν_{en}	21 MHz (300 K)
f	7 MHz	ν_{ei}	13 MHz
R	10 cm	ν_e	34 MHz
r_a	5.2 cm	f_{pe}	16.8 GHz
r_p	4.5 cm	f_{ce}	126 MHz
L_a	22 cm	f_{ci}	68.5 kHz (H+)

The helicon wavefield measurements are collected as follows: (1) Measurements of $\underline{B_r}$ and $\underline{B_z}$ wavefields are taken on axis along the length of the MAGPIE. This process provides information on the axial wave attenuation, interference patterns and parallel wavenumber. (2) Radially resolved measurements are taken at various evenly spaced axial locations from $z =$ -5 cm to $z = 35$ cm every 5 cm. This process provides information on the radial structure of the wave, transverse wavenumber and propagation.

6.4.1 Axial wave propagation

Wavefield measurements are represented in terms of magnitude and phase with respect to the antenna current. The phase difference indicates the time delay a wavefront incurs as it propagates away from the radiating source. A monotonically increasing phase difference indicates wave propagation away from the antenna.

In Figure 62a, we compare various theoretical calculations with experimentally measured $\underline{B_r}$ wave amplitude taken on axis along the length of MAGPIE. The antenna, not shown, is located between -25 and -3 cm on the "z" scale provided in the figure. The dots represent the experimental data, the solid line the 0D wave code calculation, the "dotted" and "dashed" line represent two WKB wave attenuation calculations (Eq. 238) using the "Quintic" (Eq. 230) and "Helicon Approximation" (Eq. 233) imaginary wavenumbers respectively. The WKB calculations employ (1) the experimentally measured plasma density, electron temperature axial profiles and background magnetic field shown in Figure 60 to compute the axially varying imaginary wavenumber κ_I, (2) include both electron-neutral and electron-ion collisions and (3) assume the wave is launched at z = -3 cm.

We observe that experimentally measured (1) wave amplitude, (2) attenuation length, (3) interference patterns and (4) phase variation (shown in Figure 62b) are well reproduced by the 0D wave code. However, for locations beyond z = 15 cm the 0D calculation begins to differ from experiment. This is expected as the background magnetic field increases rapidly beyond z = 15 cm (Figure 59 and Figure 60). Both WKB 1 and WKB 2 wave attenuation calculations are in good agreement with experimental results. However, they cannot reproduce the interference pattern since this approximation assumes unbounded plasma. These results indicate wave attenuation under these experimental conditions can be explained entirely through collisions (e-n and e-i). Furthermore, Figure 62b indicates that the wave propagates away from the antenna with a dominant wavelength of about 10 cm ($\kappa \approx 60$ m^{-1}).

In Figure 63 we show a schematic of MAGPIE, where the red rectangle illustrates the plasma volume relevant to these experiments. Experimental results indicate that the wave is almost completely attenuated within 3-4 wavelengths away from the antenna; hence, waves are absorbed before they reach the target region solenoid at z = 40 cm. The mechanism producing the interference pattern will become clear shortly.

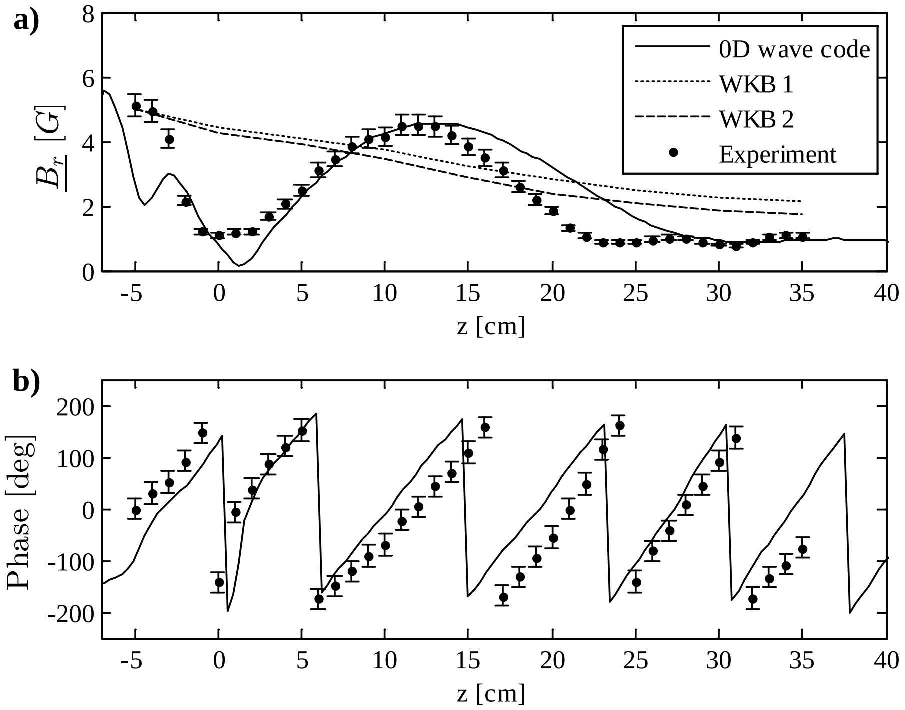

Figure 62, Theoretical (lines) and experimental (dots) $\underline{B_r}$ wavefield measured on-axis and along the length of MAGPIE. WKB 1 and 2 correspond to calculations based on the "helicon approximation" (Eq. 233) and the "quintic" equation (Eq. 230) respectively. 0D wave code calculations based on Table 6

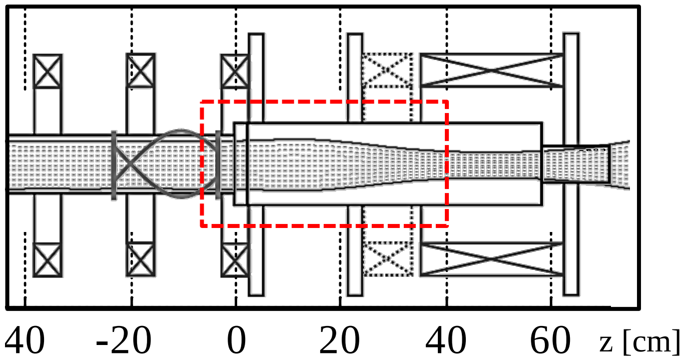

Figure 63, Schematic of MAGPIE showing the plasma volume corresponding to the experimental data from Figure 62 and Figure 64.

6.4.2 Radial wave structures

In Figure 64 we compare theoretical (0D wave code) and experimentally measured radial profiles of $\underline{B_r}$ taken at various axial "z" positions as indicated therein. The 0D wave code calculation is able to approximately reproduce the absolute amplitude of wave and radial structure. In addition, the calculated magnetic field profiles are somewhat broader than the experimentally measured profiles. This is expected since the actual plasma density is centrally peaked (Figure 61) and induces wave focusing; whereas the 0D calculation assumes a constant radial density. Nevertheless, the 0D wave code is capable of successfully reproducing the experimentally measured wave amplitudes and phases both radially and axially, provided one uses the measured average plasma density and electron temperature under the antenna and plasma gradients are kept small. We also note that standard $m = +1$ helicon wave B_r radial eigen-mode structures (see [36], [37], [150]) are not formed near the antenna but are only observed for z > 10 cm. We will comment in this aspect in the next section.

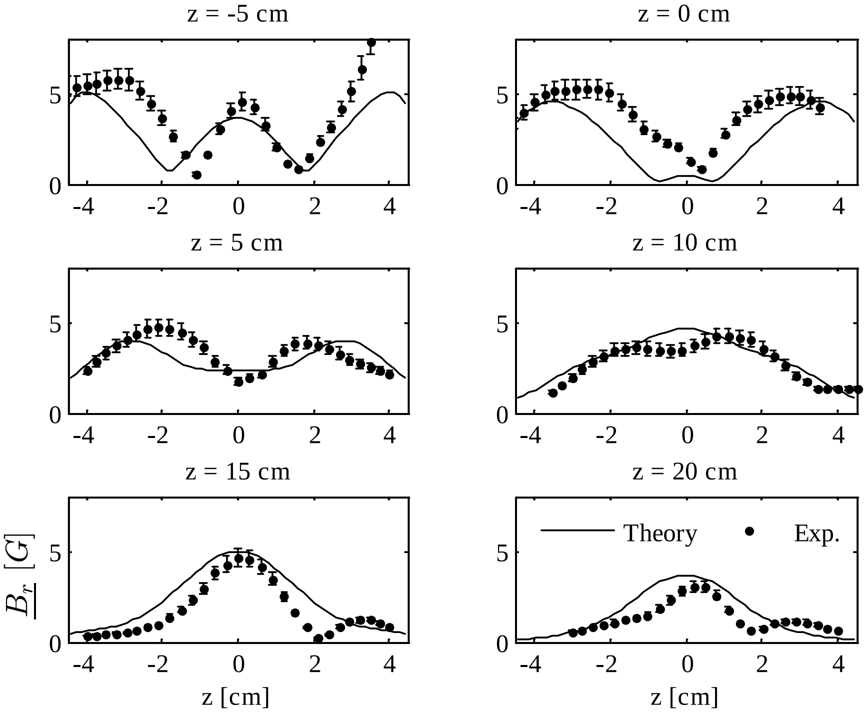

Figure 64, Theoretical (0D code) and experimentally measured $\underline{B_r}$ radial profiles at various axial locations in the target region. Solid lines and dots represent theory and experiment respectively. Each radial profile is labelled with the axial location where it was measured.

6.4.3 Whistler wave ray direction

To gain more insight into this particular discharge we take the axial and radial wavefield measurements from Figure 62 and Figure 64 and produce a smoothed (cubic interpolated) contour plot of wave amplitude over a “2D” region as shown in Figure 65a. The 0D wave code calculation corresponding to the same plasma conditions (Table 6) is shown in Figure 65b. The downstream azimuthal current ring of the antenna is shown by the black rectangle on the top-left corner of the contour plots at z = -5 cm. The helical antenna straps, to the left, are not shown. Figure 4 in Chapter 2 (page 22), provides a diagram of the helical antenna in MAGPIE and identifies the helical and azimuthal current straps.

Experimental measurements of the wave’s radial phase variation were taken along the paths represented by the two vertical white dashed lines (z = 5 cm and z = 25 cm) as indicated in Figure 65 part (a). In Figure 65 part (c) and (d) we compare experimental (dots) and 0D wave code (solid lines) radial phase profiles. Both figures indicate good agreement between theory and experiment. At z = 5 cm, the radial phase variation indicates that the wave propagates radially inwards from the edge of the plasma towards the centre as it propagates axially as shown in Figure 62b. However, at z = 25 cm phase variation indicates the wave propagates radially outwards. This indicates that the wave is launched radially inwards at the antenna location, continues to propagate along the axis and then radially outwards.

We notice that in both experimental and theoretical contour plots shown in Figure 65 part (a) and (b), the wave amplitude appears to peak along a path that connects the antenna edge with the centre of the plasma as indicated by the black dotted lines in Figure 65b. For the 0D wave code calculations and experimental measurements, these lines form an angle of approximately 13 and 15 degrees with respect to the background magnetic field respectively. The “whistler” wave ray direction is about 18-20 degrees [112], [128], [151] and the electrostatic resonance cone angle at these conditions ($\sin\theta_{res} = \omega/\Omega_{ce}$ [152]) is about 3 degrees. Based on the experimentally measured radial and axial phase variation, we can conclude that a “whistler” wave is launched by the antenna at the edge of the plasma and propagates approximately along the whistler wave ray direction towards the centre of the plasma. Closer inspection of the 0D wave code calculations indicates that the wave is excited by the azimuthal current rings of the antenna.

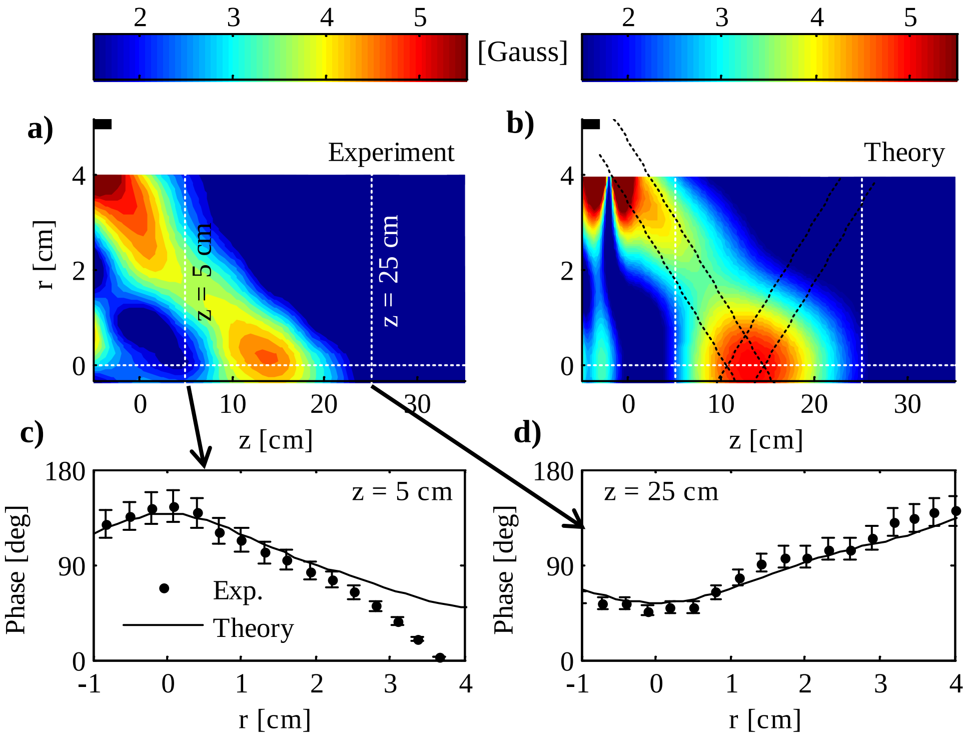

Figure 65, Contour plot of (a) experimentally measured and (b) calculated (0D code) $\underline{B_r}$ wave amplitude. The antenna's azimuthal current ring is indicated by the thick black line in the top-left corner of each contour plot. White vertical dashed lines indicate the location where the wave‘s radial phase variation was measured. Experimental (dots) and theoretical (line) radial phase variation of wave is shown in c) z = 5 cm and d) z = 25 cm.

Furthermore, in Figure 66 we show 0D wave code calculations of the $\underline{B_r}$ wave (a) magnitude and (b) phase. The antenna location is represented by the thick black lines at r = 5 and -5 cm. The wave propagates normal to the lines of constant phase as indicated by the red arrows in the phase calculation. If we translate these propagation vectors to the magnitude plot we can observe that the region where the wave packets intersect is coincident with the region where the wave amplitude is largest. This indicates that the interference pattern observed at about 13 cm in Figure 62 is produced by constructive interference of helicon waves travelling obliquely along the whistler wave ray direction and launched from the edge of the plasma by the antenna's azimuthal current rings.

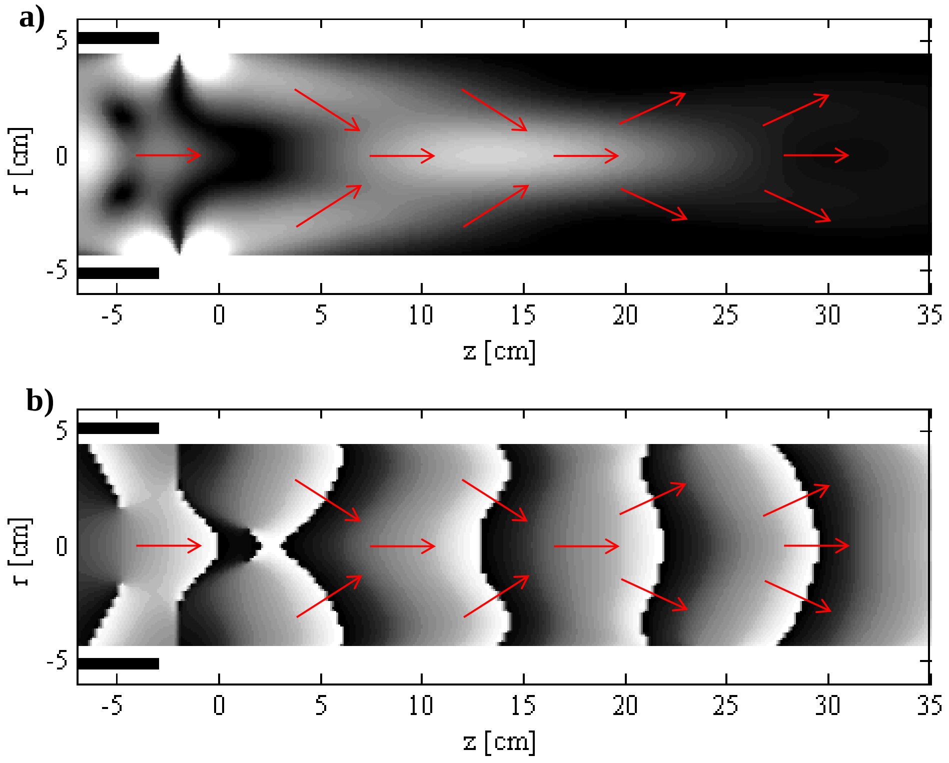

Figure 66, 0D wave code calculations of the $\underline{B_r}$ wave (a) magitude and (b) phase. Wave propagates normal to lines of constant phase. Red arrows indicate local direction of propagation of wave based on phase. Antenna location is represented by thick horizontal black lines at r = 5 and -5 cm.

6.4.4 Wave excitation mechanism in MAGPIE

The experimental data shown in Figure 62 indicates that the natural parallel wavenumber of the plasma column peaks at about 60 m^{-1}. Moreover, the helicon wave power spectrum as calculated from the 0D wave code indicates also that the dominant wavenumber is about 60 m^{-1} (Figure 67a). On the other hand, the power spectrum of the half turn helical antenna $(2\theta = \pi)$ used in these experiments (22 cm in length, 5.2 cm in radius) has its largest spectral feature at about 20 m^{-1} (Figure 67b). This indicates that the aforementioned antenna is not optimized to excite waves in this particular discharge because the periodicity of the helical antenna' straps does not match that of the natural waves in the discharge. Instead, we believe that it is the broad wavenumber spectrum of the antenna's azimuthal current rings that couples most efficiently to the natural waves in the plasma.

By increasing the number of helical turns for a given antenna length we can modify the antenna's power spectrum to match that of the natural waves in the plasma and maximize wave excitation. Using the aforementioned discharge conditions as per Table 6, we have calculated the wave amplitude spectra in the plasma driven by helical antennas 22 cm in length from 0 to 5 helical turns. Normalized calculations are shown in Figure 68. Notice that wave amplitude is maximum for parallel wavenumbers near 60 m^{-1}, e.g. for antennas with about 2 helical turns. The lower white line corresponds to conditions as per Table 6 and the half turn helical antenna $(2\theta = \pi)$ currently installed in MAGPIE. The upper white line corresponds to the case where the antenna helicity has been optimized (two helical turns) to produce maximum wave excitation.

To demonstrate the change in the wave excitation mechanism as we increase the antenna's helical turns, we calculate the wavefields generated by a half-turn antenna $(2\theta = \pi)$ and a two-turn antenna $(2\theta = 4\pi)$ both 22 cm in length using the 0D wave code for conditions as per Table 6. These wavefields are shown in Figure 69 and Figure 70 for the half-turn antenna $(2\theta = \pi)$ and for the-two turn antenna $(2\theta = 4\pi)$ respectively. In both figures, parts (a) and (b) represent the wave amplitude in Gauss and phase variation in radians respectively. The antenna location is represented by the horizontal thick black lines at r = $\pm$ 5 cm. The most important differences between these cases are the wave structures formed in the vicinity of the antennas.

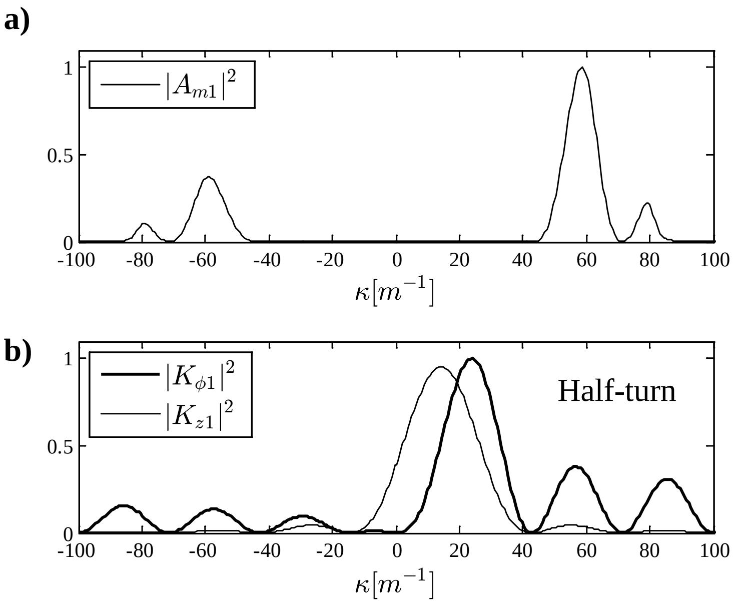

Figure 67, (a) Normalized helicon wave power spectra ($|A_{mn}|^2$) in MAGPIE for m = +1 calculated with the 0D wave code for conditions shown in Table 6 and half-turn helical antenna 22 cm in length. (b) Azimuthal and longitudinal power spectra of the half turn helical antenna ($2\theta = \pi$) used in these experiments (22 cm in length, 5.2 cm in radius)

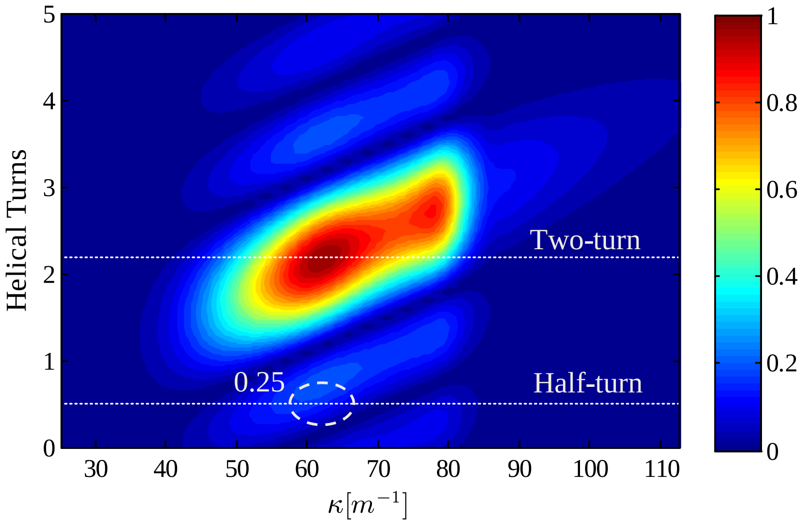

Figure 68, Normalized wave amplitude spectra (A_{mn}) in a plasma discharge as a function of antenna helicity and parallel wavenumber κ. Antenna length fixed at 22 cm. The lower dashed white line corresponds to the wave amplitude spectrum excited by MAGPIE's half turn helical antenna ($2\theta = \pi$). The peak in wave excitation occurs at about 2 helical turns (top dashed white line). Conditions as per Table 6

In the case of MAGPIE's half-turn antenna (Figure 69), the bulk of the wave excitation appears to be driven by the azimuthal current rings. These waves propagate along the whistler ray direction as discussed previously and constructively interfere at about 13 cm downstream of the antenna. It is only beyond this point ($z \geq 13$ cm) that the obliquely propagating waves interact to form radial standing wave patterns and give rise to cavity eigenmode structures. Notice that this interpretation is consistent with the results shown in Figure 64. In addition, we notice that the azimuthal current rings also launch waves upstream and into the antenna region, where they appear to be causing a standing wavefield pattern.

In the case of the two-turn antenna, wave excitation appears to be dominated by the helical current strap. We notice that for the same antenna current the two-turn helical antenna $(2\theta = 4\pi)$ is able to excite RF magnetic fields approximately 4 to 5 times larger than the half turn helical antenna $(2\theta = \pi)$. This corresponds to wave energy densities 16 to 25 times larger. This example is somewhat artificial since increasing the antenna-plasma coupling will increase the RF power deposition and thus electron density; thereby, changing the plasma dielectric properties and the resonance values for the cavity. This scenario is best described with a self-consistent full wave code; however, this calculation illustrates the following important point: maximum wave excitation is achieved by matching the antenna's periodic structure with the plasma's natural spectrum. Under these circumstances, the antenna is strongly directional as demonstrated in Figure 70, where waves are preferentially launched downstream and standing wavefields underneath the antenna no longer occur.

Both antennas show indication of oblique wave propagation along the whistler ray direction, as illustrated by the red arrows; however they indicate that waves are excited by different elements of the antenna as previously discussed. In both cases, the interference pattern downstream of the antenna can be associated with waves travelling along the whistler ray direction.

A finite length antenna will have a wavenumber spectrum of finite width and will therefore excite waves that propagate over a range of angles. The net constructive interference of all these waves leads to the observed wavefield. As the antenna spectrum becomes broad, the spectral content of the waves excited is large enough to resolve small scale structures. In the case of MAGPIE, we hypothesise that the spectrum of the azimuthal current ring excites waves with a large spectral content and enables the propagation of the wave along the ray direction. This oblique wave propagation leads to the interference pattern observed at z = 13 cm.

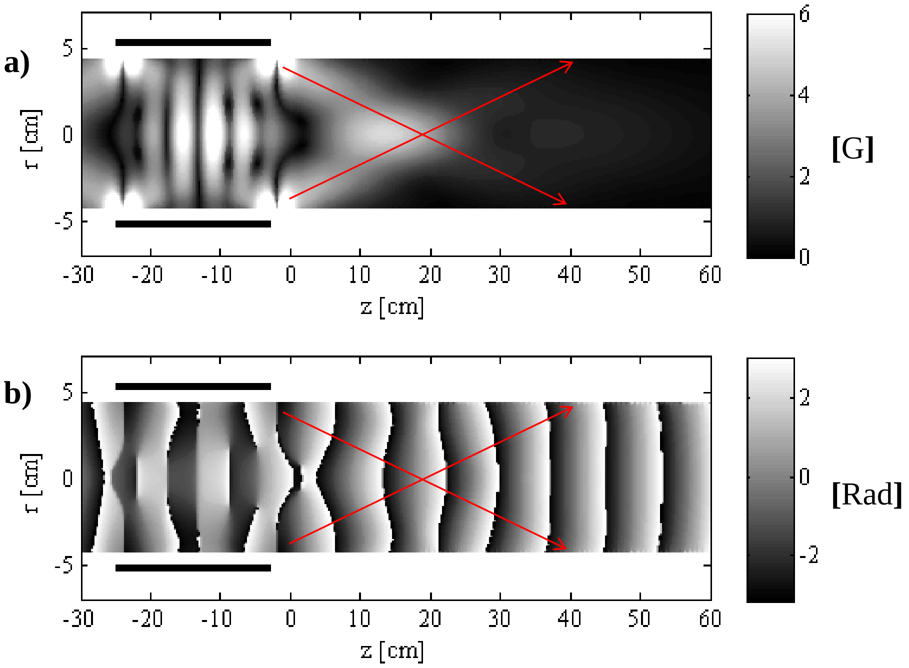

Figure 69, 0D wave code calculation of $\underline{B_r}$ helicon wave as per Table 6 using a half-turn helical antenna $(2\theta = \pi)$ 22 cm in length. The wave amplitude is shown in (a) and phase variation (b). The antenna is represented by the horizontal black lines at r = ± 5 cm. Red arrows indicate approximate direction of propagation of the wave.

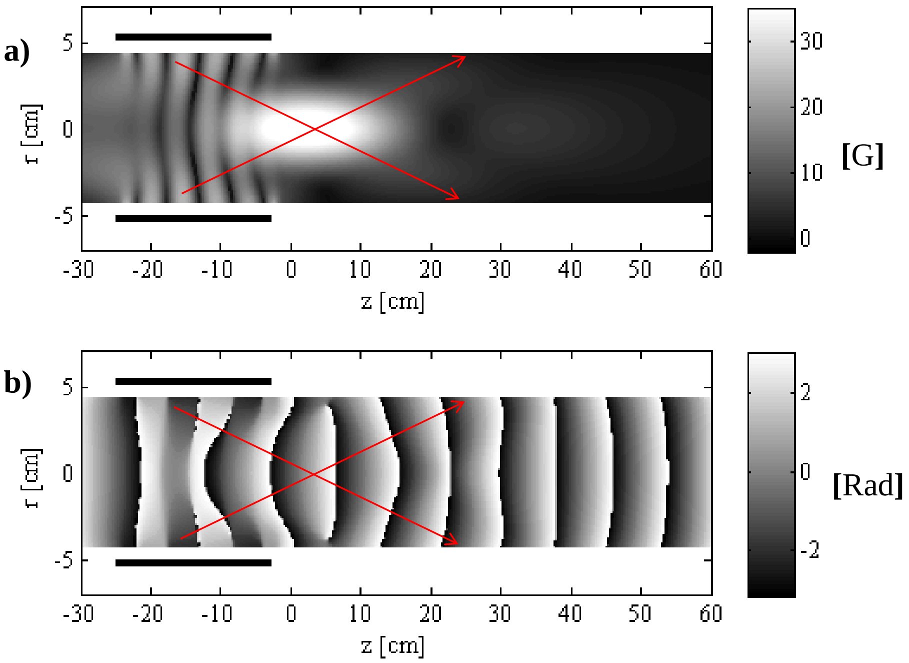

Figure 70, Same as Figure 69 but using a two-turn helical antenna $(2\theta = 4\pi)$.

In addition, we hypothesise that helicon discharges with strong wavefield interference patterns are indicative of antennas with broad spectra and not optimized to excite waves in the plasma. Under these circumstances, an optimized (narrow spectrum) antenna may increase wave-plasma coupling and reduce the interference patterns. The presence of a broad wavenumber spectrum implies the existence of waves with higher order radial modes. For this reason, we propose that the formation of wave interference patterns generally observed in long helicon discharges [30], [33], [35] can be explained by either of the following equivalent mechanisms: (1) waves travelling at an angle or (2) excitation of multiple radial modes. The former provides a physically intuitive explanation, while the latter provides a mathematical explanation in relation to the inverse Fourier transform of the plasma waveguide boundary value problem.

6.5 Helicon wave propagation in non-uniform magnetic fields

In the previous section we investigated helicon wave propagation in “quasi-uniform” magnetic fields, namely, the T100A S50A configuration (see Figure 59). We found that the 0D wave code was able to describe the helicon wave physics successfully and WKB calculations were consistent with experimentally observed wave attenuation. In the presence of strong magnetic field non-uniformities (thick line Figure 59) large plasma density gradients (parallel and radial) are formed and affect the propagation of waves. Under these circumstances a 2D full wave code is required to model wave propagation correctly.

6.5.1 Experimental observations

In Figure 71 we show experimentally measured B_r helicon wavefields along the axis of MAGPIE as the magnetic field non-uniformity is systematically increased. The blue and the red lines correspond to the “quasi-uniform” and “strong mirror” field configurations respectively. The operating conditions relevant to this experimental data are summarized in Table 7.

Figure 72 shows the corresponding “on axis” plasma density for various magnetic field configurations. The blue and red lines are associated with the “quasi-uniform” and “strong mirror” field configurations respectively. The black lines in between correspond to 50 A increments in the target region solenoid current.

As the magnetic field is increased, the magnitude of the wavefields increases, the interference pattern becomes more pronounced and its spatial frequency “compressed”. In addition, there is a corresponding increase in plasma density in the target region (Figure 72). In general, under conditions with strong magnetic field such as the “strong mirror” (red line) the radial plasma density is centrally peaked with strong radial gradients. Figure 17 in Chapter 2 (page 34) shows radial plasma density profiles associated with the “strong mirror” magnetic configuration.

Table 7, Operating conditions associated with the experimental data shown in Figure 71 and Figure 72.

Neutral gas	H_2 at 8 mTorr	Antenna radius	5.2 cm
RF power (nominal)	~20 kW at 7 MHz	Location	$-25 < z < -3$ cm
Antenna type	Half turn helical	Source solenoid current	50 A
Handedness	Left	Target solenoid current	50 - 450 A
Antenna current	180 A	Source field	40 – 75 G
Antenna length	22 cm	Maximum Target field	100 – 800 G

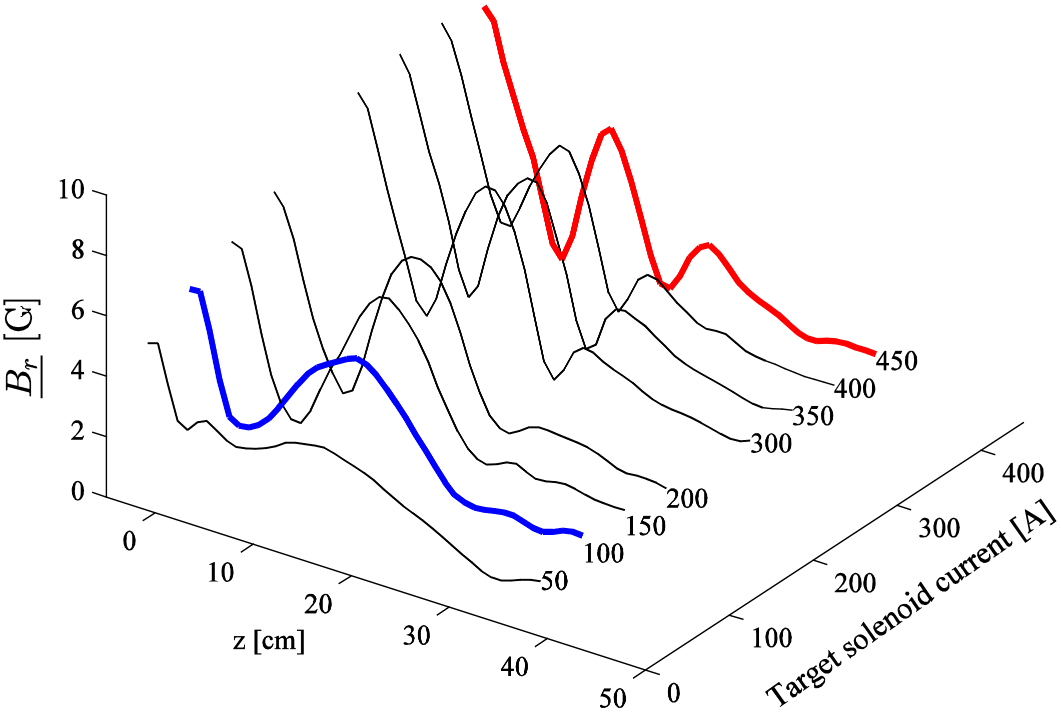

Figure 71, On-axis $\underline{B_r}$ helicon wave as a function target solenoid current. The antenna (not shown) is located between -25 < z < -3 cm. The source region solenoid current is fixed at 50 A. Operating conditions as per Table 7.

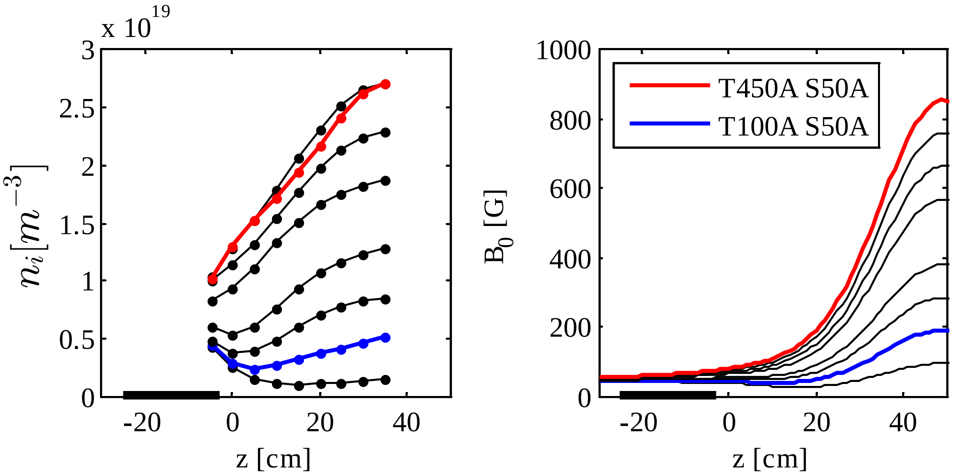

Figure 72, (a) Plasma density and (b) magnetic field along the axis of MAGPIE for various magnetic field configurations. Thick black horizontal line represents location of antenna. Operating conditions as per Table 7.

6.5.2 Axial wave attenuation

In this section, we compare theoretical and experimental axial wave attenuation based on the wavefields presented in Figure 71. Wave damping is modelled using the 0D wave code and the WKB expressions shown in Eq. 237 and Eq. 238. We calculate the imaginary wavenumber using both the “Quintic” (Eq. 230) and “helicon approximation” (Eq. 233). The motivation of this is two-fold: (1) demonstrate the discrepancy between 0D theory and experiment when strong gradients are not included and (2) demonstrate that in spite of the limitations of these theoretical tools we can still predict helicon wave damping under various conditions.

Figure 73 compares the on-axis $\underline{B_r}$ helicon wavefields presented in Figure 71 with WKB and 0D wave code calculations. For each case, the current in the source solenoid is 50 A. The corresponding target solenoid current is shown on the top label of each figure. The operating conditions are as in Table 7. WKB calculations are carried out using the experimentally measured plasma density, electron temperature and background magnetic field (Figure 72). To initialize the WKB calculation we use the measured wave amplitude at z = -5 cm. The 0D wave code calculations are based on mean plasma density, electron temperature, background magnetic field measured under the antenna region and a half-turn helical antenna at 180 A.

For all cases, we notice that the 0D wave code provides wave amplitudes and attenuation lengths that are in very good agreement with experiment. Both WKB calculations (“Quintic” and “Helicon approximation”) provide wave attenuation estimates in good agreement with experiment. Moreover, the agreement improves as we increase the magnetic field and hence plasma density. In these calculations, we find that both electron-ion and electron-neutral collisions are equally important and cannot be neglected. Failure to include any of these collisional processes leads to a non-negligible underestimation of wave damping. These results indicate that under the aforementioned operating conditions in MAGPIE, helicon wave dissipation can be explained entirely through collisional processes (e-i and e-n).

For the cases with target solenoid currents below 150 A, the experimental interference pattern is approximately reproduced by the 0D wave code. However, for cases beyond 200 A there is considerable discrepancy. The origin of the interference pattern in “quasi-uniform” field configurations is discussed in section 6.4.3. In the next section, we discuss the formation of the interference pattern formation in non-uniform plasma.

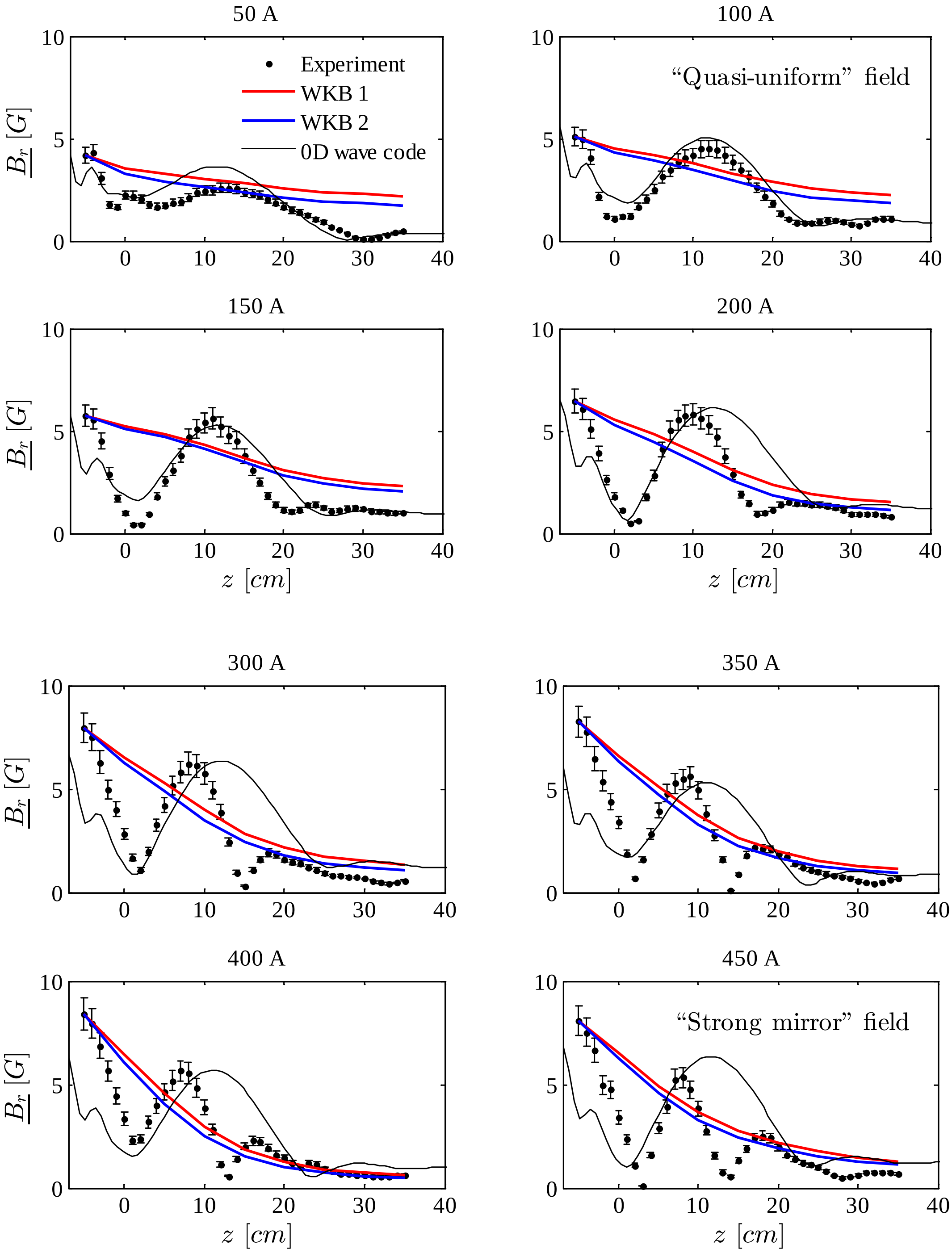

Figure 73, On-axis $\underline{B_r}$ helicon wavefields, WKB and 0D wave code calculations. The experimental data corresponds to that in Figure 71. The WKB 1 and WKB 2 calculations are based on the "helicon approximation" (Eq. 233), the "Quintic" (Eq. 230) damping relations and the WKB wave equation (Eq. 237). Operating conditions as per Table 2. The target solenoid current is labelled on each figure. Location of antenna (not shown) is -25 < z < -3 cm.

6.5.3 2D full wave code simulation

In what follows, we carry out a 2D full wave code simulation of MAGPIE and incorporate the radially and axially non-uniform plasma density, electron temperature and background magnetic field. This 2D wave code, which hereafter we refer to as EMS2D for “Electro-Magnetic Solver 2D, is described elsewhere [146], [149]. This code is based on the cold dielectric tensor in magnetized plasma and includes the effects of both electron-ion and electron-neutral collisions. The governing equations are discretised and solved using a finite difference scheme.

Input data

We model the wave propagation for the operating conditions described in Table 2 using a half-turn helical antenna 22 cm in length and the “strong mirror” (T450A S50A) magnetic field configuration. The plasma density and electron temperature axial and radial profiles are shown in Figure 74 and Figure 75 respectively. In both figures, the experimental data is approximated by analytical fits represented by coloured solid lines (see details in Appendix 6A). A conducting end plate exists in the experiment at z = 65 cm. Plasma density and electron temperature were not measured for z < -20 cm due to finite probe length. However, following the trend in the vicinity of z = -20 cm, we model the plasma density and electron temperature for z < - 20 cm using an exponential decaying function (blue line) with a length scale of about 10 cm. In Figure 75, we show the radial plasma density and electron temperature measured at z = 11 cm.

Additional experimentation and work by others [59] has shown that the shape (not magnitude) of the plasma density and electron temperature profiles in MAGPIE are approximately preserved along the magnetic field lines. Using this observation, the two dimensional data is represented by Eq. 239. The terms $T_e(z)$ and $n_i(z)$, represent the “z” variation of the electron temperature and plasma density on-axis (r = 0 cm) respectively (Figure 74). The terms $\overline{T_e}(r)$ and $\overline{n_i}(r)$, represent the “r” variation of the electron temperature and plasma density at an arbitrary axial position z_n. Quantities with an over-bar have been “normalized”, are dimensionless and describe the shape of the profile without regard to magnitude. The values of $\overline{T_e}$ and $\overline{n_i}$ are between 0 and 1.

$$T_e(r,z) = T_e(z) \times \overline{T_e}(r)\big|_{z_n} \quad n_i(r,z) = n_i(z) \times \overline{n_i}(r)|_{z_n} \qquad \text{Eq. 239}$$

In experiment, we observe that the diameter of the plasma column is reduced along the “z” direction due to the “pinching” effect of the magnetic field in the target region as demonstrated in Figure 5b Chapter 2. However, the EMS2D simulation does not include the effects of magnetic field “pinching”; therefore, the simulation domain is a cylinder with constant radius.

This simplification allows us to separate the “z” and “r” variations as described in Eq. 239. In this simulation, the terms $\overline{T_e}(r)$ and $\overline{n_i}(r)$, are scaled to describe the radial variation under the antenna (z = - 3 cm). The fitting procedure for both axial and radial experimental data is described in Appendix 6A of this Chapter.

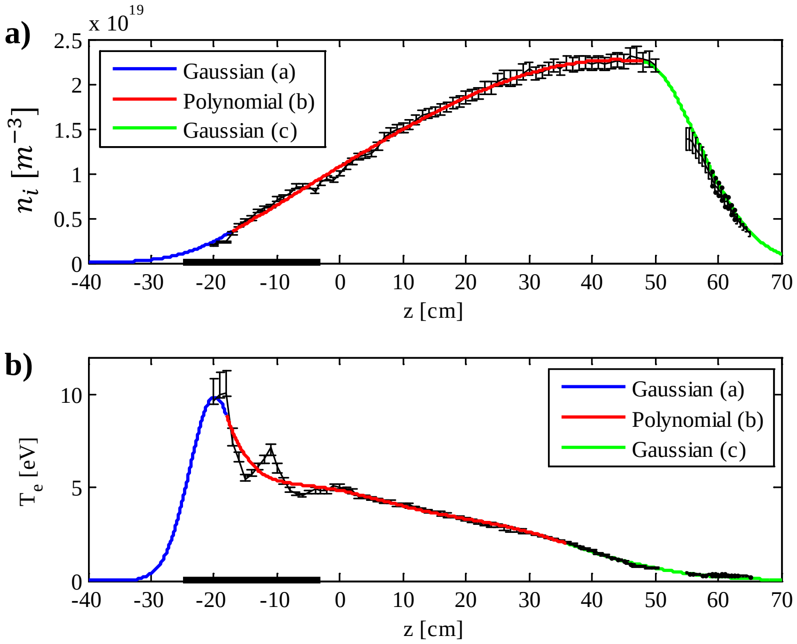

Figure 74, On-axis (a) plasma density and (b) electron temperature along the length of MAGPIE. The antenna is represented by the horizontal black line. Solid coloured lines represent analytical fits. Operating conditions as per Table 2 and “strong mirror” (T450A S50A) magnetic field configuration.

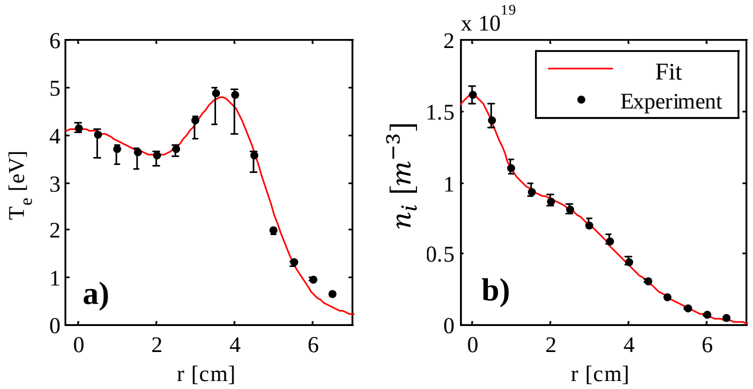

Figure 75, Radial (a) plasma density and (b) electron temperature measurements at z = 11 cm and corresponding to the measurements presented in Figure 74.

Results

Using the 2D analytical fits for the electron temperature and plasma density, the conditions in Table 2 and the “strong mirror” T450A S50A magnetic field configuration, the wavefield calculations from the EMS2D code are shown in Figure 76 and Figure 77. We have separated the numerical results into wave (a) amplitude and (b) phase. Agreement between the experimental and theoretical wave amplitude can only be achieved if we reduce the numerical amplitude by a factor of about 9. At this stage, we do not know the reason for this discrepancy and we are working to find a resolution[15]. However, regardless of this reduction factor the 2D wave code is able to approximately reproduce the experimentally measured beat pattern, parallel phase variation and attenuation length.

In Figure 76, we show “on axis” experimental data (dots) and EMS2D calculation (solid line) of B_r helicon wave amplitude and phase. The reduction factor has been applied to the EMS2D wave amplitude. We notice that the EMS2D calculation is capable of reproducing the experimentally observed interference pattern. However at z = 20 cm they are out of phase. We comment on this aspect in the next section. The phase calculation is consistent with the experimental phase variation and indicates that the wave propagates away from the antenna with a wavelength of about 10 cm.

In Figure 77, we provide 2D contour plots of B_r wavefields from the EMS2D code. Parts (a) and (b) correspond to amplitude and phase calculations respectively. The amplitude of the wave is centrally peaked and resembles the plasma density radial profile shown in Figure 75. In addition, the directionality of the antenna can be clearly seen from the axial asymmetry of the wavefields. The red arrows indicate the approximate direction of propagation of the wave based on the local phase variation in part (a). Waves are assumed to propagate normal to lines of constant phase. These arrows indicate that waves propagate away from the antenna at an angle with respect to the background magnetic field. Additionally, waves appear to be reflected inwardly before they reach the plasma edge. This effect is probably caused by strong radial density gradients which reduce the effective radius of the plasma column. Upon reflection, these waves constructively interfere on axis giving rise to the observed beat pattern. Notice that this mechanism is essentially the same as in the “quasi-uniform” field case (section 0) except that in the EMS2D calculation wave reflection happens before the plasma edge is reached.

---

[15] By reducing the effective collision frequency a factor of 10, the wave amplitude can be matched to experiment; however, the interference pattern can no longer be seen.

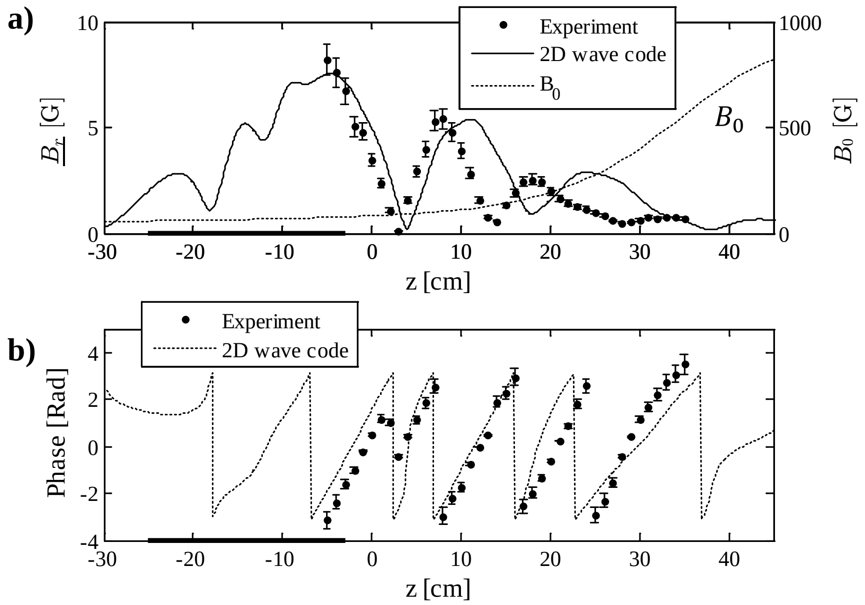

Figure 76, Experimental and theoretical (EMS2D) $\underline{B_r}$ on-axis wave (a) amplitude and (b) phase. Location of antenna represented by the horizontal thick black line. In part (a), dashed line represents the background magnetic field.

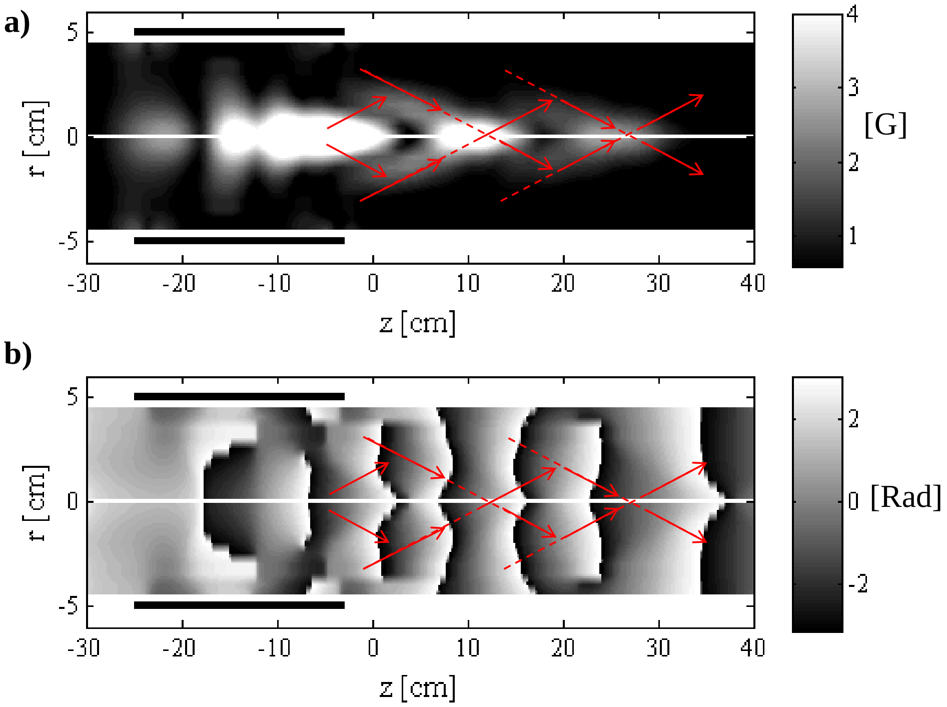

Figure 77, Numerical contour plots of (a) $\underline{B_r}$ wave amplitude and (b) phase corresponding to Figure 76. Antenna location represented by the horizontal thick black lines located at r = ± 5 cm.

6.5.4 Origin of the interference pattern

In the study of wave propagation in "quasi-uniform" magnetic fields, we found that waves are excited at the edge of the plasma by the azimuthal current rings. These waves travel inwardly at an angle to the background magnetic field, constructively interfere on axis and lead to the observed interference pattern (Figure 62 and Figure 66).

Experimental data in Figure 71 indicate that the spatial frequency of this interference pattern increases in proportion to the magnetic field in the target region. In other words, the interference pattern is "compressed" with increasing magnetic field strength. We attempted to explain this effect with the 0D wave code; but as shown in Figure 73, the 0D wave code is unable to reproduce the experimental interference patterns as the magnetic field in the target region is increased. However, by incorporating axial and radial density gradients using the EMS2D wave code, we were able to reproduce the experimental interference patterns formed during the "strong mirror" field configuration as shown in Figure 76.

The EMS2D results suggest that obliquely propagating waves are reflected by the radial density gradient before they reach the edge of the plasma[16]; thereby, reducing the effective radius of the plasma column. Since the radial density gradient scales with the magnetic field in the target region (Figure 16 and Figure 17 in Chapter 2), we anticipate that increasing the magnetic field in the target region will cause waves to be reflected at increasingly smaller radii. This effect will increase the number of times obliquely propagating waves constructively interfere on axis per unit length, thereby "compressing" the interference pattern.

The EMS2D calculation assumes the plasma radius is constant along the length of MAGPIE; from the perspective of the previously described wave reflection mechanism, a narrower plasma column caused by the magnetic compression will lead to wave reflection at smaller radii, thereby increasing the spatial frequency of the interference pattern. We hypothesise that the discrepancy in the interference pattern between the experiment and the EMS2D calculations in Figure 76, as the wave propagates into regions of stronger magnetic field, can be explained by the constant plasma radius assumption made in the EMS2D code which is clearly at odds with experimental observations as shown in Figure 17 in Chapter 2 (page 34). These experimental measurements indicate that the plasma radius is at least 4 cm at $z = 0$ cm and reduces to about 2 cm at $z = 35$ cm.

---

[16] This situation is akin to the reflection of light in a gradient-index optical fibre.

6.5.5 RF power deposition in MAGPIE

Figure 78 shows a two dimensional RF power deposition calculation from the EMS2D code. Location of the antenna is represented by the horizontal thick black lines at r = $\pm$ 5 cm. As noted previously, an amplitude reduction factor is required to match numerical wave amplitude with experimental data; therefore, we anticipate that the magnitude of the RF power deposition calculation is also overestimated. For this reason, we only consider the distribution of the RF power deposition and not its amplitude.

The RF power deposition is composed of a surface and “on-axis” contribution. The surface contribution is localized at the plasma edge under the antenna and has thin structures emanating from it at approximately 5 degrees with respect to the background magnetic field. These structures are not evident in the $\underline{B_r}$ calculation shown in Figure 77; thus, suggesting they are electrostatic in nature. Based on these observations, the aforementioned structures are recognized as electrostatic wave resonance cones; therefore, the surface power deposition is associated with the Trivelpiece-Gould wave. The “on-axis” contribution is consistent with the directionality of the helical antenna and its magnetic nature is evident from Figure 77. In addition, its angle of propagation (~14 degrees), attenuation length and interference pattern are consistent with the helicon wave. Therefore, we associate the “on-axis” RF power deposition with the helicon wave. We believe that these surface and “on-axis” RF power deposition components are responsible for the edge and “on-axis” electron temperature structures shown in Figure 75 of this Chapter and Figure 11 and Figure 18 of Chapter 2.

Since the length of MAGPIE (~70 cm) is much larger than the $1/e$ attenuation length of the helicon wave (~22 cm)[17]; the RF power deposition is expected to be axially non-uniform and localized near the antenna as shown in Figure 78. Under these conditions, RF electron heating and consequently the electron pressure will be axially non-uniform. In Figure 79, we repeat the electron pressure 2D profile presented in Chapter 2 to demonstrate that it is indeed non-uniform and consistent with the RF power deposition profile in Figure 78. For this reason, we anticipate that the non-uniform RF heating will produce pressure gradient driven flows in the plasma. We explore this matter in the next Chapter.

---

[17] The attenuation length is estimated using κ_I^{-1} (Eq. 233) and using n_e = 1× 10^{19} m^{-3}, κ_R = 60 m^{-1}, B_0 = 80 G, f = 7 MHz, T_e = 3 eV, H_2 at 8 mTorr. Including both Coulomb and electron-neutral collisions we obtain $\kappa_I^{-1} \approx$ 20 cm.

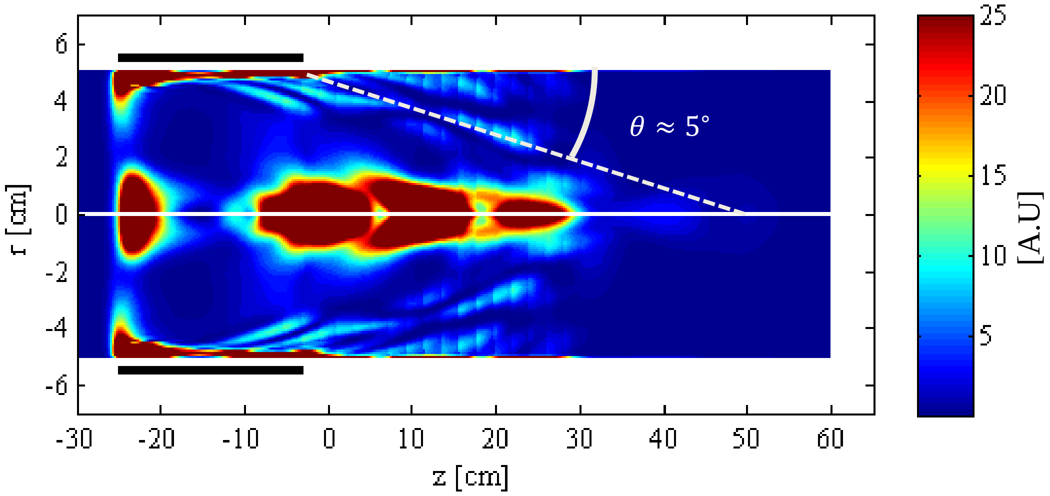

Figure 78, RF power deposition calculation (EMS2D) corresponding to Figure 76. Antenna represented by the horizontal thick black lines located at r = ± 5 cm. Plasma density and electron temperature profiles associated with this calculation are shown in Figure 74 and Figure 75.

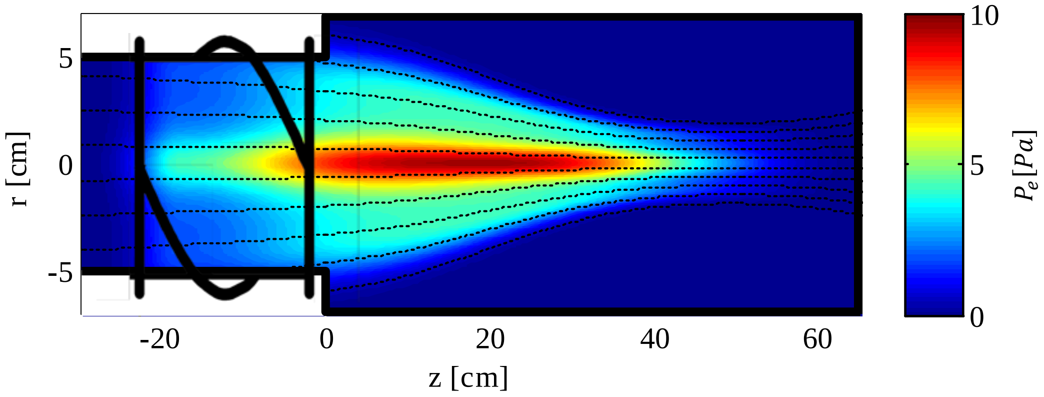

Figure 79, Electron pressure 2D representation estimated from experimental measurements of plasma density and electron temperature in MAGPIE (Figure 74 and Figure 75). Operating conditions as per Table 2 and “strong mirror” (T450A S50A) magnetic field configuration

6.6 Summary

Helicon wave propagation in the MAGPIE device has been investigated experimentally and theoretically. We have compared experimentally measured wavefields with theoretical calculations based on a 0D, 2D full wave code and WKB wave attenuation estimates.

Based on the operating conditions herein described, the main findings are the following: (1) whenever the RF antenna is not matched to the natural waves of the discharge, waves are primarily excited by the antenna's azimuthal current rings while the helical current strap plays a secondary role. (2) Helicon waves propagate approximately along the "whistler" wave ray direction and (3) constructively interfere on axis resulting in the axial interference pattern observed experimentally. (4) By correctly matching the antenna's spectrum to that of the natural waves in the plasma through an increase in the number of helical turns, simulations indicate that wave amplitude is maximized, wave excitation becomes dominated by the helical strap and wave interference under the antenna is no longer observed. (6) In addition, we demonstrate that helicon wave damping under these operating conditions can be explained entirely through collisional processes alone. (7) The 2D wave code simulation indicates that when the "strong mirror" field configuration is used radial density gradients are essential in reproducing the experimentally observed interference patterns. (8) Moreover, the RF power deposition is axially non-uniform and has both edge and on-axis components associated with the Trivelpiece-Gould and helicon wave respectively.

Appendix 6A. The WKB approximation

Let the complex valued function $f(z,t)$ represent a plane wave which satisfies the 1D wave equation shown in Eq. 240. The real valued variables z and ω represent the spatial coordinate along the direction of wave propagation and the angular frequency respectively. The complex parallel wavenumber is represented by κ and subscripts "I" and "R" indicate imaginary and real parts.

$$f'' = \left(\frac{\kappa}{\omega}\right)^2 \ddot{f} \quad \kappa = \kappa_R + i\kappa_I \qquad \text{Eq. 240}$$

Suppose the medium is non-uniform along the z coordinate and varies gradually relative to the wavelength of the waves which propagate through it. Under these conditions, we may assume a Wentzel-Kramers-Brillouin (WKB) solution as shown in Eq. 241, where $\phi(z)$ represents a complex phase and A_0 the amplitude of the wave at the location where it is launched (z = z_0).

$$f = A_0 \exp(i[\phi(z) - \omega t]) \quad \phi = \phi_R + i\phi_I \qquad \text{Eq. 241}$$

6A.1 Solution in 1D with attenuation

We take second derivatives of Eq. 241 with respect to time and space as shown in Eq. 242 and Eq. 243 respectively. Substitution of Eq. 242 and Eq. 243 in the complex wave equation (Eq. 240) yields the expression in Eq. 244.

$$\ddot{f} = -\omega^2 f \qquad \text{Eq. 242}$$

$$f'' = [i\phi'' - (\phi')^2]f \qquad \text{Eq. 243}$$

$$i\phi'' - \phi'^2 + \kappa^2 = 0 \qquad \text{Eq. 244}$$

To obtain a solution, we define the condition in Eq. 245 which hereafter is referred to the as the "WKB condition". Using this condition, Eq. 244 is reduced to the expression shown in Eq. 246, where "C" is a constant of integration and can be defined using boundary conditions. If we let $f(z = z_0, t = 0) = A_0$, the constant of integration is given by Eq. 247.

$$\phi'' \ll \phi'^2 \qquad \text{Eq. 245}$$

$$\phi(z) = \int_0^z \kappa(s)\, ds + C \qquad \text{Eq. 246}$$

$$C = -\int_0^{z_0} \kappa(s)\, ds \qquad \text{Eq. 247}$$

As a result, the WKB solution to the 1D complex wave equation (Eq. 240) can be written as in Eq. 248, where $A(z)$ and $G(z)$ are defined in Eq. 249 and z_0 is the location where the wave is initially launched. For positive κ_I, the function $A(z)$ describes the attenuation of the wave as it propagates along the "z" direction. The function $G(z)$ describes the propagation of the wave along a non-uniform medium. The validity of the WKB approximation is discussed next.

$$f = A(z)G(z,t) \quad z \geq z_0 \qquad \text{Eq. 248}$$

$$A(z) = A_0 \exp\left(-\int_{z_0}^{z} \kappa_I(s)\, ds\right) \quad G(z) = \exp\left(i\left[\int_{z_0}^{z} \kappa_R(s)\, ds - \omega t\right]\right) \qquad \text{Eq. 249}$$

6A.2 Validity criterion

If we assume a weakly damped wave such that $\kappa_R \gg \kappa_I$, we may re-express the "WKB condition" (Eq. 245) as shown in Eq. 250 by neglecting the imaginary terms. This expression states that as long as the gradient of the wavenumber is much less than the square of the local wavenumber, the WKB approximation is valid.

$$\frac{\partial \kappa_R}{\partial z} \ll \kappa_R^2 \qquad \text{Eq. 250}$$

Appendix 6B. Input data for the 2D wave code

6B.1 Radial profiles

The normalized radial profiles are expressed as a sum of three functions as shown in Eq. 251, where each term t_s and g_s is represented by a Gaussian function as shown in Table 8 and Table 9. Each of these expressions is dimensionless.

$$\overline{T_e}(r)\Big|_{z_n} = t_1 + t_2 + t_3 \quad \overline{n_i}(r)|_{z_n} = g_1 + g_2 + g_3 \qquad \text{Eq. 251}$$

Table 8, Analytical fits for the dimensionless radial electron temperature profiles.

$\overline{T_e}(r)\Big\|_{z_n}$	z_n= -3 cm	z_n= 11 cm
t_1	$\exp\left(-\frac{1}{2}\left[\frac{r}{3.4}\right]^2\right)$	$\exp\left(-\frac{1}{2}\left[\frac{r}{2.8}\right]^2\right)$
t_2	$0.8\exp\left(-\frac{1}{2}\left[\frac{r-4.74}{1.1}\right]^2\right)$	$0.8\exp\left(-\frac{1}{2}\left[\frac{r-3.9}{0.9}\right]^2\right)$
t_3	$0.8\exp\left(-\frac{1}{2}\left[\frac{r+4.74}{1.1}\right]^2\right)$	$0.8\exp\left(-\frac{1}{2}\left[\frac{r+3.9}{0.9}\right]^2\right)$

Table 9, Analytical fits for the dimensionless radial plasma density profiles.

$\overline{n_i}(r)\|_{z_n}$	z_n= -3 cm	z_n= 11 cm
g_1	$0.44\exp\left(-\frac{1}{2}\left[\frac{r}{0.75}\right]^2\right)$	$0.44\exp\left(-\frac{1}{2}\left[\frac{r}{0.62}\right]^2\right)$
g_2	$0.5\exp\left(-\frac{1}{2}\left[\frac{r-2.37}{2.2}\right]^2\right)$	$0.5\exp\left(-\frac{1}{2}\left[\frac{r-1.95}{1.81}\right]^2\right)$
g_3	$0.5\exp\left(-\frac{1}{2}\left[\frac{r+2.37}{2.2}\right]^2\right)$	$0.5\exp\left(-\frac{1}{2}\left[\frac{r+1.95}{1.81}\right]^2\right)$

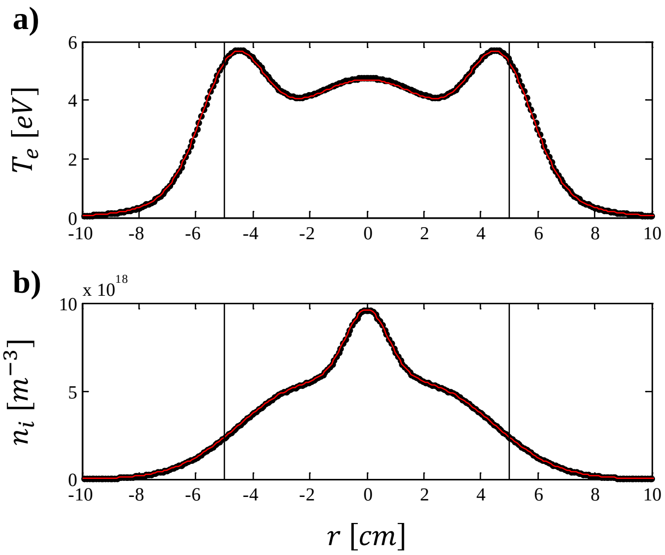

Figure 80, (a) Radial electron temperature and (b) plasma density at z = -3 cm using Eq. 251. The vertical black lines represent the plasma-dielectric interface.

6B.2 Axial profiles

The axial variation of electron temperature and plasma density in the region between z = -40 cm to z = 70 cm are described using a three part piecewise function (Eq. 252). The superscripts denote the region each part describes. We divide the axial domain into 3 regions (“a”, “b” and “c”), each corresponding to a part of the piecewise function, as shown in Table 10 and in Figure 74 (page 172). To provide a continuous and smooth connection between regions, the Gaussian functions “G” (Eq. 254) are connected with the polynomial functions “F” (Eq. 255) at the interface points z_I using the conditions shown in Eq. 253. By setting the width “w” of the Gaussian and the interface point z_I, a smooth and continuous interface is uniquely defined.

$$T_e(z) = T_e^k \quad n_i(z) = n_i^k \quad k = a, b, c \qquad \text{Eq. 252}$$

$$\frac{\partial G(z_I)}{\partial z} = \frac{\partial F(z_I)}{\partial z} \quad G(z_I) = F(z_I) \qquad \text{Eq. 253}$$

Table 10, Domain of the piecewise function for each region:

	$T_e(z)$	$n_i(z)$
Region “a” (Gaussian)	$-40 \le z \le -18\ cm$	$-40 \le z \le -18\ cm$
Region “b” (Polynomial)	$-18 \le z \le 36\ cm$	$-18 \le z \le 50\ cm$
Region “c” (Gaussian)	$36 \le z \le 70\ cm$	$50 \le z \le 70\ cm$

Region “a” (Gaussian fit)

Region “a” corresponds to the domain $-40 \le z \le -18$ cm where both electron temperature and plasma density fall exponentially. The Gaussian functions are represented as in Eq. 254 where “z” and “w” are in units of “cm”. The relevant coefficients are shown in Table 11 for the electron temperature and plasma density.

$$G(z) = A \exp\left(-\frac{1}{2}\left[\frac{z - z_0}{w}\right]^2\right) \qquad \text{Eq. 254}$$

Table 11, Region “a” Gaussian function coefficients. Valid only in the domain $-40 \le z \le -18$ cm

Region “a”	A	z_0	w
$T_e^a\ [eV]$	9.0464	-19.3107	4
$n_i^a\ [m^{-3}]$	8.819e+18	-3.3667	10

Region “b” (Polynomial fit):

In region “b” the electron temperature and plasma density axial variation are approximated by a 7th and 3rd order polynomial respectively, as shown in Eq. 255. Electron temperatures and plasma densities are given in units of eV and 10^{19} m^{-3} respectively.

$$T_e^b(z) = \sum_{s=0}^{7} C_s z^s \quad n_i^b(z) = \sum_{s=0}^{3} D_s z^s \qquad \text{Eq. 255}$$

The coefficients C_s and D_s for the electron temperature and plasma density polynomials are shown in Table 12 and Table 13 respectively. Notice that the “z” domains of the electron temperature and plasma density in region “b” do not have the same length. All significant digits shown should be retained.

Table 12, Region “b” electron temperature (eV), Valid only in the domain $-18 \le z \le 36$ cm

C_7	C_6	C_5	C_4	C_3	C_2	C_1	C_0
1.021e-11	1.096e-9	-2.528e-7	1.277e-5	-2.237e-4	3.306e-5	-0.043	4.634

Table 13, Region “b” plasma density (10^{19} $m^{-3)}$, Valid only in the domain $-18 \le z \le 50$ cm

D_7	D_6	D_5	D_4	D_3	D_2	D_1	D_0
-	-	-	-	-3.747e-6	-1.606e-4	0.0421	1.0902

Region “c” (Gaussian fit)

In both regions “a” and “c” the Gaussian functions are represented by Eq. 254 where “z” and “w” are in units of [cm]. The relevant coefficients are shown in Table 14 for the electron temperature and plasma density.

Table 14, Region “c” Gaussian function coefficients. The domains of validity are shown in the table.

Region “c”	A	z_0	w	Domain:
$T_e^c\ [eV]$	2.9387	20.6657	18	$36 \le z \le 70$ cm
$n_i^c\ [m^{-3}]$	2.3250e+19	49.9430	8	$50 \le z \le 70$ cm

Chapter 7 Plasma force balance and equilibrium profiles in MAGPIE

7.1 Introduction 186

7.2 Experimental setup 187

7.3 Experimental measurements 188

  7.3.1 Plasma density and electron temperature 188

  7.3.2 Plasma flow velocity 188

  7.3.3 Floating and plasma potential 189

  7.3.4 Electron pressure and thermal ionization 191

  7.3.5 Plasma magnetization 192

  7.3.6 Radial profiles 193

7.4 Theory 195

  7.4.1 Assumptions 195

  7.4.2 Dissociation of molecular hydrogen 195

  7.4.3 Neutral gas depletion 196

  7.4.4 Momentum exchange processes 196

  7.4.5 Momentum transport 199

  7.4.6 Particle transport 202

  7.4.7 Volumetric processes 202

  7.4.8 Equilibrium plasma density 205

7.5 Results 206

  7.5.1 Electron fluid force balance 206

  7.5.2 Particle sources and sinks 208

  7.5.3 Plasma flow velocity 211

  7.5.4 Equilibrium plasma density 213

  7.5.5 Estimating the neutral depletion and dissociation degree 214

7.6 Summary and conclusions 217

Appendix 7A. “Braginskii” two fluid formalism 220

Appendix 7B. Ion-neutral momentum transfer 222

Appendix 7C. Fluid magnetic mirror force 224

  7C.1 Plasma anisotropy 224

Appendix 7D. Neutral depletion in low-beta plasmas 225

7.1 Introduction

Experimental measurements of hydrogen plasma production in MAGPIE at 20 kW using converging background magnetic fields indicate that the plasma density increases monotonically away from the antenna region, reaches a maximum value of 2-3 $\times 10^{19}$ m^{-3} in the target region (z = 50 cm) and falls off rapidly approaching a conducting end plate located at 65 cm downstream of the antenna region.

In this chapter, we aim to understand the axial equilibrium plasma density profiles in MAGPIE. Specifically, we explore the mechanism that drives the plasma into the magnetic mirror where it reaches a maximum value. First, we describe the magnetized plasma in MAGPIE using a two fluid “Braginskii” type formalism [129], [130], where interaction between fluids is accounted for through momentum transfer collisions and the ambipolar electric field. We evaluate the forces that govern the electron fluid; namely, the electric, pressure, and thermal forces. Furthermore, we calculate the plasma sources and sinks along the length of MAGPIE by measuring the parallel plasma flux. We calculate the flow velocity and the equilibrium plasma density along the length of MAGPIE using a 1D diffusive transport model. Finally, we comment on the limitations of this analysis and summarize the main findings

Table 15, Operating conditions associated with the experimental data shown in this chapter.

Neutral gas	H_2 at 8 mTorr	Antenna radius	5.2 cm
RF power (nominal)	~20 kW at 7 MHz	Antenna location	-25 < z < -3 cm
Antenna type	Half turn helical	Source solenoid current	50 A
Handedness	Left	Target solenoid current	450 A
Antenna current	180 A amplitude	Source field	60-70 G
Antenna length	22 cm	Maximum Target field	850 G

7.2 Experimental setup

In what follows, we investigate the plasma particle and momentum transport in the "downstream" region of the MAGPIE device. MAGPIE's experimental setup is described in Chapter 2. Details specific to this section are described next. We used the "strong mirror" magnetic field configuration (T450A S50A) shown in Figure 81a. The discharge was operated with H_2 at 8 mTorr. RF power was delivered to the plasma in 2 ms pulses at a repetition rate of 10 Hz through a left-handed half turn helical antenna driven at 7 MHz, 22 cm in length, 12 cm in diameter and located between -25 cm and -3 cm along the "z" axis. For these operating conditions, it was observed that plasma diagnostic signals achieved steady state for times greater than 1 ms; hence, all measurements herein reported corresponds to times greater than this. RF power was measured by directional couplers and kept at 20 ± 2 kW. Antenna matching was adjusted to maintain the reflected RF power to a minimum. Antenna current was measured to be 180 ± 10 A amplitude. The operating conditions are summarized in Table 15. Plasma density, electron temperature and floating potential profiles where measured at the center of the discharge from z = -20 cm to z = 65 cm with 1 cm resolution using a Double Langmuir Probe (DLP). In addition, radially resolved measurements of these quantities were taken at z = 11 cm. The on-axis plasma flow velocity was measured with a Mach probe with current collecting tips 5 mm in length and 1 mm in diameter. Individual (Langmuir and Mach) probe tips where regularly cleaned with electron saturation current at 60 V, 3.5 A, 1 ms pulse length and 10 Hz repetition rate. Plasma density calculations based on ion saturation current assume H^+ as the dominant ion species[18]. In Chapter 3, we describe the measures taken to ensure DLPs were RF compensated using the ideas presented in Chapter 4.

Plasma potential measurements are often performed using the electron saturation current inflection point. However, this method can become complicated in the presence of strong magnetic fields. Whenever the probe radius is comparable to the Larmour radius, the electron current becomes strongly affected by magnetization and one cannot infer plasma potentials from the inflection point. In this experiment, we use RF compensated DLPs to measure electron temperature and floating potential; these measurements are used to infer the plasma potential using Eq. 256, which assumes Maxwell-Boltzmann distributed electrons. Hereafter, the terms V, V_f, T_e, M_i and m_e represent the plasma potential, floating potential, electron temperature, ion mass and electron mass respectively. For a proton plasma the expression in brackets is approximately 3.3. References [153], [154] describe the use of Eq. 256 to successfully infer the plasma potential. In fact, reference [153] uses this method to infer "E×B" rotation which is quantitatively consistent with Mach probe measurements. It must be noted that in the presence of significant RF rectification, there is uncertainty in the RF self-bias produced at the probe's sheath and the plasma potential cannot be correctly inferred.

---

[18] In Chapter 3, a comparative study between DLPs and microwave interferometry indicates that protons are the dominant ion species in MAGPIE above 10 kW when operating with H_2 between 2 and 8 mTorr.

$$V = V_f + T_e \ln\left(\frac{1}{0.61}\sqrt{M_i/2\pi m_e}\right) \qquad \text{Eq. 256}$$

7.3 Experimental measurements

7.3.1 Plasma density and electron temperature

Figure 81 shows plasma density and electron temperature measurements on-axis and along the length of MAGPIE. The plasma density increases away from the RF antenna, peaks at the maximum magnetic field and falls off rapidly in the vicinity of the end plate at z = 65 cm. Near the end plate the electron temperature is very low (~0.5 eV) and the plasma appears to be "detached". The electron temperature, supported by the RF power deposition, is highest in the vicinity of the antenna. Away from the antenna (z > 20 cm), wave power deposition is less important and the electron fluid heat source is small. Beyond this point, the electron fluid cools down through electron-neutral and electron-ion collisions, while being subject to microscopic thermal heat conduction and heat convection through bulk fluid flow. At this stage we are unable to explain the short length scale (< 10 cm) electron temperature structures measured under the antenna. The presence of standing wavefields excited under the antenna may lead to such electron temperature profiles. However, based on local plasma density (0.7 x 10^{19} m^{-3}), electron temperature (5-6 eV) and 8 mTorr the electron mean free path in this region is between 4 and 6 cm, which is long compared to the length scale of the observed electron temperature gradient under the antenna region. Electron temperature measurement errors due to RF rectification and/or non-Maxwellian distributions may also be important in this region where the density is the lowest and RF fields are strongest. Further investigation on this matter is required.

7.3.2 Plasma flow velocity

Figure 82 shows the on-axis plasma flow velocity (in Mach numbers) along the length of MAGPIE measured with a Mach probe and a calibration factor K = 1.66 for magnetized plasma [155]. We observe flow reversal at $z \approx$ 10-15 cm, maximum flow of Mach 0.7 at $z \approx 50$ cm and deceleration for $z > 50$ cm. Using the measured plasma density and flow, we estimate the plasma flux along the discharge and make estimates of particle sources and sinks (section 7.5.2).

7.3.3 Floating and plasma potential

Floating and plasma potential measurements on-axis and along the length of MAGPIE are shown in Figure 83. The floating potential, shown in the figure for completeness, is measured only to estimate the plasma potential from the electron temperature. Under the antenna the plasma potential appears to have some structure similar to the electron temperature; however, downstream of the antenna it decreases monotonically into the target region. This drop in plasma potential for z > 0 cm is approximately 5 eV. The mean temperature in this region is about 3 eV and the ion-neutral mean free path of about 2 cm (see section 7.4.4). This indicates that the electric field measured along the length of the plasma scales with the electron temperature over a distance of about 30 ion-neutral mean free paths. Next, we present estimates of the electron pressure, thermal ionization and plasma magnetization based on the measurements presented.

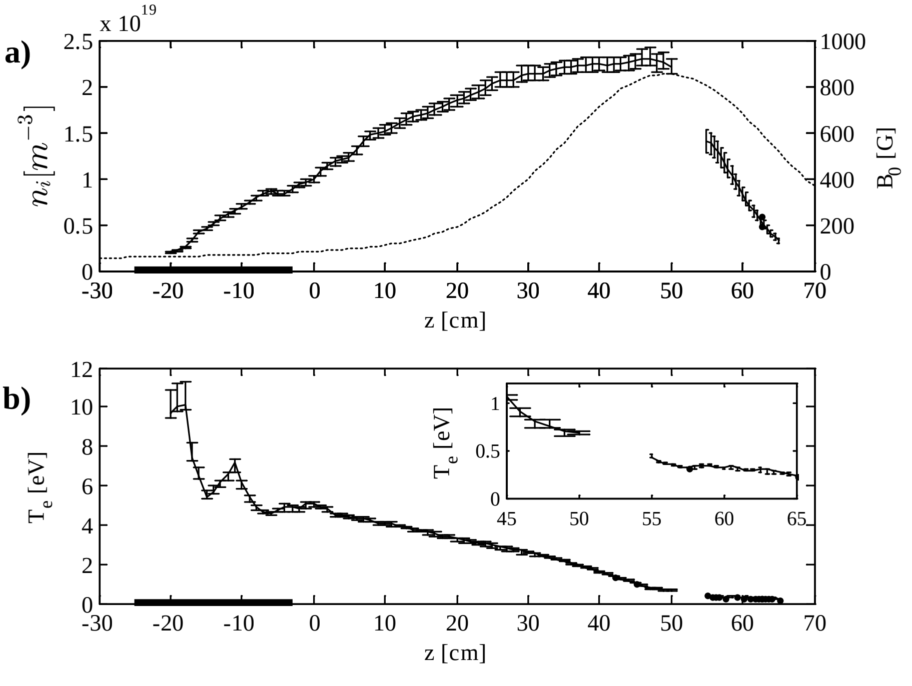

Figure 81, (a) Plasma density and (b) electron temperature measurements on-axis and along the length of MAGPIE. Magnitude of background magnetic field (thin line) is shown in part (a). A detailed plot of the electron temperature measurements near the end plate is shown in the inset. The discharge is as per Table 15.

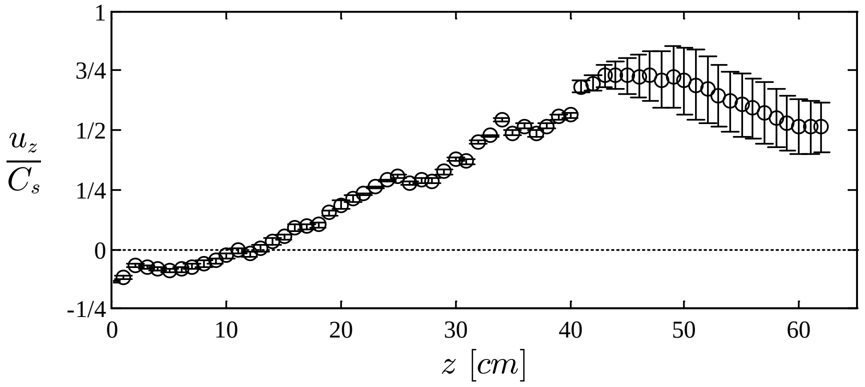

Figure 82, On-axis plasma flow measurement along the length of MAGPIE using a Mach probe with calibration factor K = 1.66 for magnetized plasma. Operating conditions as per Table 15.

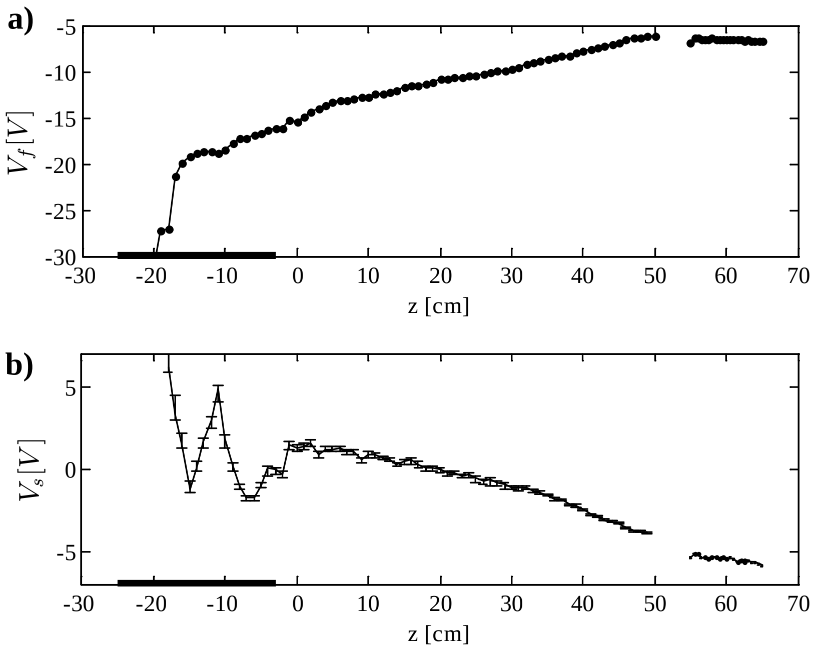

Figure 83, (a) Floating potential and (b) plasma potential measurements on-axis and along the length of MAGPIE. Plasma potential based on Eq. 256 and floating potential and electron temperature measurements. Operating condition as per Table 15.

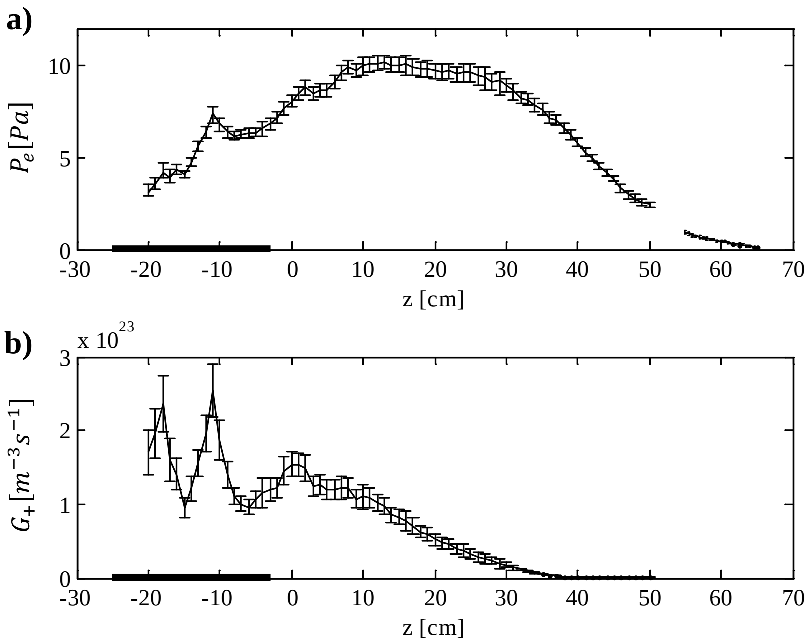

Figure 84, (a) Estimated electron pressure and (b) proton thermal ionization rate based on plasma density and electron temperature measurements shown in Figure 81. Details of the thermal ionization calculation are given in section 7.4.7. Operating condition as per Table 15 and assuming $n_H = 0.1n_{H_2}$.

7.3.4 Electron pressure and thermal ionization

Figure 84 shows the electron pressure and proton thermal ionization rate estimated from the plasma density and electron temperature measurements in Figure 81. Thermal ionization rate is based on Eq. 281 and Eq. 283. These equations are discussed section 7.4.7. Under these conditions, the length of MAGPIE (~70 cm) is larger than the $1/e$ parallel attenuation length of the helicon wave (~22 cm) as discussed in section 6.5.5; hence, RF power deposition is non-uniform in the vicinity of the antenna region. Consequently, electron heating and thermal plasma production occur mostly in the vicinity of the antenna and lead to a non-uniform electron pressure profile. In fact, the electron pressure profile shown above is consistent with the RF power deposition profile shown in Figure 78 in Chapter 6. The electron pressure peaks away from the antenna region at about z = 10 cm and the associated gradients are able to drive flow in the plasma. The proton thermal ionization rate extends from under the antenna to about 30 cm away. This indicates that the bulk of the plasma production occurs in the region $-20 < z < 20$ cm.

7.3.5 Plasma magnetization

Using the electron temperature and plasma density measurements shown in Figure 81 we assess the electron and ion magnetization in the discharge. Magnetization will be affected by momentum transfer collisions, the magnitude of the background magnetic field and the radial size of the discharge. More specifically, a charged particle can be considered magnetized if Eq. 257 is satisfied. In addition, magnetization in bounded plasma requires that Eq. 258 is simultaneously satisfied.

$$\nu_\beta/\Omega_{c\beta} \ll 1 \quad \beta = e, i \qquad \text{Eq. 257}$$

$$r_L^\beta/r_d \ll 1 \qquad \text{Eq. 258}$$

The subscript β denotes the charge particle species; namely, electron or ion. The terms ν_β , $\Omega_{c\beta}$, r_L^β and r_d represent the total momentum transfer collision frequency, Gyro-frequency, Larmour radius and the effective radius of the discharge. The total momentum transfer collision frequency includes both Coulomb and neutral collisions. Collisions with neutral are calculated as in [60, Sec. 3.3]. The electron Larmour radius was calculated using the electron thermal speed based on the local electron temperature. To calculate the ion Larmour radius we notice that ions and electrons are closely bound through the ambipolar electric field which scales with the electron temperature. For this reason we use the ion sound speed based on the local electron temperature to calculate the ion Larmour radius as done in [148]. Figure 85 shows a calculation of the aforementioned magnetization parameters for both ions and electrons on-axis and along the length of MAGPIE.

In the top figure, we observe that collisional processes allow electrons to be well magnetized throughout all the discharge ($\nu_e/\Omega_{ce} \ll 1$). Ions are marginally magnetized for z < 0 cm ($\nu_i/\Omega_{ci} \leq 1$) and well magnetized ($\nu_i/\Omega_{ci} \ll 1$) for z > 20 cm. In the vicinity of the end plate, the low electron temperature leads to a substantial increase in the Coulomb collision frequency; hence, the value of $\nu_\beta/\Omega_{c\beta}$ increases. In the bottom figure, the electron thermal Larmour-radius is much smaller than the discharge effective radius for all “z”. This is only true for ions for z > 20 cm. However, if we include the thermal distribution of ion speeds, low-energy ions will have smaller Larmour radii and ion magnetization must be considered throughout the length of MAGPIE. This calculation indicates that plasma magnetization is important over the entire length of MAGPIE.

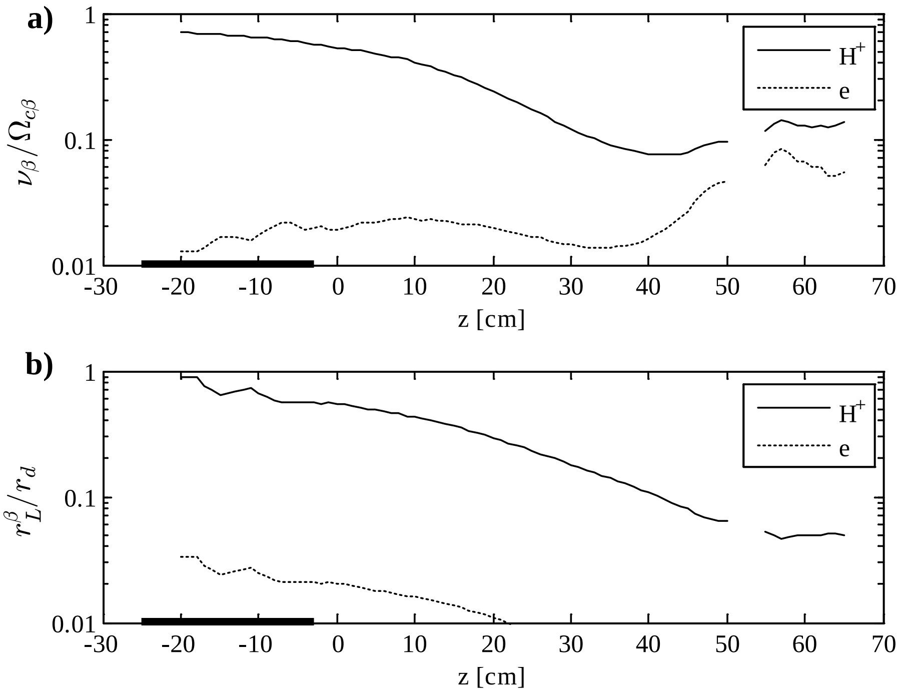

Figure 85, Magnetization parameters on-axis and along the length of MAGPIE. Part (a) represents the ratio between momentum transfer collision frequency and Gyro-frequency; part (b) represents the ratio between Larmour-radius and plasma effective radius. Operating condition as in Table 2.

7.3.6 Radial profiles

For completeness, in Figure 86 and Figure 87 we show the corresponding radial profiles of ion density, electron temperature, floating potential and plasma potential measured at z = 11 cm. The operating conditions are as per Table 2. The centrally peaked density profile is typical of helicon discharges such as MAGPIE. The electron temperature profile indicates the presence of both a central and edge heat source; possibly due to RF wave heating on-axis and at the edge associated with the helicon and TG wave respectively (Figure 78 in Chapter 6). The plasma potential, estimated from measurements of both electron temperature, floating potential and Eq. 256, indicates the presence of a radially inwards electric field which induces ion confinement. Modelling this process requires a fully 2D equilibrium/transport model which is beyond the scope of this thesis.

Curreli and Chen [148] have shown the presence of non-ambipolar radial electric fields in helicon discharges; in other words, the electric field is not ion confining. They explain this phenomenon through the "short-circuiting" effect which allows electrons to follow a Boltzmann distribution even across the magnetic field and lead to high plasma density in regions of high plasma potential. A fundamental assumption of the "short-circuiting" effect is non-magnetized ion motion, as explained in [148], [156], where the ion Larmour-radius is assumed to be much larger than the discharge size. However, in MAGPIE at the operating conditions herein described protons must be considered magnetized throughout the discharge length as shown in Figure 85. We believe that under these conditions of proton magnetization, the "short-circuiting" effect does not occur and radial ambipolar diffusion becomes important. This provides a possible explanation for the inward directed (ion confining) radial electric field measurements in MAGPIE. However, further investigation on this matter is required.

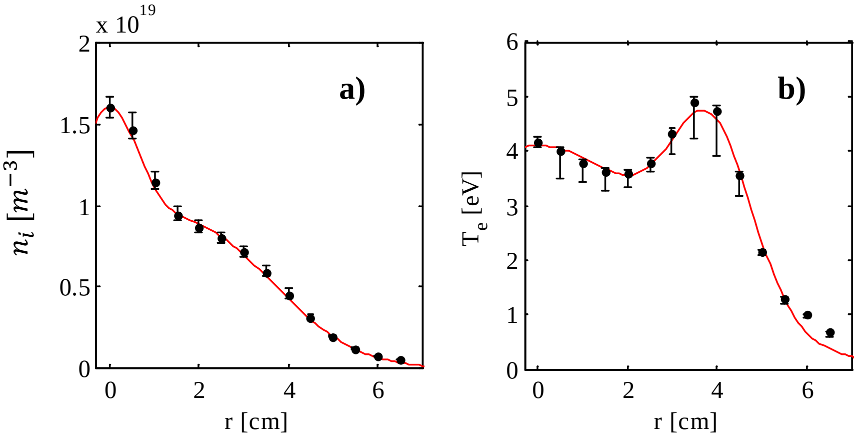

Figure 86, Radial measurements of (a) ion density and (b) electron temperature at z = 11 cm. Ion density calculation based on protons. The red line represents a smooth fit on the data. Measurements were taken with a DLP. Operating condition as per Table 2.

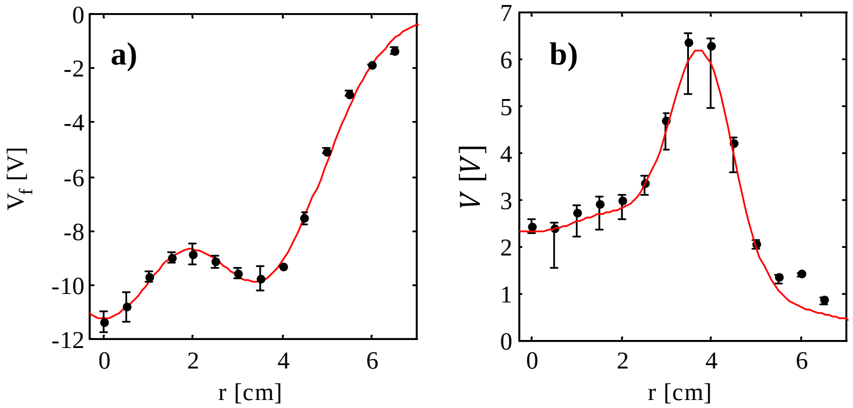

Figure 87, Radial measurements of (a) floating potential and (b) plasma potential calculated using Eq. 256 and measured with a DLP. Operating condition as per Table 2.

7.4 Theory

In this section, we present the theory for describing the plasma in MAPGIE. In section 7.5, we use the theory to explain the experimental measurements presented in section 7.3

7.4.1 Assumptions

In the theoretical analysis that follows, we assume a steady state partially ionized plasma comprised of Maxwell-Boltzmann distributed electrons at a temperature T_e. We assume the ion fluid is composed entirely of protons (H^+) at a temperature $T_i \ll T_e$, the neutral fluid is uniform, comprised of molecular (H_2) and atomic hydrogen (H) and include neutral gas depletion [49], [50], [51], [52], [53], [54], [157], [158], [159], [160], [161]. We assume the plasma is well magnetized and confined to flow only along the magnetic field lines. We neglect radial particle transport relative to parallel transport; therefore, we model the plasma as being one-dimensional. We employ a two fluid “Braginskii” type approach [1], [129], [130], [131] to study the particle and momentum transport in MAGPIE. A brief description of the “Braginskii” formalism is provided in Appendix 7A. The charged and neutral particles are modelled as interpenetrating fluids that interact with each other through momentum transfer collisions and the ambipolar electric field in the case of charged particles. We neglect viscous effects (e.g. electron pressure is isotropic) and ionization drag.

7.4.2 Dissociation of molecular hydrogen

Production of low temperature discharges in molecular gases generally leads to some dissociation of the initial gas through electron impact [46], [162]. For this reason, we include the presence of both molecular and atomic hydrogen neutral species. Hereafter, the term $n_{H_2}^0$ represents the molecular hydrogen particle density before the discharge is initiated; the terms n_{H_2} and n_H represent the molecular and atomic hydrogen particle density during the discharge respectively. Using these terms, we define the degree of dissociation η as in Eq. 259 [163] and express the atomic hydrogen density as in Eq. 260.

$$\eta = \frac{n_H}{2n_{H_2} + n_H} \qquad \text{Eq. 259}$$

$$n_H = \left(\frac{2\eta}{1-\eta}\right) n_{H_2} \qquad \text{Eq. 260}$$

7.4.3 Neutral gas depletion

In the literature of helicon plasma sources, neutral depletion [53]-[161] refers to the reduction of neutral particle density within the plasma volume during the discharge. This process is driven primarily by the following mechanisms: (1) ionization rate exceeding the neutral gas refuelling rate, (2) neutral gas heating and (3) transport of neutrals driven by friction with ions leaving regions of high electron pressure. Refer to Appendix 7D for more details on this last mechanism.

In this analysis, we neglect neutral particle and momentum transport; hence, neutral gas depletion is not explicitly modelled. However, we incorporate its effect by assuming that at the center of the plasma volume the neutral particle density is some fraction of the neutral particle density before the discharge ($n_{H_2}^0$). Hereafter, we define the neutral gas depletion fraction f as in Eq. 261.

$$f = \frac{2n_{H_2} + n_H}{2n_{H_2}^0} \qquad \text{Eq. 261}$$

Using Eq. 260 and Eq. 261, we can express the molecular and atomic hydrogen density during the discharge as a function of the initial neutral particle density ($n_{H_2}^0$), dissociation degree (η) and neutral depletion fraction (f) as shown in Eq. 262 and Eq. 263.

$$n_{H_2} = n_{H_2}^0[(1-\eta)f] \qquad \text{Eq. 262}$$

$$n_H = n_{H_2}^0[2\eta f] \qquad \text{Eq. 263}$$

Collisional processes such as electron impact ionization, electron/ion-neutral momentum transfer and plasma recombination in molecular gases depend on the neutral particle density; hence, both the depletion fraction and the dissociation degree are important quantities for correctly calculating particle, momentum and heat transport in partially ionized plasma.

7.4.4 Momentum exchange processes

In this analysis, we assume that ions exchange momentum with both molecular and atomic hydrogen. We consider only H^+ and other positive and negative ions are neglected. According to [77], the fraction of protons (H^+) increases with RF power for discharges with electron temperatures and densities comparable to MAGPIE. As described in Chapter 3, comparison between line integrated microwave interferometry and DLP ion density measurements indicate that H^+ is the dominant ion when operating at RF power levels greater than 10 kW in the 2 to

8 mTorr pressure range in MAGPIE. For H_2 discharges with comparable electron temperature, density and RF power as MAGPIE, reference [77] indicates that the molecular hydrogen population is dominated by the ground state. Therefore, the relevant momentum transfer collisions are (1) $H^+ + H_2(\nu = 0)$ and (2) $H^+ + H$, where ν represents the vibrational excitation level. In what follows, the momentum transfer cross sections for these processes are labelled σ_{H_2} and σ_H respectively.

Proton and molecular hydrogen

Krstic and Schultz [164] provide calculations of elastic (EL), momentum transfer (MT) and charge exchange (CX) cross sections for the "$H^+ + H_2$" process in the 0.1 to 10 eV centre of mass (CM) energy interval. The analysis indicates that between 0 and 8 eV the MT is larger than the CX and the inelastic (VIB,DIS) cross sections by at least an order of magnitude provided H_2 is in the ground state ($\nu = 0$). However, for vibrationally excited states of H_2 greater than 3, the CX and VIB exceed the MT cross section. In our analysis we assume $H_2(\nu = 0)$ for the bulk region of the plasma where electron temperature is above 1 eV. In the CM energy range of 0.1 to 1 eV, σ_{H_2} is between 2 and 4×10^{-19} m^{-2} for ground state H_2.

Proton and atomic hydrogen

At low energies, the scattering of protons from atomic hydrogen has a very large cross section due to the resonant charge exchange contribution [165]; For this reason, this process is an important momentum transfer channel in partially ionized hydrogen plasma. Momentum transfer for this process occurs through both elastic (EL) and charge exchange (CX) mechanism. For high velocity protons, these reactions (EL and CX) are distinguishable; hence, enabling the labelling of the projectile and the target. At low energies, quantum indistinguishability prevents classical labelling of the particles and EL and CX scattering mechanisms overlap. Under these circumstances, cross section calculations include both EL and CX contributions and are referred to as quantum indistinguishable particle (QIP) calculations. Schultz [165] provides QIP calculations of σ_H in the 10^{-4} to 10^{6} eV CM energy range. Krstic [166] compares QIP calculations of σ_H and σ_{H_2} in the CM energy range of 0.1 to 100 eV. Between 0.1 and 1 eV CM energy range, it is possible to approximate $\sigma_H \approx 3\sigma_{H_2}$ for ground state H_2. In this energy range, σ_H is between 6 and 10×10^{-19} m^{-2}.

Collision frequency

For protons colliding with molecular and atomic hydrogen, we express the total momentum transfer collision frequency as $\nu_{in} = \nu_{iH} + \nu_{iH_2}$. Using Eq. 310 from Appendix 7B, the total ion-neutral momentum transfer collision frequency can be expressed as in Eq. 264.

$$\nu_{in} = \frac{3}{8} n_H \sigma_H(\bar{v}_{rH})\bar{v}_{rH} + \frac{1}{2} n_{H_2}\sigma_{H_2}(\bar{v}_{rH_2})\bar{v}_{rH_2}$$

$$\bar{v}_{rH} = \left(\frac{10eT}{M}\right)^{1/2} \quad \bar{v}_{rH_2} = \left(\frac{15eT}{2M}\right)^{1/2} \qquad \text{Eq. 264}$$

Assuming that all three species, e.g. H_2, H and H^+, are at the same temperature T, we can approximate $\bar{v}_{rH_2} \approx \bar{v}_{rH} \equiv \bar{v_r}$ which leads to Eq. 265, where M is the proton mass.

$$\nu_{in} \approx \frac{3}{8} n_H \sigma_H(\bar{v_r})\bar{v_r} + \frac{1}{2} n_{H_2}\sigma_{H_2}(\bar{v_r})\bar{v_r} \qquad \bar{v}_r = \left(\frac{10eT}{M}\right)^{1/2} \qquad \text{Eq. 265}$$

From Krstic [166], in the CM energy range 0.1 to 1 eV, we can approximate $\sigma_H \approx 3\sigma_{H_2}$. We have selected the QIP calculation to account for both resonant CX and EL contributions to σ_H at low energies. At 1 eV CM energy we obtain $\sigma_H \approx$ 8 × 10^{-19} m^2 from Krstic's QIP calculation and $\sigma_H \approx$ 5-8 × 10^{-19} m^2 from Brennan's experiment [167] for 1 eV protons in a hydrogen discharge. Using $\sigma_H \approx 3\sigma_{H_2}$ in Eq. 265, leads to Eq. 266.

$$\nu_{in} = \sigma_H(\bar{v_r})\bar{v_r}\left(\frac{3}{8}n_H + \frac{1}{6}n_{H_2}\right) \qquad \text{Eq. 266}$$

Replacing n_{H_2} and n_H with Eq. 262 and Eq. 263, the total ion-neutral momentum transfer collision frequency is given in Eq. 267, where the dependence on the neutral depletion fraction f and dissociation degree η can be appreciated.

$$\nu_{in} = \nu_{in}^0\left[f\left(\frac{7\eta}{12} + \frac{1}{6}\right)\right] \qquad \nu_{in}^0 = \frac{\bar{v_r}}{\lambda_{in}^0} \quad \lambda_{in}^0 = \frac{1}{n_{H_2}^0 \sigma_H(\bar{v_r})} \qquad \text{Eq. 267}$$

As an example, for H_2 gas at 8 mTorr and 300 K before the discharge is initiated, the neutral gas density is approximately $n_{H_2}^0$ =2.7 × 10^{20} m^{-3}. For a proton temperature of about T_i =0.1 eV, we must evaluate σ_H at $5T_i$ CM energy. This leads to σ_H =6-8×10^{-19} m^2, $\nu_{in}^0 \approx$ 2 MHz and $\lambda_{in}^0 \approx$ 0.5 cm. If we assume a neutral depletion fraction of f = 0.2, a dissociation degree of η =0.2, the mean free path becomes $\lambda_{in} \approx$ 8 cm and the effective ion-neutral momentum transfer collision frequency ν_{in} =114 kHz. The contributions from the atomic and molecular processes are $\nu_H \approx 60$ kHz and $\nu_{H_2} \approx 54$ kHz respectively.

7.4.5 Momentum transport

The momentum transport equation (Eq. 295) presented in Appendix 7A can be further simplified by assuming: (1) the plasma is quasi-neutral and (2) in dynamic (flowing) steady state. This leads to Eq. 268, where the summation is over all neutral species X, e.g. H_2 and H.

$$m_\alpha n\left[(\boldsymbol{u}_\alpha \cdot \nabla)\boldsymbol{u}_\alpha + \sum\nolimits_X \nu_{\alpha X}(\boldsymbol{u_\alpha} - \boldsymbol{u_X})\right] = nq_\alpha(\boldsymbol{E} + \boldsymbol{u}_\alpha \times \boldsymbol{B}) - \nabla P_\alpha + \boldsymbol{f}^R_{\alpha\beta} + \boldsymbol{f}^T_{\alpha\beta} \qquad \text{Eq. 268}$$

Let us assume that the partially ionized plasma is very collisional such that the electron-neutral and ion-neutral collisional mean free paths are much smaller than the characteristic length scales of the Lorentz and pressure forces. Under these circumstances, the plasma motion is diffusive and we can neglect the kinetic energy term $(\boldsymbol{u}_\alpha \cdot \nabla)\boldsymbol{u}_\alpha$ relative to the neutral drag term. In addition, we assume that the different neutral fluids are strongly coupled through collisions such that they flow at the same velocity $\boldsymbol{u}_n$. With these simplifications, the ion and electron momentum transport equations can be expressed as in Eq. 269 and Eq. 270 respectively, where $\nu_{\alpha n} = \nu_{\alpha H} + \nu_{\alpha H_2}$ is the effective momentum transfer collision frequency and the terms with superscripts “R” and “T” represent the resistive and thermal coulomb forces.

$$Mn\nu_{in}(\boldsymbol{u_i} - \boldsymbol{u_n}) = ne(\boldsymbol{E} + \boldsymbol{u}_i \times \boldsymbol{B}) - \nabla P_i + \boldsymbol{f}^R_{ie} + \boldsymbol{f}^T_{ie} \qquad \text{Eq. 269}$$

$$mn\nu_{en}(\boldsymbol{u_e} - \boldsymbol{u_n}) = -ne(\boldsymbol{E} + \boldsymbol{u}_e \times \boldsymbol{B}) - \nabla P_e + \boldsymbol{f}^R_{ei} + \boldsymbol{f}^T_{ei} \qquad \text{Eq. 270}$$

Adding these equations (Eq. 269 and Eq. 270) and neglecting the ion pressure, we obtain the single fluid MHD description of the plasma in the diffusive regime (Eq. 271), where the current density is given by $\boldsymbol{j} = ne(\boldsymbol{u}_i - \boldsymbol{u}_e)$.

$$Mn\nu_{in}(\boldsymbol{u_i} - \boldsymbol{u_n}) + mn\nu_{en}(\boldsymbol{u_e} - \boldsymbol{u_n}) = \boldsymbol{j} \times \boldsymbol{B} - \nabla P_e \qquad \text{Eq. 271}$$

Let us assume no parallel current density ($j_z = 0$); hence, $u_{ez} = u_{iz}$ and we simply express the parallel plasma flow as u_z. Using conservation of charge ($\nabla \cdot \boldsymbol{j}$) and azimuthal symmetry leads to $j_r = 0$; hence, $u_{er} = u_{ir}$ and we express the radial plasma flow as u_r. Moreover, since the magnetic field only has radial and parallel components we obtain $\boldsymbol{j} \times \boldsymbol{B} = j_\phi B_z \hat{\boldsymbol{r}} - j_\phi B_r \hat{\boldsymbol{z}}$, where $\hat{\boldsymbol{r}}$ and $\hat{\boldsymbol{z}}$ are the radial and parallel unit vectors respectively.

Plasma flow in weakly ionized discharges

The steady state particle transport equations for neutrals and ions can be expressed as $\nabla \cdot \mathbf{\Gamma}_n = -S$ and $\nabla \cdot \mathbf{\Gamma}_+ = S$ respectively, where S represents the particle sources and sinks. Using the divergence theorem, we obtain: $\oint \mathbf{\Gamma}_+ \cdot d\boldsymbol{A} = -\oint \mathbf{\Gamma}_n \cdot d\boldsymbol{A}$. This expression states that the flux of ions out of a closed surface must be balanced by the flux of neutrals into the closed surface. Provided $n_n \gg n_+$ we can assume $\boldsymbol{u}_+ \gg \boldsymbol{u}_n$ [49]. This condition is met in most weakly ionized plasmas[19]. For example, using Eq. 261 the total neutral particle density during the discharge is $n_n = 2fn_{H2}^0$, where the factor of two accounts for the two protons in each hydrogen molecule and f describes neutral depletion. For $n_{H_2}^0 \approx 25\times10^{19}$ m^{-3} (H_2 at 8 mTorr and 300 K) and $n_+ = 1\times10^{19}$ m^{-3} we obtain $n_+/n_n = 1/(50f)$. Hence, even for neutral depletion fractions as low as $f = 0.2$ we obtain $n_+/n_n = 1/10$. Therefore, in weakly ionized plasma the neutral flow velocity can be neglected relative to the ion flow velocity. Using $\boldsymbol{j} \times \boldsymbol{B} = j_\phi B_z\, \hat{\boldsymbol{r}} - j_\phi B_r\, \hat{\boldsymbol{z}}$ and neglecting the neutral flow velocity, the radial and parallel components of Eq. 271 can be written as in Eq. 272 and Eq. 273 respectively, where v_{in}^* is given in Eq. 274.

$$Mnv_{in}^* u_r = j_\phi B_z - \frac{\partial P_e}{\partial r} \qquad \text{Eq. 272}$$

$$Mnv_{in}^* u_z = -j_\phi B_r - \frac{\partial P_e}{\partial z} \qquad \text{Eq. 273}$$

$$v_{in}^* = v_{in}\left(1 + \frac{mv_{en}}{Mv_{in}}\right) \qquad \text{Eq. 274}$$

Eq. 272 states that the radial plasma transport is driven by the radial electron pressure gradient and reduced by the magnetic $j_\phi B_z$ force. This force provides radial magnetic confinement. Eq. 273 states that the parallel plasma transport is driven by the parallel electron pressure gradient and reduced by the $j_\phi B_r$ force. This term is associated with magnetic mirror force in the presence of axially non-uniform background magnetic fields. Comfort [168] discusses the magnetic mirror force and explains that it arises only if the plasma pressure is anisotropic. For the high plasma densities and electron temperatures observed in MAGPIE, the collision frequency is high enough that we can expect an isotropic plasma pressure; hence, no mirror force according to Comfort [168]. In near collisionless conditions (low plasma density and/or high plasma temperature), the plasma pressure can be anisotropic and the mirror force can be used to impart an axial force to the plasma as in electrical thrusters with magnetically expanding plasma as demonstrated by Takahashi [169]. More details on the magnetic mirror force are given in Appendix 7C. In relation to MAGPIE, Eq. 273 is important because it describes how the pressure gradient, produced by the non-uniform RF heating, is able to drive plasma flows into the magnetic mirror.

---

[19] Under certain combinations of RF power, RF frequency and magnetic field, severe neutral depletion has been observed in helicon discharges [52], [160]. In such cases $n_n \approx n_+$, the discharge is no longer weakly ionized and we cannot assume $\boldsymbol{u}_+ \gg \boldsymbol{u}_n$.

On axis (r = 0 cm), the radial magnetic field (B_r) vanishes; hence, the magnetic mirror force also vanishes. Moreover, momentum transfer between the plasma and the neutral fluid is dominated by ion-neutral collisions; hence, we can approximate $m\nu_{en}/M\nu_{in} \ll 1$; therefore $\nu_{in}^* \approx \nu_{in}$ as indicated by Fruchtman [170]. This leads to an expression for the on-axis plasma flow velocity in the diffusive regime (Eq. 275).

$$u_z = -\frac{1}{Mn\nu_{in}}\frac{\partial P_e}{\partial z} \qquad \text{Eq. 275}$$

Electron force balance

In the absence of parallel currents ($j_z = 0$) and neglecting the neutral flow velocity ($n_n \gg n_e$), the on-axis "z" component of the electron momentum equation (Eq. 270) is given by Eq. 276, where V is the plasma potential. Using Eq. 275 to eliminate the flow term leads to Eq. 277.

$$mn\nu_{en}u_z = ne\frac{\partial}{\partial z}\left(V - 0.71T_e\right) - \frac{\partial P_e}{\partial z} \qquad \text{Eq. 276}$$

$$\frac{\partial P_e}{\partial z}\left(1 - \frac{m\nu_{en}}{M\nu_{in}^*}\right) = ne\frac{\partial}{\partial z}\left(V - 0.71T_e\right) \qquad \text{Eq. 277}$$

Using the approximation $m\nu_{en}/M\nu_{in} \ll 1$ in Eq. 277, we obtain the 1D force balance relation for the electron fluid as shown in Eq. 278. This expression states that the electron pressure force must be balanced by the electric and thermal forces. Whenever this expression is satisfied experimentally, it implies that electrons are Maxwell-Boltzmann distributed. Moreover, for vanishing electron temperature gradients, this expression reduces to the electron Boltzmann relation $n = n_0 \exp(V/T_e)$.

$$\frac{\partial P_e}{\partial z} = en\frac{\partial}{\partial z}\left(V - 0.71T_e\right) \qquad \text{Eq. 278}$$

7.4.6 Particle transport

In the analysis of particle transport in MAGPIE, we assume the plasma is well magnetized and confined to flow only along the magnetic field lines (see Figure 17 Chapter 2); hence, we neglect radial transport relative to axial particle transport. Using these assumptions, we can express the steady state 1D particle transport equation as in Eq. 279, where S is the particle source, Γ is the plasma flux and A the plasma cross sectional area.

$$S = \frac{1}{A}\frac{\partial}{\partial z}(\Gamma \mathrm{A}) \quad \text{Eq. 279}$$

The plasma flux ($\Gamma = n_e u_z$) along the length of a 1D plasma column can be measured using both Langmuir and Mach probes. The plasma cross sectional area A can be estimated from the geometry of the magnetic field. These quantities, together with Eq. 279, can be used to directly calculate the plasma sources and sinks along the length of a 1D plasma column. Application of this method is described in section 7.5.2. An additional method can be obtained by using Eq. 275 to represent the plasma flux Γ in Eq. 279. Assuming ν_{in} is constant, we can express the particle source term S as in Eq. 280. This expression shows that the particle sources and sinks in a 1D plasma can be estimated using the electron pressure profile; for this reason, we use the subscript P_e to describe Eq. 280. A similar expression to Eq. 280 is provided by Krasheninnikov [171]; however, his calculation assumes no magnetic compression of the plasma ($\partial A/\partial z = 0$).

$$S_{P_e} = -\frac{1}{M\nu_{in}}\left[\frac{\partial^2 P_e}{\partial z^2} + \left(\frac{1}{A}\frac{\partial A}{\partial z}\right)\frac{\partial P_e}{\partial z}\right] \quad \text{Eq. 280}$$

7.4.7 Volumetric processes

For the electron temperatures typically encountered in helicon based plasma devices, 1 to 6 eV, both ionization and recombination processes must be considered. Moreover, in the presence of molecular gases such as hydrogen, we must consider both three-body recombination (3BR) and Molecular Activated Recombination (MAR) [171], [172], [173], [174]

Thermal plasma production

Based on the hydrogen discharge global simulation described in reference [77] whose conditions are similar to our experiment in MAGPIE, we consider direct electron impact ionization of (1) atomic and (2) molecular hydrogen as the dominant pathways for electron production. For a discharge with Maxwell-Boltzmann distributed electrons, the rates for these processes according to reference [46] are given in Eq. 281 and Eq. 282 respectively. The subscript “iz” indicates ionization and the superscript indicates the species been ionized. These rate coefficients are consistent with those reported in [175] and [176].

$$K_{iz}^{H} = 7.89 \times 10^{-15} \times T_e^{0.41} \exp(-14.23/T_e) \quad [\mathrm{m^3 s^{-1}}]$$ Eq. 281

$$K_{iz}^{H_2} = 1.1 \times 10^{-14} \times T_e^{0.42}\, exp(-16.05/T_e) \quad [\mathrm{m^3 s^{-1}}]$$ Eq. 282

The corresponding particle source (G_{iz}) and ionization frequency (ν_{iz}) are given in Eq. 283. For a given atomic (n_H) and molecular (n_{H_2}) hydrogen density and electron temperature, we can estimate the particle source (G_{iz}) as shown in Figure 84b using Eq. 281 to Eq. 283. This figure indicates that the plasma in MAGPIE is mostly generated in the vicinity of the RF antenna (-20 < z < 25 cm) where the electron temperature, supported by the RF heating, is above 3 eV. In what follows, we assume that the plasma in MAGPIE is generated entirely through thermal ionization of atomic and molecular hydrogen (Eq. 281 to Eq. 283) and driven by RF heating.

$$G_{iz} = n_e \nu_{iz} \qquad \nu_{iz} = n_H K_{iz}^{H} + n_{H_2} K_{iz}^{H_2}$$ Eq. 283

By replacing the terms n_H and n_{H_2} in Eq. 283 with Eq. 263 and Eq. 262 respectively, the plasma source can be written as in Eq. 284. This expression takes into account the molecular hydrogen dissociation degree η and neutral gas depletion fraction f. Notice that when the dissociation degree is low (high), plasma production is dominated by molecular (atomic) ionization.

$$G_{iz} = n_e \nu_{iz} \qquad \nu_{iz} = n_{H_2}^{0} f\left[2\eta K_{iz}^{H} + (1-\eta) K_{iz}^{H_2}\right]$$ Eq. 284

Three-body recombination (3BR)

3BR is the reverse process of direct electron impact ionization ($e + H \rightarrow H^{+} + 2e$). This recombination channel is only important for electron temperatures below 1 eV. From reference [60, p. 279], the 3BR rate is given by Eq. 285. The terms b_0, $\overline{v_e}$ and n_e represent the electron-electron coulomb collision radius, electron thermal velocity and electron density. From this expression it can be shown that the 3BR rate is given by $5.38 \times 10^{-39}\, T_e^{-9/2} n_e$, where T_e is in [V] and n_e in [m^{-3}]. The corresponding proton 3BR recombination rate (L_{3BR}) and frequency (ν_{3BR}) are given in Eq. 286.

$$K_{3BR} = \pi^2 b_0^5 \overline{v_e} n_e \quad b_0 = \frac{e}{6\pi\epsilon_0 T_e}$$ Eq. 285

$$L_{3BR} = n_e \nu_{3BR} \qquad \nu_{3BR} = n_e K_{3BR}$$ Eq. 286

Molecular Activated Recombination (MAR)

This recombination process is enabled by the presence of vibrationally excited hydrogen molecules. It is most effective in the 1-2 eV electron temperature range [171] and it is believed to be essential in reducing the particle and heat fluxes to magnetic divertors in Tokamaks [174]. According to [173], [174], the MAR process involves the following reactions:

1- Electron Dissociative Attachment (DA): $H_2(\nu \geq 4) + e \rightarrow H^- + H$
2- Atomic-to-molecular Ion Conversion (IC): $H_2(\nu \geq 4) + H^+ \rightarrow H_2^+ + H$
3- Charge Exchange Recombination (CER): $H^- + H^+ \rightarrow 2H$
4- Electron Dissociative Recombination (DR): $H_2^+ + e \rightarrow 2H$

Vibrationally excited hydrogen molecules facilitate processes (1) and (2); these processes are then followed by the recombination processes (3) and (4) respectively. A detailed description of the MAR process can be found in [171], [172], [173], [174]. Fantz [177] discusses additional pathways that follow the Atomic-to-molecular Ion Conversion (IC): Molecular Assisted Dissociation (MAD) and Molecular Assisted Ionization (MAI); however, as noted by Fantz these processes do not contribute to volumetric recombination. From reference [178, Sec. 4.3], MAI reaction rates are much smaller than direct electron-impact ionization of atomic and molecular hydrogen (Eq. 281 and Eq. 282 respectively); hence, MAI can be ignored as an electron producing mechanism. We describe the MAR recombination rate (L_{MAR}) and recombination frequency (ν_{MAR}) as in Eq. 287. We use Figure 5 from reference [171] to compute the MAR reaction rate (K_{MAR}) in the electron temperature range between 0.1 to 3 eV.

$$L_{MAR} = n_e \nu_{MAR} \qquad \nu_{MAR} = n_{H_2} K_{MAR} \qquad \text{Eq. 287}$$

By replacing the term n_{H_2} in Eq. 287 with Eq. 262, the MAR recombination rate can be written as in Eq. 288. This expression takes into account the molecular hydrogen dissociation degree η and neutral gas depletion fraction f.

$$L_{MAR} = n_e \nu_{MAR}^0 [f(1-\eta)] \quad \nu_{MAR}^0 = n_{H_2}^0 K_{MAR} \qquad \text{Eq. 288}$$

Using the plasma source (Eq. 284), 3BR rate (Eq. 286) and MAR rate (Eq. 288), the total particle source S is given by the expression in Eq. 289, where the subscript "V" indicates that the source term S is calculated using volumetric processes.

$$S_V = n_e n_{H_2}^0 f\left[2\eta K_{iz}^H + (1-\eta)\left(K_{iz}^{H_2} - K_{MAR}\right)\right] - n_e \nu_{3BR} \qquad \text{Eq. 289}$$

7.4.8 Equilibrium plasma density

By equating both the particle sources S_{P_e} (Eq. 280) and S (Eq. 279) and solving for the plasma density n_+, we obtain a 2nd order differential equation with variable coefficients that describes the equilibrium plasma density in 1D as shown in Eq. 290, where the primes indicate differentiation with respect to "z". The variable coefficients P and Q are given below in Eq. 291, S is the particle source, D_a the ambipolar diffusion coefficient and ν_{in} the momentum transfer collision frequency.

$$n_+'' + n_+'P + n_+Q = -S/D_a \qquad \text{Eq. 290}$$

$$P = 2\widetilde{T_e} + \tilde{A} \qquad Q = \widetilde{T_e}' + \widetilde{T_e}^2 + \widetilde{T_e}\tilde{A}$$

$$\widetilde{T_e} = T_e'/T_e \qquad \tilde{A} = A'/A \qquad \widetilde{T_e}' = T_e''/T_e - \widetilde{T_e}^2 \quad D_a = \frac{eT_e}{M\nu_{in}} \qquad \text{Eq. 291}$$

The solution to this equation is the plasma density profile $n_+(z)$ that satisfies both the particle (Eq. 279) and momentum transport (Eq. 275) equations for a given set of input parameters; namely, electron temperature $T_e(z)$, plasma cross sectional area $A(z)$, particle source $S(z)$ and ion-neutral momentum transfer collision frequency ν_{in}. The first three input parameters (T_e, S, A) are readily obtained from electrostatic probe measurements and simple calculations. However, estimating the collision frequency requires knowledge of the neutral depletion fraction f, dissociation degree η and temperature of the neutral gas and ions. The neutral gas temperature can be estimated using spectroscopic methods [162]. The remaining parameters (f, η, T_i) can be obtained experimentally, but require sophisticated laser diagnostics such as those described in references [50], [160], [161]. Nevertheless, using constraints provided by experimentally measured plasma flow we provide an estimate of ν_{in}.

Effect of the magnetic field geometry

Using Eq. 290 to estimate how changes in the magnetic field geometry affect the equilibrium density profile requires a simultaneous change in the electron temperature profile such that the "new" solution still satisfies particle, momentum and heat transport. In order to proceed, we must include the heat transport equation to produce another differential equation involving the plasma density and electron temperature; in this case, we can solve the coupled system of differential equations subject to boundary conditions to obtain self-consistent plasma density and electron temperature estimates as we change the background magnetic field. This exercise is, however, beyond the scope of the thesis.

7.5 Results

In this section, we use experimental measurements to evaluate the “on-axis” parallel electron force balance (Eq. 278), particle sources and sinks (Eq. 279) and plasma flow velocity (Eq. 275) in MAGPIE. In addition, we evaluate the equilibrium plasma density along the length of MAGPIE using a 1D particle transport model (Eq. 290). Finally, we provide a 0D estimate of the neutral depletion and dissociation degree in MAGPIE

7.5.1 Electron fluid force balance

The electron fluid parallel force balance at r = 0 cm is given by Eq. 278. It is composed of the electric, pressure and thermal forces. In section 7.4.5, we showed that the electron-neutral drag force can be neglected because $m\nu_{en}/M\nu_{in} \ll 1$; however, we calculate its contribution for the sake of completeness. The electron-neutral scattering collision cross section is calculated as described by Lieberman in [60, Sec. 3.3 Elastic scattering]. In Figure 88a, we show the electron fluid forces on-axis (r = 0 cm) based on the experimental measurements. The red line represent the electric force (F_E) and black line the combined pressure, thermal and collisional drag force (F_{P+T+D}). The mathematical expression for these forces is shown in Eq. 292 and Eq. 293 respectively. The term C_s represents the ion sound speed. We observe that throughout the entire length of MAGPIE these forces are approximately equal and opposite and thus satisfying Eq. 278. In Figure 88b, we show the individual contributions from the pressure, thermal and collisional drag forces. We observe that the thermal force is comparable to the pressure force throughout the entire length of MAGPIE and cannot be neglected in the force balance. However, the collisional drag force is small and can be neglected. This analysis indicates that at r = 0 cm the electron fluid is in a state of equilibrium between the electric, pressure and thermal forces and that electrons under these experimental conditions can be assumed to be Maxwell-Boltzmann distributed.

$$f_E = en\frac{\partial V}{\partial z} \tag{Eq. 292}$$

$$f_{P+T+D} = \frac{\partial P_e}{\partial z} + 0.71en\frac{\partial T_e}{\partial z} + mn\nu_{en}C_s \tag{Eq. 293}$$

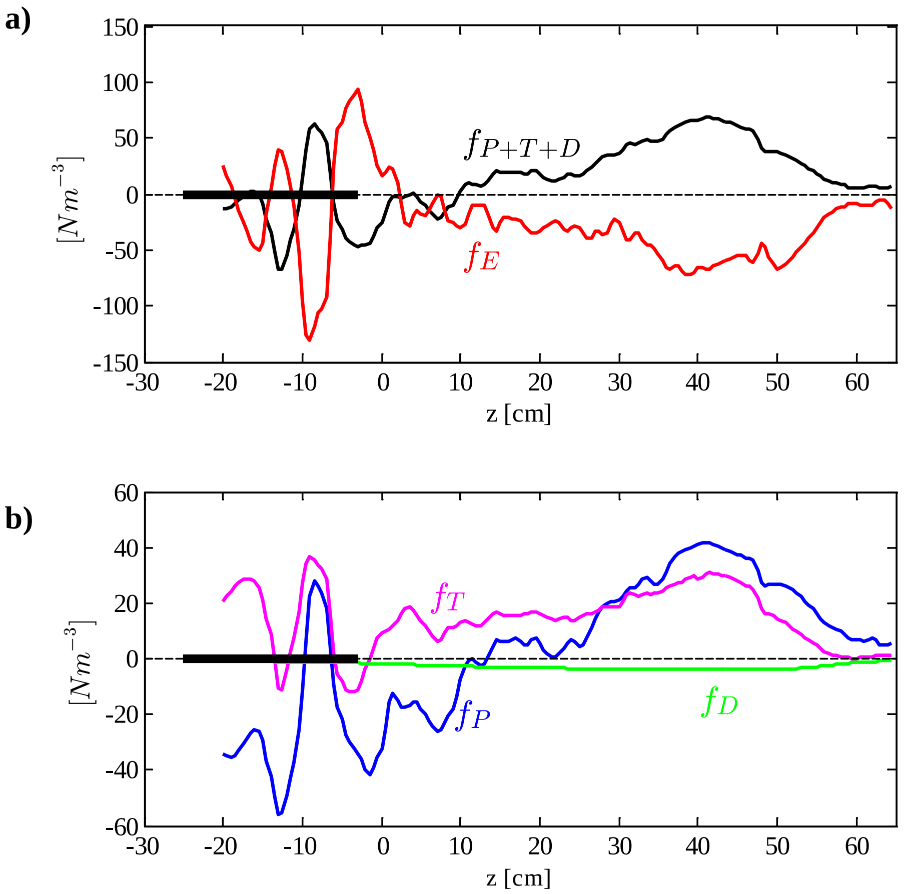

Figure 88, (a) On-axis (r = 0 cm) electric force (red line) and combined pressure, thermal and collisional drag force (black line). Location of antenna is represented by thick black line. Operating condition same as per Table 15. (b) On-axis pressure (f_P), thermal (f_T) and collisional drag force (f_D) resolved along the length of MAGPIE.

7.5.2 Particle sources and sinks

Integrating Eq. 279 we obtain $\Gamma A = \int S\, d\cancel{V}$, where S represents the particle sources and sinks in the plasma and $\cancel{V}$ the plasma volume. The term ΓA describes the total number of particles per unit time flowing through the cross sectional area of a magnetized plasma column as illustrated in Figure 89. Hereafter ΓA is referred to as the total plasma flux.

Gradients in the total flux along the length of the plasma column indicate the presence of net sources ($\partial \Gamma \mathrm{A}/\partial \mathrm{z} > 0$) and/or net sinks ($\partial \Gamma \mathrm{A}/\partial \mathrm{z} < 0$). In Figure 90a, we show the total plasma flux along the length of MAGPIE using experimentally measured plasma flow (Figure 82), plasma density (Figure 81). The cross sectional area A, shown in Figure 90b, is calculated using conservation of magnetic flux ($\nabla \cdot \boldsymbol{B}$) and the strength of the background magnetic field on axis. The area at z = 0 cm corresponds to the dielectric tube that limits the radial extent of the plasma ($r = 5$ cm). In the region $0 < z < 25$ cm, the total plasma flux increases and indicates the presence of a net source. In the region $30 < z < 60$ cm, the total plasma flux decreases and indicates the presence of a net sink.

Notice that the flux ΓA reverses direction at $z \approx 13$ cm; which, indicates that plasma created $z < 13$ cm flows into the antenna region and plasma created $z > 13$ cm flows into the target region. Moreover, since the plasma density is finite at $z = 13$ cm, the flux reversal implies that the force driving the flow changes direction. We discuss this further in the next section. Figure 90a indicates that the total number of particles flowing along the plasma column decreases for $z \geq 25$ cm. however, both the plasma density and flow velocity (Figure 81 and Figure 82) increase between 25 and 40 cm in spite of the plasma sink. This effect is caused by a reduction in the plasma cross sectional area due to magnetic compression.

The gradient of the total plasma flux ΓA provides an estimate of the net plasma sources and sinks along a magnetized plasma column (Eq. 279). Using the total plasma flux ΓA presented in Figure 90a, the net sources and sinks along the length of MAGPIE are shown in Figure 91a. Hereafter, we refer to this calculation as S_u, where the subscript "u" indicates that the experimentally measured plasma flow is used in the calculation. The corresponding electron temperature measurements are shown in Figure 91b.

Part (a) clearly shows the presence of an ionizing (source) and recombining (sink) region in the plasma column. The electron temperature at the cross-over point ($z \approx 25$ cm) is approximately 2.9 eV. The long length of the plasma column (L ≈ 60 cm) allows considerable cooling of the electrons. Near the antenna, the RF heating leads to electron temperatures of 4 to 5 eV. In this region, ionization dominates over recombination processes and leads to an ionizing plasma.

However, for $z > 35$ cm the electron temperature falls below 2 eV, recombination processes dominate over ionization and leads to a recombining plasma. The electron cooling is probably caused by collisions with neutrals as illustrated in Figure 24, i.e. as the neutral gas pressure is increased, the electron temperature decreases. Wenzel [179] reports on a magnetized plasma column in a linear device with both ionizing and recombining regions.

The magnitude of the recombination rate in Figure 91a is much larger than expected from 3BR. Using $n_e \approx 2\times10^{19}$ m^{-3}, $T_e \approx 0.5$ eV and Eq. 285 we obtain $L_{3BR} \approx 1\times10^{21}$ m^{-3}s^{-1} which is about 3 orders of magnitude lower than the observed recombination (~1×10^{24} m^{-3}s^{-1}). An estimate using MAR (Eq. 287) leads to recombination rates consistent with those observed in Figure 91a. Using H_2 at 8 mTorr and 300 K, $n_e \approx 2\times10^{19}$ m^{-3}, $T_e \approx 0.5$ to 1 eV and Eq. 287 we obtain $L_{MAR} \approx 0.3$ to 1.3×10^{24} m^{-3}s^{-1}. These calculations indicate that the recombination shown in Figure 91a is consistent with MAR.

Based on the magnitudes of the ionization and recombination rates shown in Figure 91a and the almost vanishing plasma flux for $z > 60$ cm as shown in Figure 90a, we conclude that for the fill pressure (8 mTorr) investigated in this chapter, a considerable fraction of the plasma created in the ionizing region is lost through volume recombination in the region $30 < z < 60$ cm and only a small fraction reaches the end plate at $z = 65$ cm. This is characteristic of a detached plasma.

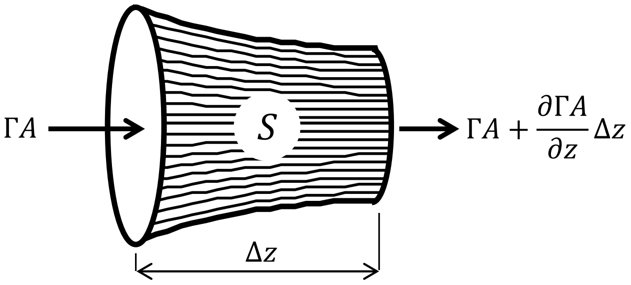

Figure 89, One-dimensional particle conservation in a magnetized plasma column with particle source/sink S. The thin lines represent the magnetic field lines confining the plasma.

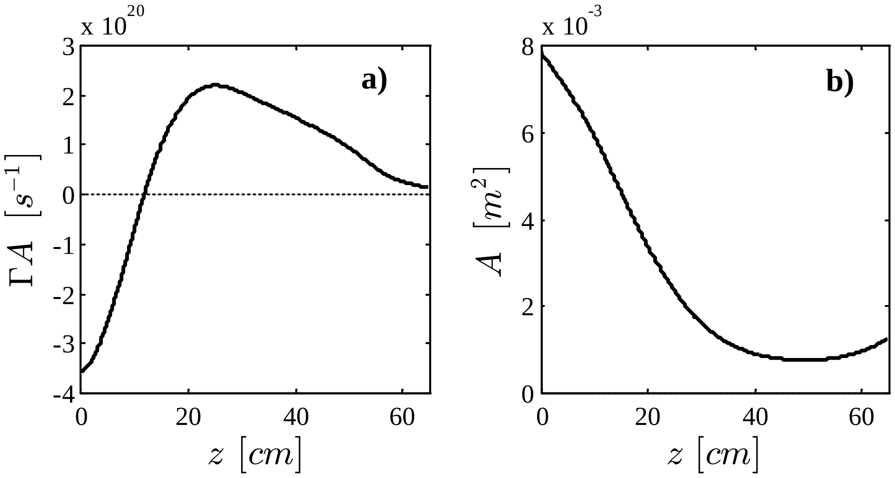

Figure 90, (a) Total plasma flux Γ*A* along the length of MAGPIE calculated using experimentally measured plasma flow (Figure 82), plasma density (Figure 81) and the cross sectional area shown in (b).

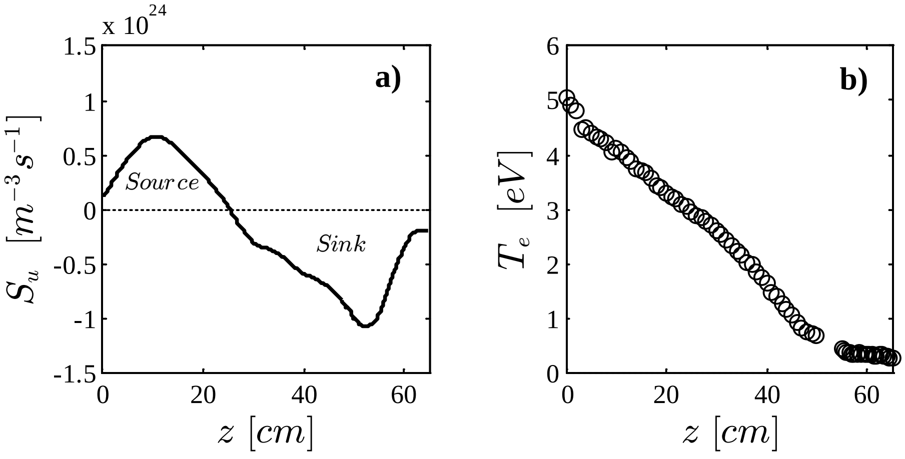

Figure 91, (a) Net plasma sources and sinks along the length of MAGPIE calculated with Eq. 280 and using experimentally measured plasma density and flow. (b) Electron temperature measured along the length of MAGPIE.

7.5.3 Plasma flow velocity

Eq. 275 describes the diffusive plasma flow driven by the electron pressure gradient. In what follows, we assume that H^+, H and H_2 neutral species are in equilibrium at a temperature T_i anywhere between 0.05 and 0.6 eV [180]. The molecular hydrogen density before the discharge is $n_{H_2}^0 = 2.7 \times 10^{20}$ m^{-3} (8 mTorr at 300 K) and using Eq. 267, we estimate $\lambda_{in}^0 \approx$ 0.5 cm. We calculate the electron pressure profile in Eq. 275 using experimentally measured plasma density and electron temperature profiles (Figure 81). Finally, we select the value of ν_{in} that best matches theory (Eq. 275) with the experimentally measured plasma flow.

In Figure 92a, the open circles represent the electron pressure based on ion density and electron temperature measurements with a DLP. The solid red line is a fit done to the experimental data using a Savitsky-Golay filter. In Figure 92b, the open circles represent the plasma flow measurements taken with a Mach probe (Figure 82). The solid red line represents the theoretical plasma flow using Eq. 275 and a value of $\nu_{in} =$ 146 kHz. We observe that regardless of the value of ν_{in}, both theory and experiment agree on the following: (1) the location of the flow reversal ($z \approx$ 13 to 16 cm), (2) the location of maximum flow and (3) the linear dependence on axial position of the accelerating and decelerating regions. These observations are strong indicators that the plasma flow is driven by the electron pressure gradient. In section 7.5.5, we discuss the physical significance of the choice $\nu_{in} =$ 146 kHz.

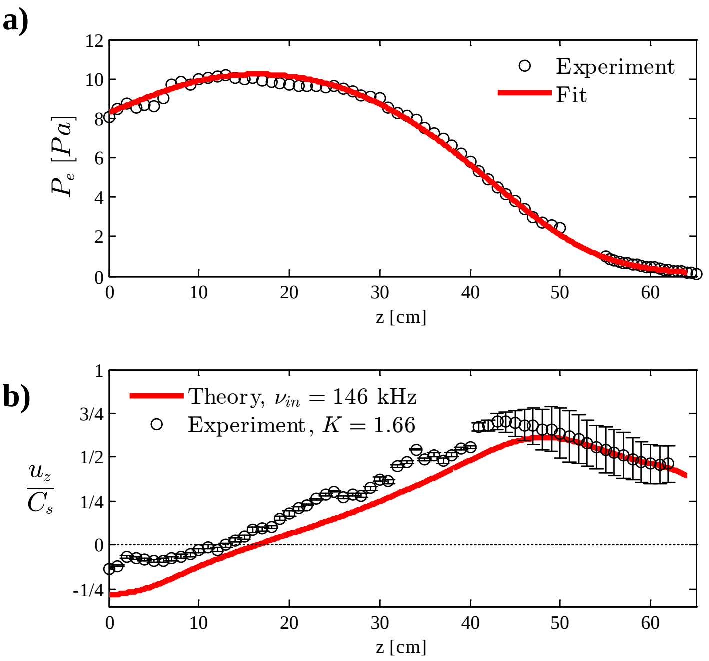

Figure 92, (a) On-axis experimental electron pressure along the length of MAGPIE. (b) Solid red line represents the theoretical on-axis plasma flow based on Eq. 275 using a value of ν_{in}= 146 kHz. The open circles represent the on-axis plasma flow measurements taken with a Mach probe using a calibration factor K = 1.66 for magnetized plasma.

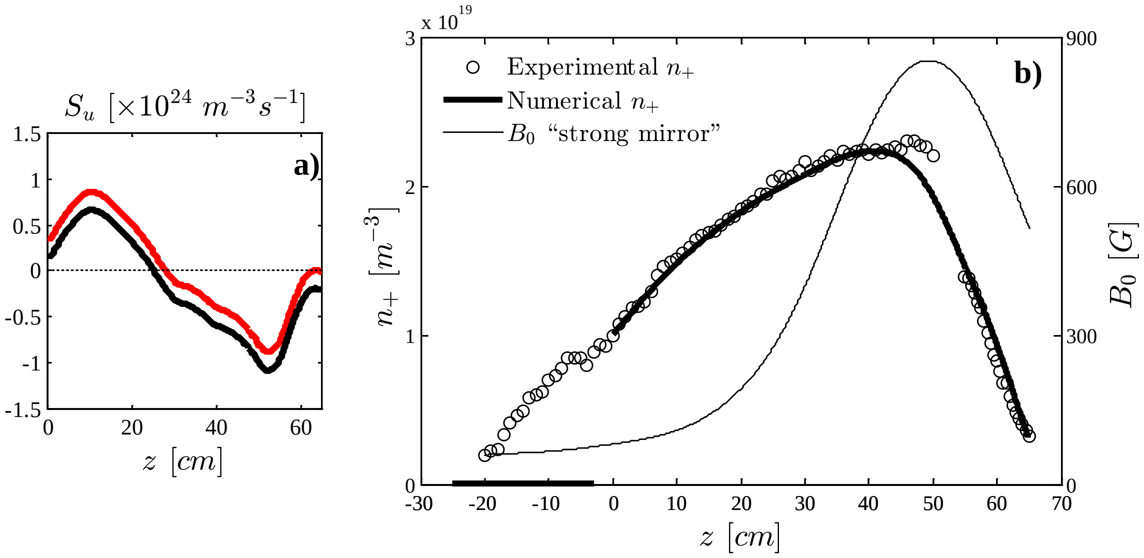

Figure 93, (a) Effect of adding an offset of 0.15×10^{24} m^{-3}s^{-1} to S_u. (b) Comparison between theoretical (Eq. 290) and experimental equilibrium plasma density profile. Horizontal black thick line represents the location of the RF antenna. The thin black line represents the magnitude of the background magnetic field.

7.5.4 Equilibrium plasma density

In this section, we calculate the equilibrium plasma density using Eq. 290. This equation describes the transport of plasma along the converging magnetic field subject to volumetric particle sources and sinks, where the transport process is driven by the electron pressure gradient. To evaluate Eq. 290, we use the measured electron temperature (Figure 81), measured plasma sources and sinks S_u (Figure 91a), the plasma cross sectional area (Figure 90b) and the estimated value of $\nu_{in} = 146$ kHz as inputs to the model. The experimentally measured plasma density and the slope at $z = 0$ cm are used as boundary conditions for Eq. 290.

For the given experimental input parameters, theory (Eq. 290) and experiment are consistent in the region $0< z < 35$ cm; however, to obtain agreement between theory and experiment over the entire length ($0< z < 65$ cm), we must offset the experimentally measured S_u by 0.15×10^{24} $\mathrm{m^{-3}s^{-1}}$; however, this offset does not considerably modify the S_u profile (Figure 93a). Its main effect is to increase the ionization and decrease the recombination rate by a small amount[20].

The comparison between theory and experiment is shown in Figure 93b. The calculation is able to replicate (1) the linear increase and decrease of the plasma density in the ionizing and recombining regions and (2) magnitude of the plasma density in the target region. These results indicate that the equilibrium plasma density along the length of MAGPIE can be described with a 1D diffusive transport model.

---

[20] The on-axis plasma density and flow velocity profiles were measured on different discharges several months apart. Changes in the vacuum chamber and the different RF power amplifiers used could have led to small differences in the equilibrium conditions between the two discharges. In addition, considering probe alignment errors and the sensitivity of the 2nd order ODE (Eq. 290) to the input data, the 20 % adjustment in S_u could account for the aforementioned uncertainties.

7.5.5 Estimating the neutral depletion and dissociation degree

In what follows, we provide a first order estimate of the neutral depletion fraction f and the dissociation degree η on axis (r = 0 cm) in MAGPIE based on: (1) volumetric processes and (2) the momentum transfer collision frequency. We assume the neutral density and temperature profiles are uniform (0D) along the length of MAGPIE; hence, we refer to the following as a 0D estimate.

Volumetric processes

The expression S_V (Eq. 289) represents the particle source and sinks based on thermal ionization, MAR and 3BR. We evaluate S_V using the experimentally measured electron temperature and select the values of f and η that best match S_V (Eq. 289) with S_u (Figure 91a).

In Figure 94, we compare S_V with S_u using the values $f = 0.26$ and $\eta = 0.28$. There is good agreement between the calculations in the region $10 < z < 30$ cm but deteriorates in the recombining region beyond z > 40 cm. We note that MAR rates used in this calculation are based on the CRAMD collisional radiative model [173], [181] designed for Tokamak divertor conditions where $T_e \approx T_h$ $(h = H^+,\ H_2,\ H)$ and $n_{H2}/n_e \approx 0.1$. In MAGPIE, we have $T_e \gg T_h$ and estimate[21] $n_{H_2}/n_e \approx 4$. The discrepancy between theory and experiment for z >40 cm may be connected to these differences in conditions. This 0D estimate indicates: (1) the neutral particle density during the discharge is depleted to about 25 % of the initial neutral density (H_2, 8 mTorr and 300 K) and (2) about 30 % of the neutral H_2 is dissociated into neutral atomic hydrogen.

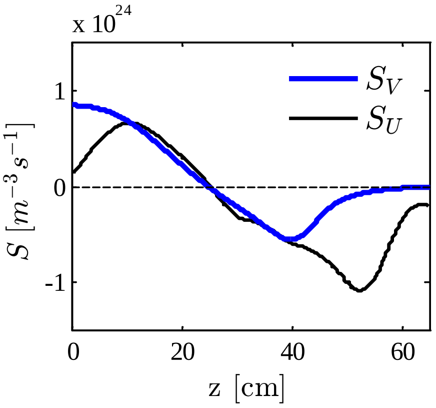

Figure 94, Comparison between S_u and S_V,using $f = 0.26$ and $\eta = 0.28$. The calculation S_u is based on experimentally measured plasma flow and density. The calculation S_V is based on the following volumetric process: (1) Thermal ionization of atomic and molecular hydrogen, (2) MAR and (3) 3BR.

---

[21] The estimate of n_{H_2}/n_e is based on H_2 at 8 mTorr and 300 K before the discharge, $\eta \approx 0.2$ and $f \approx 0.2$ during the discharge and $n_e \approx 1\times10^{19}$ m^{-3}.

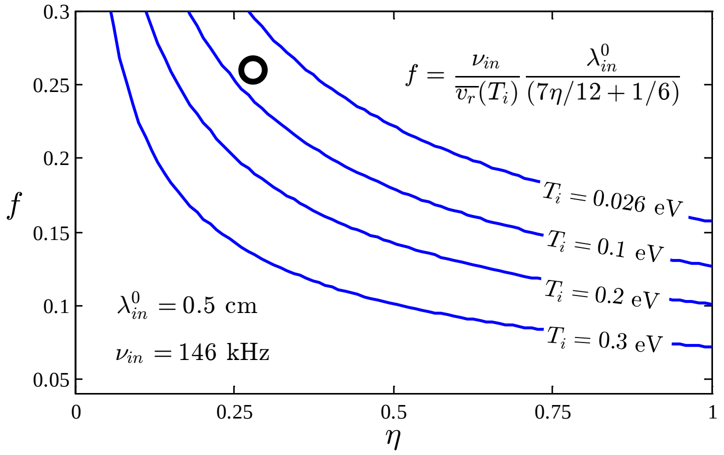

Figure 95, Neutral depletion fraction f as a function of the dissociation degree η for various values of ion temperature. The collision frequency is fixed at $\nu_{in} = 146$ kHz based on Figure 92. The open circle represents the neutral depletion and dissociation degree estimate based on volumetric processes shown in Figure 94.

Ion-neutral collision frequency

We now discuss the significance of $\nu_{in} = 146$ kHz obtained from the comparison between the theoretical and experimentally measured plasma flow. Using Eq. 267, the neutral depletion fraction f that satisfies the experimental data in Figure 92a for different values of dissociation degree η and ion temperature T_i is given in Eq. 294.

$$f = \frac{\nu_{in}}{\overline{v_r}(T_i)}\left(\frac{\lambda^0_{in}}{7\eta/12 + 1/6}\right) \qquad \overline{v_r}(T_i) = (10eT_i/M)^{1/2} \qquad \text{Eq. 294}$$

In Figure 95, we evaluate f (Eq. 294) as a function of η and various ion temperatures. The calculation shows that for any significant level of dissociation ($\eta > 0.1$), the value of f must be less than 0.5. This indicates that the neutral particle density needed to match theory and experiment is at least as low as half the initial neutral particle density. This is a clear indication of neutral depletion. This estimate is consistent with the neutral depletion estimate from volumetric processes ($f = 0.26$). The open circle in Figure 95 is the estimate of the neutral depletion fraction f and dissociation degree η based on volumetric process.and is consistent with an ion temperature of $T_i = 0.05$-0.08 eV.

We note that these are just 0D estimates and given the magnitude of the electron pressure (~10 Pa), we expect the neutral gas density profile to be non-uniform as discussed in Appendix 7D; hence, the 0D assumption is questionable. Nevertheless, these estimates clearly indicate that a reduction in the neutral particle density is required ($f \approx 0.25$-0.5) to match the theoretical (1) plasma production rate and (2) ion-neutral collision frequency with experimental measurements.

In discharges with high electron pressure, one can no longer assume a uniform neutral gas distribution and neutral depletion effects may become important. Therefore, understanding and optimizing the dynamics of the neutral gas in plasmas with high electron pressure will require the use of more sophisticated diagnostics such as TALIF [50], [51], [161] and other spectroscopic methods in conjunction with neutral transport codes such as the SOLPS (Scrape-Off Layer Plasma Simulator) package [21], [182]. Such a simulation could provide additional information on the importance of MAR and 3BR in detached plasmas observed in MAGPIE. We also emphasize the need for diagnosing the temperature of the neutral gas and ions in order to correctly evaluate the neutral gas pressure and momentum transfer collision frequency. Finally, neutral depletion in high power (≥ 20 kW) hydrogen discharges in MAGPIE should be investigated with diagnostics such as TALIF with the aim of understanding how neutral depletion may limit the highest plasma densities achievable [52].

7.6 Summary and conclusions

Force balance

The fluid analysis reveals that in MAGPIE the electron fluid exists in a state of dynamic (flowing) equilibrium between the electric, pressure and thermal forces. We show that the thermal force cannot be ignored in the electron force balance. The measured force balance implies that the electrons are Maxwell-Boltzmann distributed along the length of MAGPIE.

Particle sources and Plasma flow

We have estimated the total plasma flux along the length of MAGPIE using plasma flow and ion density measurements from electrostatic probes. These measurements reveal that the plasma column in MAGPIE, for the conditions relevant to this chapter, can be divided into an ionizing ($z <$ 25 cm) and recombining ($30 < z < 60$ cm) region. The electron temperature at the interface between these two regions is about 2.5 to 3 eV.

From the relative magnitudes of the ionization and recombination rates and the almost vanishing plasma flux near the end plate, we conclude that for the fill pressure investigated (8 mTorr) a considerable fraction of the plasma created in the ionizing region is lost through volume recombination and only a small fraction reaches the end plate. This recombination process effectively forms a “barrier” between the plasma flowing from the source region and the end plate. This is characteristic of a detached plasma.

In addition, the recombination rates estimated from the decrease in the total plasma flux are consistent with MAR; while, calculations indicate 3BR is negligible under these conditions. Moreover, we show that the measured plasma flow can be understood as a 1D diffusive transport process driven by the electron pressure gradient.

Equilibrium plasma density

Comparison between theory and experiment shows that the equilibrium plasma density profile in MAGPIE can be described with a 1D diffusive transport model. From the results in this chapter and those presented in Chapter 6, the formation of the equilibrium plasma density can be understood as follows: (1) Helicon waves are launched from the antenna and propagate along the whistler wave ray direction towards the center of the discharge where they are collisionally absorbed within 30 cm and produce a non-uniform electron pressure profile (Chapter 6). (2) RF power deposition leads to electron heating near the antenna which supports the ionizing region where the bulk of the plasma is created. (3) Near the antenna, the magnetic compression is small and the plasma density increases due to thermal ionization. The plasma created $z \geq$ 15 cm is effectively “pushed” by the electron pressure gradient towards the target region and guided by the magnetic field. (4) As the plasma is transported away from the ionizing region, electron-neutral collisions cool down the electrons and a recombining region is formed as demonstrated by the decrease in the measured plasma flux (Figure 90). (5) As the plasma is transported towards the target region and into the recombining region, both plasma density and flow velocity increase due to magnetic compression. (7) Upon reaching the region of maximum magnetic compression ($z = 50$ cm), both plasma density and flow velocity reach a maximum value (2.5×10^{19} m^{-3} and Mach 0.7 respectively); beyond this point, the combined effect of magnetic decompression and plasma recombination leads to the observed decrease in plasma density and flow velocity.

Neutral gas pressure and detachment

The importance of the neutral gas pressure can be observed from experimental measurements shown in Figure 24 Chapter 2 (page 43), where the operating conditions correspond to Table 15. The measurements suggest that as the hydrogen fill pressure is increased from 3 mTorr to 8 mTorr volume recombination becomes important. The plasma decay near the end plate for the 4 and 6 mTorr cases is remarkably different and appears to be related to the electron temperature near the end plate. Below 1 eV (6 mTorr), plasma decay is strong and “detachment” is observed; however, above 1 eV (4 mTorr) the plasma decay is weak and leads to higher plasma densities at the end plate. This indicates that we can create “detached” plasmas near the end plate of MAGPIE by varying the fill pressure.

Neutral depletion and dissociation fraction

Comparison between the measured and theoretical plasma sources indicate that the neutral gas is depleted to about 25 % of its initial value and about 30 % of the molecular hydrogen is dissociated into atomic hydrogen. In addition, the theoretical plasma flow, in conjunction with the ion-neutral collision frequency, is consistent with experiment only if we assume a considerable reduction in the neutral gas density ($f \leq 0.3$). We emphasize that these are just 0D estimates and direct measurements of the neutral density and temperature are still required. Given the high electron pressures measured (~10 Pa) relative to the initial neutral gas pressure (~1 Pa), neutral depletion under these conditions is expected. The impact of neutral depletion in limiting the achievable plasma densities in MAGPIE should be investigated in the near future.

Application to plasma-surface interactions studies

In relation to plasma-material interaction studies, the location of the ionizing and recombining regions implies that there is an optimum location for target surfaces. If the target surface is too close to the source region, it will interfere with the plasma production process. If the target is too far, the recombination region will consume most of the plasma before it reaches the desired location. In addition, magnetic compression can be used to increase the plasma density in the recombining region, although at the expense of the cross sectional area. Finally, identifying the ionizing and recombining regions in the plasma column may be useful if a source of excited neutral particles (molecules and atoms) is needed for plasma-surface interaction studies or for the extraction of negative ions.

Limitations

Several limitations are present in this analysis. For example, the densities of the various ionic and neutral hydrogenic species along the length of MAGPIE are not self-consistently calculated, radial transport is neglected, calculations are limited to the axis of the plasma, neutral dynamics are not explicitly included etc. In addition, the effect of the end plate is not included in the model. Changes in the chemistry near the end plate may lead to larger fractions of molecular ions and could lead to incorrect plasma density estimates from DLPs if protons are assumed dominant. This problem can be circumvented using electron based diagnostics near the end plate such as microwave interferometry or Thomson scattering. It is recommended that the detached plasma region be spectroscopically diagnosed in order to infer the important reactions; for example, it is well known that the 3BR spectral signature is characterized by hydrogen Balmer emission from highly excited states [183]. Moreover, recent experiments with longer pulse discharges (~10 ms) indicate that near the end plate, steady state conditions may require longer than 2 ms. Therefore, an important next step is to determine if the aforementioned plasma detachment in MAGPIE can be sustained in steady state (~100 ms) discharges.

Appendix 7A. "Braginskii" two fluid formalism

The following material is largely based on the review provided by Fitzpatrick [130, Ch. 3], the NRL plasma formulary [131] and Braginskii's paper [129]. The momentum transport equation for a charged particle fluid is shown in Eq. 295, where the subscript α denotes the charged particle species, e.g. electrons and ions. The terms $m_\alpha,\ n_\alpha,\ \boldsymbol{u}_\alpha,\ q_\alpha$ and P_α represent the mass, density, velocity, charge and pressure of the α species respectively. The terms $\boldsymbol{E}$ and $\boldsymbol{B}$ represent the electric and magnetic fields respectively.

$$m_\alpha n_\alpha\left[\frac{\partial}{\partial t}+(\boldsymbol{u}_\alpha\cdot\nabla)\right]\boldsymbol{u}_\alpha = n_\alpha q_\alpha(\boldsymbol{E}+\boldsymbol{u}_\alpha\times\boldsymbol{B})-\nabla P_\alpha+\boldsymbol{F}_\alpha \qquad \text{Eq. 295}$$

The term $\boldsymbol{F}_\alpha$ represents the momentum transfer force between the species α and all other species (neutral and charged particles). It is through this force that the electron, proton and neutral fluids interact. This force is composed of the neutral ($\boldsymbol{f}_{\alpha n}$) and Coulomb ($\boldsymbol{F}_{\alpha\beta}$) contributions as shown in Eq. 296.

$$\boldsymbol{F}_\alpha = \boldsymbol{f}_{\alpha n}+\boldsymbol{F}_{\alpha\beta} \qquad \text{Eq. 296}$$

The Coulomb force ($\boldsymbol{F}_{\alpha\beta}$) represents the momentum gained by the αth charged species through collisions with the βth and is composed of a resistive ($\boldsymbol{f}^R_{\alpha\beta}$) and a thermal ($\boldsymbol{f}^T_{\alpha\beta}$) contribution as shown in Eq. 297.

$$\boldsymbol{F}_{\alpha\beta} = \boldsymbol{f}^R_{\alpha\beta}+\boldsymbol{f}^T_{\alpha\beta} \qquad \text{Eq. 297}$$

The resistive force arises due to finite relative drift velocities between charged particle fluids (e.g. electrical currents). The thermal force arises due the non-linear electron temperature dependence of Coulomb collisions and the presence of electron temperature gradients. Conservation of momentum leads to Eq. 298.

$$\boldsymbol{f}_{n\alpha} = -\boldsymbol{f}_{\alpha n} \quad \boldsymbol{F}_{\beta\alpha} = -\boldsymbol{F}_{\alpha\beta} \qquad \text{Eq. 298}$$

The neutral ($\boldsymbol{f}_{\alpha n}$) and resistive Coulomb ($\boldsymbol{f}^R_{\alpha\beta}$) drag forces are shown in Eq. 299 and Eq. 300 respectively.

$$\boldsymbol{f}_{\alpha n} = -\sum\nolimits_X m_\alpha n_\alpha \nu_{\alpha X}(\boldsymbol{u_\alpha}-\boldsymbol{u_X}) \qquad \text{Eq. 299}$$

$$\boldsymbol{f}^R_{\alpha\beta} = -m_\alpha n_\alpha \nu_{\alpha\beta}\left(\boldsymbol{u_\alpha}-\boldsymbol{u_\beta}\right) \qquad \text{Eq. 300}$$

In Eq. 299, the summation is over all ground state neutral species X with momentum transfer collision frequencies $\nu_{\alpha X}$. In our analysis of MAGPIE, we consider molecular and atomic hydrogen neutral species; hence, $X = H_2$ and H. In partially ionized plasma, ion-neutral collisions dominate the momentum exchange process between the plasma and the neutral fluids. The ion-neutral momentum transfer collision frequency is discussed in section 7.4.4 and in Appendix 7B. In Eq. 300, the term $\nu_{\alpha\beta}$ represents the charged particle momentum transfer collision frequency. For plasma with Maxwell-Boltzmann distributed electrons, the electron-ion momentum transfer collision frequency is given by Eq. 301 [131]. Electron density and electron temperature are in [m^{-3}] and [V] respectively.

$$\nu_{ei} = 2.91 \times 10^{-12} n T_e^{-3/2} \ln \Lambda \qquad \text{Eq. 301}$$

In the strongly magnetized limit $\nu_{ei}/\Omega_{ce} \ll 1$, the thermal force ($\boldsymbol{f}_{\alpha\beta}^{T}$) in a plasma with Maxwell-Boltzmann distributed electrons and azimuthal symmetry is given by Eq. 302 [129], [130], [131]. The first and second terms on the RHS represent the drag force due to electron temperature gradients in the axial and radial directions respectively. The term $\hat{\boldsymbol{b}}$ is the unit vector of the background magnetic field.

$$\boldsymbol{f}_{\alpha\beta}^{T} = -0.71 e n_\alpha \frac{\partial T_e}{\partial z} \hat{\boldsymbol{z}} - \frac{3}{2} e n_\alpha \left(\frac{\nu_{ei}}{\Omega_{ce}}\right) \frac{\partial T_e}{\partial r} \hat{\boldsymbol{b}} \times \hat{\boldsymbol{r}} \qquad \text{Eq. 302}$$

Appendix 7B. Ion-neutral momentum transfer

In relation to the transport processes in a collisional plasma, the moments of the Boltzmann collision operator describe the exchange of particles, momentum and energy driven by short range collisions between the different species considered [130, Ch. 3]. To compute this exchange, one must define and solve the collision operator. For electron-neutral collisions, a Krook type collision operator is often be used. This operator assumes infinitely massive neutral particles; hence, the relative velocity during collisions is approximately the electron velocity [60]. For ion-neutral or neutral-neutral collisions, this approximation cannot be used and both particle velocity distribution functions need to be incorporated. To describe the ion-neutral momentum exchange process, we use the material presented in Braginskii's [129] (section 7 and appendix therein) and Brennan's paper [167].

In what follows, we calculate the momentum transfer collision frequency between two fluid species "a" and "b". The particle velocity is described as $\boldsymbol{v}_X = \boldsymbol{w}_X + \boldsymbol{u}_X$, where $\boldsymbol{w}_X$ is the random thermal velocity and $\boldsymbol{u}_X$ is the mean velocity of the *X* species. The fluids are assumed to be Maxwell-Boltzmann distributed at the same temperature T but with different mean velocities $\boldsymbol{u}_a$ and $\boldsymbol{u}_b$. Braginskii defines the friction (drag) force between species "a" and "b" as in Eq. 303, where m_{ab} is the reduced mass.

$$\boldsymbol{f}_{ab} = -m_{ab} n_a n_b \alpha_{ab} (\boldsymbol{u}_a - \boldsymbol{u}_b) \qquad m_{ab} = \frac{m_a m_b}{m_a + m_b} \tag*{Eq. 303}$$

The term α_{ab} is given by Eq. 304, where $v_r = |\boldsymbol{v}_a - \boldsymbol{v}_b|$ is the magnitude of the relative particle velocity, σ_{ab} is the momentum transfer cross section for the "$a + b$" collisional process as a function of v_r (see section 7.4.4), f_{v_r} is the relative speed distribution function given by Eq. 305, "e" is the electron charge and *T* is the gas temperature in units of Volts.

$$\alpha_{ab} = \frac{m_{ab}}{3eT} \int_0^\infty v_r^3 \, \sigma_{ab} f_{v_r} dv_r \tag*{Eq. 304}$$

$$f_{v_r} = 4\pi v_r^2 \left(\frac{m_{ab}}{2\pi eT}\right)^{3/2} \exp\left(-\frac{m_{ab} v_r^2}{2eT}\right) \tag*{Eq. 305}$$

Using Eq. 303 to Eq. 305, the friction force can be written as in Eq. 306, which is precisely the same result provided by Brennan [167].

$$\boldsymbol{f}_{ab} = -m_{ab} n_a \overline{v_{ab}} (\boldsymbol{u}_a - \boldsymbol{u}_b) \tag*{Eq. 306}$$

$$\overline{\nu_{ab}} = n_b \frac{m_{ab}}{3eT} \int_0^\infty \sigma_{ab} 4\pi v_r^5 \left(\frac{m_{ab}}{2\pi eT}\right)^{3/2} \exp\left(-\frac{m_{ab} v_r^2}{2eT}\right) dv_r$$

For the center of mass (CM) energy range of interest (0.1 to 1 eV), the momentum transfer cross section is approximately constant; hence, we approximate Eq. 306 by extracting σ_{ab} from the integral and evaluating it at the peak value of the integrand $\bar{v_r} = (5eT/m_{ab})^{1/2}$ as shown in Eq. 307.

$$\overline{\nu_{ab}} = n_b \sigma_{ab}(\bar{v}_r) \frac{m_{ab}}{3eT} \int_0^\infty 4\pi v_r^5 \left(\frac{m_{ab}}{2\pi eT}\right)^{3/2} \exp\left(-\frac{m_{ab} v_r^2}{2eT}\right) dv_r \qquad \text{Eq. 307}$$

Following Brennan derivation, Eq. 307 can be reduced to Eq. 308.

$$\overline{\nu_{ab}} = \frac{3}{4} n_b \sigma_{ab}(\bar{v}_r) \bar{v}_r \qquad \text{Eq. 308}$$

If we express the frictional force as given in Eq. 299 (no reduced mass) and use Eq. 308, the frictional force can be written as in Eq. 309 with a momentum transfer collision frequency given by Eq. 310.

$$\boldsymbol{f}_{\alpha X} = -m_\alpha n_\alpha \nu_{\alpha X} (\boldsymbol{u}_\alpha - \boldsymbol{u}_X) \qquad \text{Eq. 309}$$

$$\nu_{\alpha X} = \left(\frac{3}{4} \frac{m_{\alpha X}}{m_\alpha}\right) n_X \sigma_{\alpha X}(\bar{v}_r) \bar{v}_r \qquad \bar{v}_r = \left(\frac{5eT}{m_{\alpha X}}\right)^{1/2} \qquad \text{Eq. 310}$$

Appendix 7C. Fluid magnetic mirror force

To describe the magnetic mirror force mathematically, we assume the background magnetic field ($\boldsymbol{B}_0$) is azimuthally symmetric and axially non-uniform. Using the condition $\nabla \cdot \boldsymbol{B}_0 = 0$, the magnetic field components are approximately related by Eq. 311.

$$B_r \approx -\frac{r}{2}\frac{\partial B_z}{\partial z} \qquad \text{Eq. 311}$$

Using this expression in Eq. 273, we obtain Eq. 312, where the j_ϕ represents the diamagnetic current density; and as the name implies, its field opposes the applied magnetic field $\boldsymbol{B_0}$.

$$Mn\nu_{in}^{*}u_z = j_\phi \frac{r}{2}\frac{\partial B_z}{\partial z} - \frac{\partial P_e}{\partial z} \qquad \text{Eq. 312}$$

It can be shown that in the presence of a non-uniform magnetic field, the diamagnetic current experiences a Lorentz force due to B_r which points away from regions with stronger magnetic fields. This expression indicates that the plasma flow is driven by the electron pressure gradient and decelerated by the magnetic mirror force. However, due to the radial dependence of the radial magnetic field (Eq. 311), the fluid magnetic mirror force vanishes on axis (r = 0 cm).

7C.1 Plasma anisotropy

The radial component of a non-uniform background magnetic field is finite off-axis and the presence of the magnetic mirror force depends on the plasma pressure anisotropy. Comfort [168] discusses the magnetic mirror force and explains that it arises only if the plasma pressure is anisotropic. For the high densities and electron temperatures observed in MAGPIE, the collision frequency is high enough that can we expect an isotropic plasma pressure; hence, no mirror force according to Comfort [168]. In near collisionless conditions (low plasma density and/or high plasma temperature), the plasma pressure can be anisotropic and the mirror force can be used to impart an axial force to the plasma as in electrical thrusters with magnetically expanding plasma as demonstrated by Takahashi [169].

Appendix 7D. Neutral depletion in low-beta plasmas

In what follows, we describe the neutral depletion mechanism based on Fruchtman [159] and O'Connell [184]. We assume the plasma is quasineutral, partially ionized and in steady state. We neglect the ion pressure relative to the electron pressure, transport is diffusive and the neutral fluid is comprised of a single species. Adding the ion and electron momentum equations (Eq. 295), we obtain the MHD plasma momentum equation shown in Eq. 313, where $\boldsymbol{B}$ represents the background magnetic field, $\boldsymbol{f}_{en}$ and $\boldsymbol{f}_{in}$ the electron-neutral and ion-neutral drag forces respectively. The corresponding momentum transport equation for the neutral gas is given in Eq. 314.

$$\nabla P_e = \boldsymbol{j} \times \boldsymbol{B} + (\boldsymbol{f}_{en} + \boldsymbol{f}_{in}) \qquad \text{Eq. 313}$$

$$\nabla P_n = -(\boldsymbol{f}_{en} + \boldsymbol{f}_{in}) \qquad \text{Eq. 314}$$

Adding Eq. 313 and Eq. 314, we obtain the pressure balance for the combined plasma-neutral system embedded in a magnetic field $\nabla(P_e + P_n) = \boldsymbol{j} \times \boldsymbol{B}$. Using $\nabla \times \boldsymbol{B} = \mu_0 \boldsymbol{j}$ and assuming the magnetic field is uniform (no curvature) we obtain Eq. 315 [184].

$$\nabla(P_e + P_n) = -\nabla(B^2/2\mu_0) \qquad \text{Eq. 315}$$

If we consider that in laboratory experiments the plasma and neutral gas are contained inside a vacuum chamber, this expression states that the total thermal pressure inside the vacuum chamber $(P_e + P_n)$ is balanced by the magnetic pressure. This expression implies Eq. 316, where P_W is the neutral pressure at the wall[22] and B_0 is the magnitude of the magnetic field outside the plasma. In a low-beta plasma ($P_e \ll B_0^2/2\mu_0$), the magnetic field can be considered unaffected by the plasma diamagnetism and Eq. 316 can be reduced to Eq. 317, which is essentially the pressure balance of a non-magnetized plasma [159].

$$P_e + P_n + B^2/2\mu_0 = P_W + B_0^2/2\mu_0 \qquad \text{Eq. 316}$$

$$P_e + P_n = P_W \qquad \text{Eq. 317}$$

In low power discharges, the electron pressure is usually much less than the neutral pressure ($P_e \ll P_n$). For example, a 10 mTorr Argon discharge with $n_e \approx 10^{17}$ m^{-3} at 3 eV leads to

---

[22] During the discharge, P_W is usually greater than the pressure before the discharge due to gas heating.

$P_e/P_n \approx 1/100$ and the neutral gas pressure is essentially uniform at a value of P_W. Under these circumstances, the neutral gas is unperturbed by the presence of the plasma.

However, an 8 mTorr hydrogen discharge with $n_e \approx 1\times10^{19}$ m^{-3} at 4 eV leads to $P_e/P_n \approx 1$ for $T_n \approx 0.15$ eV; in this case, the neutral gas will be strongly affected by the plasma. Regions of high electron pressure will correspond to regions of low neutral pressure. If gas heating is considered, regions with low neutral pressure will be further depleted of neutral particles. This effect is referred to as neutral depletion and must be considered whenever $P_e \approx P_n$. Magee [52] discusses how neutral depletion can limit the maximum density achievable in helicon discharges.

Chapter 8 Conclusions and further research

8.1 Introduction 227
8.2 Characterization of MAGPIE 227
8.3 RF compensation of double Langmuir probes 228
8.4 Wave propagation in MAGPIE 229
8.5 Formation of equilibrium density profiles in MAGPIE 230

8.1 Introduction

In this thesis, we have investigated several matters related to the operation of MAGPIE such as: characterization of high density hydrogen plasma, RF compensation of electrostatic probes, wave propagation and RF power deposition, and the formation of equilibrium density profiles in in the presence of converging magnetic fields. In what follows, we summarize our main findings from each topic investigated, together with recommendations for future research.

8.2 Characterization of MAGPIE

Conclusions

In Chapter 2, we introduced MAGPIE and provided an overview of typical hydrogen discharge behaviour for a range of magnetic field configurations, RF powers and fill pressures. Characterization of MAGPIE in hydrogen plasma using microwave interferometry and electrostatic probes revealed the following important points:

- The plasma density in MAGPIE increases monotonically away from the antenna region until it reaches a maximum value in the target region.
- MAGPIE is capable of producing high density hydrogen plasma (2-3 x 10^{19} m^{-3}) at low electron temperatures (1-8 eV) with 20 kW of RF power. Producing these plasma densities requires the use of converging magnetic fields. In addition, the density in the target region scales approximately linearly with the magnetic field.
- Helicon waves propagating away from the RF antenna are absorbed within 40 cm and do not reach the peak of the magnetic field region.
- For hydrogen fill pressures above 6 mTorr, MAGPIE is capable of producing “detached” plasmas in the vicinity of a conducting plate located 70 cm away from the RF antenna. The 70 cm connection length between the plasma source and the conducting end plate

allows substantial electron cooling from 5-7 eV under the RF antenna to less than 0.5 eV at the end plate.

- In Chapter 3, we found that protons are the dominant ions in MAGPIE above 10 kW and fill pressures between 2 to 8 mTorr. Discharges operated outside this parameter space appear to have non-negligible content of molecular ions (H_2^+ and H_3^+).

Recommendations

In relation to this topic, the following points provide some ideas and recommendations for future research in MAGPIE:

- Characterization of MAGPIE with material targets inserted in hydrogen plasma. One difficulty with this study is the interaction of the plasma with the target. This process could lead to molecular ion production (H_2^+ and H_3^+) in amounts that render ion saturation current measurements unable to estimate electron density as discussed in Chapter 3. This can be circumvented with the use of microwave interferometry or other electron based diagnostics.
- Systematic study of the effect of magnetic field strength under the RF antenna. Preliminary studies in MAGPIE indicate the presence of low frequency instabilities for magnetic fields that satisfy the lower hybrid resonance in accordance with Mori [33].
- In regard to the “detached” hydrogen plasma observed in MAGPIE, the low electron temperature ($<$ 1 eV) and high plasma density (1x10^{19} m^{-3}) in the “detached” region may be favourable for the production of negative ion (H^-).
- Neutral depletion in high power (≥ 20 kW) hydrogen discharges in MAGPIE should be investigated with diagnostics such as TALIF with the aim of understanding how neutral depletion may limit the highest plasma densities achievable.

8.3 RF compensation of double Langmuir probes

Conclusions

Chapter 4 provides a detailed analysis of the RF compensation of the Double Langmuir Probe (DLP). We provide means of assessing under what conditions a DLP can be considered RF compensated. Moreover, we investigate the effect of RF rectification on probe measurements. The most important conclusions reached include:

- A DLP can be modelled as a floating probe passively driven by the RF plasma potential. Using the ideas presented in Chapter 4, we describe the ability of a floating probe to follow oscillations in the plasma potential.

- RF compensation can be quantified by measuring the ion saturation current, the magnitude of the RF plasma potential and the effective stray capacitance of the probe. In addition, we describe how to design RF compensated DLPs, single Langmuir probes and RF floating probes for measuring the RF plasma potential.
- RF rectification increases the ion current collected by a DLP; thereby, causing an overestimation of the ion density relative to the RF compensated case.
- Provided electrons are Maxwell-Boltzmann distributed, our results indicate that the electron temperature measurement is weakly affected by RF rectification.

Recommendations

The following points provide some ideas and recommendations for future research:

- The analysis provided in Chapter 4 does not include the presence of multiple frequencies on the RF plasma potential. Numerical solutions are required to model these conditions.
- To confirm the expected RF immunity of the electron temperature measurement (see [88] and Figure 50a in Chapter 4) in DLPs, it is advisable to extend these experiments to a wider range of plasma densities, gas species, RF frequencies and RF potentials.

8.4 Wave propagation in MAGPIE

Conclusions

In Chapter 6, we investigated how helicon waves in MAGPIE are excited by the RF antenna. We observed the helicon wave two-dimensional propagation characteristics and attenuation. Using experimental measurements and full wave codes, the most important conclusions reached include:

- Results suggest that the 22 cm half-turn helical antenna in MAGPIE is not optimized to excite waves at the conditions investigated (40-70 G, 7 MHz, $5\text{x}10^{18}$ m^{-3}). The antenna requires a higher helicity or a higher magnetic field at the antenna region.
- Under the conditions investigated, wave excitation is mainly driven by the near field of the antenna's azimuthal current rings, while the helical current strap plays a secondary role. Waves travel from the edge of the plasma towards the center of the discharge approximately along the whistler wave ray direction.
- Interference patterns in the wavefields can be explained through constructive interference of these obliquely travelling waves.

- Comparison between experiment and theory indicate that helicon wave attenuation in MAGPIE under the conditions investigated can be explained entirely through collisional processes.
- Full wave code simulations with an optimized, higher helicity antenna indicate that wave excitation is driven primarily by the helical current strap, antenna-wave coupling is maximized and interference patterns are reduced.
- When operating with the “strong mirror” magnetic field configuration, the RF power deposition is composed of an edge and an on-axis component associated with the Trivelpiece-Gould and Helicon wave respectively.
- RF power deposition in MAGPIE is axially non-uniform and qualitatively consistent with the electron pressure profile. We suspect that the non-uniform RF heating in MAGPIE leads to pressure gradient driven flows.

Recommendations

The following points provide some ideas and recommendations for future research:

- By optimizing the helical antenna in MAGPIE, can higher plasma densities be achieved for the same RF power? To answer this question, we recommend a systematic study of wave excitation with different antenna lengths and helicities for a constant RF power and magnetic field configuration.
- In reference to the wave excitation mechanism, a detailed two-dimensional characterization of the wavefields in the vicinity of the antenna as a function of antenna helicity may reveal the transition from azimuthal to helical strap wave excitation. These experiments can be used to study the formation of interference patterns when using optimum and sub-optimum antenna helicities.
- To improve our understanding of the RF power deposition mechanism in MAGPIE, the 1/9 amplitude factor required to match the EMS2D wave amplitude calculations with experiment needs to be resolved.

8.5 Formation of equilibrium density profiles in MAGPIE

Conclusions

In Chapter 7, we have investigated the mechanism that drives plasma into the target region where it reaches a maximum value. In addition, we have calculated the magnitude and location of the particle sources and sinks along the length of MAGPIE. Using experimental measurements and performing a 1D fluid analysis of MAGPIE, we reached the following conclusions:

- Electrons are in dynamic (flowing) equilibrium between the electric, pressure and thermal forces.
- The plasma is transported into the target region by the electron pressure gradient.
- Mach probe measurements indicate that the plasma flow reaches Mach numbers close to 0.7 near the end plate.
- Measurements of the plasma flux indicate that the plasma column in MAGPIE can be divided into an ionizing ($z < 30$ cm) and recombining region ($35 < z < 60$ cm).
- The equilibrium plasma density along the length of MAGPIE can be quantitatively explained using a 1D particle transport calculation that includes:
    - Pressure gradient driven plasma flow.
    - Magnetic compression of the plasma.
    - Volumetric particle sources and sinks (ionization and recombination).
- Recombination rates, estimated from the decrease in the measured total plasma flux (ΓA), are approximately three orders of magnitude higher than those predicted from three-body recombination (3BR). Estimates of Molecular Activated Recombination (MAR) rates using experimental values of plasma density and electron temperature are consistent with the measured plasma recombination.
- At fill pressures equal or greater than 8 mTorr, a large fraction of the plasma created in the ionizing region is lost in the recombining region and only a small fraction of the plasma reaches the end plate at $z = 65$ cm. This is characteristic of a detached plasma.
- Experimental measurements of plasma density near the end plate shown in Figure 24 Chapter 2 (page 43) suggest that “detachment” occurs whenever the electron temperature falls below 1 eV.
- Theoretical estimates of the ion-neutral collision frequency, in conjunction with the measured plasma flow profile, suggest the presence of neutral depletion. The theoretical and experimental plasma flows are consistent only if the neutral gas density is reduced to less than half the value before the discharge.

Recommendations

The following points provide some ideas and recommendations for future research:

- The force balance analysis of MAGPIE presented in Chapter 7 is performed on axis (r = 0 cm); hence, we recommend an extension of this analysis to include the entire plasma volume. This analysis may reveal the interplay between axial and azimuthal plasma flow and the effect of the magnetic mirror force in MAGPIE.

- We recommend the inclusion of the neutral gas momentum and particle transport in the analysis in order to model the neutral dynamics. This additional physics will allow modelling neutral depletion effects.
- What is the spectral signature of the optical emission in the recombining region? This may reveal the presence of MAR, 3BR or a combination of both. The intensities of high order Balmer series could be investigated as indicators of 3BR (private communication Prof. Kieran Gibson, 2015). We also recommend these measurements to be done as a function of fill pressure and RF power.
- In order to investigate the plasma “detachment” in MAGPIE, inert gas discharges (e.g. helium, argon) could be used to reduce the complexity involved in modelling the plasma chemistry.
- We recommend self-consistently calculating the spatial distribution of the various ionic and neutral hydrogenic species along the length of MAGPIE with codes such as the SOLPS (Scrap-Off Layer Plasma Simulation) package as described in [21], [182]. Such a simulation could provide additional information to evaluate the relative importance of Molecular Activated Recombination (MAR) and Three-Body Recombination (3BR) in detached plasmas observed in MAGPIE.
- Neutral depletion in high power (≥ 20 kW) hydrogen discharges in MAGPIE should be investigated with diagnostics such as TALIF with the aim of understanding how neutral depletion may limit the highest plasma densities achievable.

Bibliography

[1] J. P. Freidberg, *Plasma Physics and Fusion Energy*. Cambridge: Cambridge University Press, 2007.

[2] C. L. Smith and S. Cowley, “The path to fusion power,” *Philos Trans A Math Phys Eng Sci*, vol. 368, no. 1914, pp. 1091–1108, Mar. 2010.

[3] K. M. McGuire, H. Adler, P. Alling. et al. “Review of deuterium–tritium results from the Tokamak Fusion Test Reactor,” *Physics of Plasmas (1994-present)*, vol. 2, no. 6, pp. 2176–2188, Jun. 1995.

[4] A. Gibson and J. E. T. Team, “Deuterium–tritium plasmas in the Joint European Torus (JET): Behavior and implications,” *Physics of Plasmas (1994-present)*, vol. 5, no. 5, pp. 1839–1847, May 1998.

[5] M. Keilhacker, A. Gibson, C. Gormezano,et al. “High fusion performance from deuterium-tritium plasmas in JET,” *Nuclear Fusion*, vol. 39, no. 2, pp. 209–234, Feb. 1999.

[6] M. Keilhacker, A. Gibson, C. Gormezano, and P. H. Rebut, “The scientific success of JET,” *Nucl. Fusion*, vol. 41, no. 12, p. 1925, Dec. 2001.

[7] B. J. Green and I. I. T. and P. Teams, “ITER: burning plasma physics experiment,” *Plasma Physics and Controlled Fusion*, vol. 45, no. 5, pp. 687–706, May 2003.

[8] K. Ehrlich and A. Möslang, “IFMIF – An international fusion materials irradiation facility,” *Nuclear Instruments and Methods in Physics Research Section B: Beam Interactions with Materials and Atoms*, vol. 139, no. 1–4, pp. 72–81, Apr. 1998.

[9] A. Möslang, “IFMIF: the intense neutron source to qualify materials for fusion reactors,” *Comptes Rendus Physique*, vol. 9, no. 3, pp. 457–468, 2008.

[10] S. Konishi, S. Nishio, and K. Tobita, “DEMO plant design beyond ITER,” *Fusion engineering and design*, vol. 63, pp. 11–17, 2002.

[11] A. Fasoli, C. Gormenzano, H. . Berk, B. Breizman, S. Briguglio, D. . Darrow, N. Gorelenkov, W. . Heidbrink, A. Jaun, S. . Konovalov, R. Nazikian, J.-M. Noterdaeme, S. Sharapov, K. Shinohara, D. Testa, K. Tobita, Y. Todo, G. Vlad, and F. Zonca, “Chapter 5: Physics of energetic ions,” *Nuclear Fusion*, vol. 47, no. 6, pp. S264–S284, Jun. 2007.

[12] G. Conway, “Turbulence measurements in fusion plasmas,” *Plasma Physics and Controlled Fusion*, vol. 50, p. 124026, 2008.

[13] T. Evans, R. Moyer, J. Watkins, T. Osborne, P. Thomas, M. Becoulet, J. Boedo, E. Doyle, M. Fenstermacher, K. Finken, and others, “Suppression of large edge localized modes with edge resonant magnetic fields in high confinement DIII-D plasmas,” *Nuclear fusion*, vol. 45, p. 595, 2005.

[14] G. Federici, C. . Skinner, J. . Brooks, J. . Coad, C. Grisolia, A. . Haasz, A. Hassanein, V. Philipps, C. . Pitcher, J. Roth, W. . Wampler, and D. . Whyte,

"Plasma-material interactions in current tokamaks and their implications for next step fusion reactors," *Nuclear Fusion*, vol. 41, pp. 1967–2137, Dec. 2001.

[15] U. Samm, "Controlled thermonuclear fusion at the beginning of a new era," *Contemporary Physics*, vol. 44, pp. 203–217, May 2003.

[16] U. Samm, "Plasma wall interaction in magnetically confined fusion plasmas," *Trans. Fusion Sci. Technol*, vol. 53, pp. 223–228, 2008.

[17] H. Bolt, V. Barabash, W. Krauss, J. Linke, R. Neu, S. Suzuki, N. Yoshida, and ASDEX Upgrade Team, "Materials for the plasma-facing components of fusion reactors," *Journal of Nuclear Materials*, vol. 329–333, Part A, pp. 66–73, Aug. 2004.

[18] G. L. Jackson, J. Winter, T. S. Taylor, K. H. Burrell, J. C. DeBoo, C. M. Greenfield, R. J. Groebner, T. Hodapp, K. Holtrop, E. A. Lazarus, L. L. Lao, S. I. Lippmann, T. H. Osborne, T. W. Petrie, J. Phillips, R. James, D. P. Schissel, E. J. Strait, A. D. Turnbull, W. P. West, and DIII-D Team, "Regime of very high confinement in the boronized DIII-D tokamak," *Phys. Rev. Lett.*, vol. 67, no. 22, pp. 3098–3101, Nov. 1991.

[19] G. Janeschitz, K. Borrass, G. Federici, Y. Igitkhanov, A. Kukushkin, H. D. Pacher, G. W. Pacher, and M. Sugihara, "The ITER divertor concept," *Journal of Nuclear Materials*, vol. 220–222, pp. 73–88, Apr. 1995.

[20] L. Perkins, B. Logan, M. Rosen, M. Perry, T. Rubia, N. Ghoniem, T. Ditmire, P. Springer, and S. Wilks, "The investigation of high intensity laser driven micro neutron sources for fusion materials research at high fluence," *Nuclear fusion*, vol. 40, p. 1, 2000.

[21] J. Rapp, L. W. Owen, X. Bonnin, J. F. Caneses, J. M. Canik, C. Corr, and J. D. Lore, "Transport simulations of linear plasma generators with the B2.5-Eirene and EMC3-Eirene codes," *Journal of Nuclear Materials*.

[22] H. J. N. van Eck, W. R. Koppers, G. J. van Rooij, W. J. Goedheer, B. de Groot, P. Smeets, J. Scholten, M. van de Pol, S. Brons, R. Koch, B. Schweer, U. Samm, V. Philipps, R. A. H. Engeln, D. C. Schram, N. J. Lopes Cardozo, and A. W. Kleyn, "Pre-design of Magnum-PSI: A new plasma–wall interaction experiment," *Fusion Engineering and Design*, vol. 82, no. 15–24, pp. 1878–1883, Oct. 2007.

[23] G. van Rooij, V. Veremiyenko, W. Goedheer, B. de Groot, A. Kleyn, P. Smeets, T. Versloot, D. Whyte, R. Engeln, D. Schram, and others, "Extreme hydrogen plasma densities achieved in a linear plasma generator," *Applied physics letters*, vol. 90, no. 12, pp. 121501–121501, 2007.

[24] D. M. Goebel, G. Campbell, and R. W. Conn, "Plasma surface interaction experimental facility (PISCES) for materials and edge physics studies," *Journal of Nuclear Materials*, vol. 121, pp. 277–282, May 1984.

[25] A. Kreter, "Reactor-Relevant Plasma-Material Interaction Studies in Linear Plasma Devices," *FST*, vol. 59, no. 1T, pp. 51–56, Jan. 2011.

[26] D. Naujoks, *Plasma-Material Interaction in Controlled Fusion*. Springer Science & Business Media, 2006.

[27] B. Unterberg, R. Jaspers, R. Koch, V. Massaut, J. Rapp, D. Reiter, S. Kraus, A. Kreter, V. Philipps, H. Reimer, U. Samm, L. Scheibl, B. Schweer, J. Schuurmans, I. Uytdenhouwen, R. Al, M. A. van den Berg, S. Brons, H. J. N. van Eck, W. J. Goedheer, M. F. Graswinckel, T. van der Grift, A. Kleyn, W. R. Koppers, O. Kruyt, A. Lof, H. J. van der Meiden, W. Melissen, M. van de Pol, G. J. van Rooij, P. Smeets, J. Scholten, D. C. Schram, G. De Temmerman, W. Vijvers, P. A. Z. van Emmichoven, and J. J. Zielinski, “New linear plasma devices in the trilateral euregio cluster for an integrated approach to plasma surface interactions in fusion reactors,” *Fusion Engineering and Design*.

[28] J. Roth, E. Tsitrone, A. Loarte, T. Loarer, G. Counsell, R. Neu, V. Philipps, S. Brezinsek, M. Lehnen, P. Coad, C. Grisolia, K. Schmid, K. Krieger, A. Kallenbach, B. Lipschultz, R. Doerner, R. Causey, V. Alimov, W. Shu, O. Ogorodnikova, A. Kirschner, G. Federici, and A. Kukushkin, “Recent analysis of key plasma wall interactions issues for ITER,” *Journal of Nuclear Materials*, vol. 390–391, pp. 1–9, Jun. 2009.

[29] C. S. Pitcher and P. C. Stangeby, “Experimental divertor physics,” *Plasma Physics and Controlled Fusion*, vol. 39, pp. 779–930, Jun. 1997.

[30] X. M. Guo, J. Scharer, Y. Mouzouris, and L. Louis, “Helicon experiments and simulations in nonuniform magnetic field configurations,” *Physics of Plasmas*, vol. 6, no. 8, p. 3400, 1999.

[31] J. Prager, T. Ziemba, R. Winglee, and B. R. Roberson, “Wave propagation downstream of a high power helicon in a dipolelike magnetic field,” *Physics of Plasmas*, vol. 17, no. 1, p. 013504, Jan. 2010.

[32] H. KIKUCHI, Y. SAKAWA, and T. SHOJI, “Hydrogen Plasma Production in the Lower-Hybrid Frequency Range.,” *J Plasma Fusion Res Ser*, vol. 5, pp. 302–305, 2003.

[33] Y. Mori, H. Nakashima, F. W. Baity, R. H. Goulding, M. D. Carter, and D. O. Sparks, “High density hydrogen helicon plasma in a non-uniform magnetic field,” *Plasma Sources Science and Technology*, vol. 13, no. 3, pp. 424–435, Aug. 2004.

[34] Y. Mori, H. Nakashima, F. W. Baity, R. H. Goulding, M. D. Carter, and D. O. Sparks, “Focusing magnetic field contribution for helicon plasma on Mini-RFTF,” *Thin Solid Films*, vol. 506–507, pp. 583–587, May 2006.

[35] M. Light, I. D. Sudit, F. F. Chen, and D. Arnush, “Axial propagation of helicon waves,” *Physics of Plasmas*, vol. 2, no. 11, pp. 4094–4103, Nov. 1995.

[36] M. Light and F. F. Chen, “Helicon wave excitation with helical antennas,” *Physics of Plasmas*, vol. 2, p. 1084, 1995.

[37] F. F. Chen, I. D. Sudit, and M. Light, “Downstream physics of the helicon discharge,” *Plasma Sources Sci. Technol.*, vol. 5, no. 2, p. 173, May 1996.

[38] D. A. Schneider, G. G. Borg, and I. V. Kamenski, “Measurements and code comparison of wave dispersion and antenna radiation resistance for helicon waves in a high density cylindrical plasma source,” *Physics of Plasmas*, vol. 6, no. 3, pp. 703–712, Mar. 1999.

[39] M. Light, F. F. Chen, and P. L. Colestock, “Low frequency electrostatic instability in a helicon plasma,” *Physics of Plasmas*, vol. 8, no. 10, p. 4675, Oct. 2001.

[40] Y. Sakawa, T. Takino, and T. Shoji, “Contribution of slow waves on production of high-density plasmas by m=0 helicon waves,” *Physics of Plasmas (1994-present)*, vol. 6, no. 12, pp. 4759–4766, Dec. 1999.

[41] F. F. Chen, “Experiments on helicon plasma sources,” *Journal of Vacuum Science & Technology A*, vol. 10, no. 4, pp. 1389–1401, Jul. 1992.

[42] V. F. Virko, K. P. Shamrai, Y. V. Virko, and G. S. Kirichenko, “Wave phenomena, hot electrons, and enhanced plasma production in a helicon discharge in a converging magnetic field,” *Physics of Plasmas (1994-present)*, vol. 11, no. 8, pp. 3888–3897, Aug. 2004.

[43] K. Takahashi, C. Charles, R. Boswell, M. A. Lieberman, and R. Hatakeyama, “Characterization of the temperature of free electrons diffusing from a magnetically expanding current-free double layer plasma,” *J. Phys. D: Appl. Phys.*, vol. 43, no. 16, p. 162001, Apr. 2010.

[44] B. D. Blackwell, J. F. Caneses, C. M. Samuell, J. Wach, J. Howard, and C. Corr, “Design and characterization of the Magnetized Plasma Interaction Experiment (MAGPIE): a new source for plasma–material interaction studies,” *Plasma Sources Sci. Technol.*, vol. 21, no. 5, p. 055033, Oct. 2012.

[45] C. Charles, “Hydrogen ion beam generated by a current-free double layer in a helicon plasma,” *Applied Physics Letters*, vol. 84, no. 3, pp. 332–334, Jan. 2004.

[46] A. T. Hjartarson, E. G. Thorsteinsson, and J. T. Gudmundsson, “Low pressure hydrogen discharges diluted with argon explored using a global model,” *Plasma Sources Sci. Technol.*, vol. 19, no. 6, p. 065008, Dec. 2010.

[47] Y. Sakawa, M. Ohshima, Y. Ohta, and T. Shoji, “Production of high-density hydrogen plasmas by helicon waves in a simple torus,” *Physics of Plasmas*, vol. 11, no. 1, pp. 311–319, Jan. 2004.

[48] M. D. Carter, F. W. Baity, G. C. Barber, R. H. Goulding, Y. Mori, D. O. Sparks, K. F. White, E. F. Jaeger, F. R. Chang-Díaz, and J. P. Squire, “Comparing experiments with modeling for light ion helicon plasma sources,” *Physics of Plasmas*, vol. 9, no. 12, pp. 5097–5110, Dec. 2002.

[49] L. Liard, J.-L. Raimbault, J.-M. Rax, and P. Chabert, “Plasma transport under neutral gas depletion conditions,” *J. Phys. D: Appl. Phys.*, vol. 40, no. 17, p. 5192, Sep. 2007.

[50] A. Aanesland, L. Liard, G. Leray, J. Jolly, and P. Chabert, “Direct measurements of neutral density depletion by two-photon absorption laser-induced fluorescence spectroscopy,” *Applied Physics Letters*, vol. 91, no. 12, p. 121502, Sep. 2007.

[51] L. Liard, A. Aanesland, and P. Chabert, “Dynamics of neutral gas depletion investigated by time- and space-resolved measurements of xenon atom ground state density,” *J. Phys. D: Appl. Phys.*, vol. 45, no. 23, p. 235201, Jun. 2012.

[52] R. M. Magee, M. E. Galante, J. C. Jr, G. Lusk, D. W. McCarren, and E. E. Scime, “Neutral depletion and the helicon density limit,” *Physics of Plasmas (1994-present)*, vol. 20, no. 12, p. 123511, Dec. 2013.

[53] A. Degeling, T. Sheridan, and R. Boswell, “Model for relaxation oscillations in a helicon discharge,” *Physics of Plasmas*, vol. 6, p. 1641, 1999.

[54] A. W. Degeling, T. E. Sheridan, and R. W. Boswell, “Intense on-axis plasma production and associated relaxation oscillations in a large volume helicon source,” *Physics of Plasmas (1994-present)*, vol. 6, no. 9, pp. 3664–3673, Sep. 1999.

[55] D. G. Miljak and F. F. Chen, “Helicon wave excitation with rotating antenna fields,” *Plasma Sources Science and Technology*, vol. 7, no. 1, pp. 61–74, Feb. 1998.

[56] D. J. D. Hartog, D. J. Craig, G. Fiksel, and J. S. Sarff, “Impurities, temperature and density in a miniature electrostatic plasma and current source,” *Plasma Sources Science and Technology*, vol. 6, pp. 492–498, Nov. 1997.

[57] D. M. Goebel, Y. Hirooka, and T. A. Sketchley, “Large-area lanthanum hexaboride electron emitter,” *Review of Scientific Instruments*, vol. 56, no. 9, pp. 1717–1722, Sep. 1985.

[58] D. M. Goebel and R. M. Watkins, “Compact lanthanum hexaboride hollow cathode,” *Review of Scientific Instruments*, vol. 81, p. 083504, 2010.

[59] C. M. Samuell, B. D. Blackwell, J. Howard, and C. S. Corr, “Plasma parameters and electron energy distribution functions in a magnetically focused plasma,” *Physics of Plasmas*, vol. 20, no. 3, p. 034502, Mar. 2013.

[60] M. A. Lieberman and A. J. Lichtenberg, *Principles of Plasma Discharges and Materials Processing*. John Wiley & Sons, 2005.

[61] I. H. Hutchinson, *Principles of Plasma Diagnostics*. Cambridge University Press, 2005.

[62] A. J. H. Donné, “High spatial resolution interferometry and polarimetry in hot plasmas,” *Review of Scientific Instruments*, vol. 66, no. 6, pp. 3407–3423, Jun. 1995.

[63] X. D. Feng, G. Zhuang, Z. J. Yang, L. Gao, and X. W. Hu, “Design and implementation of a 150 GHz single-channel millimeter wave interferometer on Joint TEXT tokamak,” *Review of Scientific Instruments*, vol. 84, no. 4, pp. 044705–044705–4, Apr. 2013.

[64] K. Dittmann, C. Küllig, and J. Meichsner, “160 GHz Gaussian beam microwave interferometry in low-density rf plasmas,” *Plasma Sources Sci. Technol.*, vol. 21, no. 2, p. 024001, Apr. 2012.

[65] J. D. Swift and M. J. R. Schwar, *Electrical probes for plasma diagnostics*. 42 Russell square London: Iliffe Books, 1970.

[66] R. H. Huddlestone, *Plasma diagnostic techniques*. Academic Press, 1965.

[67] I. D. Sudit and F. F. Chen, “RF compensated probes for high-density discharges,” *Plasma Sources Science and Technology*, vol. 3, no. 2, pp. 162–168, May 1994.

[68] J. G. Laframboise, “THEORY OF SPHERICAL AND CYLINDRICAL LANGMUIR PROBES IN A COLLISIONLESS, MAXWELLIAN PLASMA AT REST,” Jun. 1966.

[69] B. Beal, L. Johnson, D. Brown, J. Blakely, and D. Bromaghim, “Improved analysis techniques for cylindrical and spherical double probes,” *Review of Scientific Instruments*, vol. 83, no. 7, pp. 073506–073506–5, Jul. 2012.

[70] L. Oksuz, F. Soberón, and A. R. Ellingboe, “Analysis of uncompensated Langmuir probe characteristics in radio-frequency discharges revisited,” *Journal of Applied Physics*, vol. 99, no. 1, p. 013304, Jan. 2006.

[71] P. C. Stangeby and G. M. McCracken, “Plasma boundary phenomena in tokamaks,” *Nuclear Fusion*, vol. 30, pp. 1225–1379, Jul. 1990.

[72] J. A. Tagle, P. C. Stangeby, and S. K. Erents, “Errors in measuring electron temperatures using a single Langmuir probe in a magnetic field,” *Plasma Phys. Control. Fusion*, vol. 29, no. 3, p. 297, Mar. 1987.

[73] V. A. Godyak and V. I. Demidov, “Probe measurements of electron-energy distributions in plasmas: what can we measure and how can we achieve reliable results?,” *Journal of Physics D: Applied Physics*, vol. 44, no. 23, p. 233001, Jun. 2011.

[74] D. Batani, S. Alba, P. Lombardi, and A. Galassi, “Use of Langmuir probes in a weakly ionized, steady-state plasma with strong magnetic field,” *Review of Scientific Instruments*, vol. 68, no. 11, pp. 4043–4050, Nov. 1997.

[75] R. Zorat, J. Goss, D. Boilson, and D. Vender, “Global model of a radiofrequency H2 plasma in DENISE,” *Plasma Sources Sci. Technol.*, vol. 9, no. 2, p. 161, May 2000.

[76] R. Zorat and D. Vender, “Global model for an rf hydrogen inductive plasma discharge in the deuterium negative ion source experiment including negative ions,” *J. Phys. D: Appl. Phys.*, vol. 33, no. 14, p. 1728, Jul. 2000.

[77] F. Gaboriau and J. P. Boeuf, “Chemical kinetics of low pressure high density hydrogen plasmas: application to negative ion sources for ITER,” *Plasma Sources Sci. Technol.*, vol. 23, no. 6, p. 065032, Dec. 2014.

[78] M. Tuszewski, “A compact mass spectrometer for plasma discharge ion analysis,” *Review of Scientific Instruments*, vol. 67, no. 6, pp. 2215–2220, Jun. 1996.

[79] E. T. Everson, P. Pribyl, C. G. Constantin, A. Zylstra, D. Schaeffer, N. L. Kugland, and C. Niemann, “Design, construction, and calibration of a three-axis, high-frequency magnetic probe (B-dot probe) as a diagnostic for exploding plasmas,” *Review of Scientific Instruments*, vol. 80, no. 11, pp. 113505–113505–8, Nov. 2009.

[80] C. M. Franck, O. Grulke, and T. Klinger, “Magnetic fluctuation probe design and capacitive pickup rejection,” *Review of Scientific Instruments*, vol. 73, no. 11, pp. 3768–3771, Nov. 2002.

[81] S. Messer, D. D. Blackwell, W. E. Amatucci, and D. N. Walker, “Broadband calibration of radio-frequency magnetic induction probes,” *Review of Scientific Instruments*, vol. 77, no. 11, pp. 115104–115104–7, Nov. 2006.

[82] R. R. J. Gagné and A. Cantin, “Investigation of an rf Plasma with Symmetrical and Asymmetrical Electrostatic Probes,” *Journal of Applied Physics*, vol. 43, no. 6, pp. 2639–2647, Jun. 1972.

[83] V. A. Godyak and R. B. Piejak, “Probe measurements of the space potential in a radio frequency discharge,” *Journal of Applied Physics*, vol. 68, no. 7, pp. 3157–3162, Oct. 1990.

[84] B. M. Annaratone and N. S. J. Braithwaite, “A comparison of a passive (filtered) and an active (driven) probe for RF plasma diagnostics,” *Measurement Science and Technology*, vol. 2, no. 8, pp. 795–800, Aug. 1991.

[85] B. M. Annaratone, G. F. Counsell, H. Kawano, and J. E. Allen, “On the use of double probes in RF discharges,” *Plasma Sources Science and Technology*, vol. 1, no. 4, pp. 232–241, Nov. 1992.

[86] M. Tuszewski and J. A. Tobin, “The accuracy of Langmuir probe ion density measurements in low-frequency RF discharges,” *Plasma Sources Science and Technology*, vol. 5, no. 4, pp. 640–647, Nov. 1996.

[87] S.-J. Oh, I.-J. Choi, J.-Y. Kim, and C.-W. Chung, “Double probe diagnostics based on harmonic current detection for electron temperature and electropositive ion flux measurement in RF plasmas,” *Measurement Science and Technology*, vol. 23, no. 8, p. 085001, Aug. 2012.

[88] A. Stampa and H. O. Wulf, “The behaviour of electrostatic double probes in plasmas with high-amplitude RF fields,” *J. Phys. D: Appl. Phys.*, vol. 11, no. 7, p. 1119, May 1978.

[89] J. F. Caneses and B. Blackwell, “RF compensation of double Langmuir probes: modelling and experiment,” *Plasma Sources Sci. Technol.*, vol. 24, no. 3, p. 035024, Jun. 2015.

[90] N. S. J. Braithwaite, T. E. Sheridan, and R. W. Boswell, “Transient RF self-bias in electropositive and electronegative plasmas,” *Journal of Physics D: Applied Physics*, vol. 36, no. 22, pp. 2837–2844, Nov. 2003.

[91] K.-T. Hwang, S.-J. Oh, I.-J. Choi, and C.-W. Chung, “Measurement of electron temperature and ion density using the self-bias effect in plasmas,” *Physics of Plasmas*, vol. 17, no. 6, pp. 063501–063501–4, Jun. 2010.

[92] M.-H. Lee, S.-H. Jang, and C.-W. Chung, “Floating probe for electron temperature and ion density measurement applicable to processing plasmas,” *Journal of Applied Physics*, vol. 101, no. 3, pp. 033305–033305–6, Feb. 2007.

[93] K.-U. Riemann, “The validity of Bohm’s sheath criterion in rf discharges,” *Physics of Fluids B: Plasma Physics*, vol. 4, no. 9, pp. 2693–2695, Sep. 1992.

[94] F. F. Chen, “Time-varying impedance of the sheath on a probe in an RF plasma,” *Plasma Sources Sci. Technol.*, vol. 15, no. 4, p. 773, Nov. 2006.

[95] A. Boschi and F. Magistrelli, “Effect of a R.F, signal on the characteristic of a langmuir probe,” *Nuovo Cim*, vol. 29, no. 2, pp. 487–499, Jul. 1963.

[96] N. S. J. Braithwaite, J. P. Booth, and G. Cunge, “A novel electrostatic probe method for ion flux measurements,” *Plasma Sources Science and Technology*, vol. 5, no. 4, pp. 677–684, Nov. 1996.

[97] J. W. Coburn and E. Kay, “Positive ion bombardment of substrates in rf diode glow discharge sputtering,” *Journal of Applied Physics*, vol. 43, no. 12, pp. 4965–4971, 1972.

[98] J. A. Boedo, D. Gray, R. W. Conn, P. Luong, M. Schaffer, R. S. Ivanov, A. V. Chernilevsky, and G. Van Oost, “On the harmonic technique to measure electron temperature with high time resolution,” *Review of Scientific Instruments*, vol. 70, no. 7, pp. 2997–3006, Jul. 1999.

[99] E. O. Johnson and L. Malter, “A Floating Double Probe Method for Measurements in Gas Discharges,” *Phys. Rev.*, vol. 80, no. 1, pp. 58–68, Oct. 1950.

[100] E. A. Edelberg and E. S. Aydil, “Modeling of the sheath and the energy distribution of ions bombarding rf-biased substrates in high density plasma reactors and comparison to experimental measurements,” *Journal of Applied Physics*, vol. 86, no. 9, pp. 4799–4812, Nov. 1999.

[101] E. Kawamura, V. Vahedi, M. A. Lieberman, and C. K. Birdsall, “Ion energy distributions in rf sheaths; review, analysis and simulation,” *Plasma Sources Sci. Technol.*, vol. 8, no. 3, p. R45, Aug. 1999.

[102] A. E. Wendt, “Passive external radio frequency filter for Langmuir probes,” *Review of Scientific Instruments*, vol. 72, no. 7, pp. 2926–2930, Jul. 2001.

[103] C. Steinbrüchel, “A new method for analyzing Langmuir probe data,” 1990.

[104] F. F. Chen, “Langmuir probe analysis for high density plasmas,” *Physics of Plasmas*, vol. 8, no. 6, pp. 3029–3041, Jun. 2001.

[105] G. Narasimhan and C. Steinbruchel, “Analysis of Langmuir probe data: Analytical parametrization, and the importance of the end effect,” *Journal of Vacuum Science & Technology A: Vacuum, Surfaces, and Films*, vol. 19, no. 1, pp. 376–378, 2001.

[106] A. Brockhaus, C. Borchardt, and J. Engemann, “Langmuir probe measurements in commercial plasma plants,” *Plasma Sources Science and Technology*, vol. 3, no. 4, pp. 539–544, Nov. 1994.

[107] D. A. Herman and A. D. Gallimore, “An ion thruster internal discharge chamber electrostatic probe diagnostic technique using a high-speed probe positioning system,” *Review of Scientific Instruments*, vol. 79, no. 1, pp. 013302–013302–10, Jan. 2008.

[108] F. F. Chen, “dc probe detection of phased EEDFs in RF discharges,” *Plasma Phys. Control. Fusion*, vol. 39, no. 10, p. 1533, Oct. 1997.

[109] F. F. Chen and D. D. Blackwell, “Upper Limit to Landau Damping in Helicon Discharges,” *Phys. Rev. Lett.*, vol. 82, no. 13, pp. 2677–2680, Mar. 1999.

[110] Y. Zhang, J. Liu, Y. Liu, and X. Wang, “Characteristics of a plasma sheath in a radio frequency biased voltage,” *Physics of Plasmas*, vol. 11, no. 8, pp. 3840–3844, Jul. 2004.

[111] D. Bose, T. R. Govindan, and M. Meyyappan, “Ion dynamics model for collisionless radio frequency sheaths,” *Journal of Applied Physics*, vol. 87, no. 10, pp. 7176–7184, May 2000.

[112] P. Chabert and N. Braithwaite, *Physics of Radio-Frequency Plasmas*. Cambridge University Press, 2011.

[113] R. T. Hilbish, R. M. Montgomery, and R. A. Holmes, “Frequency Conversion in the Sheath Capacitance of a Glow Discharge Plasma,” *Journal of Applied Physics*, vol. 39, no. 12, pp. 5782–5791, Nov. 1968.

[114] S.-J. Oh, Y.-K. Lee, and C.-W. Chung, “Measurement of the sheath capacitance of a planar probe,” *Physics of Plasmas*, vol. 18, no. 10, pp. 103511–103511–5, Oct. 2011.

[115] E. van Lanen, R. Smeets, M. Popov, and L. van der Sluis, “Vacuum Circuit Breaker Postarc Current Modelling Based on the Theory of Langmuir Probes,” *IEEE Transactions on Plasma Science*, vol. 35, no. 4, pp. 925–932, Aug. 2007.

[116] K. P. Shamrai and V. B. Taranov, “Volume and surface rf power absorption in a helicon plasma source,” *Plasma Sources Sci. Technol.*, vol. 5, no. 3, p. 474, Aug. 1996.

[117] F. F. Chen and D. Arnush, “Generalized theory of helicon waves. I. Normal modes,” *Physics of Plasmas*, vol. 4, no. 9, pp. 3411–3421, Sep. 1997.

[118] D. Arnush and F. F. Chen, “Generalized theory of helicon waves. II. Excitation and absorption,” *Physics of Plasmas*, vol. 5, no. 5, pp. 1239–1254, May 1998.

[119] G. G. Borg and R. W. Boswell, “Power coupling to helicon and Trivelpiece–Gould modes in helicon sources,” *Physics of Plasmas (1994-present)*, vol. 5, no. 3, pp. 564–571, Mar. 1998.

[120] D. Arnush, “The role of Trivelpiece–Gould waves in antenna coupling to helicon waves,” *Physics of Plasmas (1994-present)*, vol. 7, no. 7, pp. 3042–3050, Jul. 2000.

[121] D. D. Blackwell, T. G. Madziwa, D. Arnush, and F. F. Chen, “Evidence for Trivelpiece-Gould Modes in a Helicon Discharge,” *Phys. Rev. Lett.*, vol. 88, no. 14, p. 145002, Mar. 2002.

[122] F. F. Chen, “Plasma ionization by helicon waves,” *Plasma Physics and Controlled Fusion*, vol. 33, p. 339, 1991.

[123] D. G. Swanson, “Plasma Waves (2nd edition),” *Plasma Phys. Control. Fusion*, vol. 45, no. 6, p. 1069, Jun. 2003.

[124] J. E. Hipp, M. Kristiansen, and M. O. Hagler, “Traveling-Wave Antenna for Exciting Waves in a Cylindrical Anisotropic Plasma,” *Journal of Applied Physics*, vol. 42, no. 12, pp. 4887–4898, Nov. 1971.

[125] J. E. Cato, “Wave propagation and damping in a hot, bounded plasma,” Texas Tech University, 1971.

[126] I. V. Kamenski and G. G. Borg, “An evaluation of different antenna designs for helicon wave excitation in a cylindrical plasma source,” *Physics of Plasmas (1994-present)*, vol. 3, no. 12, pp. 4396–4409, Dec. 1996.

[127] P. L. Colestock and W. D. Getty, “Excitation and propagation of lower-hybrid waves in a bounded, inhomogeneous plasma,” *Physics of Fluids*, vol. 19, no. 8, p. 1229, 1976.

[128] T. H. Stix, *Waves in Plasmas*. New York: American Institute of Physics, 1992.

[129] S. I. Braginskii, “Transport Processes in a Plasma,” in *Reviews of Plasma Physics*, Edited by M.A. Leontovich., vol. 1, New York: Consultants Bureau, 1965, p. 205.

[130] R. Fitzpatrick, *Plasma Physics: An Introduction*. CRC Press, 2014.

[131] J. D. Huba, “NRL Plasma Formulary,” Naval Research Laboratory, Washington, DC, Formulary NRL/PU/6790--11-551, 2011.

[132] S. Cho and M. A. Lieberman, “Self-consistent discharge characteristics of collisional helicon plasmas,” *Physics of Plasmas (1994-present)*, vol. 10, no. 3, pp. 882–890, Feb. 2003.

[133] Y. Mouzouris and J. E. Scharer, “Modeling of profile effects for inductive helicon plasma sources,” *IEEE Transactions on Plasma Science*, vol. 24, no. 1, pp. 152–160, Feb. 1996.

[134] Y. Mouzouris and J. E. Scharer, “Wave propagation and absorption simulations for helicon sources,” *Physics of Plasmas*, vol. 5, no. 12, pp. 4253–4261, Dec. 1998.

[135] D. Melazzi, D. Curreli, M. Manente, J. Carlsson, and D. Pavarin, “SPIREs: A Finite-Difference Frequency-Domain electromagnetic solver for inhomogeneous magnetized plasma cylinders,” *Computer Physics Communications*, vol. 183, no. 6, pp. 1182–1191, Jun. 2012.

[136] S. Cho, “The dependence of the plasma density on the magnetic field and power absorption in helicon discharges,” *Physics Letters A*, vol. 216, no. 1–5, pp. 137–141, Jun. 1996.

[137] S. Cho and J.-G. Kwak, “The effects of the density profile on the power absorption and the equilibrium density in helicon plasmas,” *Physics of Plasmas*, vol. 4, no. 11, pp. 4167–4172, Nov. 1997.

[138] K. P. Shamrai and V. B. Taranov, “Resonance wave discharge and collisional energy absorption in helicon plasma source,” *Plasma Phys. Control. Fusion*, vol. 36, no. 11, p. 1719, Nov. 1994.

[139] K. P. Shamrai and S. Shinohara, “Modeling electromagnetic field excitation and rf power absorption in a large helicon plasma,” *Thin Solid Films*, vol. 506–507, pp. 555–558, May 2006.

[140] K. P. Shamrai and S. Shinohara, “Spectral and spatial characterization of a radio frequency power absorption in high pressure helicon plasmas,” *Physics of Plasmas*, vol. 8, no. 10, pp. 4659–4674, Oct. 2001.

[141] M. Kramer, “Propagation and damping of m=+1 and m=−1 helicon modes in an inhomogeneous plasma column,” *Physics of Plasmas*, vol. 6, no. 4, pp. 1052–1058, Apr. 1999.

[142] T. Enk and M. Krämer, “Radio frequency power deposition in a high-density helicon discharge with helical antenna coupling,” *Physics of Plasmas*, vol. 7, no. 10, pp. 4308–4319, Oct. 2000.

[143] M. Kramer, T. Enk, and B. Lorenz, “Effect of the Plasma Inhomogeneity on the Wave Excitation and the rf Power Deposition in Helicon Discharges,” *Phys. Scr.*, vol. 2000, no. T84, p. 132, Jan. 2000.

[144] M. Kramer, B. Lorenz, and B. Clarenbach, “Helicon sources with m = +1 and m = +2 helical antenna coupling.,” *Plasma Sources Science and Technology*, vol. 11, no. 3A, pp. A120–A130, Aug. 2002.

[145] B. Fischer, M. Kramer, and T. Enk, “Helicon wave coupling to a finite plasma column,” *Plasma Phys. Control. Fusion*, vol. 36, no. 12, p. 2003, Dec. 1994.

[146] G. Chen, A. V. Arefiev, R. D. Bengtson, B. N. Breizman, C. A. Lee, and L. L. Raja, “Resonant power absorption in helicon plasma sources,” *Physics of Plasmas*, vol. 13, no. 12, p. 123507, Dec. 2006.

[147] D. Curreli, “Transition from edge-localized to center-localized power deposition in helicon discharges,” *The European Physical Journal - Applied Physics*, vol. 56, no. 02, Nov. 2011.

[148] D. Curreli and F. F. Chen, “Equilibrium theory of cylindrical discharges with special application to helicons,” *Physics of Plasmas (1994-present)*, vol. 18, no. 11, p. 113501, Nov. 2011.

[149] L. Chang, M. J. Hole, J. F. Caneses, G. Chen, B. D. Blackwell, and C. S. Corr, “Wave modeling in a cylindrical non-uniform helicon discharge,” *Physics of Plasmas*, vol. 19, no. 8, pp. 083511–083511–10, Aug. 2012.

[150] T. Shoji, Y. Sakawa, S. Nakazawa, K. Kadota, and T. Sato, “Plasma production by helicon waves,” *Plasma Sources Sci. Technol.*, vol. 2, no. 1, p. 5, Feb. 1993.

[151] L. R. O. Storey, “An Investigation of Whistling Atmospherics,” *Philosophical Transactions of the Royal Society of London. Series A, Mathematical and Physical Sciences*, vol. 246, no. 908, pp. 113–141, Jul. 1953.

[152] A. W. Degeling, G. G. Borg, and R. W. Boswell, “Transitions from electrostatic to electromagnetic whistler wave excitation,” *Physics of Plasmas (1994-present)*, vol. 11, no. 5, pp. 2144–2155, May 2004.

[153] J. E. Maggs, T. A. Carter, and R. J. Taylor, “Transition from Bohm to classical diffusion due to edge rotation of a cylindrical plasma,” *Physics of Plasmas (1994-present)*, vol. 14, no. 5, p. 052507, May 2007.

[154] S. Oldenbürger, S. Inagaki, T. Kobayashi, H. Arakawa, N. Ohyama, K. Kawashima, Y. Tobimatsu, A. Fujisawa, K. Itoh, and S.-I. Itoh, “Dynamics of particle flux in a cylindrical magnetized plasma,” *Plasma Phys. Control. Fusion*, vol. 54, no. 5, p. 055002, May 2012.

[155] K.-S. Chung, “Mach probes,” *Plasma Sources Sci. Technol.*, vol. 21, no. 6, p. 063001, Dec. 2012.

[156] F. F. Chen and D. Curreli, “Central peaking of magnetized gas dischargesa),” *Physics of Plasmas (1994-present)*, vol. 20, no. 5, p. 057102, May 2013.

[157] S. Cho, “A self-consistent global model of neutral gas depletion in pulsed helicon plasmas,” *Physics of Plasmas (1994-present)*, vol. 6, no. 1, pp. 359–364, Jan. 1999.

[158] S. Yun, K. Taylor, and G. R. Tynan, “Measurement of radial neutral pressure and plasma density profiles in various plasma conditions in large-area high-density plasma sources,” *Physics of Plasmas (1994-present)*, vol. 7, no. 8, pp. 3448–3456, Aug. 2000.

[159] A. Fruchtman, G. Makrinich, P. Chabert, and J. M. Rax, “Enhanced Plasma Transport Due To Neutral Depletion,” *Phys. Rev. Lett.*, vol. 95, no. 11, p. 115002, Sep. 2005.

[160] R. M. Magee, M. E. Galante, N. Gulbrandsen, D. W. McCarren, and E. E. Scime, “Direct measurements of the ionization profile in krypton helicon plasmas,” *Physics of Plasmas (1994-present)*, vol. 19, no. 12, p. 123506, Dec. 2012.

[161] M. E. Galante, R. M. Magee, and E. E. Scime, “Two photon absorption laser induced fluorescence measurements of neutral density in a helicon plasmaa),” *Physics of Plasmas (1994-present)*, vol. 21, no. 5, p. 055704, May 2014.

[162] C. M. Samuell and C. S. Corr, “Atomic and molecular hydrogen gas temperatures in a low-pressure helicon plasma,” *Plasma Sources Sci. Technol.*, vol. 24, no. 4, p. 045003, Aug. 2015.

[163] N. Škoro, N. Puač, S. Lazović, U. Cvelbar, G. Kokkoris, and E. Gogolides, “Characterization and global modelling of low-pressure hydrogen-based RF plasmas suitable for surface cleaning processes,” *J. Phys. D: Appl. Phys.*, vol. 46, no. 47, p. 475206, Nov. 2013.

[164] P. S. Krstić and D. R. Schultz, “Elastic processes involving vibrationally excited molecules in cold hydrogen plasmas,” *J. Phys. B: At. Mol. Opt. Phys.*, vol. 36, no. 2, p. 385, Jan. 2003.

[165] D. R. Schultz, P. S. Krstic, T. G. Lee, and J. C. Raymond, “Momentum Transfer and Viscosity from Proton-Hydrogen Collisions Relevant to Shocks and Other Astrophysical Environments,” *ApJ*, vol. 678, no. 2, p. 950, May 2008.

[166] P. Krstić, “Consistent definitions for, and relationships among, cross sections for elastic scattering of hydrogen ions, atoms, and molecules,” *Phys. Rev. A*, vol. 60, no. 3, pp. 2118–2130, 1999.

[167] M. H. Brennan and R. Morrow, “Proton-hydrogen atom momentum transfer cross section at approximately 5 eV,” *J. Phys. B: At. Mol. Phys.*, vol. 4, no. 7, p. L53, Jul. 1971.

[168] R. H. Comfort, “The Magnetic Mirror Force in Plasma Fluid Models,” in *Modeling Magnetospheric Plasma*, T. E. Moore, J. H. W. Jr, T. W. Moorehead, and W. B. Hanson, Eds. American Geophysical Union, 1988, pp. 51–53.

[169] K. Takahashi, T. Lafleur, C. Charles, P. Alexander, and R. W. Boswell, “Axial force imparted by a current-free magnetically expanding plasma,” *Physics of Plasmas*, vol. 19, no. 8, pp. 083509–083509–8, Aug. 2012.

[170] A. Fruchtman, G. Makrinich, and J. Ashkenazy, “Two-dimensional equilibrium of a low temperature magnetized plasma,” *Plasma Sources Sci. Technol.*, vol. 14, no. 1, p. 152, Feb. 2005.

[171] S. I. Krasheninnikov, A. Y. Pigarov, D. A. Knoll, B. LaBombard, B. Lipschultz, D. J. Sigmar, T. K. Soboleva, J. L. Terry, and F. Wising, “Plasma recombination and molecular effects in tokamak divertors and divertor simulators,” *Physics of Plasmas (1994-present)*, vol. 4, no. 5, pp. 1638–1646, May 1997.

[172] S. I. Krasheninnikov, A. Y. Pigarov, and D. J. Sigmar, “Plasma recombination and divertor detachment,” *Physics Letters A*, vol. 214, no. 5–6, pp. 285–291, May 1996.

[173] A. Y. Pigarov and S. I. Krasheninnikov, “Application of the collisional-radiative, atomic-molecular model to the recombining divertor plasma,” *Physics Letters A*, vol. 222, no. 4, pp. 251–257, Nov. 1996.

[174] N. Ohno, N. Ezumi, S. Takamura, S. I. Krasheninnikov, and A. Y. Pigarov, “Experimental Evidence of Molecular Activated Recombination in Detached Recombining Plasmas,” *Phys. Rev. Lett.*, vol. 81, no. 4, pp. 818–821, Jul. 1998.

[175] I. Méndez, F. J. Gordillo-Vázquez, V. J. Herrero, and I. Tanarro, “Atom and Ion Chemistry in Low Pressure Hydrogen DC Plasmas,” *J. Phys. Chem. A*, vol. 110, no. 18, pp. 6060–6066, May 2006.

[176] W. Lotz, “Electron-Impact Ionization Cross-Sections and Ionization Rate Coefficients for Atoms and Ions,” *The Astrophysical Journal Supplement Series*, vol. 14, p. 207, May 1967.

[177] U. Fantz, D. Reiter, B. Heger, and D. Coster, “Hydrogen molecules in the divertor of ASDEX Upgrade,” *Journal of Nuclear Materials*, vol. 290–293, pp. 367–373, Mar. 2001.

[178] R. E. H. Clark and D. Reiter, *Nuclear Fusion Research: Understanding Plasma-Surface Interactions*. Springer Science & Business Media, 2005.

[179] U. Wenzel, D. Schroder, W. Bohmeyer, and G. Fussmann, “A plasma beam passing from the ionizing to the recombining state,” *IEEE Transactions on Plasma Science*, vol. 33, no. 2, pp. 366–367, Apr. 2005.

[180] J. L. Kline, E. E. Scime, R. F. Boivin, A. M. Keesee, and X. Sun, “Slow wave ion heating in the HELIX helicon source,” *Plasma Sources Sci. Technol.*, vol. 11, no. 4, p. 413, Nov. 2002.

[181] S. I. Krasheninnikov, A. Y. Pigarov, T. K. Soboleva, and D. J. Sigmar, “Plasma-neutral gas interaction in a tokamak divertor: Effects of hydrogen molecules and plasma recombination,” *Journal of Nuclear Materials*, vol. 241–243, pp. 283–287, Feb. 1997.

[182] H. Kastelewicz and G. Fussmann, “Plasma Modelling for the PSI Linear Plasma Device,” *Contrib. Plasma Phys.*, vol. 44, no. 4, pp. 352–360, Jul. 2004.

[183] K. J. Gibson, P. K. Browning, B. Mihaljcic, D. A. Forder, and J. Hugill, “Studies of detached plasmas on the ULS divertor simulator,” *Journal of Nuclear Materials*, vol. 313–316, pp. 1253–1257, Mar. 2003.

[184] D. O’Connell, T. Gans, D. L. Crintea, U. Czarnetzki, and N. Sadeghi, “Neutral gas depletion mechanisms in dense low-temperature argon plasmas,” *J. Phys. D: Appl. Phys.*, vol. 41, no. 3, p. 035208, Feb. 2008.